Role of $Na_v1.6$ and Visual Experience in Retinal and Brain Maturation during the Early Postnatal Period

by

Leona W. G. Chu

Submitted in partial fulfilment of the requirements
for the degree of Master of Science

at

Dalhousie University
Halifax, Nova Scotia
August 2016

Dedicated to my Father, K.B. Chu
Whose memory has served as a constant reminder of this once impossible dream.

TABLE OF CONTENTS

LIST OF TABLES

LIST OF FIGURES

Abstract

The *Scn8a* gene encodes the voltage-gated sodium channel isoform $Na_v1.6$, playing a key role in saltatory conduction across the nodes of Ranvier in the CNS. One *Scn8a* mutation, termed **d**egenerating **mu**scle (*dmu*) (*Scn8a*$^{dmu/dmu}$) results in premature protein synthesis, causing reduced retinal function, hindlimb paralysis and premature death, suggesting possible disruptions to overall cellular integrity and functions. In my dissertation, I sought to understand how the *Scn8a*^{dmu} mutation asserts its pathology. Disparity in gene expression patterns were identified between mutants and wildtype animals through qRT-PCR analysis of 11 genes. Results suggested a trend towards downregulation of genes involved with intracellular transport in mutants. Next, I examined the state of the intracellular scaffold within the neurons of mutant animals by staining for neurofilaments. The neurofilamentous network of mutant retina and cerebella are in a state of disarray. This disruption may be the root cause of observed phenotypes manifested by mutant animals.

LIST OF ABBREVIATIONS AND SYMBOLS USED

A

α	alpha
Aβ	amyloid beta peptide
AC	amacrine cell
AD	Alzheimer's disease
AIS	Axon initial segment
ALS	Amyotrophic lateral sclerosis
Ank3	Ankyrin G
ANOVA	analysis of variance
App	Amyloid beta precursor protein

B

β	beta
Bdnf	Brain-derived neurotrophic factor
BP	bipolar cell
bp	base pair
Bsl1	Serine - threonine protein phosphatase BSL1

C

cDNA	complementary deoxynucleic acid
CMT	Charot-Marie-Tooth disease
CNS	central nervous system
Cntf	Ciliary neural trophic factor
C_T	cycle threshold
CTRL	control

D

Da	Dalton
dmu	degenerating muscle
DNA	deoxyribonucleic acid
dNTP	delta (N) deoxyribonucleotide. (N) indicates that it is a mixture of 4 base deoxyribonucleotides ATP, TTP, CTP and GTP
DR	dark-reared

E

E(#)	Embryonic day (#)
ER	endoplasmic reticulum
ERG	electroretinogram
ERK	Extracellular signal-related kinases
Erk5	mitogen-activated protein kinase 5

G

γ	gamma
Gapdh	Glyceraldehyde 3-phosphate dehydrogenase
GC	Ganglion cells
GCL	Ganglion cell layer
Gfap	Glial fibrillary acidic protein

H

H&E	hematoxylin & eosin
HC	horizontal cell
HCl	hydrochloric acid
HEPA	high efficiency particulate arrestance
Hprt1	hypoxanthine phosphoribosyltransferase 1

I

IFAPS	intermediate-filament-associated proteins
IHC	immunohistochemistry
INL	inner nuclear layer
IPL	inner plexiform layer

J

Jak-STAT	Janus kinase/Signal Transducers and Activators of Transcription
JAX	The Jackson Laboratory
Jip1	JNK-interacting protein 1
JNK	Jun N-terminal kinase

L

LCA	Leber's congenital amaruosis
LGN	lateral geniculate nucleus
LR	light-reared

M

Map1b	microtubule-associated protein 1b
MAPK	Mitogen-activated protein kinase
med	motor endplate disease
Mef2	myocyte enhancing factor 2
miRNA	micro-RNA
mRNA	messenger ribonucleic acid
Mut	Mutant (= *Scn8a*$^{dmu/dmu}$)

N

$Na_v1.6$	voltage-gated sodium channel 1.6
NBF	neutral buffered formalin
NF	neurofilament
NF-H	neurofilament-heavy chain
NF-L	neurofilament-light chain
NF-M	neurofilament-medium chain
NTSC	National Television System Committee

O

O.C.T.	Optimal Cutting Temperature
ONL	outer nuclear layer
OPL	outer plexiform layer
OS	outer segments

P

P(#)	Postnatal day (#)
p75NTR	p75 neurotrophin receptor (low-affinity)
Pax6	Paired Box gene 6
PB	phosphate buffer
PBS	phosphate buffered saline
PCR	polymerase chain reaction
PD	Parkinson's disease
PFA	paraformaldehyde
PI3K	Phosphatidylinositol 3-kinase
PI3K-Akt	Phosphatidylinositol-3 kinase-Protein kinase B
PLCγ	phospholipase C gamma
PNS	peripheral nervous system
PKA	protein kinase A
PKC	protein kinase C
Pum2	Pumilio RNA-binding family member 2
PVC	poly(vinyl chloride)

Q

qRT-PCR	quantative reverse transcriptase polymerase chain reaction

R

RGC	retinal ganglion cell
RNA	ribonucleic acid
RPE	retinal pigment epithelium

S

SC	superior colliculus
Scn10a	sodium channel subunit alpha-10
Scn11a	sodium channel subunit alpha-11
Scn1a	sodium channel subunit alpha-1
Scn1b	sodium channel subunit beta-1
Scn2a	sodium channel subunit alpha-2
Scn3a	sodium channel subunit alpha-3
Scn4a	sodium channel subunit alpha-4
Scn4b	sodium channel subunit beta-4
Scn5a	sodium channel subunit alpha-5
Scn6a	sodium channel subunit alpha-6
Scn7a	sodium channel subunit alpha-7
Scn8a	sodium channel subunit alpha-8
Scn9a	sodium channel subunit alpha-9
SDS	sodium dodecyl sulfate
SEM	standard error of the mean
snr	spontaneous $Na_v1.6$ rescue
SYBR Green	N',N'-dimethyl-N-[4-[(E)-(3-methyl-1,3-benzothiazol-2-ylidene)methyl]-1-phenylquinolin-1-ium-2-yl]-N-propylpropane-1,3-diamine

T

Trk	Tropomyosin-related kinase
TrkB	Tropomyosin receptor kinase B (high-affinity)
TTX	tetrodotoxin
TTX-R	tetrodotoxin-resistant
TTX-S	tetrodotoxin-sensitive

V

VGSC	voltage-gated sodium channel

W

WT	wildtype (= *Scn8a*$^{+/+}$)

Acknowledgements

I sincerely thank my Supervisory Committee (Supervisors Dr. Patrice Côté, Dr. Sara Iverson, and Committee members Dr. Tamara Franz-Odendaal, Dr. Paul Bentzen and Dr. Steven Barnes). I am very grateful for all of your high expectations and attention to detail, which has instilled a work ethic in me to reach for the impossible. Thank you all for your encouragement, support and believing in me, and providing me opportunities that, although I thought were impossible at first, has taught me more than other graduate students would encounter.

To my lifetime best friend, Melvin Kwok, thank you for your endless encouragement, patience and understanding. Like family, you always stood firmly by my side, supporting me in my times of struggle. You saw something in me that I thought I had lost and I am thankful for your constant reminders that there is light at the end of this dark tunnel. You are my sanity, and in many ways, this is your achievement as well.

Thank you to my family for your constant support. Although you live on the other side of the country, your support and "presence" has kept me grounded and held me together outside of academia.

I thank Dr. R. Kothary (*Scn8a*^{dmu} mouse line, University of Ottawa, Canada) for providing the *Scn8a*^{dmu} mouse line. Thank you to Dr. P. Bentzen (Dalhousie University, Canada) for allowing me to use his Roche Lightcycler II 480 Real-Time PCR system, and to Dr. J. Laroche (Dalhousie University, Canada) for allowing me to use her NanoDrop 2000 spectrophotometer. I thank Zabrina Prescott and Dr. B.K. Hall (Dalhousie University) for showing me how to paraffin embed and section murine brain tissues and allowing me to use their histology lab reagents and equipment. Thank you to the Retina and Optic Nerve Research Laboratory (Dalhousie University) for allowing me to use their confocal microscope. Thank you to Honours students Nada Ismaiel, Catherine Smith, and Myuran Thana (Dalhousie University) for their assistance in the behavioural studies performed using *snr* mice (behavioural monitoring study, balance beam study, Rotarod study). I sincerely thank Melvin Kwok for scoring all of the behavioural study videos. I also acknowledge Dalhousie University for partial doctoral funding for L.W.G.C.

Lastly, I would like to express my gratitude to Dr. Patrick Lett for financial assistance when I needed it the most.

The work presented in this thesis was supported by discovery and equipment grants from the Natural sciences and Engineering Research Council (NSERC), and also from the Canadian Foundation for Innovation (CFI) for the Leaders Opportunity Fund to P.D.C.

CHAPTER 1: INTRODUCTION

1.1 Voltage-gated sodium channels (VGSC) and their role in the central nervous system

Voltage-gated sodium channels (VGSC) are a class of macromolecular protein complexes that span the lipid bilayer of the cell membrane, allowing an influx of sodium ions (Na^+) into the cell in a very efficient manner (Felix, 2000). This flow of Na^+ creates electrical potentials, producing rapid changes in the transmembrane voltage (Felix, 2000). VGSC are widely distributed in both excitable and non-excitable cells, where they play a critical role in the initiation and propagation of action potentials (Catterall *et al*., 2005). These channels are essential in the process of saltatory conduction, where nerve impulses are propagated from one node of Ranvier to the next along myelinated axons, thereby increasing the conduction velocity of action potentials. In mammals, the VGSC family consists of ten channel isoforms ($Na_v1.1$-$Na_v1.9$) encoded by ten genes (*Scn1a-Scn11a*) that have more than 50% amino acid identity (Goldin *et al*., 2000; Yu and Catterall, 2003; Catterall *et al*., 2005). The channels are characterized by their relative sensitivities to tetrodotoxin (TTX) and inactivation kinetics into two groups: (1) TTX-sensitive (TTX-S) channels are blocked with TTX in the nanomolar (nM) range and have faster inactivation kinetics, and (2) TTX-resistant (TTX-R) channels that are blocked with TTX in the micromolar-millimolar (μM-mM) range and have slower inactivation kinetics (Table 1.1) (Koopmann *et al*., 2006; Savio-Galimberti *et al*., 2012). Out of the ten sodium channel isoforms, the *Scn6a*/*Scn7a* gene is part of the $Na_v2.1$ subfamily that has significant amino acid differences (George *et al*., 1992), and has been proposed to be involved in the mechanism that senses extracellular sodium concentrations in the brain (Hiyama *et al*., 2002; Noda, 2006; Noda and Hiyama, 2015).

Sodium channels consist of a large α-subunit (~260kDa) that associates with auxiliary β-subunits (~36kDa) (Yu and Catterall, 2003). The α-subunits are organized into four homologous domains (I-IV), each of which contain six α-helical transmembrane segments (S1-S6), with three large intracellular loops as well as cytoplasmic N-terminal and C-terminal domains (Figure 1.1). The S4 transmembrane of each domain contains a high concentration of positively charged amino acids, functioning as the core of the voltage sensor responsible for the voltage-dependent channel activation (Savio-

Table 1.1: Channelopathies that have been described in the voltage-gated sodium channel (VGSC) family.

Gene	Channel	Primary tissues of channel expression	Tetrodotoxin (TTX) sensitivity	Channelopathy	Model	References
Scn1a	$Na_v1.1$	CNS/PNS	sensitive	Doose syndrome (myoclonic astatic epilepsy)	Human	Escayg et al., 2000;
				Dravet syndrome [severe myoclonic	Human	Spampanato et al., 2001;
				epilepsy of infancy, (SMEI)]		Suguwara et al., 2001;
				familial autism	Human	Wallace et al., 2001;
				familial febrile convulsions	Human	Fujiwara et al., 2003;
				familial hemiplegic migraine (FHM)	Human	Nabbout et al., 2003;
				generalized epilepsy with febrile seizures plus (GEFS+)	Human	Wallace et al., 2003;
				intractable childhood eiplepsy with	Human	Weiss et al., 2003;
				generalized tonic-clonic seizures		Fukuma et al., 2004;
				Lennox-Gastaut syndrome	Human	Kanai et al., 2004;
				Panayiotopoulos syndrome	Human	Dichgans et al., 2005;
				Rasmussen's encephalitis	Human	Mantegazza et al., 2005;
				West syndrome (infantile spasms)	Human	Meisler and Kearney, 2005; Lossin, 2009
Scn2a	$Na_v1.2$	CNS/PNS	sensitive	benign familial infantile epilepsy	Human	Sugawara et al., 2001b;
				early infantile epileptic encephalopathy	Human	Heron et al., 2002;
				familial autism	Human	Weiss et al., 2003;
				familial neonatal-infantile seizures	Human	Berkovic et al., 2004;
				inherited febrile seizures and epilepsy	Human	Kamiya et al., 2004
				severe myoclonic epilepsy of infancy	Human	
Scn3a	$Na_v1.3$	CNS/PNS	sensitive	focal epilepsy in children	Human	Gastaldi et al., 1997;
				potential contributor to peripheral neuropathic pain after spinal cord injury	Human	Whitaker et al., 2001; Hains et al., 2003
Scn4a	$Na_v1.4$	skeletal muscle	sensitive	Congenital myasthenic syndrome	Human	Fontaine et al., 1990; Ptacek et al., 1991;

Gene	Channel	Primary tissues of channel expression	Tetrodotoxin (TTX) sensitivity	Channelopathy	Model	References
				Hyperkalemic periodic paralysis	Human	Ptacek et al., 1992; Cannon and Strittmatter, 1993;
				Hypokalemic periodic paralysis	Human	Lerche et al., 1993; Chahine et al., 1994;
				malignant hyperthermia susceptibility	Human	Mitrović et al., 1995; Cannon, 1996; Cannon, 1997;
				Paramyotonia congenita	Human	Bulman et al., 1999; Jurkat-Rott et al., 2000;
				potassium-aggravated myotonia	Human	Bendahhou et al., 2001; Kuzmenkin et al., 2002
Scn5a	$Na_v1.5$	cardiac tissue	resistant	Atrial standstill	Human	Bennett et al., 1995; Wang et al., 1995;
				Brugada syndrome (idiopathic ventricular fibrillation)	Human	Wang et al., 1995b; Chen et al., 1998;
				Dilated cardiomyopathy	Human	Bezzina et al., 1999; Schott et al., 1999;
				Familial atrial fibrillation	Human	Akai et al., 2000; Ackerman et al., 2001;
				isolated cardiac conduction system defects, diseases, disorders and arrhythmias	Human	Bezzina et al., 2001; Benson et al., 2003; Groenewegen et al., 2003; Tan et al., 2003;
				Lenegre-Lev syndrome (progressive familial heart block)	Human	Veldcamp et al., 2003; McNair et al., 2004;
				Long QT syndrome	Human	George et al., 2005; Meregalli et al., 2005;
				Nonprogressive familial heart block	Human	Probst et al., 2006
				Paroxysmal familial ventricular fibrillation	Human	

Gene	Channel	Primary tissues of channel expression	Tetrodotoxin (TTX) sensitivity	Channelopathy	Model	References
				Sick sinus syndrome, autosomal-recessive	Human	
				Sudden infant death syndrome (SIDS)	Human	
Scn6a/ *Scn7a*	Na_x	brain	unknown	lack of Na_x in neurons from CVO part of brain affects the ability to control body fluids and ionic balance	Human, Mouse	Hiyama et al., 2002; Noda, 2006;
				Temporal lobe epilepsy	Human	Gorter et al., 2010
Scn8a	$Na_v1.6$	CNS/PNS	sensitive	absence epilepsy	Human	Burgess et al., 1995; Kohrman et al., 1996b; Meisler et al., 2004; Trudeau et al., 2005; Wasserman et al., 2005; Papale et al., 2009; Noujaim et al., 2012; Veeramah et al., 2012; de Kovel et al., 2014; Vaher et al., 2014; Blanchard et al., 2015; Larson et al., 2015; Wagnon and Meisler, 2015
				ataxia, tremors and other movement disorders	Human, Mouse	
				cerebellar ataxia in ***jolting*** mice	Mouse	
				cerebellar atrophy	Human, Mouse	
				cognitive impairment with or without cerebellar ataxia	Human	
				early infantile epileptic encephalopathy and sudden unexplained death in epilepsy (SUDEP)	Human	
				early lethality (in ***Scn8a***-null animal models)	Mouse	
				mental retardation	Human	
				motor end-plate disease (***med***) in mice	Mouse	
				prolonged cardiac action potentials	Mouse	
				Severe depression/suicide attempt	Human	

Gene	Channel	Primary tissues of channel expression	Tetrodotoxin (TTX) sensitivity	Channelopathy	Model	References
Scn9a	$Na_v1.7$	PNS	sensitive	congenital insensitivity to pain (CIP), autosomal-recessive	Human	Cummins et al., 2004;
				familial primary erythermalgia	Human	Yang et al., 2004;
				familial rectal pain	Human	Dib-Hajj et al., 2005;
				paroxysmal extreme pain disorder (PEPD)	Human	Nassar et al., 2005;
				Small fiber neuropathy	Human	Lampert et al., 2010
Scn10a	$Na_v1.8$	PNS	resistant	aberrant ventricular conduction in the heart	Human	Rabert et al., 1998;
				Brugada syndrome	Human	Yoshimura et al., 2001;
				upregulated in some models of inflammatory pain	Human	Lai et al., 2002;
				pain sensitization	Mouse	Chambers et al., 2010
				peripheral pain syndromes	Human	
Scn11a	$Na_v1.9$	PNS	resistant	Loss of pain perception	Human	Dib-Hajj et al., 1998;
				pain sensitization	Mouse	Tate et al., 1998;
				potential role in nociception, hyperalgesic syndromes	Human	Priest et al., 2005

Gene	β-unit	α-unit (VGSC association)	Primary tissues of β-unit expression	Channelopathy	Model	References
Scn1b	$Na_v\beta 1$	$Na_v1.1$-$Na_v1.7$	CNS/PNS, glia cardiac muscle skeletal muscle	Brugada syndrome	Human	Wallace et al., 1998; Coward et al., 2001; Meadows et al., 2002; Wallace et al., 2002; Audenaert et al., 2003; Chen et al., 2004; Pertin et al., 2005; Pertin et al., 2007; Scheffer et al., 2007; O'Malley et al., 2009; Orrico et al., 2009; Patino et al., 2009
				Dravet syndrome	Human, Mouse	
				epileptic syndromes	Human	
				febrile seizures	Human	
				Generalized epilepsy with febrile seizures plus (GEFS+)	Human	
				temporal lobe epilepsy	Human	
				traumatic nerve injury	Human	
Scn2b	$Na_v\beta 2$	$Na_v1.1$, $Na_v1.2$, $Na_v1.5$-$Na_v1.7$	CNS/PNS, glia cardiac tissue	inflammatory pain	Mouse	Coward et al., 2001; Pertin et al., 2005; Lopez-Santiago et al., 2006; O'Malley et al., 2009
				multiple sclerosis	Mouse	
				post-trauma neuropathic pain	Mouse	
				traumatic nerve injury	Human	
Scn3b	$Na_v\beta 3$	$Na_v1.1$-$Na_v1.3$ $Na_v1.5$	CNS/PNS adrenal glands, kidney	Temporal epilepsy	Human	Casula et al., 2004; van Gassen et al., 2009
Scn4b	$Na_v\beta 4$	$Na_v1.1$, $Na_v1.2$, $Na_v1.5$	CNS/PNS, glia cardiac muscle skeletal muscle	Huntington's disease	Human, Mouse	Domingo et al., 2006; Oyama et al., 2006
				Long QT syndrome	Human	
				traumatic nerve injury	Human	

Figure 1.1: Structure of the α-subunit of the voltage-gated sodium channels. (**A**) An unfolded schematic representation of the voltage-gated sodium channels (VGSC) α-subunit is presented. Extracellular space is located above the lipid bilayer and intracellular compartment is below the lipid bilayer. Roman numerals (I - IV) depict the individual domains of the VGSC starting with the first domain at the N-terminus on the left to the fourth domain at the C-terminus on the right. Each domain is colour coded to identify and separate domains I - IV. The fourth α-helical transmembrane segment of each domain is enriched with positively charged amino acids as represented in this schematic by (**+**) symbol. The elongated extracellular loops between transmembrane segments 5 and 6 of each domain as well as the inherent space between them are responsible for the formation of the functional sodium ion pore is indicated. The intracellular segment connecting domain (III) to domain (IV) forms the functional inactivation gate in the final VGSC confirmation. Indicated by red dots in domain (I) are the locations of both the *Scn8a*^{med} and *Scn8a*^{dmu} mutations. (**B**) An enlarged domain (I) is presented to illustrate the characteristics of a single domain. Each domain consists of 6 α-helical transmembrane segments. These segments are numbered with Arabic numerals (1 – 6) with segment 1 being the closest to the N-terminus. The fourth α-helical transmembrane segment is enriched with positively charged amino acids forming the voltage sensor in the properly folded VGSC. Red dots mirror the locations of *Scn8a*^{med} and *Scn8a*^{dmu} mutations above. (**C**) A diagram of the three-dimensional conformation for VGSC is depicted. The central hydrophobic core formed by the domains I - IV becomes the sodium ion channel. The fourth transmembrane segments of each domain are coloured grey in this figure to illustrate the locations of the voltage sensor relative to the overall structure of the VGSC. The formation of a sodium ion pore along with voltage sensor transmembrane domains and the inactivation gate together forms a functional VGSC. In **(A)**, **(B)**, and **(C)** the VGSC is flanked by a schematic representation of β-subunits that are necessary for both transport and proper function of VGSCs. Figure adapted from Meisler and Kearney, 2005). Illustration drawn by L.W.G. Chu, 2016.

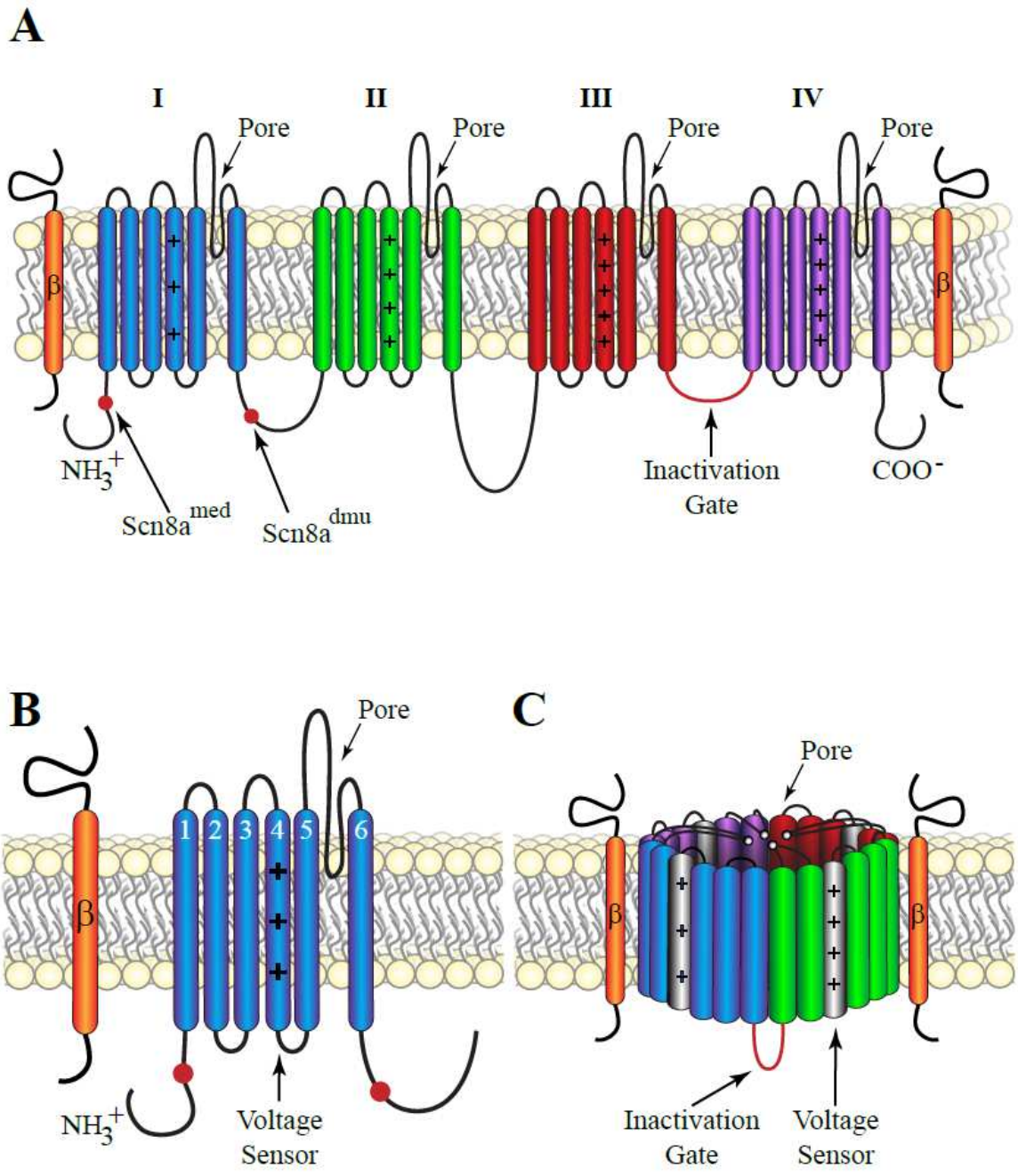
A
I
II
III
IV
Pore
Pore
Pore
Pore
β
β
+
NH_3^+
$Scn8a^{med}$
$Scn8a^{dmu}$
Inactivation
Gate
COO^-
B
Pore
1
2
3
4
5
6
β
NH_3^+
Voltage
Sensor
C
Pore
β
β
Inactivation
Gate
Voltage
Sensor

Galimberti *et al*., 2012). The hairpin-like P(ore)-loop between S5-S6 segments is part of the channel pore, forming a narrow, ion-selective filter that controls ion selectively (Caterall, 2000; Yu and Catterall, 2003; Savio-Galimberti *et al*., 2012). The short intracellular loop connecting domains III and IV serves as the inactivation gate; folding into and thereby blocking the pore of the channel structure during membrane depolarization (Catterall *et al*., 2005). Distinct α-subunit isoforms are expressed in tissue-specific patterns, displaying differences in gating behaviour, allowing for specific physiological roles (Waxman, 2012).

The pore-forming α-subunit is sufficient for functional expression; but when assembled with β-subunits, the kinetics and voltage dependence of channel gating are modified (Catterall *et al*., 2005). There are four β-subunit isoforms (β1-β4), encoded by four genes (*Scn1b-Scn4b*) respectively (Cusdin *et al*., 2008; Brakenbury and Isom, 2011; O'Malley and Isom, 2015). These auxiliary β-subunits are involved in channel localization, trafficking, facilitate the interaction of VGSC with cell adhesion molecules, the extracellular matrix, and the intracellular cytoskeleton (Qu *et al*., 2001; McEwen *et al*., 2004; Namadurai *et al*., 2015).

Inherited channelopathies do not necessarily only affect specific tissues or organs, but some can also affect the entire nervous system. In order to understand how these mutations in ion channel genes results in disease, the normal function and location of the channel must first be determined. Consequences of the mutation that alter its formation and physiological properties, and possible compensatory changes in other channels can then be examined through the use of animal models of monogenic channelopathies. Although many VGSC are predominantly expressed in both the central and peripheral nervous systems (CNS and PNS), *Scn4a* is the main channel expressed in skeletal muscle, while *Scn5a* predominates in cardiac tissue (Plummer and Meisler, 1999). Because of the crucial role that VGSC play in excitable tissues and their distribution, mutations in these genes result in multiple inherited diseases, channelopathies, with potentially dire consequences. Epilepsy, seizures, paralysis, ataxia, and neuropathic pain are just a few of the symptoms that result from VGSC channelopathies (Table 1.1) (Caterall, 2000; Felix, 2000; Koopmann *et al*., 2006; Andavan and Lemmens-Gruber, 2011; Vacher and Trimmer, 2012). The VGSC $Na_v1.6$ channel, which is highly expressed in both the CNS and PNS, is the focus for the remainder of this thesis.

The $Na_v1.6$ channel, encoded by the *Scn8a* gene (Catterall, 2000; Goldin *et al*., 2000) is one of the most abundant VGSCs in the brain, and plays an essential role in action potential initiation and propagation in the CNS and PNS (Meisler *et al*., 2001; Trudeau *et al*., 2006). This channel was identified as the major channel in the axon initial segments (AIS) and nodes of Ranvier in both the CNS and PNS (Burgess *et al*., 1995; Schaller *et al*., 1995; Caldwell, 2000; Caldwell *et al*., 2000; Krzemien *et al*., 2000; Schaller and Caldwell, 2000; Tzoumaka *et al*., 2000; Boiko *et al*., 2001; Boiko *et al*., 2003; Van Wart and Matthews, 2006; Van Wart *et al*., 2007; Lorincz and Nusser, 2008; 2010), highlighting the importance of this VGSC in saltatory conduction. In the adult retina, major sites of $Na_v1.6$ expression include both the ganglion cell layer and the inner nuclear layer (Fjell *et al*., 1997; Krzemien *et al*., 2000; Côté *et al*., 2005; Mojumder *et al*., 2007). In addition, $Na_v1.6$ is found to be concentrated specifically at the nodes of Ranvier of myelinated but absent from the unmyelinated axons in the optic nerve (Boiko *et al*., 2001). Because *Scn8a* is widely expressed in neurons throughout both the CNS and PNS, a deficiency in this gene will therefore affect many different neuronal populations.

Numerous mouse strains, either naturally occurring or intentionally produced, harbour mutations in *Scn8a* (Meisler *et al*., 2001) (Table 1.2). Initially described by Duchen, the original ***m****otor* ***e****ndplate* ***d****isease* (*med*) mouse ($Scn8a^{med}$) was a null mutation in *Scn8a*, resulting in reduced neuromuscular transmission, leading to paralysis and death at approximately three weeks of age (Duchen *et al*., 1967; Duchen, 1970; Burgess *et al*., 1995). Null mutations of *Scn8a* in the mouse result in neurological disorders including tremor, ataxia, progressive paralysis and eventually lethality by approximately three weeks of age (Burgess *et al*., 1995; Kohrman *et al*., 1996; Meisler *et al*., 2001). Electrophysiological abnormalities of cerebellar Purkinje cells, pyramidal neurons, motor neurons, and the dorsal cochlear nucleus have been observed in mice that are deficient for the $Na_v1.6$ sodium channel protein (Raman *et al*., 1997; Chen *et al*., 1999; Maurice *et al*., 2001; Khaliq *et al*., 2003). In the hypomorphic allele, $Scn8a^{medJ}$, *Scn8a* mRNA and $Na_v1.6$ sodium channel protein is reduced to 10% of normal levels (Kearney *et al*., 2002). $Scn8a^{medJ/medJ}$ homozygous mice display tremors, ataxia, and develop a progressive

Table 1.2: Murine mutations that have been described in the *Scn8a* gene. The coloured dots illustrate the positions of the various mouse mutations in *Scn8a*. Illustration drawn by L.W.G. Chu, 2016.

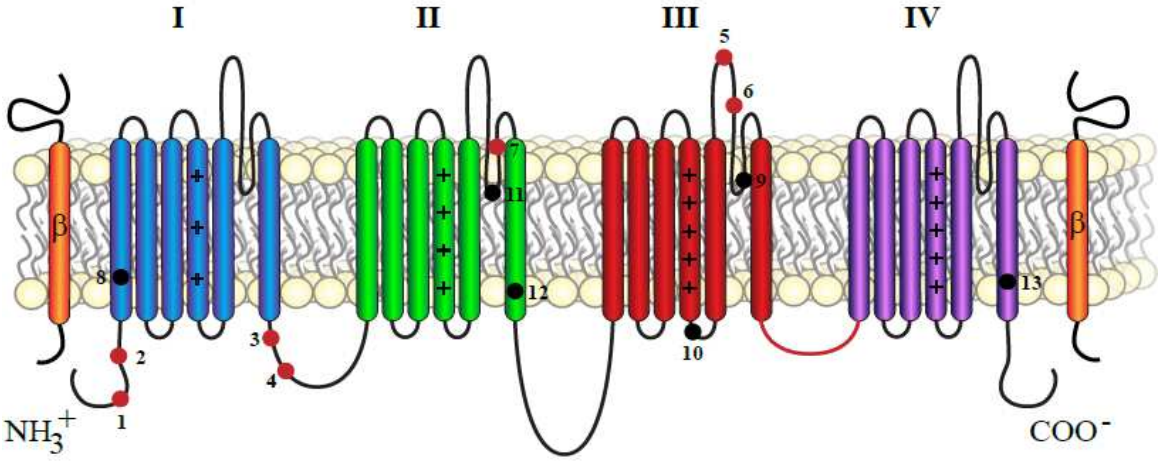

● = Null Alleles (null mutations that do not produce functional $Na_V1.6$)

● = Hypomorph Alleles (mutations that express $Na_V1.6$ at reduced levels)

	Allele	Phenotype of Homozygotes	Mutation details	Notes	References
1	ataxia3	null	S21P	trafficking mutant	Sharkey et al., 2009a
2	med	null	LINE insertion into exon 2		Kohrman et al., 1996
3	med-tg	null	20 kb deletion at site of transgene insertion		Kohrman et al., 1995
4	dmu	null	single nucleotide deletion in exon 10A		De Repentigny et al., 2001
5	nmf2	null	N1370T (missense mutation)	nmf2 (mouse line) (ENU-induced mutation)	Buchner et al., 2004
6	nmf5	null	I1392F (missense mutation)	nmf5 (mouse line) (ENU-induced mutation)	Buchner et al., 2004
7	8J	null	V929F	spike-wave discharges in heterozygotes	Papale et al., 2009
8	med-J	severe hypomorph	4 base pair deletion in 5' donor site of exon 3	5-10% of wildtype channel expression splicing (strain dependent)	Kohrman et al., 1996
9	nmf58	severe hypomorph	L1404H (missense mutation)	nmf58 (mouse line) (ENU-induced mutation)	Buchner et al., 2004
10	med-jo	mild hypomorph	A1319T	10 mV positive shift in voltage dependence of activation	Smith and Goldin, 1999
11	tremorD	mild hypomorph	W935L (missense mutation)	ENU-induced mutation	Timms and Beutler, 2008 (JAX, unpublished)
12	Clth	mild hypomorph	D981V	defective hearing	Mackenzie et al., 2009
13	9J	mild hypomorph	DI1750 (single amino acid deletion in last exon)	deletion located in domain IV, segment S6 (D4S6)	Jones et al., 2016

dystonic phenotype, resembling primary torsion dystonia in humans (Hamann *et al*., 2003). Subsequently, the ***d****egenerating* ***mu****scle* (*dmu*) (*Scn8a*^{dmu}) mutation arose as a novel spontaneous autosomal recessive mutation within a colony of (C57BL/6 X C3H) F_1 hybrid mice (De Repentigny *et al*., 2001). *Scn8a*^{dmu} has been identified to be allelic to *Scn8a*^{med}, and has been mapped to the (*med*) locus (Figure 1.1) (De Repentigny *et al*., 2001). At birth, these mice are indistinguishable from other littermates. As littermates start to grow, gain weight and begin to walk, in contrast, mutant mice lose weight, gradually display hindlimb paralysis, skeletal and cardiac muscle degeneration, and have difficulty breathing, eventually dying at approximately three weeks of age (around the time of weaning) from unknown causes (De Repentigny *et al*., 2001). Previous experiments have determined that the *dmu* mutation consists of a single nucleotide deletion in exon 10A of the *Scn8a* coding sequence (position 1538 of GenBank accession number NM_011323) (Côté *et al*., 2005). This deletion results in a frameshift mutation in the *Scn8a* gene, resulting in the premature termination of protein synthesis (Côté *et al*., 2005). As a consequence, these mutant mice are unable to produce a functional voltage-gated sodium channel isoform $Na_v1.6$ (Côté *et al*., 2005). Electroretinogram (ERG) measurements on dark-adapted postnatal day (P16) *Scn8a*$^{dmu/dmu}$ mice show defects in their photoreceptors (Côté *et al*., 2005). The activation of the light-induced hyperpolarization of photoreceptor cells (the a-wave) is markedly reduced, while 'downstream' components of the ERG, the b-wave and its subcomponents, the oscillatory potentials, are almost extinguished (Côté *et al*., 2005; Smith and Côté, 2012). Interestingly, the waveform of the P16 *Scn8a*$^{dmu/dmu}$ ERG displays a strong resemblance to the P12 ERG from normal immature mice (Côté *et al*., 2005). The period between P12-P16 is characterized by the elongation and maturation of the photoreceptor outer segments, with eye opening at around P14. However, morphological abnormalities were not detected in retinal histology, vasculature, or ultrastructure in *Scn8a*$^{dmu/dmu}$ mice (Côté *et al*., 2005). In addition, the onset of *Scn8a* transcript expression occurs at around P10 in the ganglion cell and inner nuclear layers, shortly before the elongation of the photoreceptor outer segments (Côté *et al*., 2005). Therefore, this suggests that the $Na_v1.6$ sodium channel is crucial for the physiological maturation of the photoreceptors, but not for the morphological development of the retina (Côté *et al*., 2005).

Since both *Scn8a*$^{med/med}$ and *Scn8a*$^{dmu/dmu}$ mice display abnormal ERG recordings mice (Côté *et al*., 2005), this provides evidence that the mutation in *Scn8a* plays a pivotal role in normal photoreceptor development (Côté *et al*., 2005; Smith and Côté, 2012). However, the lethality of this mutation poses a difficult challenge for prolonged studies as mice typically die at a very young age. As a consequence, the essential role that *Scn8a* plays in the developing retina cannot be accurately examined.

The neural retina is considered an exceptional model for studying the complexities of the developing nervous system due to its relatively simple structure and ease of accessibility (Flannery, 1999; Fletcher *et al*., 2011; London *et al*., 2013). Vertebrate retinas are composed of seven major cell types and organized into three main laminar structures (Blackshaw *et al*., 2004; Dowling, 2012). Lineage-tracing studies and other gene targeting strategies have shown that these seven cell types differentiate from a common pool of multipotent progenitors (Turner and Cepko, 1987; Dyer and Cepko, 2001). As vertebrate retinal development progresses, all seven cell types are generated in a precise and evolutionarily conserved chronological order, and integrate together to establish the complex architecture and connectivity of a functional retina (Figure 1.2) (Cepko *et al*., 1996; Livesey and Cepko, 2001).

1.2 Genes potentially regulated by visual experience or sodium channel activity

Deviations from this conserved developmental program results in deficiencies in function. Consequences of deviating away from normal development has been documented in studies that use the presence or absence of light stimulation to study how development is affected (Tian and Copenhagen, 2001; Akerman *et al*., 2002; Tian and Copenhagen, 2001; 2003; Wu and Chiao, 2007; He *et al*., 2011; Akimov *et al*., 2014). One of the seven cell types, bipolar cells, transmits signals from photoreceptors to ganglion cells. A study comparing light-reared (LR) to dark-reared (DR) animals found that bipolar cells from DR animals were developmentally delayed during the retinal maturation process prior to eye-opening (Wu and Chiao, 2007). Although both LR and DR animals possessed mature bipolar cells at the time of eye-opening, this study suggests that visual experience has a facilitating effect on the temporal and morphological differentiation of bipolar cells during postnatal development (Wu and Chiao, 2007). Comparisons between LR and DR animals proved that visual experience is necessary for

Figure 1.2: **(A)** Schematic representation illustrating the laminar structures of the mature murine retina. The neural retina comprises three main laminar structures: the ganglion cell layer (GCL), which contains ganglion cells and displaced amacrine cells, the inner nuclear layer (INL), containing amacrine, horizontal, bipolar interneurons and Müller glia cells, and the outer nuclear layer (ONL), which contains cone and rod photoreceptors. In between the nuclear layers are the plexiform layers. The inner plexiform layer (IPL) contains ganglion cell dendrites and amacrine and bipolar cell axons. The outer plexiform layer (OPL) consists of a dense network of synapses between bipolar and horizontal cell dendrites, and photoreceptor axons. Light enters at the bottom of the figure (yellow arrow), where the ganglion cells are located. **(B)** Murine retinal cell type differentiation occurs in two main waves. The first wave peaks at around E14.5, giving rise to 'early-born' cell types, including retinal ganglion cells (RGC), amacrine cells, horizontal cells, and cone photoreceptors. The second wave peaks at around P4, giving rise to 'late-born' cell types, including rod photoreceptors, bipolar cells and Müller glia cells. The curves depict the relative number of retinal progenitors that exit the cell cycle and commit to a specific cell fate over developmental time (e.g. RGCs start differentiating at E11, with peak differentiation at E15, and persist until shortly after birth). Figure drawn by L.W.G. Chu, 2016.

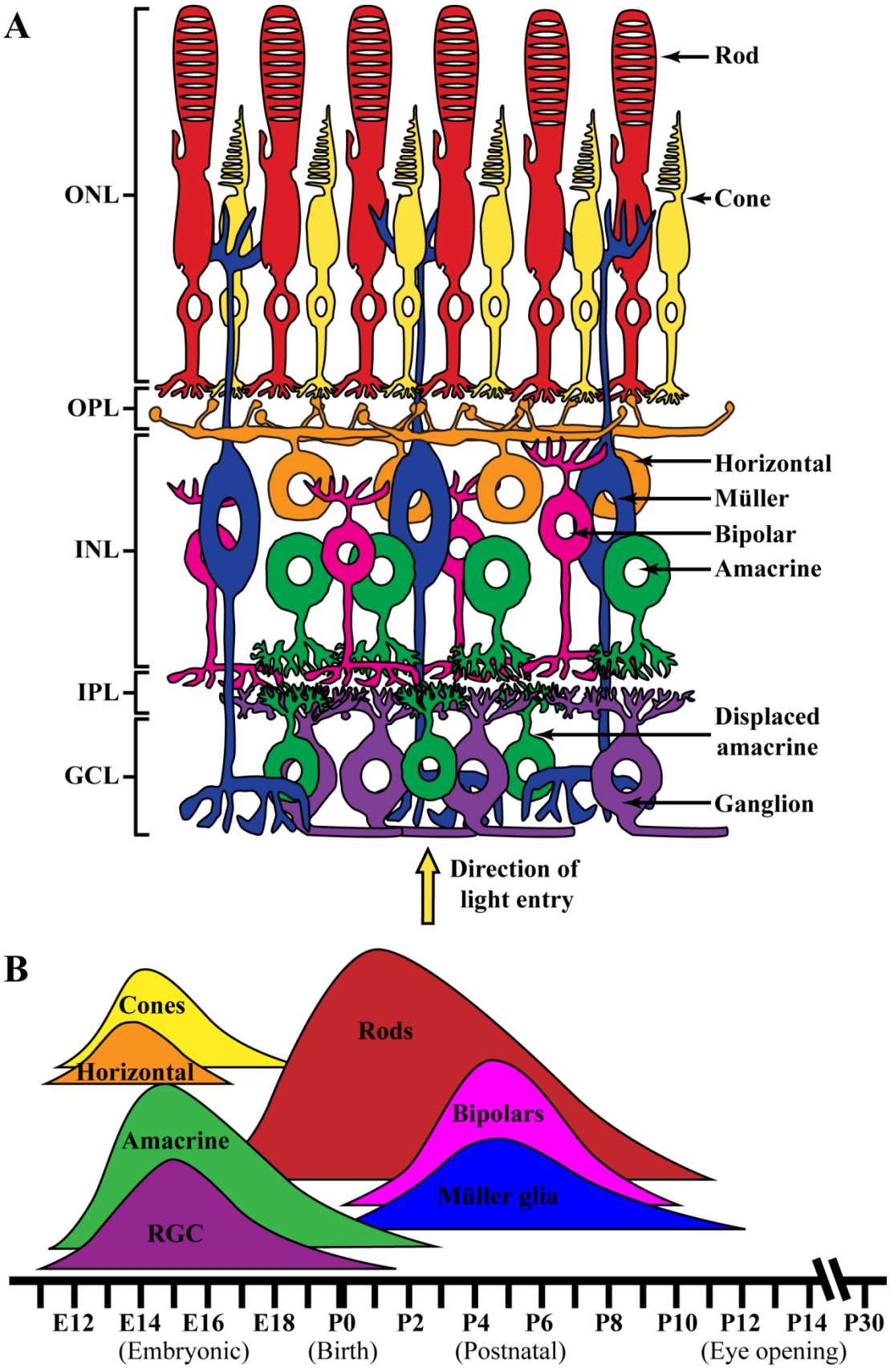
A
Rod
Cone
ONL
OPL
INL
IPL
GCL
Horizontal
Müller
Bipolar
Amacrine
Displaced
amacrine
Ganglion
Direction of
light entry
B
Cones
Horizontal
Rods
Bipolars
Amacrine
Müller glia
RGC
E12
E14
E16
E18
P0
P2
P4
P6
P8
P10
P12
P14
P30
(Embryonic)
(Birth)
(Postnatal)
(Eye opening)

synaptic pruning and maturation of RGCs in the INL, allowing RGCs to differentiate into the ON-OFF RGCs that are responsible for relaying contrasts in luminance signals (Tian and Copenhagen, 2003). In addition, it has been demonstrated that light stimulation plays an important role in the development of the retinogeniculate pathway even before eye-opening, as naturalistic visual stimuli are presented through unopened eyelids (Akerman *et al*., 2002). Light stimulation and visual experience have consequently been demonstrated to play a key role in the proper development and maturation of the retina, and even in connecting neuronal circuits that extend into the visual cortex (Tian and Copenhagen, 2001; Akerman *et al*., 2002; Tian and Copenhage, 2003; Wu and Chiao, 2007; He *et al*., 2011; Akimov *et al*., 2014).

As photons of light are received by photoreceptors of the retina, they convert the light stimuli into electrical signals. The processing of visual signals leads to the ganglion cells (GC) that transmit the visual signals as action potentials to the brain for further image processing. As the GCs are the only output cells of the retina, any disruptions in the ability to generate or propagate action potentials leads to disruptions in the ability to relay information from the eyes to the visual cortex.

When sodium channel-mediated action potentials were blocked from birth to eye-opening with the sodium channel blocker TTX, Kalil *et al*. (1986) demonstrated that connections made by GC axons with lateral geniculate nucleus (LGN) neurons and retinogeniculate synapses strongly resembled those observed in newborns. By using TTX in the eye, the generation of action potentials from $Na_v1.1$, $Na_v1.2$, and $Na_v1.6$ are abolished. This study illustrates the significance that action potentials have on the ability for the eye to carry out proper differentiation and neuron pruning required to mature into a functional adult eye (Kalil *et al*., 1986).

1.2.1 Group 1 genes: recruitment, transportation to the cell surface and function of $Na_v1.6$

In an effort to elucidate the origins of the visual abnormalities observed in *Scn8a*$^{dmu/dmu}$ mice and to determine if any changes in these genes parallel the effect of light deprivation since birth, I selected 11 genes for analysis by qRT-PCR using total RNA samples extracted from four different genotypes. These genes were divided into three different groups. The first group contained five genes that are involved in the recruitment, transportation to the cell surface and function of $Na_v1.6$. The genes studied

are involved in the trafficking of $Na_v1.6$, from the site of synthesis in the ER and Golgi apparatus, into endosomes. In turn, these endosomes become cargo vesicles that are carried along microtubules down the length of the axon to eventual incorporation into the nodes of Ranvier. These genes include neurofilament light chain (*NF-L*), JNK-interacting protein 1 (*Jip1*), amyloid precursor protein (*App*), ankyrin G (*Ank3*), and voltage-gated sodium channel type 1 beta subunit (*Scn1b*).

1.2.1.1 Neurofilament light chain (NF-L) (gene symbol: Nefl)

The most abundant form of intermediate filaments in the nervous system, NF-L serve as scaffolding proteins along with neurofilament medium chain (NF-M) and neurofilament heavy-chains (NF-H) (Perrot *et al.*, 2008; Yuan *et al.*, 2012). Neurofilaments (NF) are transported along the axon to their final destination after assembly in the cell body. They provide structural support on which microtubules can be built along the length of axons, thereby facilitating the transport of vesicular cargo by kinesin and dynein molecular motors. The proper formation of an axonal NF network is fundamental for the establishment and maintenance of axonal calibre and optimization of conduction velocity (Perrot *et al.*, 2008). The presence of a disorganized NF network is a recurring observation that is a hallmark in several neurodegenerative diseases, such as Amyotrophic lateral sclerosis, Alzheimer's disease, Charcot-Marie-Tooth disease, and Parkinson's disease (Mersiyanova *et al.*, 2000; De Jonghe *et al.*, 2001; Al-Chalabi and Miller, 2003; Perrot *et al.*, 2008; Yuan *et al.*, 2012).

1.2.1.2 JNK-interacting protein 1 (Jip1) (gene symbol: Mak8ip1)

The long-distance transport of proteins and organelles is essential in maintaining neuronal homeostasis and function (Fu and Holzbaur, 2013). In axons, the family of kinesin and dynein motors transports cargos on microtubule tracks of uniform polarity (Fu and Holzbaur, 2013). Therefore, anterograde transport, i.e. from the cell body to the synapse, is controlled by kinesins, whereas retrograde transport, i.e. from the synapse to the cell body, is controlled by dyneins (Hirokawa and Takemura, 2004).

The JNK-interacting protein 1 (Jip1) is a bidirectional scaffolding protein that interacts directly with both kinesin and dynein motor complexes (Verhey *et al.*, 2001; Fu and Holzbaur, 2013). Jip1 mediates the axonal transport of cargos, which include synaptic vesicles, signaling endosomes, lysosomes, and organelles (Hirokawa *et al.*,

2010). In addition, the phosphorylation of Jip1 by JNK kinase acts as a molecular switch to regulate axonal transport direction (Fu and Holzbaur, 2013).

1.2.1.3 Amyloid precursor protein (App)

Commonly associated with Alzheimer's disease, App is a type 1 transmembrane protein that is ubiquitously expressed in mammalian cells (Groemer *et al.*, 2011). Under normal physiological conditions, *App* has been associated as a regulator of synapse formation and function (Priller *et al.*, 2006), and neural plasticity and memory (Turner *et al.*, 2003). Despite the immense interest in the involvement of App in the pathology of Alzheimer's disease, the endogenous role and physiological functions of *App* are largely unknown. However, the dysregulation of App trafficking is thought to play a central role in Alzheimer's disease, because the formation of senile plaques characteristic of the neurodegenerative disease is closely linked to App metabolism (Sisodia and Price, 1995). Recently, Liu *et al.* (2015) demonstrated that App interacts with and regulates $Na_v1.6$, enhancing its cell surface expression through a G_o-coupled JNK pathway.

1.2.1.4 Ankyrin G (Ank3)

Ankyrin G (Ank3) is a multidomain cytoskeletal adaptor protein that is abundantly expressed at the AIS and nodes of Ranvier in myelinated axons, directly interacting with axonal VGSCs (Kordeli *et al.*, 1995; Bennett and Baines, 2001). It has been demonstrated that Ank3 regulates neuronal excitability through the clustering and modification of gating behaviours of $Na_v1.6$ channels (Shirahata *et al.*, 2006). It plays an essential role in saltatory conduction of myelinated axons: in *Ank3* knockout mice, VGSCs were absent from the AIS and the nodes of Ranvier, and the neurons of these mice displayed severe deficits in action potential firing (Zhou *et al.*, 1998; Jenkins and Bennet, 2001). Recently, Barry *et al.* (2014) demonstrated that Ank3 functions as an adaptor to link VGSCs to kinesin motors during axonal transport, before anchoring them to the AIS and nodes of Ranvier. In particular, Ank3 is required for the preferential insertion of $Na_v1.6$ channels into the AIS plasma membrane during neuronal development via vesicular trafficking for action potential propagation (Akin *et al.*, 2015).

1.2.1.5 Voltage-gated sodium channel β1 (Scn1b)

Voltage-gated sodium channel β1 (Scn1b) subunits are multifunctional proteins that have essential roles in Na^+ current modulation (Isom *et al.*, 1992), regulate channel cell surface expression (Isom *et al.*, 1995), cell adhesion, cell migration (Xiao *et al.*, 1999), cellular aggregation (Malhotra *et al.*, 2000), cytoskeletal recruitment (Malhotra *et al.*, 2002; Malhotra *et al.*, 2004), and neurite outgrowth (Davis *et al.*, 2004; Fein *et al.*, 2007). The co-expression of Scn1b with VGSC α-subunits increases the cell surface levels of sodium channels by 2- to 4-fold (Isom *et al.*, 1995). *Scn1b*-null mice exhibit seizure activity, ataxia, slowed action potential conduction, deceased numbers of mature nodes of Ranvier in myelinated axons, and differences in VGSC α-subunit localization (Chen *et al.*, 2004). Scn1b subunits interact in a trans-homophilic fashion, resulting in the recruitment of the cytoskeletal protein Ank3; demonstrating that the cytoplasmic domains of Scn1b are required for cytoskeletal interactions (Malhotra *et al.*, 2000; Malhotra *et al.*, 2002). These factors suggest that Scn1b may play a role in $Na_v1.6$ localization and axonal trafficking.

1.2.2 Group 2 genes: Regulation of Scn8a *production through postnatal development*

The second group contained four genes that are involved in how *Scn8a* transcription is induced and regulated during the critical eye-opening period of postnatal retinal development. They were chosen due to the involvement of these genes at various levels of important signaling cascades that directly regulates *Scn8a* expression. These genes include brain-derived neurotrophic factor (*Bdnf*), tropomyosin receptor kinase B (*TrkB*), and Pumilio RNA-binding family member 2 (*Pum2*). *Scn8a* has also been included in this group for reasons explained below.

Through the activation of mitogen-activated protein kinase 5 (Erk5), the Bdnf:TrkB signaling complex controls Pum2 activity (Fiore *et al.*, 2009). This in turn activates myocyte enhancing factor 2 (Mef2), which activates the transcription of the micro-RNA cluster miR379-410 (Fiore *et al.*, 2009; Khudayberdiev *et al.*, 2009). A part of this cluster, micro-RNA-134, inhibits *Pum2* translation (Khudayberdiev *et al.*, 2009). Pum2 acts as a direct translational repressor of *Scn8a* (Driscoll *et al.*, 2013). Therefore, Bdnf appears to indirectly control *Scn8a* transcription in wildtype (WT) animals. Pum2 was included in my qRT-PCR study to further examine how *Scn8a* transcription is regulated by the levels of its repressor.

Electrical activity stimulates Bdnf expression (Shieh and Ghosh, 1999; Vermehren-Schmaedick *et al.*, 2015). Since $Na_v1.6$ plays an essential role in action potential initiation and propagation in the CNS and PNS (Meisler *et al.*, 2001; Trudeau *et al.*, 2006), any genetic variation or physiological modification involving this sodium channel will influence synaptic strength (Caldwell, 2000; Caldwell *et al.*, 2000; Meisler *et al.*, 2001). This in turn may influence the activity-dependent expression of Bdnf and, indirectly, the expression of genes regulated by Bdnf.

1.2.2.1 Brain-derived neurotrophic factor (Bdnf)

Bdnf is a neurotrophin secreted by both neurons and glia cells (Wilson *et al.*, 2007; van Oterendorp *et al.*, 2014). It is able to initiate the activation of various intracellular signaling cascades, such as MAPK/ERK, PLCγ, and PI3K pathways (Huang and Reichardt, 2003; Minichiello, 2009; Russo *et al.*, 2009; Numakawa *et al.*, 2010a). Bdnf is involved in multiple signaling pathways by regulating numerous cellular processes such as gene expression, including that of *Scn8a* (Fiore *et al.*, 2009; Khudayberdiev *et al.*, 2009; Driscoll *et al.*, 2013). Bdnf is known to promote the survival of neighbouring neurons by the activation of prosurvival pathways while inhibiting apoptotic ones (van Oterendorp *et al.*, 2014). It has been proposed that Bdnf released by Müller glia cells together with another neurotrophic factor, Cntf, may enhance retinal cell survival, specifically, photoreceptors (Harada *et al.*, 2002; Wilson *et al.*, 2007). Because photoreceptors do not express receptors for this neurotrophin, Bdnf released from Müller glia cells increases Cntf production, thereby enhancing photoreceptor survival (Harada *et al.*, 2002; Wilson *et al.*, 2007).

1.2.2.2 Tropomyosin receptor kinase B (TrkB)

TrkB is a very well-studied high-affinity cognate receptor for Bdnf. Upon binding with Bdnf, TrkB undergoes dimerization and phosphorylation of its critical intracellular tyrosine residues (Iuvone *et al.*, 2014). This leads to the activation of downstream signalling pathways, allowing Bdnf to exert its prosurvival effects on receptor cells of the inner retina (Gupta *et al.*, 2014; Iuvone *et al.*, 2014). Upon binding to Bdnf, the Bdnf/TrkB complex is also internalized as part of a signaling endosome during retrograde transport, further facilitating Bdnf function on signalling cascades (Mitchell *et al.*, 2012).

1.2.2.3 Pumilio RNA-binding family member 2 (Pum2)

Neuronal homeostasis enables neurons to adapt and maintain consistency to changing synaptic excitation, from rapid ion channel turnover or neural network disruptions that potentially destabilize circuit activity (Driscoll *et al*., 2013). Compensatory mechanisms are in place to prevent neural network destabilization through maintaining membrane excitability (Turrigiano *et al*., 1994; Turrigiano, 1999). Homeostatic synaptic mechanisms include the alteration of neurotransmitter release (Turrigiano and Nelson, 2004; Erickson and Spana, 2006) and/or postsynaptic receptor expression (Ehlers, 2003). In contrast, intrinsic mechanisms include the ability of neurons to alter their membrane excitability through changes in the relative density or functional properties of ion channels, such as VGSCs (Turrigiano and Nelson, 1998; Desai *et al*., 1999; Baines, 2003; Zhang and Linden, 2003; Marder and Goaillard, 2006). In response to changing synaptic excitation, a translational repressor, Pum2, regulates the translation of the voltage-gated sodium conductance, leading to a concomitant adjustment in action potential firing (Mee *et al*., 2004; Muraro *et al*., 2008; Driscoll *et al*., 2013; Lin and Baines, 2015). It has been demonstrated that Pum2 is able to directly bind to the *Scn8a* transcript expressed in neurons, and through doing so, regulates translation of this key determinant of membrane excitability (Driscoll *et al*., 2013).

1.2.2.4 Voltage-gated sodium channel type 8 alpha subunit (Scn8a)

The expression of *Scn8a* was included in this qRT-PCR analysis in order to examine the regulation of expression by visual experience throughout postnatal retinal development. Interestingly, a study demonstrating the importance of the N-terminus of this protein segment was recently published by O'Brien *et al*. (2012). The researchers used part of this initial segment as "bait" in a yeast two-hybrid screen and identified that the N-terminus of $Na_v1.6$ was capable of binding to a protein that may affect microtubule dynamics, microtubule-associated protein Map1b (O'Brien *et al*., 2012). Another study by Liu *et al*. (2015) demonstrated that App, a possible adaptor protein in vesicular trafficking, was an interaction partner with $Na_v1.6$. Taken together, these studies illustrate that $Na_v1.6$ is involved with, or at least, is a part of intracellular processes, such as microtubule dynamics, trafficking, and possibly other novel functions, despite knowing the presence of the *Scn8a*^{dmu} mutation creating a functionally-null sodium channel *in vivo*.

1.2.3 Group 3 genes: Müller glia cell support through postnatal development

The third group included two genes that are indicative of the overall state of Müller cells, which are essential to retinal homeostasis. Müller cells are the major type of glia cells in the retina responsible for a host of supportive roles (Reichenbach and Bringmann, 2013). They are known to control the concentration of critical ions (Ca^+, Na^+), provide trophic and anti-oxidative support to all retinal cell types (Tsacopoulos and Magistretti, 1996), support synaptic activity by neurotransmitter recycling (Bringmann *et al*., 2009b), and even serve as a substrate during the growth and refinement of the retina (Reichenbach and Bringmann, 2013). In addition, Müller cells serve as internal living optical fibers that guide light with minimal loss through the inner retinal tissues towards photoreceptors (Franze *et al*., 2007).

The first gene of this group, glial fibrillary acidic protein (*Gfap*), the main type of intermediate filament expressed in glial cells, is a good indicator of the overall Müller cell fitness. Another neurotrophic factor, ciliary neurotrophic factor (*Cntf*) is included in this group; Cntf is known to be secreted by Müller cells. Together along with Bdnf, both of these neurotrophic factors support prosurvival signals during times of retinal stress and disease.

1.2.3.1 Glial fibrillary acidic protein (Gfap)

Gfap is a type III intermediate filament protein found exclusively in astrocytes and, in the case of the maturing retina, Müller cells (Middeldorp and Hol, 2011). Gfap is involved with structural and mechanical support as part of an astrocyte's cytoskeleton, as well as functions associated with transduction of biomechanical and molecular signals (Middeldorp and Hol, 2011). Gfap served as a fitness monitor for astrocytes, and in this case, Müller cells, as there are numerous diseases, such as astrogliosis and experimental autoimmune encephalomyelitis (a model for multiple sclerosis), where the upregulation of Gfap was a hallmark for disease states (Lewis and Fisher, 2003; Brenner, 2014; Hol and Pekny, 2015). Given the importance of Müller glia as supporting cells to all other cell types within the retina and their normal functions, Gfap expression was examined in this qRT-PCR analysis as a gauge to measure the overall state of these cells.

1.2.3.2 Ciliary neurotrophic factor (Cntf)

Cntf is one of the most studied neurotrophic factors for the neuroprotection of the retina, and studies have repeatedly demonstrated its prosurvival effects since it was first reported in 1992 (LaVail *et al.*, 1992; Wen *et al.*, 2012). Cntf is an important signaling factor during retinal development, playing a role in regulating the differentiation of rod and cone photoreceptors (LaVail *et al.*, 1992; LaVail *et al.*, 1998; Li *et al.*, 2010). During postnatal development, Cntf serves other important functions, such as influence the survival, proliferation, and function in neurons (LaVail *et al.*, 1992; LaVail *et al.*, 1998; Wen *et al.*, 2012).

Studies examining the state of astrocytes and Müller cells reveal that the mRNA expression of both Gfap and Cntf deviate away from normal levels as a response to retinal injuries or stress from a chronic disease (Erickson *et al.*, 1992; Cao *et al.*, 1997; Gomes *et al.*, 1999; Lundkvist *et al.*, 2004; Dutta *et al.*, 2007; Roesch *et al.*, 2012; Astafurov *et al.*, 2014). These lines of evidence indicated the importance of Gfap and Cntf as indicators of Müller cell homeostasis. Therefore they were chosen for qRT-PCR analysis.

1.3 The neurofilament network in the brain and retina

Neurons are specialized cells that are able to process and transmit information through electrical and chemical signals. Through the extension of long processes, neurons are able to relay signals to each other via synapses, forming vast neural networks. Like all other eukaryotic cells, the cytoskeleton of neurons comprises three structural complexes, each with distinct properties: microfilaments, microtubules, and intermediate filaments. Each of the cytoskeletal filaments has a characteristic shape and intracellular distribution and is composed by the polymerization of different subunits.

Microfilaments are made up of actin polymers and have a diameter of ~7nm (Fuchs and Cleveland, 1998). Making up the main components of the membrane cytoskeleton, actin microfilaments play important roles in neuronal growth and secretion (Hitt and Luna, 1994; Beck and Nelson, 1996).

Microtubules are formed by the polymerization of α- and β-tubulin heterodimers and have a diameter of ~25nm (Nogales, 2000). Microtubules play several important roles in neurons. They are involved in cell structure maintenance, and also provide the platforms for the intracellular transport of secretory vesicles and organelles (Heidemann, 1996).

Intermediate filaments are composed of a family of various proteins and have a diameter of ~10nm (Herrmann *et al*., 2007). Based on similarities in amino acid sequence and protein structure, intermediate filaments are subcategorized into six types (Steinert *et al*., 1999). In particular, neurofilaments belong to the type IV family of intermediate filaments and are specifically found in high concentrations along the axons of vertebrate neurons. They are assemblies of three subunits: neurofilament light-chain (NF-L, 68kDa), neurofilament medium-chain (NF-M, 160kDa), and neurofilament heavy-chain (NF-H, 200kDa), forming heteropolymeric 10nm protofilaments that run parallel along the length of axons, mainly serving a structural function (Lee and Cleveland, 1996; Ruiz-Ederra *et al*., 2004). Once assembled, the 'neurofilament triplet' is transported from the neuronal soma down the axon via slow axonal transport (Hoffman and Lasek, 1975; Black and Lasek, 1980). Interestingly, not all neurons have the same combination of neurofilament subunits, and even between species, there are distinct differences (Lee and Cleveland, 1996; Carter *et al*., 1998). In particular, rodent neurofilaments are obligate heteropolymers that require NF-L plus either NF-M or NF-H for proper filament formation (Carter *et al*., 1998).

Neurofilaments play an essential role in brain development, maintenance, regeneration and plasticity of the neural cytoskeleton (Ruiz-Ederra *et al*., 2004). In addition to the well-established role that neurofilaments play in the regulation of axonal calibre, there is growing evidence that neurofilaments can affect the dynamics and function of other cytoskeletal elements, such as microtubules and actin filaments (Perrone Capano *et al*., 2001). Unique "side-arms" formed by NF-M and NF-H tail domains project perpendicular from the protofilament backbone (Nixon and Sihag, 1991). These "side-arms" form lateral cross-bridges between neighbouring protofilaments, organizing them into parallel arrays along the axon (Perrone Capano *et al*., 2001). Integrating into this neurofilament scaffold matrix is the microtubule network. Interaction with neurofilaments by means of cross-bridges composed of microtubule-associated proteins (MAPs or tau) (Bloom and Vallee, 1983; Bulinski *et al*., 1997; Ebneth *et al*., 1998; Trinczek *et al*., 1999; Stamer *et al*., 2002) and microtubule motors (kinesins and dyneins) (Gyoeva and Gelfand, 1991; Prahlad *et al*., 1998; Shah *et al*., 2000; Helfand *et al*., 2002; Helfand *et al*., 2003), the microtubule network acts as the substrate ("tracks") for the anterograde/retrograde transport of secretory vesicles and organelles (Heidemann, 1996; Perrone Capano *et al*., 2001). Yet another system of cross-linking proteins connects

neurofilaments and microtubules with actin microfilaments. The interaction of intermediate-filament-associated proteins (IFAPS, such as plectin) (Svitkina *et al*., 1996) and microfilament motors (myosins) (Tint *et al*., 1991; Rao *et al*., 2002), the microfilament meshwork plays a role in the regulation of neurofilament motility. Therefore, in mature neurons, the axonal cytoskeleton consists of a highly stable and extensively cross-linked network of neurofilaments, microtubules, and actin microfilaments (Yuan *et al*., 2009). While these cytoskeletal components are composed of different proteins, all three are connected through cross-linking proteins, allowing for constant and intimate communication, thereby acting as a unified system (Chang and Goldman, 2004; Gardiner *et al*., 2013). However, because these cytoskeletal components are intimately linked to each other, perturbations to one component affect the entire network.

Neurofilaments regularly appear altered in numerous neurodegenerative diseases (Julien, 1999), with the presence of neurofilament deposits a common hallmark, including amyotrophic lateral sclerosis (ALS), Alzheimer's disease and Parkinson's disease (Julien and Mushynski, 1998). Disorganized neurofilaments can induce neuronal degeneration and death, and emerging evidence suggests that an interference of axonal transport by disorganized neurofilaments has been proposed as a possible mechanism of neurofilament-induced pathology (Julied and Mushynski, 1998).

My preliminary data using the *Scn8a*^{dmu} mouse strain demonstrated irregularities in the neurofilament network; the irregularities were further exacerbated in the absence of light stimulation. The presence of the NF-L disruptions bears a resemblance to neurofilament aggregations observed in other neurodegenerative diseases. Currently, there is no link between sodium channels and cytoskeletal network organization. The use of *Scn8a*^{dmu} mice provides a unique opportunity to determine and characterize the extent of neurofilament network disruptions in the absence of functional $Na_v1.6$.

1.4 Objectives

With these studies in mind, I am in the unique position to further examine and refine the understanding that the $Na_v1.6$ sodium channel may have on eye development. By using the *Scn8a*^{dmu} mouse model, I am able to specifically examine the developmental effects that a lack of a $Na_v1.6$ will have on retinal maturity. As RGC is the cell type that expresses the highest levels of $Na_v1.6$ in the retina, the *Scn8a*^{dmu} mouse model provides

an ideal opportunity to examine if axonal trafficking-related genes (encoding proteins involved in transporting $Na_v1.6$ along the axon to the nodes of Ranvier) in the optic nerve would be affected. As it has been demonstrated that visual experience is necessary for the proper development and refinement of the functional mature retina, the presence/absence of visual experience serves as an ideal experimental condition to include in my present study.

1.4.1 Examining the mRNA expression patterns of three interacting groups of genes in the absence of Scn8a

The use of gene expression studies can be a powerful tool to uncover novel roles for known genes. The objectives for this qRT-PCR study were to examine the expression of three groups of genes in the absence of *Scn8a* during retina development. The first group contains genes that are involved in the trafficking of $Na_v1.6$. To examine how gene regulation may change in the absence of *Scn8a*, I will characterize the gene expression differences that may occur in the absence of $Na_v1.6$. The second group contains genes from a signalling cascade that is involved in the regulation of *Scn8a* expression. I will characterize the differences in the expression of these genes that may occur in the absence of $Na_v1.6$. The third group contains genes that assess the state of Müller glia cells within the retina. Because Müller cells act in a supportive role for the other retinal cells during development, therefore examining the state of Müller cells in the absence of $Na_v1.6$ may provide insight into the overall state of the retina. In studying the development of retinal tissues, these analyses can provide insights into complex regulatory networks that coordinate axonal trafficking, gene transcription expression patterns and structural organization.

1.4.2 Examining the neurofilament network on a Scn8a-*null background*

The objectives of this study were to examine the neurofilament distribution in WT, and Mut ($Scn8a^{dmu/dmu}$) animals in an effort to further characterize the $Scn8a^{dmu}$ mutation and understand how this mutation might affect the distribution of neurofilaments. To do this, I examined the neurofilament network across postnatal development in the retina and brain (cerebellum and visual cortex). The postnatal development ranges from P7-P30; covering before and after eye-opening in mice (immature retinal stages to mature retina with synapse maturation in adults). The

presence/absence of light stimulation was also examined. This study aimed to illustrate the organization and potential disruption of the neurofilament network with the presence of NF-L accumulations, and whether this disruption potentially leads to developmental delays in the retina and cerebellum.

1.5 The discovery of the *spontaneous $Na_v1.6$ rescue* (snr) *substrain*

To complete this study, I describe the serendipitous discovery of a substrain within the *Scn8a*^{dmu} mouse line, tentatively termed the **s**pontaneous **N**a$_v$1.6 **r**escue (*snr*). The *snr* mutants arose suddenly during the regular breeding of the *Scn8a*^{dmu} mouse line. *Snr* mutants displayed similar visual impairment as *Scn8a*$^{dmu/dmu}$ animals. However, they retained full control of their motor coordination facilities, and did not exhibit the hindlimb paralysis and limited lifespan that is characteristic of *Scn8a*$^{dmu/dmu}$ mutant animals.

CHAPTER 2: MATERIALS & METHODS

2.1 qRT-PCR materials and methods

2.1.1 Retinal tissue collection and preparation for qRT-PCR

A total of 54 murine retinal tissues were collected; 27 pairs of retinas from mice that were raised in light-reared (LR) conditions, and 27 pairs of retinas from mice that were raised in dark-reared (DR) conditions. All LR mice were housed under a 12h light/dark cycle while all DR mice were housed under a 24h dark cycle. All mice had *ad libitum* access to food and water and were maintained according to the guidelines of the Canadian Council on Animal Care (CCAC), with all procedures and protocols approved by the Dalhousie University Committee on Laboratory Animals (UCLA).

Mating cages with pregnant females were placed in the 24h dark room a few days before giving birth. Each light condition was further subdivided by genotype: 30 pairs of wildtype (WT, *Scn8a*$^{+/+}$) retinas, and 24 pairs of mutant [Mut, *Scn8a*$^{dmu/dmu}$, (-/-)] retinas were collected (Table 2.1) (Appendix 2.1). Retinal tissues collected were between the ages of P10-P30, depending on the genotype. Since *Scn8a*$^{dmu/dmu}$ mice die at a young age, the experimental endpoint for tissue collection was set at P21 for humane reasons due to the deteriorating health of the animals. Aside from *Scn8a*$^{dmu/dmu}$ mice, an experimental timepoint was set at P30 for WT animals; as a means to examine if retinal development into adulthood was delayed in the absence of *Scn8a*.

Before tissue collection, all animals were screened by genotyping. All animals were first anesthetized with isoflurane and then euthanized by cervical dislocation. The head was quickly separated from the body and the eyes were collected and immediately submerged into RNA*later* RNA stabilization reagent (Qiagen, Hilden, Germany). Retinas were carefully dissected out from the rest of the eye tissues with sterilized forceps that were treated with RNase*Zap* RNase decontamination solution (Ambion, Austin, Texas, USA). The dissected retinas were then submerged in RNA*later* RNA stabilization reagent and stored at 4^{o}C until further processing.

Table 2.1: The total number of retina samples that were collected for qRT-PCR experiments. A total of 54 retina samples were collected. For each developmental timepoint, there are several different genotypes, with an n = 3 for each genotype (experimental triplicate). Each retina tissue sample collected was run in triplicate in qRT-PCR experiments (technical triplicate) (refer to Appendix 2.1 for work flow of qRT-PCR experiments).
Abbreviations: WT = *Scn8a*$^{+/+}$ wildtype, (-/-) = *Scn8a*$^{dmu/dmu}$ mutant, LR = light-reared, DR = dark-reared, p = postnatal day.

qRT- P C R					
	P10	P12	P16	P21	P30
WT-LR	3	3	3	3	3
(-/-)-LR	3	3	3	3	
WT-DR	3	3	3	3	3
(-/-)-DR	3	3	3	3	

2.1.2 Retinal tissue RNA extraction and quantification for qRT-PCR

Total RNA was isolated using the RNeasy Plus Mini Kit (Qiagen) according to manufacturer's instructions. Purified RNA was then quantified using a nanodrop spectrophotometer (NanoDrop 2000, Thermo Scientific, USA). The ratio of the absorbance at 260 nm and 280 nm ($A_{260/280}$) of ~2 was used to assess the purity of the RNA. Each RNA sample was quantified a minimum of three times before the mean concentration was calculated.

2.1.3 Quantitative reverse transcriptase polymerase chain reaction (qRT-PCR)

All purified RNA samples were first diluted to a working concentration of 100 ng/µL and then reverse transcribed using Oligo(dT) $_{12\text{-}18}$ Primers (Invitrogen, Carlsbad, CA, USA), 10 mM dNTP Mix (Invitrogen), RNaseOUT Ribonuclease Inhibitor (Invitrogen), and SuperScript III Reverse Transcriptase (Invitrogen) (refer to Appendix 2.2 for reverse transcription details). The resulting cDNA samples were diluted to a working concentration of 0.1 ng/uL and stored at -20^{o}C.

qRT-PCR was performed using PerfeCTa SYBR Green FastMix (Quanta BioSciences, Gaithersburg, MD, USA) and validated primers for *Gapdh*, *Hprt1*, *Scn1b*, *NF-L*, *Gfap*, *Bdnf*, *Cntf*, *Ank3*, *Pum2*, *Jip1*, *TrkB* (RealTimePrimers.com, Elkins Park, PA, USA) and *App* and *Scn8a* primers (Integrated DNA Technologies, Coralville, Iowa, USA) (refer to Appendix 2.3 for details regarding qRT-PCR primer sequences and qRT-PCR programs). All qRT-PCR experiments were performed using 384-well white opaque microplates with pressure sensitive sealing film lids (Axygen Scientific from VWR, Radnor, PA, USA), adhesive seal plate roller (Light Labs, Dallas, TX, USA), filter tips, and the Roche Lightcycler II 480 Real-Time PCR system (Roche Diagnostics, Risch-Rotkreuz, Switzerland). All samples were run in triplicate (refer to Appendix 2.1 for work flow of qRT-PCR experiments). Results were analyzed using Microsoft Excel (Microsoft, Redmond, WA, USA) by the relative standard curve method (Larionov *et al*., 2005; Kubista *et al*., 2006) and normalized to both *Gapdh* and *Hprt1* as internal controls. All data were analyzed according to the mathematical model developed by Liu and Saint (Liu and Saint, 2002; Hrytsenko *et al*., 2007). All error bars represent standard error of the mean (SEM). Statistical analyses were performed by one-way ANOVA and Tukey's post-hoc tests using GraphPad Prism, Version 5.0 (GraphPad Software, La Jolla, CA, USA) (Table 3.1).

For each normalized gene expression graph, the relative expression of a specific gene was normalized to the combined average of both housekeeping genes (*Gapdh* and *Hprt1*). For each fold change bar graph, the fold change was calculated by taking the expression of each genotype and divided by the LR WT expression at each specific timepoint, and then taking them as 100% normal expression at each postnatal timepoint to clearly illustrate the increases and decreases in genetic expression at each postnatal timepoint.

2.2 Immunohistochemistry materials and methods

2.2.1 Isolation and embedding of retinal tissues for frozen sections

A total of 64 murine retinal tissues were collected; 40 pairs of retinas from mice that were raised in LR conditions, and 24 pairs of retinas from mice that were raised in DR conditions. Each light condition was further subdivided by genotype: 32 pairs of WT (*Scn8a*$^{+/+}$) retinas, and 32 pairs of mutant [(-/-), *Scn8a*$^{dmu/dmu}$] retinas were collected (Table 2.2). Retinal tissues collected were between the ages of P7-P21, depending on the genotype and rearing condition. Since *Scn8a*$^{dmu/dmu}$ mice die at a young age, the experimental endpoint for tissue collection was set at P21 for humane reasons due to the deteriorating health of the animals. Aside from *Scn8a*$^{dmu/dmu}$ mice, the experimental timepoint was also set at P21 for WT animals, as a means to examine if retinal development into adulthood was developmentally delayed in the absence of *Scn8a*.

Before tissue collection, all animals were genotyped. All animals were first anesthetized with isoflurane then euthanized by cervical dislocation. After decapitation, the eyes were removed and immediately submerged into 4% paraformaldehyde (PFA) solution; the retinal tissue was fixed for 24 hours. After fixation, the lens was carefully removed from each eye and the retinal tissue was cryoprotected with a 30% sucrose/phosphate buffer (PB) solution. All retinal tissues were embedded with O.C.T. compound (optimal cutting temperature, Tissue-Tek, Sakura Finetek, USA), flash frozen with liquid nitrogen-chilled isopentane (Fisher Scientific, New Hampshire, USA), and stored at -80^{o}C until further use (refer to Appendix 2.4 for details on embedding frozen retinal tissues).

Table 2.2: The total number of retina samples that were collected for immunohistochemistry (IHC) experiments. A total of 64 retina samples were collected. For each developmental timepoint, there are several different genotypes, with an n = 4 for each genotype.
Abbreviations: WT = *Scn8a*$^{+/+}$ wildtype, (-/-) = *Scn8a*$^{dmu/dmu}$ mutant, LR = light-reared, DR = dark-reared, p = postnatal day.

Retinal tissues for IHC staining					
	P7	P10	P12	P16	P21
WT-LR	4	4	4	4	4
(-/-)-LR	4	4	4	4	4
[redacted]					
WT-DR	[redacted]		4	4	4
(-/-)-LR			4	4	4

2.2.2 Isolation and paraffin embedding of brain tissues

A total of 66 murine brain tissues were collected; 33 samples of brains from mice that were raised in LR conditions, and 33 samples of brains from mice that were raised in DR conditions. Each light condition was further subdivided by genotype: 36 samples of WT (*Scn8a*$^{+/+}$) retinas, and 30 samples of mutant [(-/-), *Scn8a*$^{dmu/dmu}$] retinas were collected (Table 2.3). Brain tissues collected were between the ages of P7-P30, depending on the genotype. Since *Scn8a*$^{dmu/dmu}$ mice die at a young age, the experimental endpoint for *Scn8a*$^{dmu/dmu}$ tissue collection was set at P21 for humane reasons due to the deteriorating health of the animals. Aside from *Scn8a*$^{dmu/dmu}$ mice, the experimental timepoint was set at P30 for WT animals.

Before tissue collection, all animals were genotyped. All animals were first deeply anesthetized with isoflurane, and then fixed by transcardial perfusion using a 4% paraformaldehyde (PFA) solution. After decapitation, the brains were carefully removed from the skull, sliced in a sagittal plane and immediately immersed into 10% neutral buffered formalin (NBF) solution (Fisher Scientific, New Hampshire, USA); the brain tissue was fixed for five days. After fixation, all brain tissues were dehydrated through a series of graded ethanol solutions and infiltrated with paraffin wax (TissuePrep, Fisher Scientific, New Hampshire, USA). All paraffin embedded brain tissues were stored at room temperature until further use (refer to Appendix 2.5 for details on paraffin embedding of brain tissues).

2.2.3 Immunohistochemistry of retina and brain tissues

Immunohistochemical staining procedures for frozen retinal tissues varied from paraffin embedded brain tissues.

For frozen retinal tissues, antigen retrieval was performed by using a 1% SDS/PBS solution for 5 minutes. Non-specific binding sites were blocked with 5% normal goat serum for 1 hour, and washings were performed with PBS buffer. Primary antibodies were applied for 24 hours at 4^{o}C (refer to Table 2.4 for details on antibodies used in this thesis). The corresponding secondary antibody was subsequently applied for 1 hour. A nuclear stain was then applied for 10 minutes (depending on particular microscope used). The retinal tissues were then mounted using an aqueous mounting

Table 2.3: The total number of brain samples that were collected for immunohistochemistry (IHC) experiments. A total of 66 brain samples were collected. For each developmental timepoint, there are several different genotypes, with an n = 3 for each genotype.
Abbreviations: WT = *Scn8a*$^{+/+}$ wildtype, (-/-) = *Scn8a*$^{dmu/dmu}$ mutant, LR = light-reared, DR = dark-reared, p = postnatal day.

Brain tissues for IHC staining						
	P7	**P10**	**P12**	**P16**	**P21**	**P30**
WT-LR	**3**	**3**	**3**	**3**	**3**	**3**
(-/-)-LR	**3**	**3**	**3**	**3**	**3**	[redacted]
[redacted]						
WT-DR	**3**	**3**	**3**	**3**	**3**	**3**
(-/-)-DR	**3**	**3**	**3**	**3**	**3**	[redacted]

Table 2.4: The antibodies and nuclear stains that were used for the immunohistochemistry experiments.

Primary antibody name	Type	Host species	Antigen retrieval required frozen/paraffin	Dilution	Company/catalog number
Neurofilament-L (NF-L) (C28E10)	monoclonal	Rabbit	no/yes	1:200	Cell Signalling Technology, Cat# 2837
Amyloid precursor protein (App) (C-terminal 751-770)	polyclonal	Rabbit	no/yes	1:1000	Calbiochem, Cat# 171610

Secondary antibody name	Type	Host species	Antigen retrieval	Dilution	Company/catalog number
Cyanine (Cy3)-conjugated AffiniPure Goat Anti-Rabbit IgG	polyclonal	Goat	N/A	1:200	Jackson ImmunoResearch Laboratories, Inc., Cat# 111-165-144

Name of nuclear stain used	Type	Host species	Antigen retrieval	Dilution	Company/catalog number
Hoechst 33342 nuclear stain (for fluorescent microscopes)	N/A	N/A	N/A	1:5000	ThermoFisher Scientific, Cat# 62249 (20mM stock solution)
TO-PRO-3 iodide (642/661) stain (for confocal microscopes)	N/A	N/A	N/A	1:1000	ThermoFisher Scientific Molecular Probes, Cat# T3605 (1mM stock solution)

medium, with the coverslips sealed with clear nail polish (refer to Appendix 2.6 for details on immunohistochemistry of frozen retinal tissues).

For paraffin embedded brain tissues, the sections were first deparaffinized through a series of graded ethanol solutions, and antigen retrieval was performed by using a 1N HCl solution for 20 minutes. Non-specific binding sites were blocked with 5% normal goat serum for 1 hour, and washings were performed with PBS buffer. Primary antibodies were applied overnight at 4^{o}C (refer to Table 2.4 for details on antibodies used in this thesis). The corresponding secondary antibody was subsequently applied for 1 hour. A nuclear stain was then applied for 10 minutes (depending on particular microscope used). The brain tissues were then mounted using an aqueous mounting medium, with the coverslips sealed with clear nail polish (refer to Appendix 2.7 for details on immunohistochemistry of paraffin embedded brain tissues).

2.2.4 Histology of brain tissues using hematoxylin and eosin stain

For studying the gross anatomy of brain tissue, the paraffin embedded sections were stained using a standard protocol of hematoxylin & eosin stain (Appendix 2.8).

2.2.5 Microscopy

A Zeiss Axiovert 200M microscope (Zeiss, Oberko-chen, Germany) equipped with a Zeiss Axiocam ICc5 FluoArc HR digital camera was used to examine retinal and brain tissues (fluorescent cerebella images, and hematoxylin and eosin images). A Zeiss Axiovert Observer.Z1 Colibri (Zeiss, Oberko-chen, Germany) equipped with a Zeiss Axiocam HRM monochromatic camera was used to examine brain tissues (fluorescent visual cortex images stained with App antibody).

A confocal microscope (Nikon C1, Nikon Canada Inc., Toronto, ON, Canada) equipped with narrow-band fluorescent filters centered for excitation wavelengths of 488, 594 and 633 nm was used to examine retinal and brain tissues stained with NF-L antibody. Fluorescent images were captured with Nikon EZ-C1 software with 2048 X 2048 pixel frame size.

2.3 Discovery of *snr* mouse substrain materials and methods

2.3.1 Animal husbandry of mouse lines used in this thesis

All mice (both LR and DR conditions) were housed as previously stated in subsection 2.1.1.

The Scn8a^{dmu} *Mouse Line (pre-established line, discovered by the Kothary Lab, University of Ottawa, Canada).* The genotype of all animals was first confirmed by PCR (as described in Côté *et al*., 2005 and briefly in this thesis). The *dmu* recessive allele was maintained by mating confirmed heterozygous mice to produce homozygous offspring that display the *dmu* motor phenotype. These offspring were then collected as experimental animals at specific developmental timepoints.

2.3.2 Genotyping assay of mouse lines used in this thesis

The *Scn8a*$^{dmu/dmu}$ mutation consists of a single nucleotide deletion in exon 10A of the *Scn8a* coding sequence (position 1538 of GenBank accession number NM_011323) (Côté *et al*., 2005). This mutation results in the loss of a *Bsl*I recognition sequence (Côté *et al*., 2005). Using the primers (forward) 5'-CGG-GCA-CCG-TCT-CAG-AAG-AT-3' and (reverse) 5'-TCC-TTC-TCA-TGC-CAT-CTT-CC-3', and genomic DNA isolated from ear or tail biopsies by phenol chloroform extraction (Appendix 2.9), a 215bp fragment of *Scn8a* containing the mutation was amplified by PCR. This PCR product was then incubated with *Bsl*I (Thermo Fisher Scientific) for a minimum of five minutes at room temperature. Since the *Bsl*I restriction enzyme recognizes the CCNNNNN^NNGG site, only the WT (*Scn8a*$^{+/+}$) sequences were digested with *Bsl*I, resulting in a 174bp and 41bp fragments. Mice that were heterozygotes (*Scn8a*$^{dmu/+}$) produced three fragments: 215bp, 174bp, and 41bp fragments. Homozygous mutant (*Scn8a*$^{dmu/dmu}$) mice only produced the 215bp PCR product (Figure 2.1). (More details for genotyping the *Scn8a*^{dmu} strain is found in Appendix 2.10). In addition, the genotyping of all *snr* mice also used *Scn8a*^{dmu} primers (Appendix 2.10). A *Scn8a*$^{dmu/dmu}$ mouse was only considered to be a *snr* if the characteristic motor phenotype was absent.

Figure 2.1: *BslI* cleavage of *Scn8a*^{dmu} PCR product. The *BslI* restriction enzyme recognizes the CCNNNNN^NNGG site. When *Scn8a* WT sequences were digested with *BslI*, the results were 174bp and 41bp fragments. Mice that were heterozygotes (*Scn8a*$^{dmu/+}$) produced three fragments: 215bp, 174bp, and 41bp fragments. Homozygous (*Scn8a*$^{dmu/dmu}$) mice only produced the 215bp PCR product. (* the 41bp PCR product is difficult to detect).

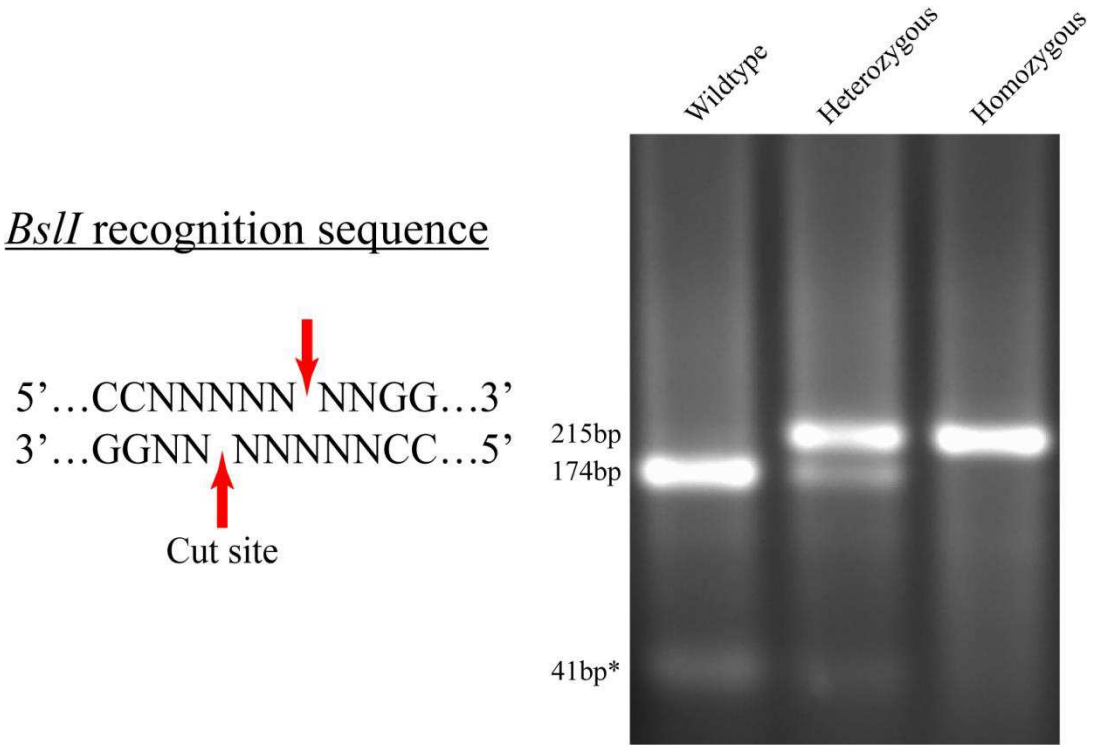
BslI recognition sequence
5'…CCNNNNN NNGG…3'
3'…GGNN NNNNNCC…5'
Cut site
Wildtype
Heterozygous
Homozygous
215bp
174bp
41bp*

2.3.3 Behavioural studies performed using **snr** *mice*

There were a total of four *snr* mice identified: two females (from the same litter) and one male and one female (from another litter). All *snr* mice were screened with PCR using *Scn8a*^{dmu} primers (Appendix 2.10). All four *snr* mice were used throughout the following three behavioural studies at two developmental timepoints, P16 and P30 with four age-matched controls and four *Scn8a*$^{dmu/dmu}$ mice. The *Scn8a*$^{dmu/dmu}$ mice were only included in the balance beam and Rotarod behavioural studies. The average weight for a total of 12 mice [wildtype (n = 4), *snr* (n = 4), and *Scn8a*$^{dmu/dmu}$ (n = 4)] were also measured using an animal mass balance with weighing basket (Explorer Ohaus Corp., Canada). Wildtype and *snr* mice were weighed every other day, from P9-P65. Since the *Scn8a*$^{dmu/dmu}$ mice do not survive past P21, they were weighed every other day, from P9-P18 (humane endpoint for *Scn8a*$^{dmu/dmu}$ mice) (Figure 3.20).

2.3.3.1 Behavioural monitoring study

Behavioural monitoring is an assay designed to examine the natural behaviour of rodents. It consisted of individually-housed animals that had each been acclimated in a new cage for 1 hour, and then monitored for 30 minutes by two researchers who did not know the genotype of the animals beforehand (Figure 3.21A).

Test subjects were carried to the test room in their home cages. Each mouse was placed into a new cage to acclimate for 1 hour before behavioural monitoring began (Figure 3.21A). After acclimation, each mouse was monitored for 30 minutes/day for five consecutive days. Observations of behavioural monitoring were recorded in the same room at the same time, every day, by the same researcher who did not know the genotype of the experimental mice. Well-defined behaviours (rearing itself upright on its hind legs, climbing upside down on wire lid, grooming, walking, sniffing, digging, eating, standing still, drinking, jumping, sleeping, and running) were recorded every 15 seconds for each mouse (Figure 3.21B). A total of eight mice [wildtype (n = 4), and *snr* (n = 4)] were all compared, using an unpaired Student's *t*-test with significance indicated as * = $p \leq 0.05$, ** = $p \leq 0.01$, and *** = $p \leq 0.001$. Error bars represent ±SEM (Figure 3.21B).

2.3.3.2 Sensorimotor integration and hindlimb function study using the balance beam

Balance beam walking is a test of fine motor coordination and balance. The beam was composed of wood, coated entirely with black paint and marked with white paint at 5 cm and 1 cm intervals. The beam was 100 cm in length, 2 cm in width and was elevated 40 cm in height. Individual test subjects were filmed with a video camera (Canon 2R800 NTSC MiniDV digital video camcorder) and later scored by a researcher that did not know the genotype of the animals beforehand (Figure 3.22A).

Test subjects were carried to the test room in their home cages. Each mouse was given a 2 hour learning period. After the learning period, each mouse was removed from its home cage and placed at one end of the balance beam. After the mouse had secured its grip on the beam, the test trial began and lasted for a maximum of two minutes. All animals tested were each subjected to two trials/day for five consecutive days. The balance beam was cleaned with 70% ethanol and allowed to dry between each test trial. If a test subject fell off, the animal was not placed back on the beam but was returned to their home cage. The total distance traveled (number of white lines crossed, in cm) (Figure 3.22B) and hindlimb function (number of times one of the subject's hind feet slips from the balance beam) (Figure 3.22C) were measured. A total of 12 mice [wildtype (n = 4), *snr* (n = 4), and *Scn8a*$^{dmu/dmu}$ (n = 4)] were all compared, using a 1-way ANOVA with Tukey's post-hoc test with significance indicated as * = $p \leq 0.05$, ** = $p \leq 0.01$, and *** = $p \leq 0.001$. Lack of statistical significance was mainly due to high variance (some animals did not want to walk along the beam, stopped or fell off during the test). Error bars represent ±SEM. Since the four *Scn8a*$^{dmu/dmu}$ mice do not survive for very long, they were all P18/P19 in age, while the other mice were >2 months old.

2.3.3.3 Sensorimotor coordination and overall motor function study using the Rotarod

The AccuRotor RotaRod (Omnitech Electronics, Inc., Canada) is designed to test motor coordination and function in rodents. It is a motor driven apparatus with a grooved cylinder (30 mm in diameter for mice, solid PVC) that allows test subjects to grip onto, with a standard fall height of 38 cm for mice (Figure 3.23A). The Rotarod had four chambers to accommodate up to four animals at the same time. Each of the four chambers was 11 cm in width and had its own start button and a pressure-sensitive indicator that detected when an individual animal fell from the grooved cylinder. The grooved cylinder could spin in both clockwise and counter clockwise directions and could

be set to rotate at a constant speed or programed to rotate at a desired acceleration rate. Individual test subjects were filmed with a video camera (Canon 2R800 NTSC MiniDV digital video camcorder) and later scored by a researcher that did not know the genotype of the animals beforehand (Figure 3.23A).

Test subjects were carried to the test room in their home cages. Each mouse was given a 2 hour learning period by performing three test trials/day. After the learning period, each mouse was removed from its home cage and placed within one of the four chambers of the Rotarod. After all four mice had secured their grip on the grooved cylinder, the test trial began, with the Rotarod set to go from 0 to 50 rotations/minute for a maximum of six minutes (360 seconds). All animals tested were subjected to six trials/day for five consecutive days. The Rotarod apparatus was cleaned with 70% ethanol and allowed to dry between each test trial. The latency to fall (in seconds) was recorded, as there were timers that stopped the moment a mouse fell on a pressure-sensitive surface (Figure 3.23A). A total of 12 mice [wildtype (n = 4), *snr* (n = 4), and *Scn8a*$^{dmu/dmu}$ (n = 4)] were all compared, using a 1-way ANOVA with Bonferroni post-hoc test with significance indicated as * = $p \leq 0.05$, ** = $p \leq 0.01$, and *** = $p \leq 0.001$. Error bars represent ±SEM (Figure 3.23B). Since the four *Scn8a*$^{dmu/dmu}$ mice do not survive for very long, they were all P18/P19 in age, while the other mice were > 2 months old.

CHAPTER 3: RESULTS

3.1 Regulation of selected genes by visual experience or by $Na_v1.6$

A total of 11 genes were examined using qRT-PCR. These genes were subdivided into three groups: (1) genes that are involved in the recruitment, transportation to the cell surface and function of $Na_v1.6$; (2) genes that regulate *Scn8a* production throughout postnatal development; and (3) genes that are indicative of the overall state of the retinal support structure. Results are first presented on a gene by gene basis; expression changes within each gene are assessed individually in the presence (*Scn8a*$^{+/+}$, WT) and absence (*Scn8a*$^{dmu/dmu}$, Mut) of a functional *Scn8a* gene (i.e. capable of encoding a fully functional $Na_v1.6$ channel). Second, differences in gene expression observed in the presence and absence of light as a rearing condition are presented between light-reared (LR) and dark-reared (DR) animals.

I present my results for each gene as follows: (a) I first review the normal occurrences in LR wildtype expression (LR WT) and particular patterns of interest, to establish a baseline against which all experimental conditions are compared; (b) I then present comparisons between LR WT (*Scn8a*$^{+/+}$) compared to LR Mut (*Scn8a*$^{dmu/dmu}$); (c) followed by a comparison of the differences between LR WT compared to DR WT so that I can then make comparisons for DR WT vs. DR Mut.

The two reference genes used for qRT-PCR data analysis are plotted in Figure 3.1. Data for each timepoint represents the combined average of all genotypes as well as rearing conditions for the qRT-PCR study.

Each normalized gene expression graph represents changes in expression level of one specific gene across five developmental timepoints; two different genotypes and the LR or DR rearing condition are compared. Gene expression is normalized to the combined average of two housekeeping genes at a specific developmental timepoint (*Gapdh* and *Hprt1*), the "master denominator" (Figure 3.1). For each normalized gene expression graph, values are given arbitrary units since the y-axis is a numerical representation of the ratio, calculated as the averaged copy number of a target gene (of each genotype at a specific timepoint and rearing condition) value over the "master denominator" of the same specific timepoint value.

Figure 3.1: Reference genes *Gapdh* and *Hprt1* are plotted in graphs **(A)** and **(B)** respectively. Error bars represent calculatedstandeard error of the mean (±SEM). There is little variability in gene expression as animal ages to defined timepoints in this experiment. Notably, there is a slight decrease in expression of both reference genes at P10, possibly due to the young age and still developing retina at this stage in the immature postnatal eye. Data gathered for both reference genes represent light- and dark-reared conditions as well as all genotypes present in this study.

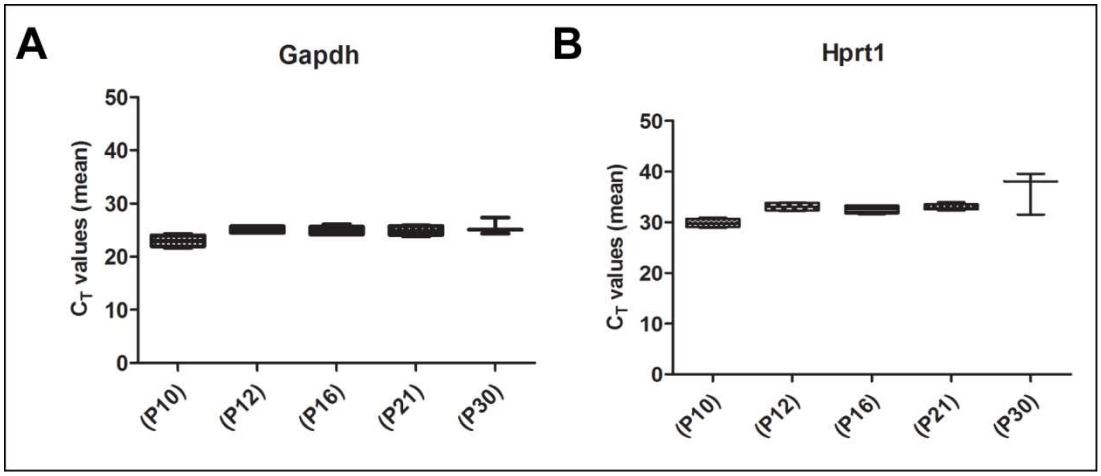
A
Gapdh
B
Hprt1
C_T values (mean)
50
40
30
20
10
0
(P10)
(P12)
(P16)
(P21)
(P30)

Each fold change bar graph represents changes in gene expression relative to the LR WT gene expression at each specific timepoint. Therefore, the LR WT gene expression at each timepoint is equal to one. Each bar graph shows relative fold change of one specific gene across five developmental timepoints, comparing two different genotypes and the LR or DR rearing conditions.

ANOVA results for each gene comparing all genotype groups and rearing conditions for each timepoint are compiled in Table 3.1.

3.1.1 Recruitment, transportation to cell surface and function of $Na_v1.6$

The group consists of five genes that play important roles in both the transport and function of $Na_v1.6$ at the nodes of Ranvier. These include neurofilament light-chain (*NF-L*), JNK-interacting protein 1 (*Jip1*), amyloid beta precursor protein (*App*), ankyrin G (*Ank3*), and voltage-gated sodium channel type 1 beta subunit (*Scn1b*).

3.1.1.1 Neurofilament light-chain (NF-L) (gene symbol: Nefl)

Expression of *NF-L* in LR WT animals was similar between the ages of P10 to P16; however, there was a significant drop in expression at P21 when compared to initial *NF-L* expression at P10 (Tukey's post-hoc, $p<0.05$) (Figure 3.2A). This dip in expression however, was recovered back to the pre-P21 levels by the age of P30, the experimental endpoint.

An ANOVA analysis of the *NF-L* transcript expression data revealed significant differences between expression profiles for LR WT animals compared to that observed for LR Mut animals ($p<0.0001$). For LR Mut, the *NF-L* expression levels were comparable to that observed for LR WT across all developmental ages. The pattern observed for LR Mut exhibited a strong trend towards lower *NF-L* expression than LR WT across most timepoints as experimental animals aged. The dip in expression level observed at P21 for LR WT animals was replicated by LR Mut animals; however, there appeared to be a temporal shift from P21 in LR WT to P16 in LR Mut (Tukey's post-hoc, $p<0.05$ for P10 LR Mut vs. P16 LR Mut). This dip in expression returned to pre-P16 levels as evident by the data from P21 LR Mut.

When examining the presence or absence of light as a rearing condition, ANOVA analysis revealed differences between LR and DR animals (WT and Mut) ($p<0.0001$) (Figure 3.2A).

Table 3.1: Compiled ANOVA statistic results for each gene comparing all genotype groups and rearing conditions for each developmental timepoint. For example, for *NF-L* at P10, an ANOVA was performed on all data from P10 LR WT, P10 LR Mut, P10 DR WT and P10 DR Mut.
Abbreviations: WT = *Scn8a*$^{+/+}$ wildtype, Mut = *Scn8a*$^{dmu/dmu}$ mutant, LR = light-reared, DR = dark-reared, p = postnatal day.

	P10			P12			P16		
Gene	P value	F statistic	R^2 value	P value	F statistic	R^2 value	P value	F statistic	R^2 value
NF-L	0.0862	2.4300	0.2066	0.1423	1.9580	0.1685	0.0873	2.2000	0.1881
Jip1	0.8727	0.2328	0.0262	0.0301	3.4250	0.2616	0.0225	3.2270	0.2536
App	0.0644	2.6750	0.2056	0.1173	2.1360	0.1810	0.3207	1.2160	0.1162
Ank3	0.5262	0.7575	0.0663	0.4259	0.9587	0.0932	0.0275	3.0820	0.2499
Scn1b	0.6016	0.6314	0.0704	0.1849	1.7570	0.1932	0.0451	2.7300	0.2431
Bdnf	0.0032	5.6950	0.3553	0.1426	1.9570	0.1683	0.0039	4.5750	0.3139
TrkB	0.1529	1.8980	0.1690	0.1758	1.8310	0.2243	0.2465	1.4710	0.2189
Pum2	P<0.0001	18.3800	0.6401	0.0369	3.2960	0.2834	0.0097	3.9310	0.3100
Scn8a	0.0068	4.9730	0.3476	0.2157	1.5700	0.1283	0.3968	1.0240	0.0989
Gfap	0.7370	0.4242	0.0394	0.0378	3.2720	0.2820	0.3136	1.2370	0.1271
Cntf	0.0419	3.1170	0.2503	0.0373	3.1890	0.2358	P<0.0001	8.9070	0.5045

	P21			P30			All Time Points		
Gene	P value	F statistic	R^2 value	P value	F statistic	R^2 value	P value	F statistic	R^2 value
NF-L	0.0527	2.5720	0.2087	0.3821	1.0020	0.0770	P<0.0001	6.1260	0.4368
Jip1	0.0838	2.2370	0.1947	0.3924	0.9730	0.0750	P<0.0001	3.4920	0.3120
App	0.2887	1.2940	0.1146	0.3001	1.2720	0.1036	0.1174	1.4260	0.1520
Ank3	0.0003	6.8750	0.4400	0.3280	1.1680	0.0887	P<0.0001	5.5450	0.4155
Scn1b	0.2709	1.3460	0.1241	0.0037	8.0970	0.5030	0.0014	2.4280	0.2645
Bdnf	0.0003	6.8780	0.4075	0.0571	3.2700	0.2292	P<0.0001	3.1730	0.2815
TrkB	0.0105	4.1690	0.4100	0.1210	2.4650	0.2604	0.0047	2.2300	0.2962
Pum2	0.0088	3.9430	0.2879	0.8505	0.1630	0.0134	P<0.0001	47.7800	0.8612
Scn8a	0.2894	1.3060	0.1091	0.2959	t = 1.118	0.1352	0.0686	1.6140	0.1679
Gfap	0.0334	2.9430	0.2464	0.0897	2.6960	0.1969	0.0097	2.0110	0.2137
Cntf	0.0053	4.3870	0.3217	0.5797	0.5632	0.0621	P<0.0001	6.3780	0.4629

Figure 3.2: Neurofilament light-chain (*NF-L*) expression throughout retinal development. **(A)** depicts the normalized expression levels of *NF-L* across defined ages throughout postnatal development, spanning the time of eye-opening. **(B)** depicts fold change of each genotype at defined timepoints where gene expression has been calculated as expression relative to light-reared wildtype (LR WT) animals. Error bars represent standard error of the mean (±SEM). Statistics were performed in GraphPad Prism 5. **Abbreviations:** WT = *Scn8a*$^{+/+}$ wildtype, Mut = *Scn8a*$^{dmu/dmu}$ mutant, LR = light-reared, DR = dark-reared, p = postnatal day.

A

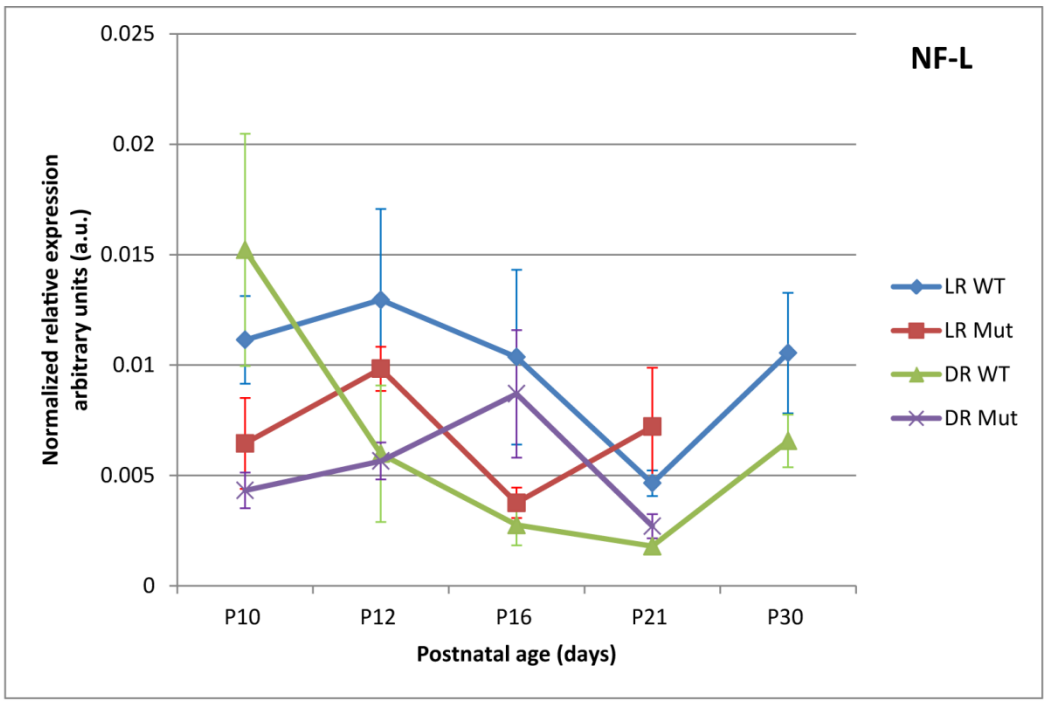
NF-L
0.025
0.02
0.015
0.01
0.005
0
Normalized relative expression arbitrary units (a.u.)
P10
P12
P16
P21
P30
Postnatal age (days)
LR WT
LR Mut
DR WT
DR Mut

B

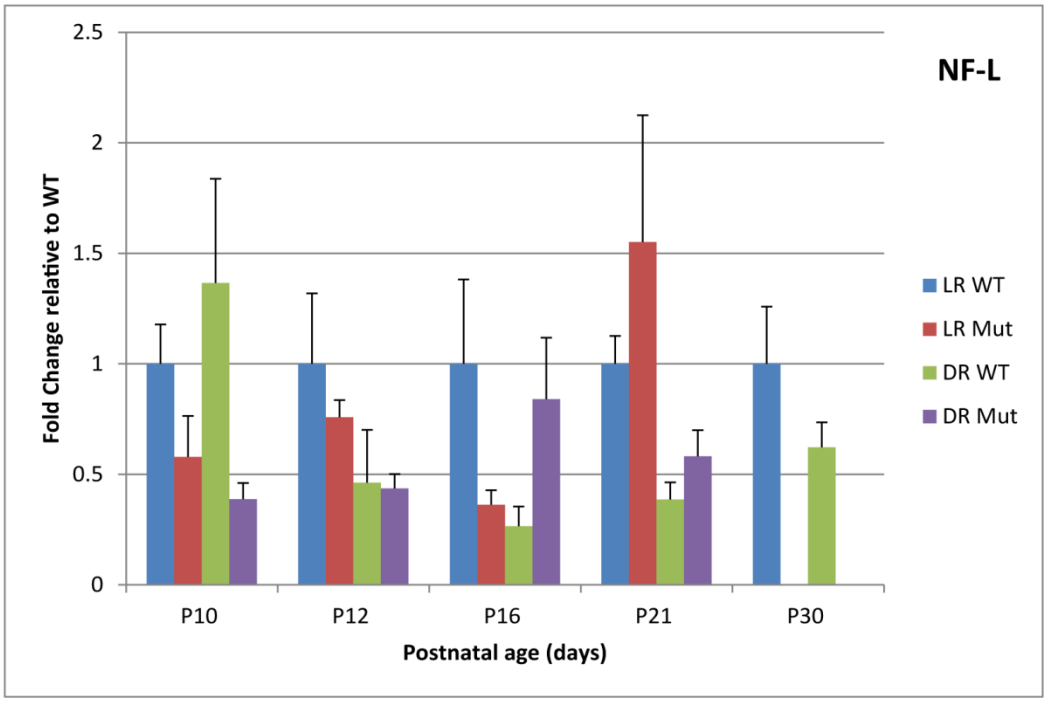
NF-L
2.5
2
1.5
1
0.5
0
Fold Change relative to WT
P10
P12
P16
P21
P30
Postnatal age (days)
LR WT
LR Mut
DR WT
DR Mut

Specifically, *NF-L* expression for DR WT animals at P10 was the highest level observed across all developmental timepoints and genotypes studied. DR WT at P10 were significantly different from P10 DR Mut (Tukey's post-hoc, $p<0.05$). DR WT animals exhibited a drop in *NF-L* expression by P12; in the older timepoints, the *NF-L* expression levels were not significantly different than those observed for LR WT animals. Similar to LR Mut, the DR WT animals exhibited a strong trend towards lower *NF-L* expression when compared to LR WT animals, showing a dip in expression at P21, followed by a rise to higher *NF-L* expression by P30.

DR Mut animals also exhibited a similar expression pattern as that observed for LR WT animals, showing a dip in expression at P21. The DR Mut had similar levels of *NF-L* expression as that observed for LR Mut; however, the temporal shift in lower *NF-L* expression seen in LR Mut at P16 was not replicated by DR Mut.

In the *NF-L* fold change bar graph (Figure 3.2B), the general trends observed in the normalized expression graph (Figure 3.2A) were also seen. There was an overall trend towards WT animals (LR and DR) having higher *NF-L* expression than their Mut counterparts before eye-opening (P10-P12), but lower *NF-L* expression after eye-opening (P16-P21). *NF-L* expression for LR Mut was typically lower when compared to LR WT. Although the *NF-L* expression in LR Mut appeared to show a 1.55-fold increase at P21 when compared to LR WT, this observation was not statistically significant (Figure 3.2B). DR Mut appeared to show a higher *NF-L* expression compared to DR WT at P16, but this observation was also not statistically significant.

3.1.1.2 JNK-interacting protein 1 (Jip1) (gene symbol: Mak8ip1)

An ANOVA analysis of the *Jip1* transcript expression data revealed significant differences between LR WT and LR Mut animals ($p<0.0001$). *Jip1* expression in LR WT animals remained fairly stable (albeit with a large margin of error at P12) between the ages of P10 to P16 (Figure 3.3A). There was a drop in expression at P21 that is significantly different from the initial expression levels observed at P10 (Tukey's post-hoc, $p<0.05$). This drop in *Jip1* expression remained lower than that observed for P10 through to the experimental endpoint of P30 (Tukey's post-hoc, $p<0.05$). At P12, there was a slight peak in *Jip1* expression, although this change was insignificant when compared to expression levels at P10 and P16.

Figure 3.3: JNK-interacting protein (*Jip1*) expression throughout retinal development. **(A)** depicts the normalized expression levels of *Jip1* across defined ages throughout postnatal development, spanning the time of eye-opening. **(B)** depicts fold change of each genotype at defined timepoints where gene expression has been calculated as expression relative to light-reared wildtype (LR WT) animals. 1-way ANOVA with Tukey's post-hoc test with significance indicated as * = $p \leq 0.05$, ** = $p \leq 0.01$, and *** = $p \leq 0.001$ were performed. Error bars represent standard error of the mean (±SEM). Statistics were performed in GraphPad Prism 5.
Abbreviations: WT = *Scn8a*$^{+/+}$ wildtype, Mut = *Scn8a*$^{dmu/dmu}$ mutant, LR = light-reared, DR = dark-reared, p = postnatal day.

A

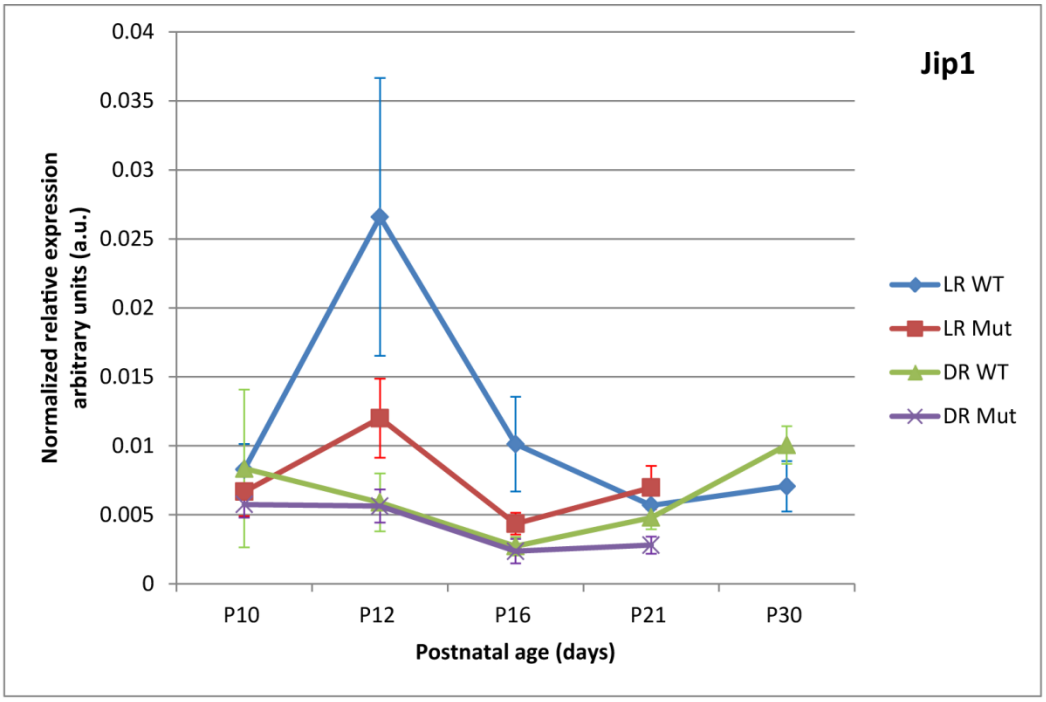
Jip1
Normalized relative expression arbitrary units (a.u.)
0.04
0.035
0.03
0.025
0.02
0.015
0.01
0.005
0
P10
P12
P16
P21
P30
Postnatal age (days)
LR WT
LR Mut
DR WT
DR Mut

B

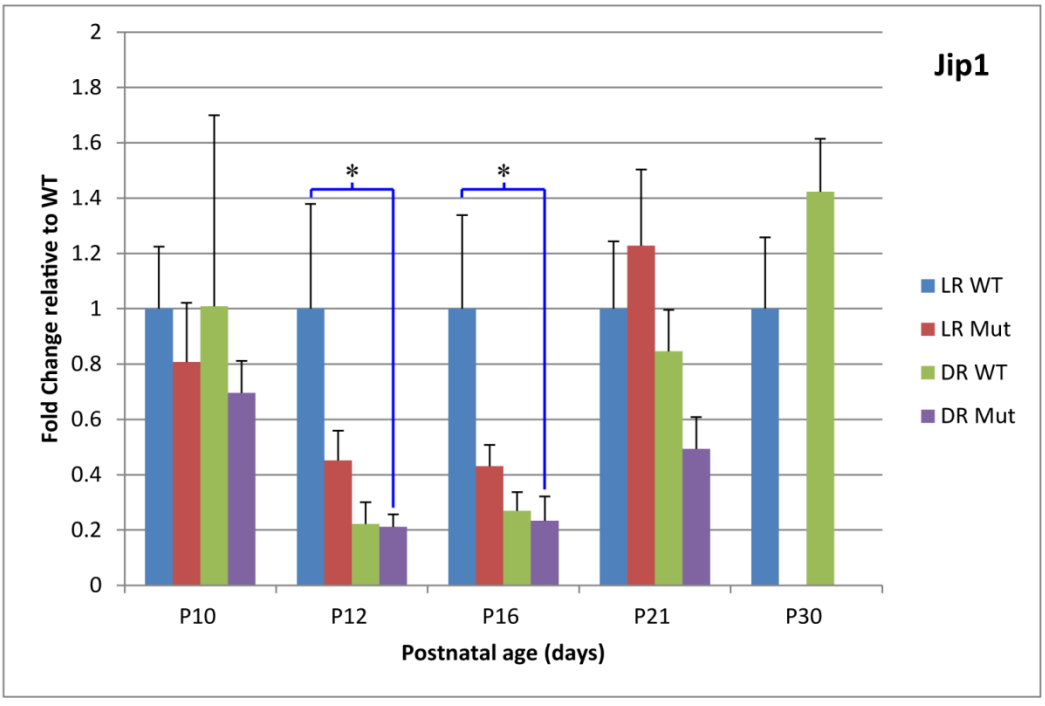
Jip1
Fold Change relative to WT
2
1.8
1.6
1.4
1.2
1
0.8
0.6
0.4
0.2
0
*
*
P10
P12
P16
P21
P30
Postnatal age (days)
LR WT
LR Mut
DR WT
DR Mut

LR Mut animals exhibited a similar *Jip1* expression profile as that observed for LR WT animals. Mutants consistently expressed less *Jip1* transcripts than WT counterparts. Specifically, *Jip1* expression at P12, P16 and P21 were lower than the initial expression of WT expression at P10 (Tukey's post-hoc, $p<0.05$). Just as there was a dip in expression level at P21 for LR WT animals, there is a similar dip in *Jip1* expression at P16 in LR Mut that was significantly different from initial levels of expression (Tukey's post-hoc, $p<0.05$) (Figure 3.3A). This dip in expression level was recovered by P21. Similar to what was observed in *NF-L* expression, there appeared to be a temporal shift in LR Mut expression levels from P21 to P16.

An ANOVA analysis between LR and DR animals revealed significant differences in *Jip1* expression (Figure 3.3A). This suggests that light stimulus has an effect on the level of *Jip1* transcripts on experimental animals starting at P10, through eye-opening and into adulthood. DR Mut animals expressed a statistically significant lower level of *Jip1* at P12 and P16 when compared to LR WT animals (Tukey's post-hoc, $p<0.05$). Although statistically insignificant, there was an overall trend that showed *Jip1* expression levels in DR animals (WT and Mut) were lower than that of LR counterparts across all developmental timepoints.

In the *Jip1* fold change bar graph, there was an overall trend towards DR animals having lower *Jip1* expression when compared to LR animals (Figure 3.3B). Additionally, there was a trend towards DR Mut having consistently lower expression than their DR WT counterparts. LR Mut also appeared to have lower *Jip1* expression when compared to LR WT, except at P21, when LR Mut showed a 1.23-fold increase than LR WT. However, this fold change observation was not statistically significant.

At the P12 timepoint, an ANOVA analysis revealed a statistically significant difference between LR WT and DR Mut animals ($p<0.05$). At this developmental age, DR Mut expressed a 4.76-fold decrease (equivalent to a 78.79% downregulation) when compared to LR WT animals (Figure 3.3B). Similarly, at the P16 timepoint, an ANOVA analysis revealed a significant difference between LR WT and DR Mut animals ($p<0.05$). At this developmental age, DR Mut expressed a 4.28-fold decrease (equivalent to a 76.61% downregulation) when compared to LR WT animals.

3.1.1.3 Amyloid beta precursor protein (App)

ANOVA analysis of *App* transcript expression data sets between LR WT and LR Mut animals revealed no significant changes in expression levels across all age groups (Figure 3.4A). The expression levels of *App* remained nearly consistent across all developmental timepoints. There was a small trend that expression levels of *App* is higher in LR WT animals than in LR Mut; however, the difference was insignificant. An ANOVA analysis revealed that there were no significant differences between LR and DR animals (Figure 3.4A). Just as observed in LR animals, DR animals had relatively steady *App* expression levels across all developmental timepoints measured. Although there was a dramatic increase in *App* expression in DR WT animals at P16, this observation was not statistically significant when compared to the other genotypes during this developmental timepoint.

In the *App* fold change bar graph, *App* expression across all developmental timepoints remained relatively stable, as ANOVA analysis did not reveal significant differences (Figure 3.4B). However, an ANOVA analysis revealed a statistically significant difference at the P16 developmental timepoint ($p<0.001$). DR WT animals expressed a 7.49-fold increase when compared to the other genotypes during this timepoint. As all the experimental triplicates and technical triplicates were within 0.5 C_T values, these data points were not omitted as outliers.

3.1.1.4 Ankyrin G (Ank3)

Significant differences were found between LR WT and LR Mut *Ank3* expression patterns through ANOVA analysis ($p<0.0001$) (Figure 3.5A). *Ank3* expression of LR WT animals started off at a relatively low level, but rose significantly, as both P12 and P16 expression levels were above initial levels measured at P10 (Tukey's post-hoc, $p<0.05$). As LR WT animals aged, the rise in *Ank3* expression diminished, as both P21 and P30 expression levels were significantly lower than initial measurements at P10 (Tukey's post-hoc, $p<0.05$).

LR Mut exhibited a similar *Ank3* expression pattern as that observed for LR WT; LR Mut showed a similar increase in *Ank3* expression at P12 over initial measurements at P10 (Tukey's post-hoc, $p<0.05$). However, this increase in *Ank3* expression quickly dropped as measurements at P16 and P21 were significantly lower than initial

Figure 3.4: Amyloid beta precursor protein (*App*) expression throughout retinal development. **(A)** depicts the normalized expression levels of *App* across defined ages throughout postnatal development, spanning the time of eye-opening. **(B)** depicts fold change of each genotype at defined timepoints where gene expression has been calculated as expression relative to light-reared wildtype (LR WT) animals. 1-way ANOVA with Tukey's post-hoc test with significance indicated as * = $p \leq 0.05$, ** = $p \leq 0.01$, and *** = $p \leq 0.001$ were performed. Error bars represent standard error of the mean (±SEM). Statistics were performed in GraphPad Prism 5.
Abbreviations: WT = *Scn8a*$^{+/+}$ wildtype, Mut = *Scn8a*$^{dmu/dmu}$ mutant, LR = light-reared, DR = dark-reared, p = postnatal day.

A

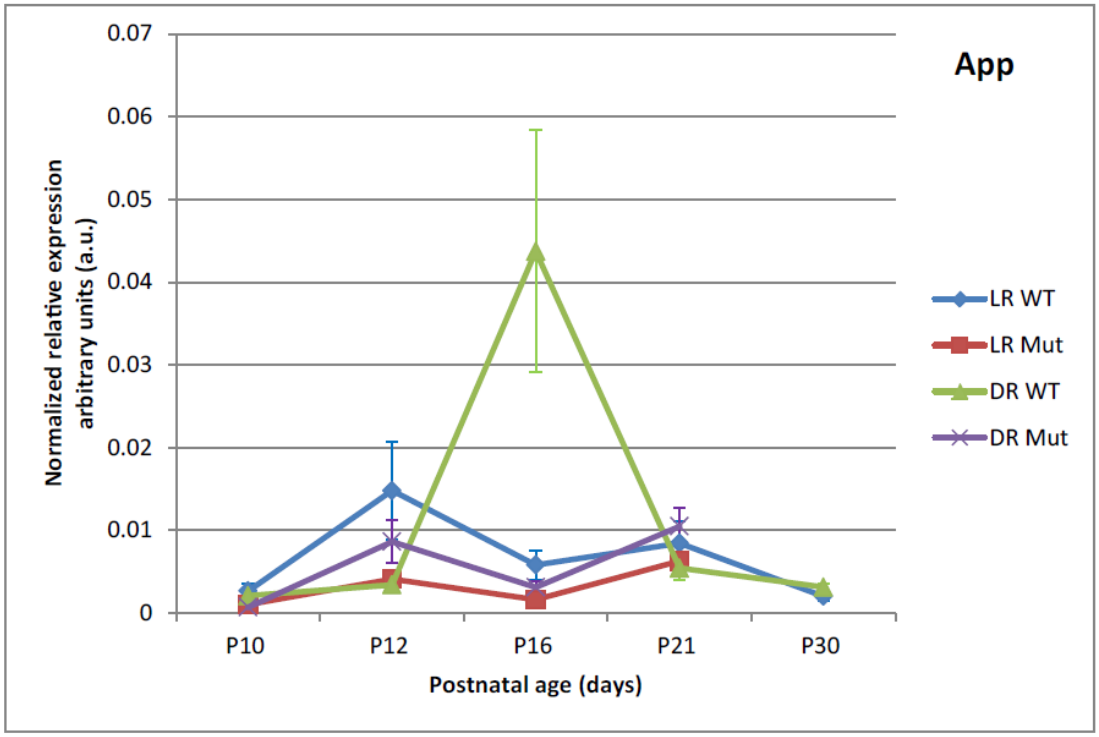
App
0.07
0.06
0.05
0.04
0.03
0.02
0.01
0
Normalized relative expression arbitrary units (a.u.)
P10
P12
P16
P21
P30
Postnatal age (days)
LR WT
LR Mut
DR WT
DR Mut

B

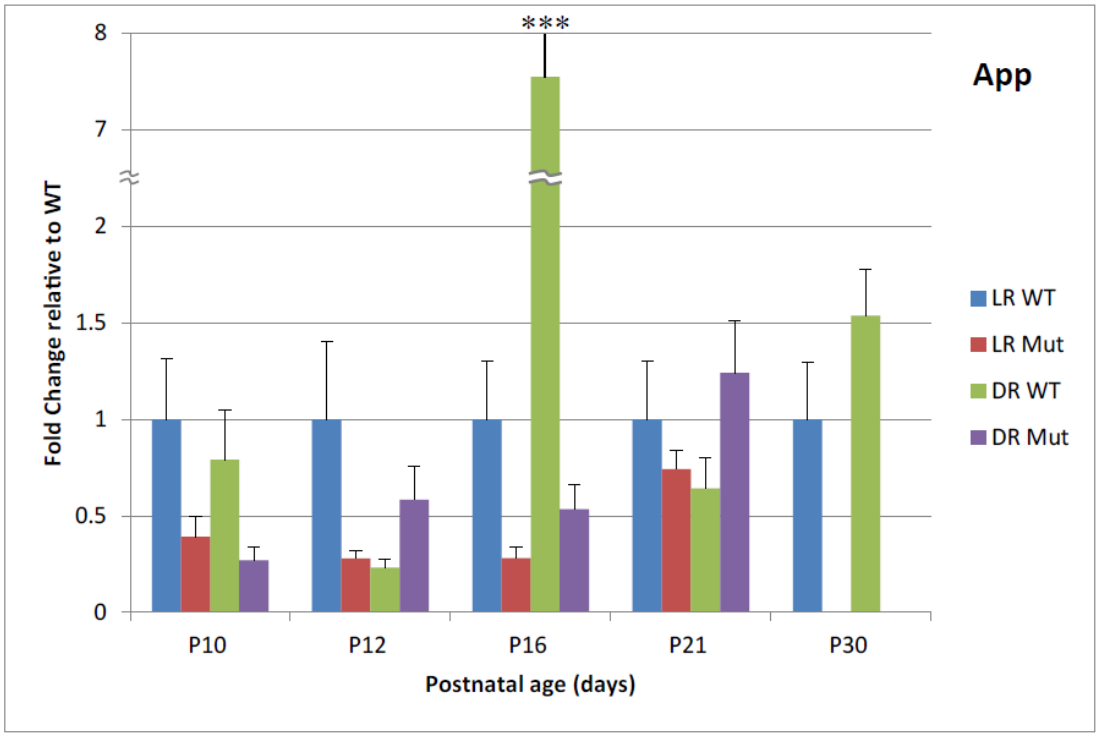
***
App
8
7
2
1.5
1
0.5
0
Fold Change relative to WT
P10
P12
P16
P21
P30
Postnatal age (days)
LR WT
LR Mut
DR WT
DR Mut

Figure 3.5: Ankyrin G (*Ank3*) expression throughout retinal development. **(A)** depicts the normalized expression levels of *Ank3* across defined ages throughout postnatal development, spanning the time of eye-opening. **(B)** depicts fold change of each genotype at defined timepoints where gene expression has been calculated as expression relative to light-reared wildtype (LR WT) animals. 1-way ANOVA with Tukey's post-hoc test with significance indicated as * = $p \leq 0.05$, ** = $p \leq 0.01$, and *** = $p \leq 0.001$ were performed. Error bars represent standard error of the mean (±SEM). Statistics were performed in GraphPad Prism 5.
Abbreviations: WT = *Scn8a*$^{+/+}$ wildtype, Mut = *Scn8a*$^{dmu/dmu}$ mutant, LR = light-reared, DR = dark-reared, p = postnatal day.

A

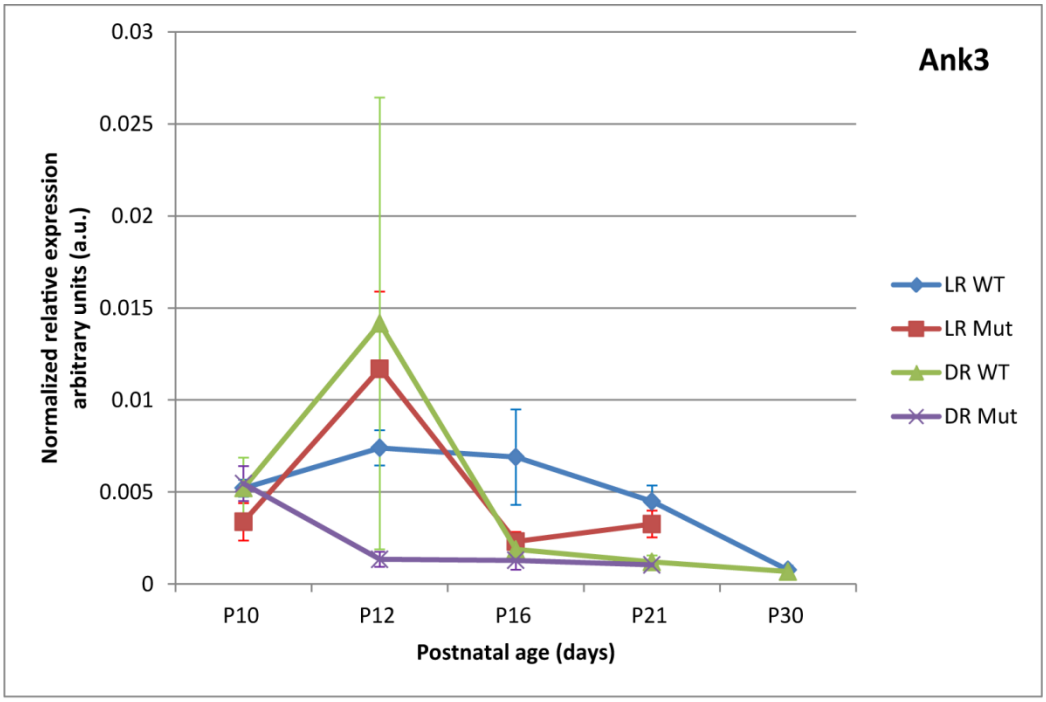
Ank3
Normalized relative expression arbitrary units (a.u.)
0.03
0.025
0.02
0.015
0.01
0.005
0
P10
P12
P16
P21
P30
Postnatal age (days)
LR WT
LR Mut
DR WT
DR Mut

B

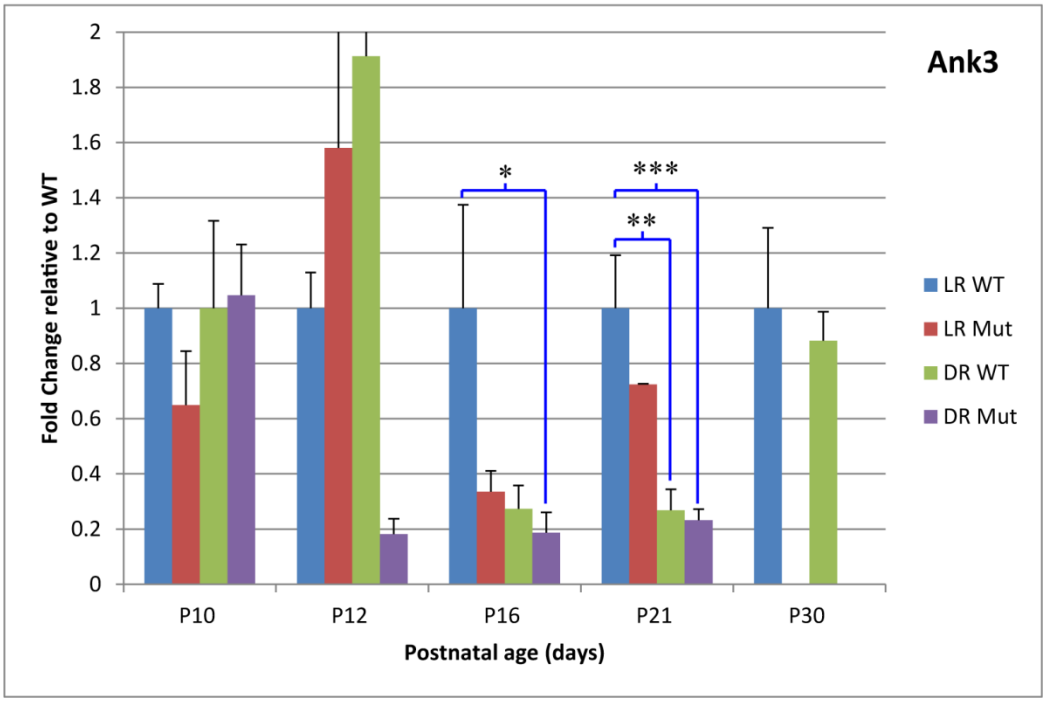
Ank3
Fold Change relative to WT
2
1.8
1.6
1.4
1.2
1
0.8
0.6
0.4
0.2
0
*
***
**
P10
P12
P16
P21
P30
Postnatal age (days)
LR WT
LR Mut
DR WT
DR Mut

measurements at P10 (Tukey's post-hoc, $p<0.05$) (Figure 3.5A). There was a trend of lower *Ank3* expression seen in LR Mut animals throughout retinal development when compared to LR WT animals.

Ank3 expression patterns for DR animals started off at a relatively low level at P10, comparable to that observed for LR WT counterparts (Figure 3.5A). ANOVA analysis between LR and DR animals exhibited significant differences between the two rearing conditions ($p<0.001$). This difference was dramatically observed by P16, where *Ank3* expression levels for DR animals (WT and Mut) were significantly diminished from that observed at P10 (Tukey's post-hoc, $p<0.05$). This diminished *Ank3* expression level in DR animals remained constant and indistinguishable from the lowered expression level observed at P30 for LR WT animals (Figure 3.5A).

In the *Ank3* fold change bar graph, the general trends observed in the normalized expression graph were also seen. In particular, there was an overall trend towards all genotypes having less *Ank3* expression when compared to LR WT after eye-opening (P16-P30) (Figure 3.5B). This trend was not observed in the earlier timepoints (P10-P12); however, ANOVA analysis did not reveal any significant differences.

At the P16 timepoint, an ANOVA analysis revealed a statistically significant difference between LR WT and DR Mut animals ($p<0.05$). At this developmental age, DR Mut expressed a 5.34-fold decrease (equivalent to a 81.27% downregulation) when compared to LR WT (Figure 3.5B). In addition, at the P21 timepoint, an ANOVA analysis revealed significant differences between WT animals (LR and DR, $p<0.01$), and also between LR WT and DR Mut animals ($p<0.001$). At this developmental age, DR WT animals expressed a 3.72-fold decrease (equivalent to a 73.13% downregulation) in *Ank3* expression when compared to LR WT counterparts; while DR Mut expressed a 4.30-fold decrease (equivalent to a 76.76% downregulation) in *Ank3* expression (Figure 3.5B).

3.1.1.5 Voltage-gated sodium channel type 1 beta subunit (Scn1b)

ANOVA analysis of *Scn1b* expression profiles between LR WT and LR Mut animals revealed small, but significant differences for some developmental timepoints ($p = 0.0156$) (Figure 3.6A). LR WT animals exhibited a trend of increasing *Scn1b* expression from the initial measurement at P10, increasing at P12, and reaching peak

Figure 3.6: Voltage-gated sodium channel type 1 beta subunit (*Scn1b*) expression throughout retinal development. **(A)** depicts the normalized expression levels of *Scn1b* across defined ages throughout postnatal development, spanning the time of eye-opening. **(B)** depicts fold change of each genotype at defined timepoints where gene expression has been calculated as expression relative to light-reared wildtype (LR WT) animals. 1-way ANOVA with Tukey's post-hoc test with significance indicated as * = $p \leq 0.05$, ** = $p \leq 0.01$, and *** = $p \leq 0.001$ were performed. Error bars represent standard error of the mean (±SEM). Statistics were performed in GraphPad Prism 5.
Abbreviations: WT = *Scn8a*$^{+/+}$ wildtype, Mut = *Scn8a*$^{dmu/dmu}$ mutant, LR = light-reared, DR = dark-reared, p = postnatal day.

A

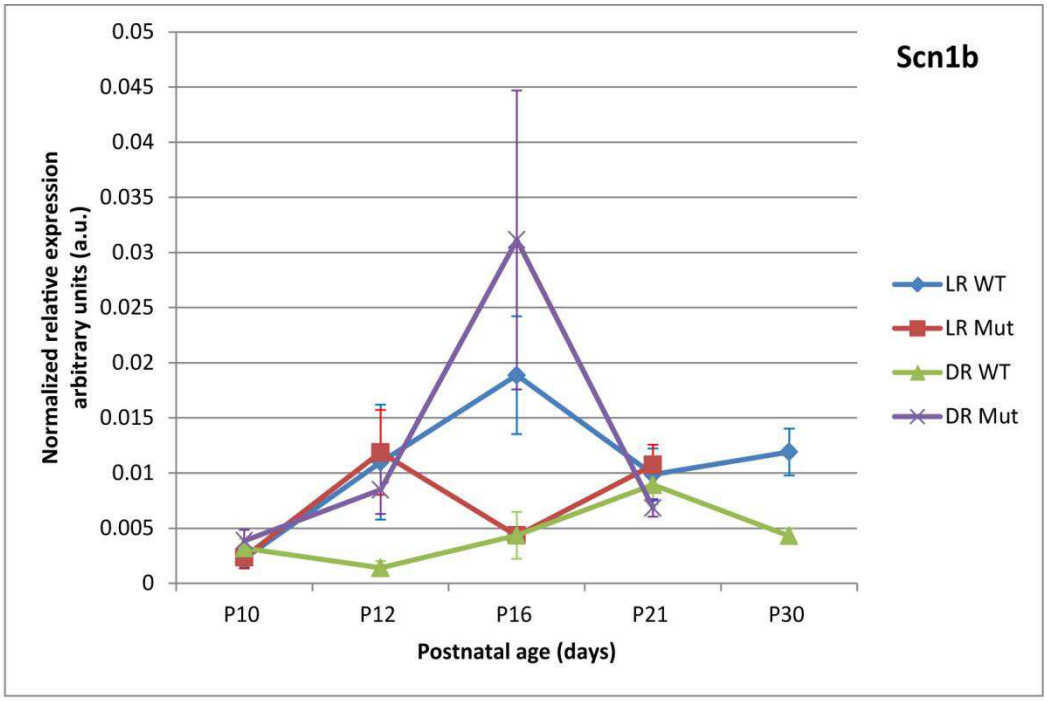
Scn1b
Normalized relative expression arbitrary units (a.u.)
0.05
0.045
0.04
0.035
0.03
0.025
0.02
0.015
0.01
0.005
0
P10
P12
P16
P21
P30
Postnatal age (days)
LR WT
LR Mut
DR WT
DR Mut

B

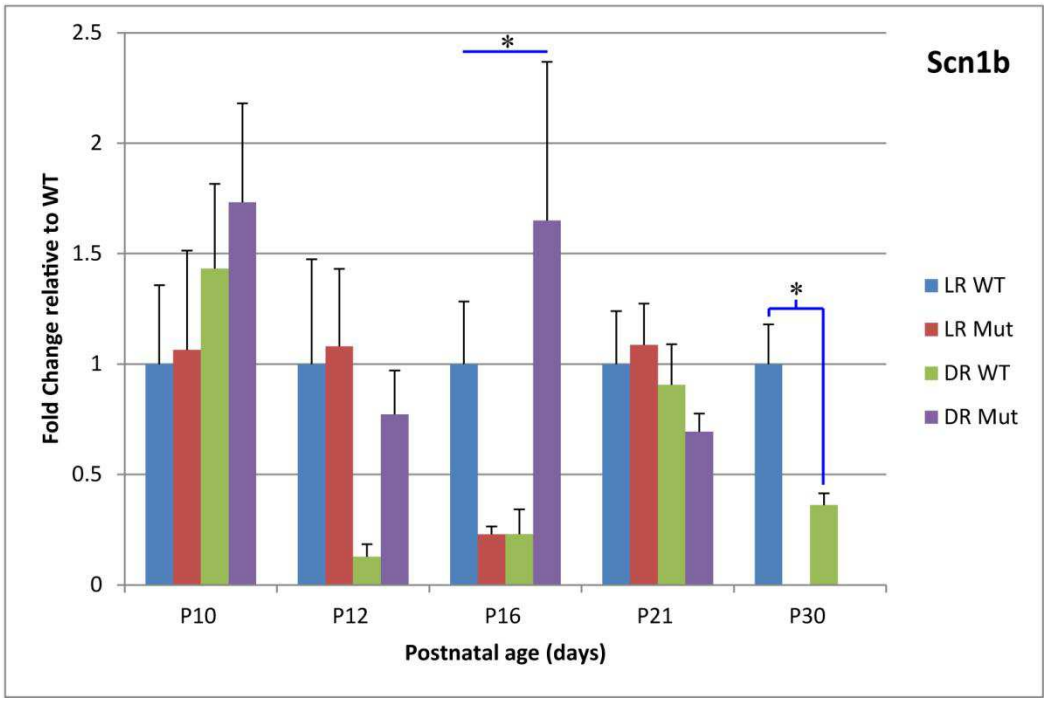
Scn1b
Fold Change relative to WT
2.5
2
1.5
1
0.5
0
*
*
P10
P12
P16
P21
P30
Postnatal age (days)
LR WT
LR Mut
DR WT
DR Mut

expression at P16. It is at this timepoint, soon after eye-opening, that *Scn1b* expression in LR Mut deviate from LR WT, showing a significantly lower level of *Scn1b* transcript when compared to LR WT (Tukey's post-hoc, $p<0.05$).

An ANOVA analysis between LR and DR animals revealed that there were marginal, but significant, differences between the two groups ($p = 0.0018$). The expression pattern for DR WT animals exhibited a strong trend towards decreased *Scn1b* expression throughout most developmental timepoints (Figure 3.6A). DR Mut appeared to have *Scn1b* expression levels that more closely matched the LR WT expression profile, with a peak expression at P16.

In the *Scn1b* fold change bar graph, there was a general overall trend towards Mut animals (LR and DR) having slightly higher *Scn1b* expression compared to their WT counterparts across most developmental timepoints (Figure 3.6B). Of important note, while an ANOVA analysis revealed significant differences between the genotypes at P16 ($p = 0.0451$), a Tukey's post-hoc test was inconclusive and did not identify actual pairings of significance. Interestingly, LR Mut animals had a 4.36-fold decrease (equivalent to a 77.08% downregulation) of *Scn1b* expression, while DR Mut expressed a 1.65-fold increase in *Scn1b* expression when compared to LR WT at P16. As all the experimental triplicates and technical triplicates were within 0.5 C_T values, the data points for the DR Mut were not omitted as outliers. At the P30 timepoint, ANOVA analysis ($p = 0.0075$) revealed that DR WT animals expressed a 2.77-fold decrease (equivalent to a 63.86% downregulation) in *Scn1b* expression when compared to LR WT counterparts (Figure 3.6B).

3.1.2 Regulation of Scn8a *production through postnatal development*

It has been documented that a strong increase in retinal *Scn8a* expression occurs during the period coinciding with retinal function maturation that follows eye-opening (Côté *et al.*, 2005). I first examined the influence of visual experience on *Scn8a* expression. Then, I examined a group consisting of three genes that play key roles in regulating *Scn8a* expression throughout postnatal development (Shieh and Ghosh, 1999; Caldwell, 2000; Caldwell *et al.*, 2000; Meisler *et al.*, 2001; Trudeau *et al.*, 2006; Fiore *et al.*, 2009; Khudayberdiev *et al.*, 2009; Driscoll *et al.*, 2013; Vermehren-Schmaedick *et*

al., 2015). These include brain-derived neurotrophic factor (*Bdnf*), tropomyosin receptor kinase B (*TrkB*), and Pumilio RNA-binding family member 2 (*Pum2*).

3.1.2.1 Voltage-gated sodium channel alpha subunit 8 (Scn8a)

LR WT expression of *Scn8a* was relatively stable across all postnatal development timepoints, starting with a low transcript level at P10, increasing at P12 through to P21, and finally declining by P30 (Figure 3.7A).

In addition, light stimulation did not appear to be a determinant on *Scn8a* expression. However, there was a strong trend towards higher *Scn8a* expression levels in DR animals when compared to LR counterparts (Figure 3.7A). In DR animals, there was a trend towards increased *Scn8a* expression levels at P12, just before eye-opening, which then decreased at P16 and P21, and by P30, *Scn8a* expression levels in DR animals was similar to the expression level observed in LR WT animals.

In the *Scn8a* fold change bar graph, an ANOVA analysis indicated a statistically significant difference between LR and DR WT animals at P10. Specifically, DR WT exhibited a 6.66-fold decrease (equivalent to a 84.99% downregulation) in *Scn8a* expression when compared to their LR WT counterparts (Figure 3.7B). At P12, it is interesting to note the sharp increase in *Scn8a* expression observed in DR WT animals, although an ANOVA analysis did not reveal any significant differences between the LR and DR genotype groups at this age (Figure 3.7B).

3.1.2.2 Brain-derived neurotrophic factor (Bdnf)

An ANOVA analysis indicated that LR WT expression of *Bdnf* transcript was significantly different from that observed for LR Mut animals ($p = 0.0003$) (Figure 3.8A). LR WT expression of *Bdnf* was relatively stable throughout postnatal development, as all of the experimental timepoints were statistically insignificant from each other; there was a trend towards higher *Bdnf* expression at P12, around the time of eye-opening, followed by a decline in expression by P16 and P21. This expression profile was also observed in LR Mut animals, although to a lesser degree across all experimental timepoints. Specifically, LR WT animals expressed a significantly higher level of *Bdnf* at P12 when compared to LR Mut (Tukey's post-hoc, $p<0.05$).

Figure 3.7: Voltage-gated sodium channel alpha subunit 8 (*Scn8a*) expression is presented at defined timepoints across postnatal development, spanning the critical time of eye-opening through to adulthood. **(A)** depicts the normalized expression levels of *Scn8a*, illustrating the changes in gene expression across postnatal timepoints. **(B)** depicts fold change of each genotype, illustrating the changes in gene expression relative to light-reared wildtype (LR WT) animals for each postnatal timepoint. 1-way ANOVA with Tukey's post-hoc test with significance indicated as * = $p \leq 0.05$, ** = $p \leq 0.01$, and *** = $p \leq 0.001$ were performed. Error bars represent standard error of the mean (±SEM). Statistics were performed in GraphPad Prism 5.
Abbreviations: WT = $Scn8a^{+/+}$ wildtype, Mut = $Scn8a^{dmu/dmu}$ mutant, LR = light-reared, DR = dark-reared, p = postnatal day.

A

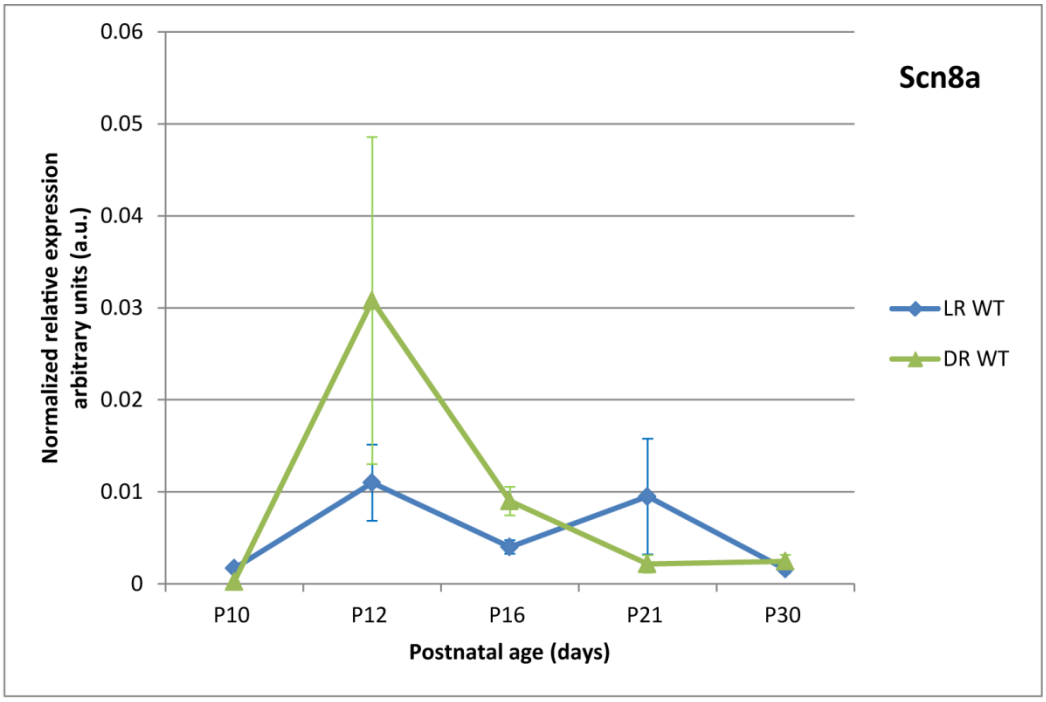
Scn8a
Normalized relative expression arbitrary units (a.u.)
0.06
0.05
0.04
0.03
0.02
0.01
0
P10
P12
P16
P21
P30
Postnatal age (days)
LR WT
DR WT

B

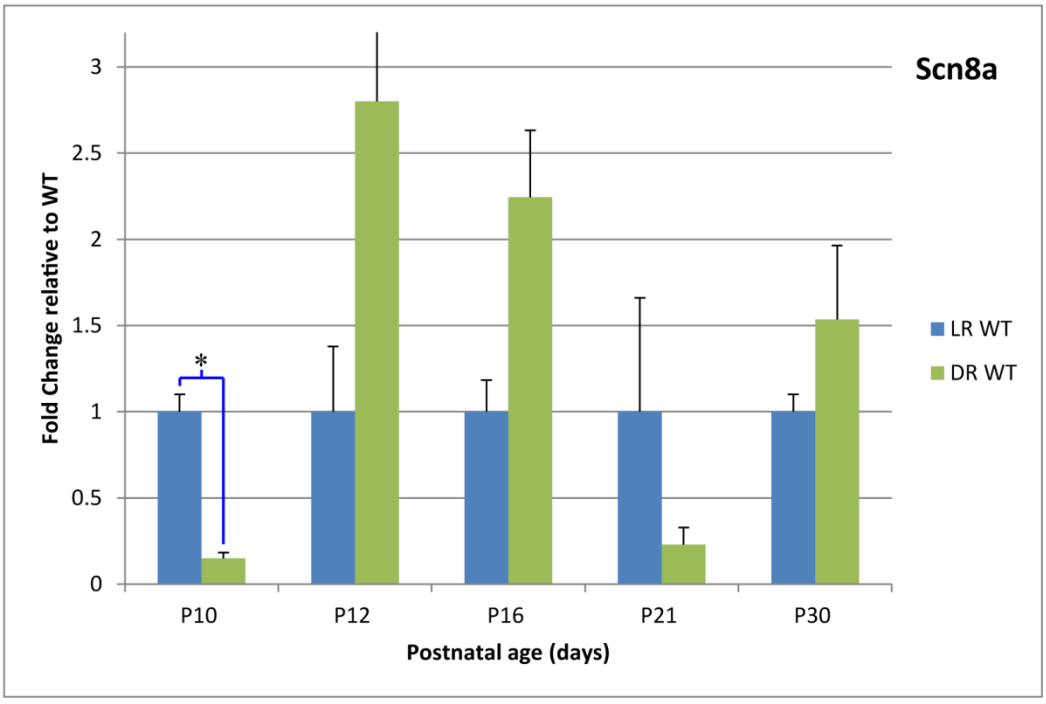
Scn8a
Fold Change relative to WT
3
2.5
2
1.5
1
0.5
0
*
P10
P12
P16
P21
P30
Postnatal age (days)
LR WT
DR WT

Figure 3.8: Brain-derived neurotrophic factor (*Bdnf*) expression is presented at defined timepoints across postnatal development, spanning the critical time of eye-opening through to adulthood. **(A)** depicts the normalized expression levels of *Bdnf*, illustrating the changes in gene expression across postnatal timepoints. **(B)** depicts fold change of each genotype, illustrating the changes in gene expression relative to light-reared wildtype (LR WT) animals for each postnatal timepoint. 1-way ANOVA with Tukey's post-hoc test with significance indicated as * = $p \leq 0.05$, ** = $p \leq 0.01$, and *** = $p \leq 0.001$ were performed. Error bars represent standard error of the mean (±SEM). Statistics were performed in GraphPad Prism 5.
Abbreviations: WT = *Scn8a*$^{+/+}$ wildtype, Mut = *Scn8a*$^{dmu/dmu}$ mutant, LR = light-reared, DR = dark-reared, p = postnatal day.

A

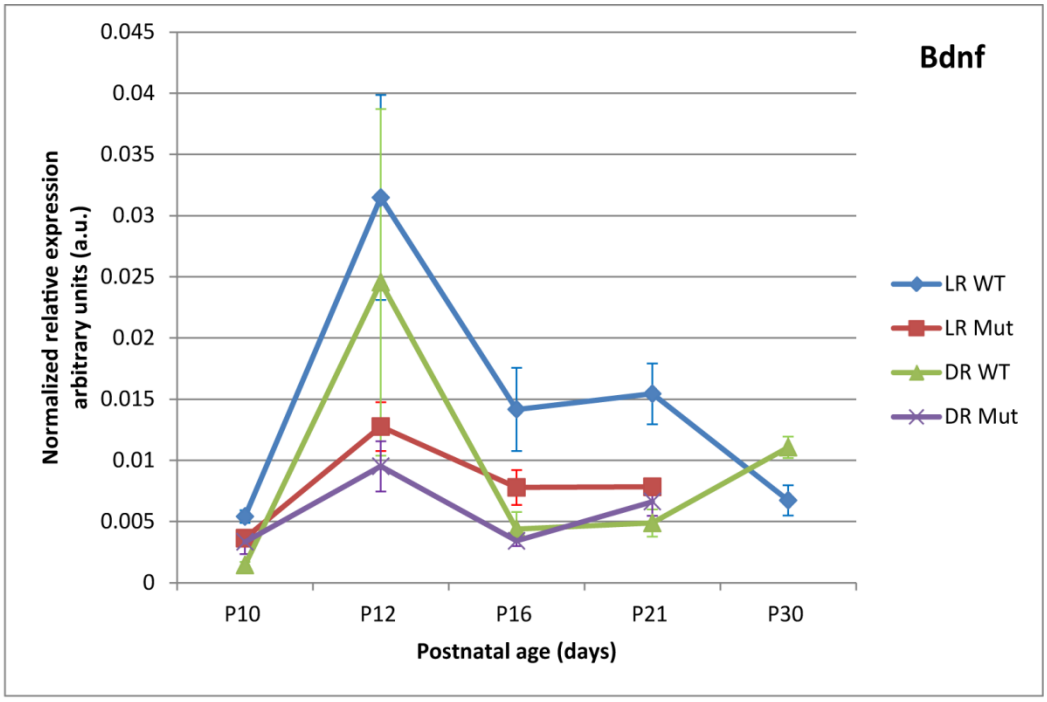
Bdnf
Normalized relative expression arbitrary units (a.u.)
0.045
0.04
0.035
0.03
0.025
0.02
0.015
0.01
0.005
0
P10
P12
P16
P21
P30
Postnatal age (days)
LR WT
LR Mut
DR WT
DR Mut

B

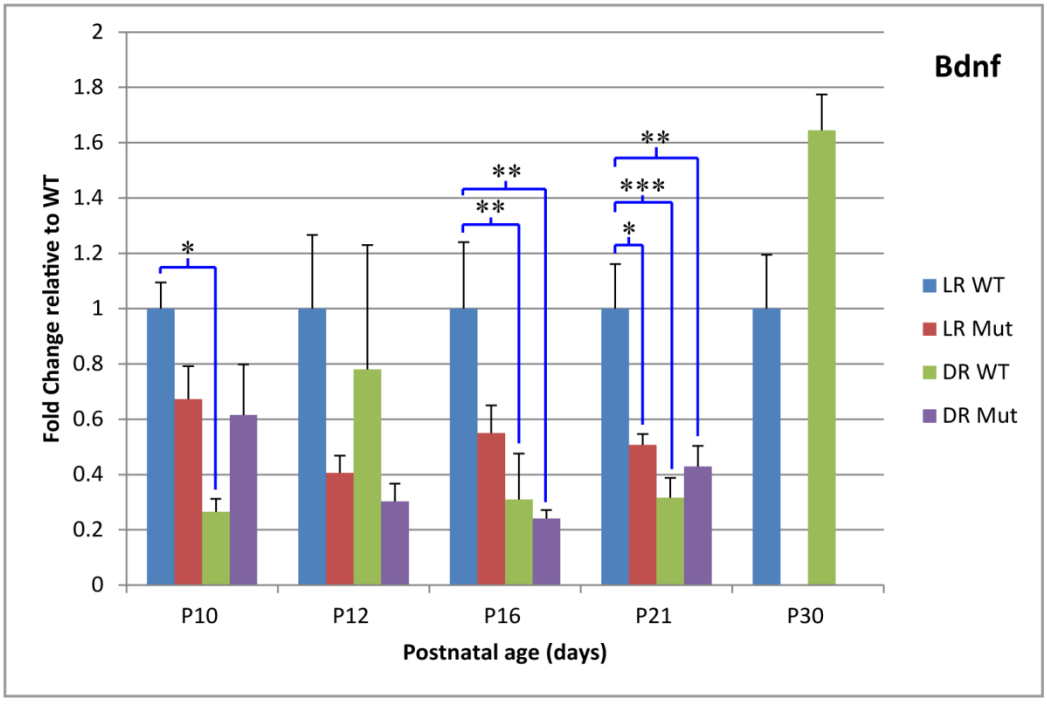
Bdnf
Fold Change relative to WT
2
1.8
1.6
1.4
1.2
1
0.8
0.6
0.4
0.2
0
*
**
**
**
***
*
P10
P12
P16
P21
P30
Postnatal age (days)
LR WT
LR Mut
DR WT
DR Mut

The presence or absence of light stimulation appeared to be a factor that affects *Bdnf* expression levels; LR animals had higher *Bdnf* expression than DR animals (ANOVA, $p<0.0001$) (Figure 3.8A). Similar trends of *Bdnf* expression were observed for DR animals as that seen in LR animals, including a peak in *Bdnf* expression at P12. However, almost all developmental timepoints displayed *Bdnf* expression levels that were significantly lower when compared to LR animals (Tukey's post-hoc, $p<0.05$ for P10, P16 and P21). DR Mut animals also displayed a similar *Bdnf* expression profile as LR Mut animals, including a peak in expression at P12. Taken together, there was an overall trend towards lower levels of *Bdnf* expression in DR animals (WT and Mut) when compared to LR animals (WT and Mut) across all developmental timepoints (Figure 3.8A).

In the *Bdnf* fold change bar graph, there was a strong trend towards LR WT having the highest level of *Bdnf* expression when compared to the other genotypes across all developmental timepoints (Figure 3.8B). Specifically, LR Mut consistently expressed at least half the level of *Bdnf* when compared to their LR WT counterparts. At P10, an ANOVA analysis ($p = 0.0032$) indicated a statistical difference between LR and DR WT animals. DR WT exhibited a 3.77-fold decrease (equivalent to a 73.45% downregulation) of *Bdnf* expression when compared to LR WT (Figure 3.8B).

At the P16 developmental timepoint, an ANOVA analysis revealed that both DR WT and DR Mut animals were statistically different compared to LR WT ($p = 0.0039$). Specifically, DR WT had a 3.22-fold decrease (equivalent to a 68.99% downregulation) of *Bdnf* expression; while DR Mut exhibited a 4.15-fold decrease (equivalent to a 75.88% downregulation) of *Bdnf* expression when compared to LR WT animals (Figure 3.8B).

At P21, ANOVA analysis revealed that all the genotypes were statistically different from LR WT animals ($p = 0.0003$). Interestingly, LR Mut animals expressed about half the level of *Bdnf* compared to LR WT animals; LR Mut expressing a 1.97-fold decrease (equivalent to a 49.27% downregulation) of LR WT *Bdnf* expression levels. In addition, DR animals (WT and Mut) expressed less than half the *Bdnf* levels observed in LR WT; DR WT having a 3.17-fold decrease (equivalent to a 68.41% downregulation) of expression and DR Mut showing a 2.33-fold decrease (equivalent to a 57.11% downregulation) of LR WT *Bdnf* expression levels (Figure 3.8B).

3.1.2.3 Tropomyosin receptor kinase B (TrkB)

The expression profile for *TrkB* in LR WT animals remained relatively stable across postnatal developmental timepoints (Figure 3.9A). Although there appeared to be a peak in *TrkB* expression at P12, this peak was not statistically significant when compared to other timepoints. LR Mut animals exhibited a very similar *TrkB* expression pattern as that observed for LR WT animals (Figure 3.9A). ANOVA analysis revealed a small but significant difference ($p = 0.0141$) between LR WT and LR Mut, mainly that the decline in *TrkB* expression after the peak at P12 was more dramatic in LR Mut than it was in LR WT animals.

An ANOVA analysis indicated that the expression patterns between LR and DR animals were significantly different ($p = 0.0047$) (Figure 3.9A). However, this difference was mostly attributed to the initial levels of *TrkB* transcripts measured at P10, where it was significantly different between LR animals (WT and Mut) and DR WT (Tukey's post-hoc, $p<0.05$). There was a strong trend towards DR animals (both WT and Mut) exhibiting lower levels of *TrkB* expression across all postnatal developmental timepoints studied, but there was insufficient evidence to conclude that this difference in *TrkB* expression levels was attributed solely to light stimulation.

In the *TrkB* fold change bar graph, the general trends observed in the normalized expression graph were also seen (Figure 3.9B). There was a general trend towards *TrkB* expression being relatively stable across all developmental timepoints, as ANOVA analysis did not reveal any statistical significance. The LR Mut animals appeared to have slightly higher expression compared to LR WT animals before eye-opening (P10-P12), and then lower *TrkB* expression after eye-opening (P16-P21). This general observation was also seen in DR animals. At the P21 timepoint, an ANOVA analysis indicated that LR Mut expressed a 3.27-fold decrease (equivalent to a 69.46% downregulation) of *TrkB* levels when compared to LR WT animals ($p = 0.0105$).

3.1.2.4 Pumilio RNA-binding family member 2 (Pum2)

Pum2 expression for LR WT animals was very low at P10, followed by a significant increase at P12 (Figure 3.10A). However, this peak expression of *Pum2* began to decline by P16 and P21, followed by a sharp decrease by P30, where the expression level of *Pum2* returned to initial levels measured at P10. LR Mut animals exhibited a similar *Pum2* expression pattern as that observed for LR WT counterparts (Figure 3.10A).

Figure 3.9: Tropomyosin receptor kinase B (*TrkB*) expression is presented at defined timepoints across postnatal development, spanning the critical time of eye-opening through to adulthood. **(A)** depicts the normalized expression levels of *TrkB*, illustrating the changes in gene expression across postnatal timepoints. **(B)** depicts fold change of each genotype, illustrating the changes in gene expression relative to light-reared wildtype (LR WT) animals for each postnatal timepoint. 1-way ANOVA with Tukey's post-hoc test with significance indicated as * = $p \leq 0.05$, ** = $p \leq 0.01$, and *** = $p \leq 0.001$ were performed. Error bars represent standard error of the mean (±SEM). Statistics were performed in GraphPad Prism 5.
Abbreviations: WT = *Scn8a*$^{+/+}$ wildtype, Mut = *Scn8a*$^{dmu/dmu}$ mutant, LR = light-reared, DR = dark-reared, p = postnatal day.

A

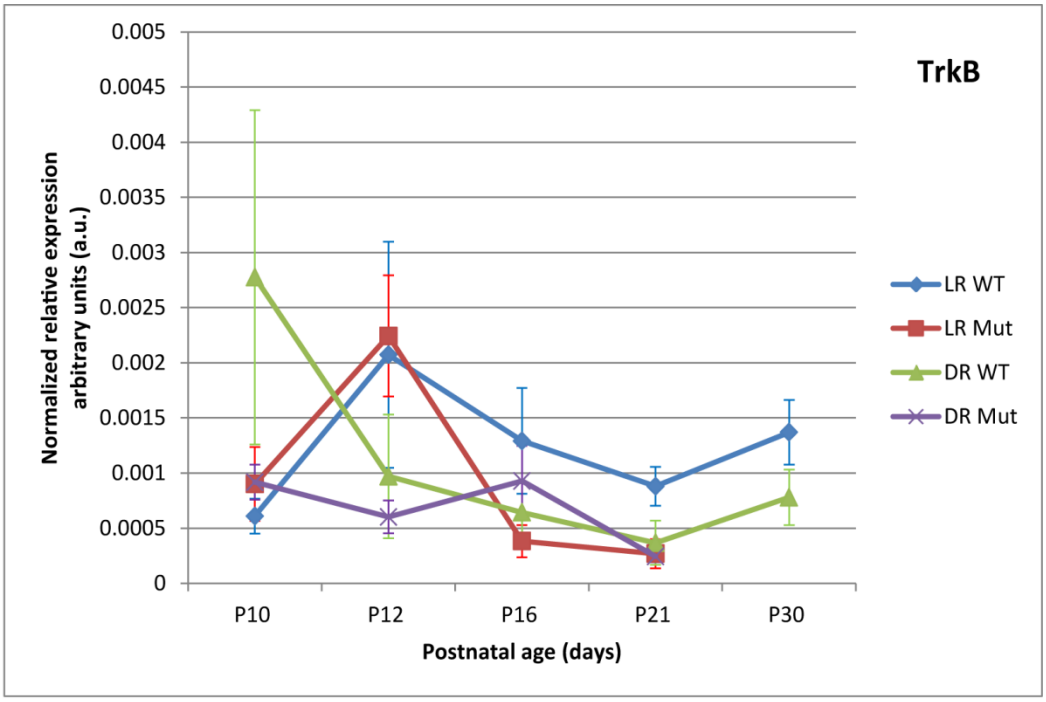
TrkB
Normalized relative expression arbitrary units (a.u.)
0.005
0.0045
0.004
0.0035
0.003
0.0025
0.002
0.0015
0.001
0.0005
0
P10
P12
P16
P21
P30
Postnatal age (days)
LR WT
LR Mut
DR WT
DR Mut

B

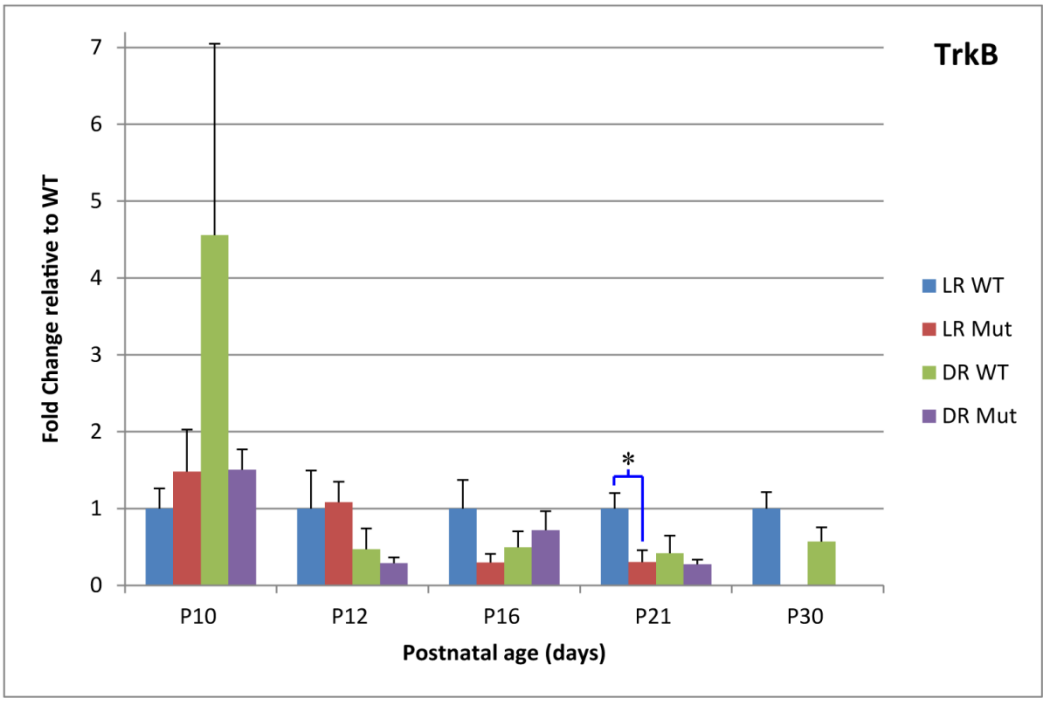
TrkB
Fold Change relative to WT
7
6
5
4
3
2
1
0
*
P10
P12
P16
P21
P30
Postnatal age (days)
LR WT
LR Mut
DR WT
DR Mut

Figure 3.10: Pumilio RNA-binding family member 2 (*Pum2*) expression is presented at defined timepoints across postnatal development, spanning the critical time of eye-opening through to adulthood. **(A)** depicts the normalized expression levels of *Pum2*, illustrating the changes in gene expression across postnatal timepoints. **(B)** depicts fold change of each genotype, illustrating the changes in gene expression relative to light-reared wildtype (LR WT) animals for each postnatal timepoint. 1-way ANOVA with Tukey's post-hoc test with significance indicated as * = $p \leq 0.05$, ** = $p \leq 0.01$, and *** = $p \leq 0.001$ were performed. Error bars represent standard error of the mean (±SEM). Statistics were performed in GraphPad Prism 5.
Abbreviations: WT = *Scn8a*$^{+/+}$ wildtype, Mut = *Scn8a*$^{dmu/dmu}$ mutant, LR = light-reared, DR = dark-reared, p = postnatal day.

A

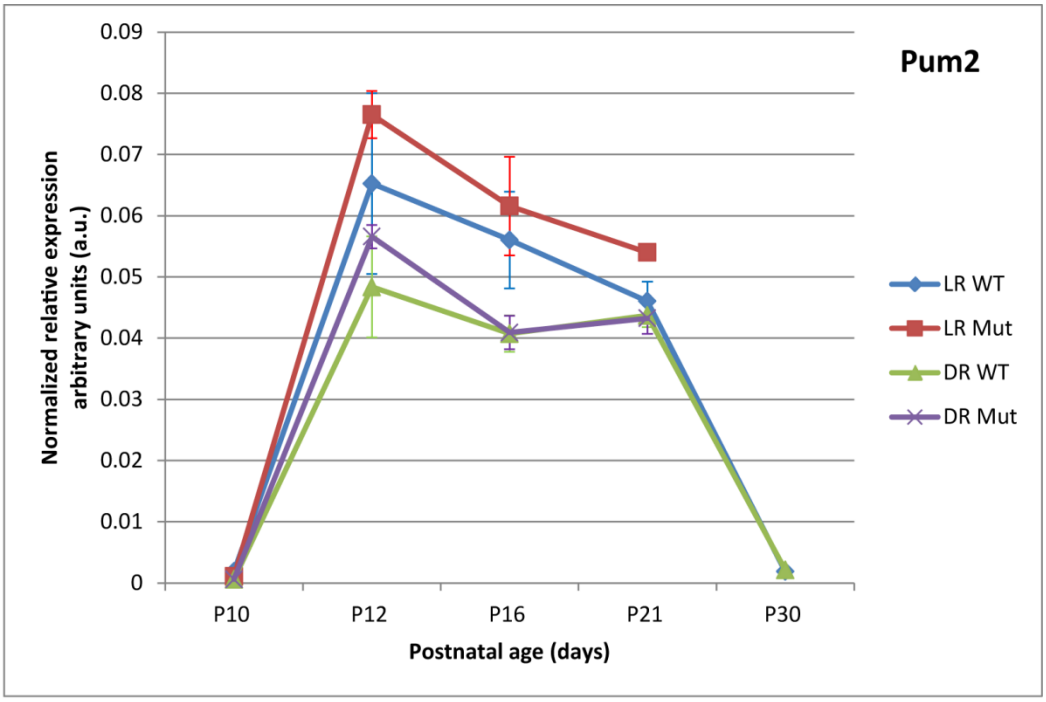
Pum2
Normalized relative expression arbitrary units (a.u.)
0.09
0.08
0.07
0.06
0.05
0.04
0.03
0.02
0.01
0
P10
P12
P16
P21
P30
Postnatal age (days)
LR WT
LR Mut
DR WT
DR Mut

B

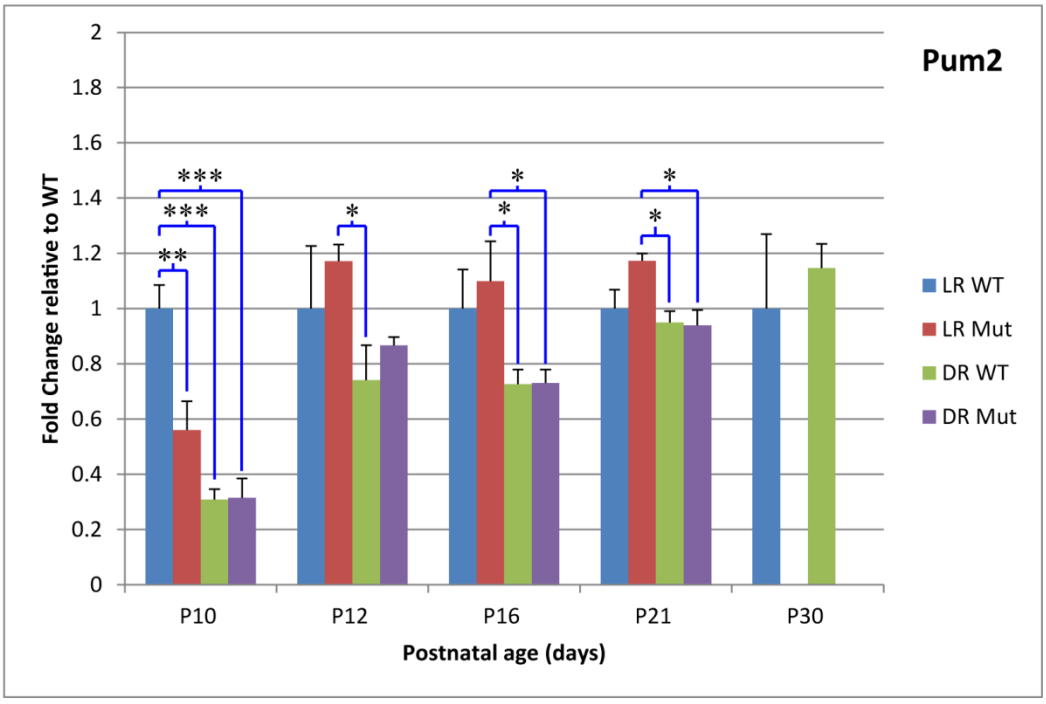
Pum2
Fold Change relative to WT
2
1.8
1.6
1.4
1.2
1
0.8
0.6
0.4
0.2
0
***
***
**
*
*
*
*
*
P10
P12
P16
P21
P30
Postnatal age (days)
LR WT
LR Mut
DR WT
DR Mut

An ANOVA analysis revealed that LR WT and LR Mut were significantly different from each other ($p<0.0001$). This difference was mostly attributed to the sharp increase in *Pum2* expression observed for P10 to P12. There was a strong trend towards decreased *Pum2* expression in DR animals when compared to LR counterparts. DR WT and DR Mut had similar *Pum2* expression levels; by P16, they were nearly indistinguishable from each other (Figure 3.10A). Taken together, there was a general trend that Mut (*Scn8a*$^{dmu/dmu}$) animals (LR and DR) have slightly increased *Pum2* expression levels when compared to their WT (*Scn8a*$^{+/+}$) counterparts.

In the *Pum2* fold change bar graph, the general trends observed in the normalized expression graph were also seen. DR animals (WT and Mut) appeared to express lower *Pum2* levels compared to LR animals across all developmental timepoints (Figure 3.10B). As well, across most timepoints (P16-P21), LR Mut had higher *Pum2* expression when compared to LR WT.

At the P10 timepoint, an ANOVA analysis revealed significant differences between all genotypes examined ($p<0.0001$). Specifically, LR Mut expressed a 1.79-fold decrease (equivalent to a 44.00% downregulation) of LR WT *Pum2* levels; DR WT expressed a 3.24-fold decrease (equivalent to a 69.09% downregulation) and DR Mut expressed a 3.18-fold decrease (equivalent to a 68.52% downregulation) of *Pum2* levels when compared to LR WT (Figure 3.10B).

At P12, an ANOVA analysis indicated a statistically significant difference between LR Mut and DR WT animals ($p = 0.0369$). While LR Mut showed a 1.17-fold increase in *Pum2* expression, DR WT showed a 1.35-fold decrease (equivalent to a 25.88% downregulation) in *Pum2* expression levels. However, neither LR Mut nor DR WT were significantly different from LR WT, but they were significant when compared to each other (Figure 3.10B).

Similarly, at P16, an ANOVA analysis indicated significant differences between LR Mut, DR WT and DR Mut animals ($p = 0.0097$). At this developmental timepoint, LR Mut exhibited a 1.10-fold increase in *Pum2* expression; while both DR WT and DR Mut animals showed a 1.38-fold decrease (equivalent to a 27.33% downregulation) of *Pum2* levels. However, neither LR Mut nor DR animals (WT and Mut) were significantly different from LR WT, but DR animals were significantly different from LR Mut (Figure 3.10B).

At the P21 developmental timepoint, an ANOVA analysis revealed statistically significant differences between LR Mut and DR animals (WT and Mut) ($p = 0.0088$). In particular, LR Mut exhibited a 1.17-fold increase in *Pum2* expression; DR WT showed a 1.05-fold decrease (equivalent to a 5.07% downregulation) of expression and DR Mut showed a 1.06-fold decrease (equivalent to a 6.05% downregulation) of expression in *Pum2* expression levels. Neither LR Mut nor DR animals (WT and Mut) were significantly different from LR WT, but DR animals were significantly different from LR Mut (Figure 3.10B).

3.1.3 Müller glia cell support through postnatal development

This group consists of two genes that are expressed by Müller glia cells throughout postnatal development. These include glial fibrillary acidic protein (*Gfap*) and ciliary neurotrophic factor (*Cntf*).

3.1.3.1 Glial fibrillary acidic protein (Gfap)

Gfap transcript expression of LR WT animals started off quite low at P10, but increased sharply at P12, around the age when eye-opening occurs (Figure 3.11A). Following this increase, *Gfap* expression levels decreased relatively steadily by P16 to P30, with a small increase at P21. However, in LR Mut animals, the expression of *Gfap* did not follow the pattern observed in LR WT counterparts. The peak expression at P12 and subsequent decrease at P16 to P21 were almost missing. The *Gfap* expression level remained relatively stable across all postnatal developmental timepoints in LR Mut. There was a significant difference between LR WT and LR Mut expression profiles (ANOVA, $p = 0.0146$). This difference was mostly attributed to the peak *Gfap* expression at P12 observed in LR WT animals (Tukey's post-hoc, $p<0.05$) (Figure 3.11A).

An ANOVA analysis between LR and DR animals revealed a small but significant difference on *Gfap* transcripts ($p = 0.0097$). A Tukey's post-hoc analysis showed that at the ages of P12 and P21, DR WT animals expressed *Gfap* at significantly lower levels when compared to LR counterparts (Tukey's post-hoc, $p<0.05$). Overall, there was a trend towards slightly higher *Gfap* expression in DR Mut when compared to

Figure 3.11: Glial fibrillary acidic protein (*Gfap*) expression is illustrated across five different timepoints in postnatal development, spanning the critical eye-opening time period into adulthood. **(A)** shows the normalized expression levels of *Gfap*, illustrating the changes in gene expression at each stage of postnatal retinal development. **(B)** depicts fold change gene expression of *Gfap*, illustrating the changes in gene expression relative to light-reared wildtype (LR WT) animals for each postnatal timepoint. 1-way ANOVA with Tukey's post-hoc test with significance indicated as * = $p \leq 0.05$, ** = $p \leq 0.01$, and *** = $p \leq 0.001$ were performed. Error bars represent standard error of the mean (±SEM). Statistics were performed in GraphPad Prism 5.
Abbreviations: WT = *Scn8a*$^{+/+}$ wildtype, Mut = *Scn8a*$^{dmu/dmu}$ mutant, LR = light-reared, DR = dark-reared, p = postnatal day.

A

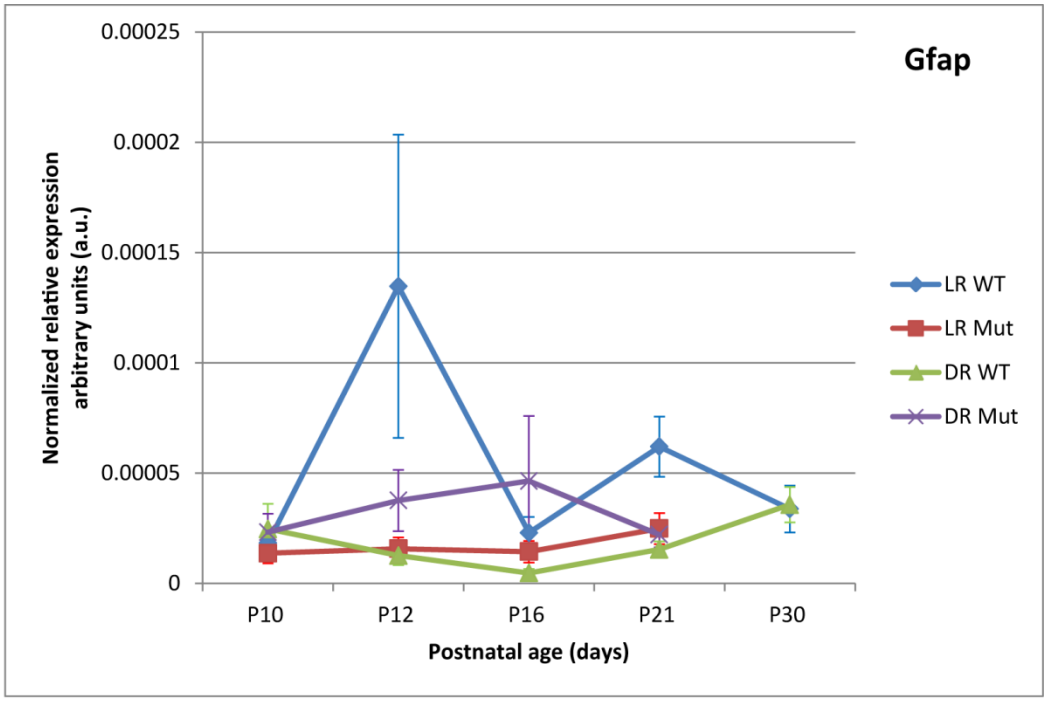
Gfap
Normalized relative expression arbitrary units (a.u.)
0.00025
0.0002
0.00015
0.0001
0.00005
0
P10
P12
P16
P21
P30
Postnatal age (days)
LR WT
LR Mut
DR WT
DR Mut

B

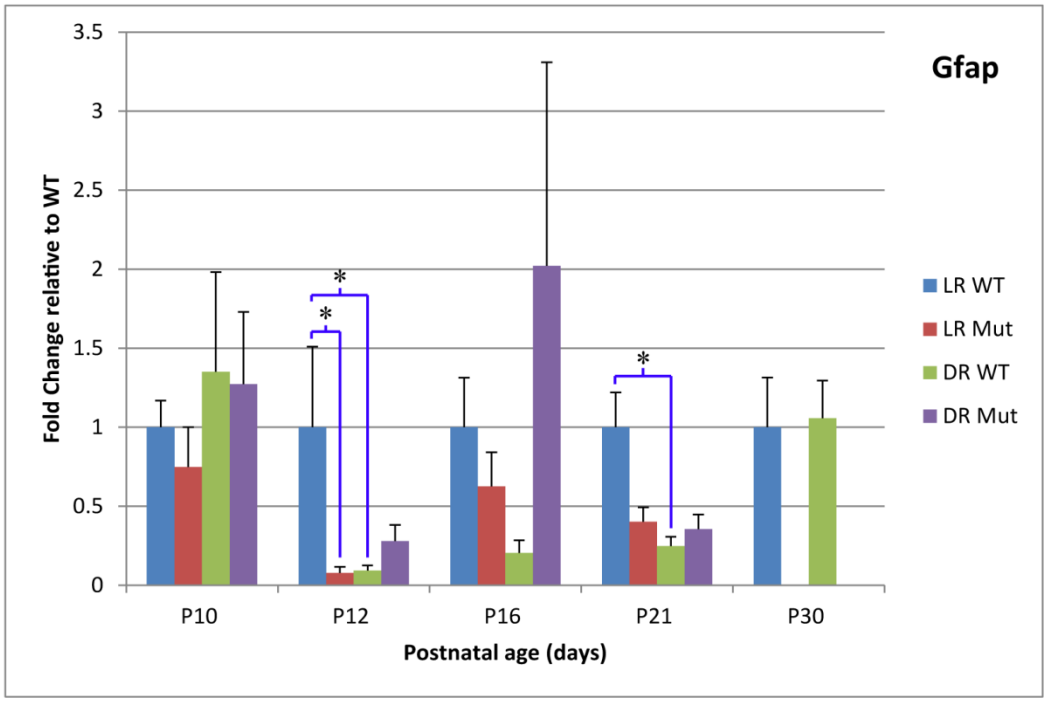
Gfap
Fold Change relative to WT
3.5
3
2.5
2
1.5
1
0.5
0
*
*
*
P10
P12
P16
P21
P30
Postnatal age (days)
LR WT
LR Mut
DR WT
DR Mut

LR Mut counterparts at P12 and P16, but there was no statistical significance found at these timepoints (Figure 3.11A).

In the *Gfap* fold change bar graph, there was an overall trend towards LR Mut consistently expressing lower *Gfap* when compared to their LR WT counterparts (Figure 3.11B). At the P12 timepoint, an ANOVA analysis revealed a statistical difference in LR Mut and DR WT when compared to LR WT animals ($p = 0.0179$). At this timepoint, LR Mut animals showed a 12.84-fold decrease (equivalent to a 92.22% downregulation) in expression, while DR WT animals exhibited a 10.71-fold decrease (equivalent to a 90.66% downregulation) in *Gfap* expression (Figure 3.11B). At P21, an ANOVA analysis revealed a significant difference in DR WT animals ($p = 0.0334$). Specifically, DR WT animals showed a 4.04-fold decrease (equivalent to a 75.23% downregulation) in *Gfap* expression (Figure 3.11B).

3.1.3.2 Ciliary neurotrophic factor (Cntf)

Cntf transcript expression in LR WT animals changed dramatically as postnatal development approached eye-opening at around P12 (Figure 3.12A). By P16, *Cntf* expression reached a peak expression level, finally declining sharply by P21. By P30, the steady decline of *Cntf* expression dropped to nearly undetectable levels in adulthood. However, the expression profiles between LR WT and LR Mut were significantly different from each other (ANOVA, $p<0.0001$) (Figure 3.12A). Most notably, *Cntf* expression in LR Mut was already measured at a lower level than LR WT at P10, with a peak in *Cntf* expression observed at P12, matching levels seen in LR WT animals. However, this peak expression was not sustained through to P16, but dropped dramatically instead (Tukey's post-hoc, $p<0.05$).

When comparing the effects of light stimulation on *Cntf* expression in WT and Mut animals, the difference was clear (Figure 3.12A). An ANOVA analysis indicated that the expression patterns of LR animals were significantly different from those of DR animals ($p<0.0001$). The *Cntf* expression of DR animals (WT and Mut) lacked the characteristic extended peak observed at the critical timepoints P12 and P16 of postnatal retinal development. DR animals started off with low levels of *Cntf* expression that waned throughout postnatal development, until reaching similar undetectable levels in adulthood by P30 (Figure 3.12A).

Figure 3.12: Ciliary neurotrophic factor (*Cntf*) expression is illustrated across five different timepoints in postnatal development, spanning the critical eye-opening time period into adulthood. **(A)** shows the normalized expression levels of *Cntf*, illustrating the changes in gene expression at each stage of postnatal retinal development. **(B)** depicts fold change gene expression of *Cntf*, illustrating the changes in gene expression relative to light-reared wildtype (LR WT) animals for each postnatal timepoint. 1-way ANOVA with Tukey's post-hoc test with significance indicated as * = $p \leq 0.05$, ** = $p \leq 0.01$, and *** = $p \leq 0.001$ were performed. Error bars represent standard error of the mean (±SEM). Statistics were performed in GraphPad Prism 5.
Abbreviations: WT = *Scn8a*$^{+/+}$ wildtype, Mut = *Scn8a*$^{dmu/dmu}$ mutant, LR = light-reared, DR = dark-reared, p = postnatal day.

A

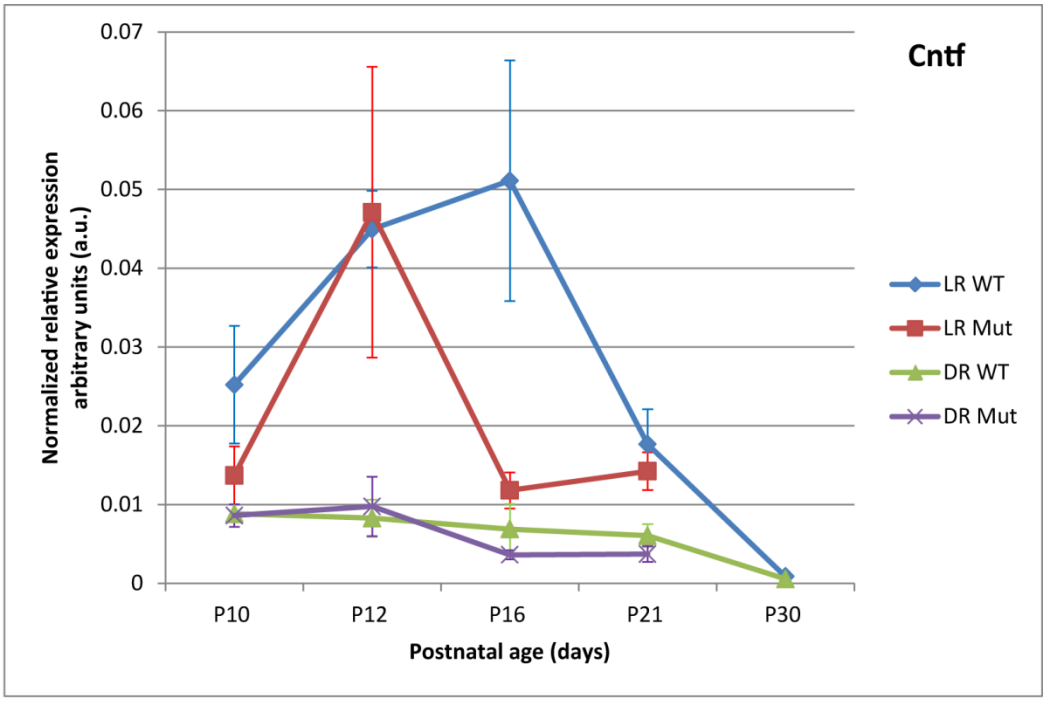
Cntf
Normalized relative expression arbitrary units (a.u.)
0.07
0.06
0.05
0.04
0.03
0.02
0.01
0
P10
P12
P16
P21
P30
Postnatal age (days)
LR WT
LR Mut
DR WT
DR Mut

B

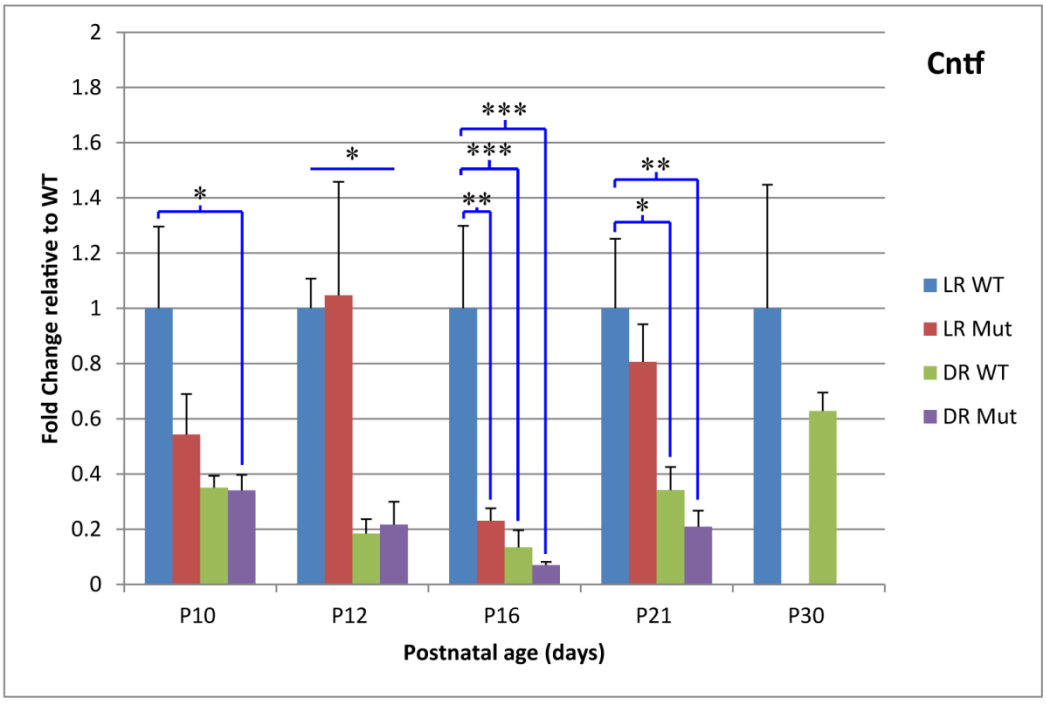
Cntf
Fold Change relative to WT
2
1.8
1.6
1.4
1.2
1
0.8
0.6
0.4
0.2
0
*
*
***
***
**
**
*
P10
P12
P16
P21
P30
Postnatal age (days)
LR WT
LR Mut
DR WT
DR Mut

In the *Cntf* fold change bar graph, there was an overall trend towards LR WT animals expressing the highest levels of *Cntf* expression across all developmental timepoints when comparing all of the genotype groups (Figure 3.12B). In addition, *Cntf* expression was higher in LR animals than in DR animals. In the DR animals, there was a trend towards DR Mut having consistently lower *Cntf* expression when compared to their DR WT counterparts (Figure 3.12B). At the P10 developmental timepoint, an ANOVA analysis indicated a significant difference in DR Mut ($p = 0.0419$). Specifically, DR Mut showed a 2.93-fold decrease (equivalent to a 65.89% downregulation) of *Cntf* expression level when compared to LR WT animals.

Of important note, while an ANOVA analysis revealed significant differences between the four genotypes at P12 ($p = 0.0373$), a Tukey's post-hoc test was inconclusive and did not identify actual pairings of significance. Interestingly, LR Mut animals had a 1.05-fold increase of *Cntf* expression, while DR WT expressed a 5.43-fold decrease (equivalent to a 81.58% downregulation) of *Cntf* levels and DR Mut showed a 4.61-fold decrease (equivalent to a 78.31% downregulation) in *Cntf* expression (Figure 3.12B).

At the P16 developmental timepoint, an ANOVA analysis revealed several significant differences between the genotype groups ($p<0.0001$). Specifically, LR Mut had a 4.33-fold decrease (equivalent to a 76.93% downregulation) of *Cntf* expression level; DR WT animals showed a 7.42-fold decrease (equivalent to a 86.33% downregulation) in *Cntf* expression; and DR Mut showed a 14.12-fold decrease (equivalent to a 92.92% downregulation) in *Cntf* expression (Figure 3.12B). By P21, an ANOVA analysis indicated some significant differences in DR animals. In particular, at this developmental timepoint, DR WT animals had a 2.92-fold decrease (equivalent to a 65.71% downregulation) in expression while DR Mut had a 4.76-fold decrease (equivalent to a 78.98% downregulation) in *Cntf* expression (Figure 3.12B).

3.2 Regulation of neurofilament distribution by visual experience or by $Na_v1.6$

3.2.1 Neurofilament accumulation in Scn8a$^{dmu/dmu}$ *retina*

Using confocal microscopy, an examination of neurofilament distribution in postnatal retinal development was performed. Retinas from animals reared in both LR and DR conditions at different postnatal developmental ages from P7 to P21 were collected and stained for the presence of neurofilaments (Figure 3.13). Staining for

Figure 3.13: Differential neurofilament accumulation in *Scn8a*^{dmu} mutants. Confocal images of retinas from P7 to P21 animals are stained with neurofilament (NF-L) antibody to highlight sites of accumulation as the retina matures under light-reared (LR) and dark-reared (DR) conditions. Wildtype (WT) animals displayed NF-L accumulation at the outer plexiform layer (OPL) only at P7. LR mutants have differential OPL expression compared to LR WT time points at P10 and P12; this OPL staining is further diminished at P16 and P21. There is strong staining in the ganglion cell layer (GCL) in LR Mut P16 animals. The removal of light stimulation causes further differential accumulation of NF-L at the OPL in DR mutant animals with greater intensity compared to LR Mut counterparts. DR animals demonstrate NF-L staining in the GCL at P12 which then intensifies by P16 and continues into P21. DR Mut at P12 also had punctate NF-L staining in the inner plexiform layer (IPL); this punctate staining pattern is carried through to P21. Primary antibody was absent in control section. N = 3 for each genotype examined. Scale bar = 25µm.

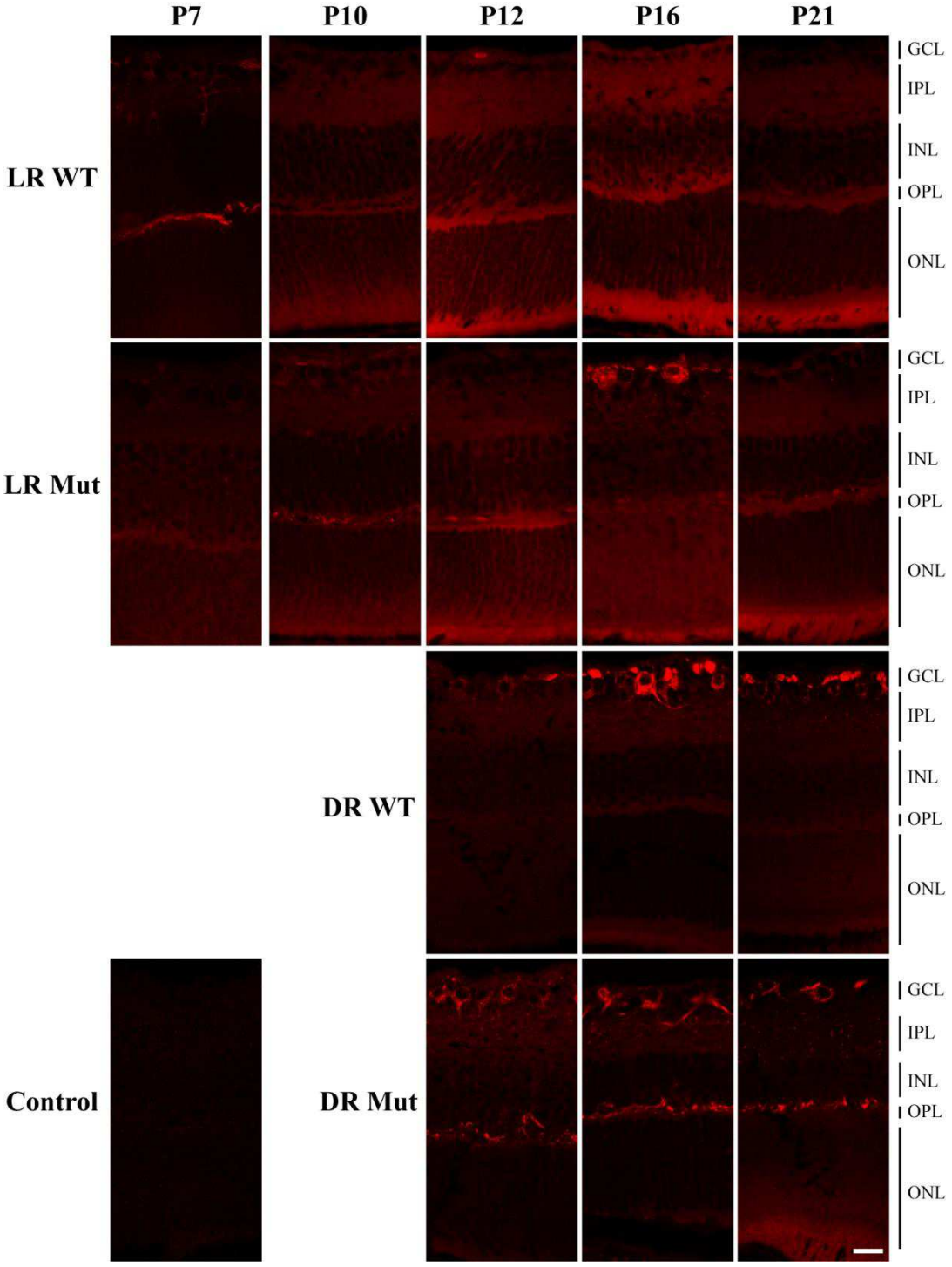
P7
P10
P12
P16
P21
LR WT
LR Mut
DR WT
DR Mut
Control
GCL
IPL
INL
OPL
ONL

Table 3.2: Qualitative analysis of confocal retinal images stained with neurofilament light-chain (NF-L).

LIGHT-REARED Neurofilament stained tissue					
WT	**P7**	**P10**	**P12**	**P16**	**P21**
GCL	some GC (+) are labeled with some processes (only in 1)	GC/processes do not appear to be labeled	GC/processes do not appear to be labeled	GC/processes do not appear to be labeled	some GC (+) are labeled with some processes (only in 1)
	labeled nerve fiber layer not observed in all images (only in 2)	labeled fiber layer not observed in any images	labeled fiber layer not observed in any images	labeled fiber layer not observed in most images (only in 1)	labeled fiber layer not observed in any images
IPL	observe faint specking (0.5-1X +), but not consistent	do not observe any specking	do not observe any specking	do not observe any specking	do not observe any specking
	IPL appears more "solid" and uniform	IPL appears more "solid" and uniform	IPL appears more "solid" and uniform	IPL appears more "solid" and uniform	IPL appears more "solid" and uniform
OPL	noticable staining (1-2 ++)	do not observe any "line" in images	do not observe any "line" in images	do not observe any "line" in images	do not observe any "line" in images
	mainly located in central retina (near optic nerve)				
	line is not uniform				
Mutant	**P7**	**P10**	**P12**	**P16**	**P21**
GCL	few GC (+) are labeled with some processes (only in 1)	GC/processes do not appear to be labeled	some GC (+) are labeled with some processes (only in 1)	some GC (+) are labeled with some processes (only in 2)	few GC (+) are labeled with some processes (only in 2)
	labeled nerve fiber layer not observed in all images (only in 2)	labeled nerve fiber layer not observed in all images (only in 1)	labeled fiber layer not observed in any images	labeled nerve fiber layer not observed in all images (only in 2)	labeled nerve fiber layer not observed in all images (only in 2)
IPL	observe faint specking (0.5-1X +), but not	observe faint specking (0.5-1X +),	do not observe any specking	observe faint specking (0.5-1X +), but not	observe faint specking (0.5-1X +), but not

	consistent	but not consistent		consistent	consistent
	IPL appears more "solid" and uniform	IPL appears more "solid" and uniform	IPL appears more "solid" and uniform	IPL appears more "solid" and uniform	IPL appears more "solid" and uniform
OPL	faintly stained (0.5-1 +)	faintly stained (0.5-1 +)	do not observe any "line" in images	faintly stained (0.5-1 +)	faintly stained (0.5-1 +) (only in 1)
	mainly located in central retina (near optic nerve)	mainly located in central retina (near optic nerve)		mainly located in central retina (near optic nerve)	mainly located in central retina (near optic nerve)
	line is not uniform	line is not uniform		line is not uniform	line is not uniform

DARK-REARED Neurofilament stained tissue					
WT	**P7**	**P10**	**P12**	**P16**	**P21**
GCL			most GC (+) are consistently labeled with some processes	most GC (++) are consistently labeled with some processes	most GC (+) are consistently labeled with some processes
			labeled nerve fiber layer not observed in all images	labeled nerve fiber layer not observed in all images	labeled nerve fiber layer not observed in all images
IPL			some speckling (1.5X +)	some speckling (1.5X +)	some speckling (1.5X +)
			appears very irratic in IPL	appears very irratic in IPL	appears very irratic in IPL
OPL			faintly stained (0.5-1 +)	faintly stained (0.5-1 +)	faintly stained (0.5-1.5 +)
			mainly located in central retina (near optic nerve)	mainly located in central retina (near optic nerve)	mainly located in central retina (near optic nerve)
			line is not uniform	line is not uniform	line is not uniform

Mutant	P7	P10	P12	P16	P21
GCL			more GC (++) consistently labeled with more processes	more GC (++) consistently labeled with more processes	most GC (+) are consistently labeled with some processes
			labeled nerve fiber layer not observed in all images	labeled nerve fiber layer not observed in all images	labeled nerve fiber layer not observed in all images
IPL			more profuse specking (+++)	more profuse specking (++++)	more profuse specking (+++)
			more uniform in appearance in IPL	more uniform in appearance in IPL	more uniform in appearance in IPL
OPL			intensely stained (+++)	intensely stained (++++)	intensely stained (++)
			mainly located in central retina (near optic nerve)	mainly located in central retina (near optic nerve)	mainly located in central retina (near optic nerve)
			line is not uniform	line is not uniform	line is not uniform

neurofilament light-chain (NF-L) was examined in the five well characterized layers in the retina: the ganglion cell layer (GCL), inner plexiform layer (IPL), inner nuclear layer (INL), outer plexiform layer (OPL), and outer nuclear layer (ONL).

At the youngest age in this study, P7, LR WT (*Scn8a*$^{+/+}$) animals had a mild accumulation of NF-L in the GCL as well as punctate accumulations of NF-L in the OPL. As the LR WT animals progressed through postnatal development, the NF-L accumulation in the OPL observed in P7 was quickly dissipated by P10 right through to adulthood. NF-L continued to be very mildly accumulated in ganglion cells in the GCL at P12 (Figure 3.14A). By P16, LR WT animals showed weak accumulation of NF-L in the ganglion cells of the GCL only (Figure 3.15A). By P21, the NF-L accumulation in the GCL was barely detectable (Figure 3.16A). In general, NF-L became diffused throughout the different layers of the retina from P10 onwards, leading to the diffused adult distribution observed in P21 animals (Figures 3.13-3.16) (Table 3.2).

LR Mut (*Scn8a*$^{dmu/dmu)}$ animals had a different version of this neurofilament distribution as the Mut retina matured through postnatal development into adulthood. At P7, the Mut OPL layer was devoid of NF-L accumulations which were present in LR WT animals. The overall NF-L distribution was diffused across all layers without even the mildly detectable amounts in the ganglion cells of the GCL. However, as the animals progressed through postnatal development, by P10, NF-L accumulations could be mildly detected in ganglion cells as well as present in punctate accumulations along the OPL, similar to that observed in P7 LR WT animals. This pattern of NF-L accumulation was carried through to P12 (Figure 3.14B), until there was an increase in NF-L proteins in the GCL at P16 (Figure 3.15B). LR Mut animals displayed a more intense accumulation of NF-L in the GCL, when compared to LR WT animals. Interestingly, in addition to the GCL, LR Mut also displayed punctate and concentrated clusters of NF-L in the OPL. NF-L was also detected in punctate accumulations speckled throughout the IPL at P16 (Figure 3.15B). This increase in accumulation became diffused; NF-L in the GCL became mildly detectable again in the matured adult Mut retina by P21 (Figure 3.16B), with the speckling of punctate NF-L accumulations at the IPL also diminishing by adulthood (Figures 3.13-3.16) (Table 3.2).

DR animals, in general, displayed an even more exaggerated and striking NF-L distribution pattern when compared to LR animals. DR WT animals had an increased

Figure 3.14: Differential neurofilament accumulation in P12 retina. Confocal images of P12 retinas are displayed for **(A)** wildtype (WT), **(B)** *Scn8a*^{dmu} mutant (Mut), **(C)** dark-reared wildtype, and **(D)** dark-reared *Scn8a*^{dmu} mutant animals. Light-reared (LR) WT animals at this timepoint display weak neurofilament (NF-L) staining in only the ganglion cells layer (GCL), while LR Mut display a mild accumulation of NF-L at the outer plexiform layer (OPL) only. Dark-reared (DR) animals display both strong NF-L staining in the GCL, with intense punctate accumulation along the inner plexiform layer (IPL). In addition to this, DR Mut also have increased NF-L staining along the OPL that is far greater in intensity than that observed in LR Mut. Meanwhile, the outer nuclear layer (ONL) of all genotypes and rearing conditions remain unremarkable for NF-L staining. Images are magnified 400x to better illustrate the punctate NF-L staining observed in IPL. N = 3 for each genotype examined. Scale bar = 25µm.

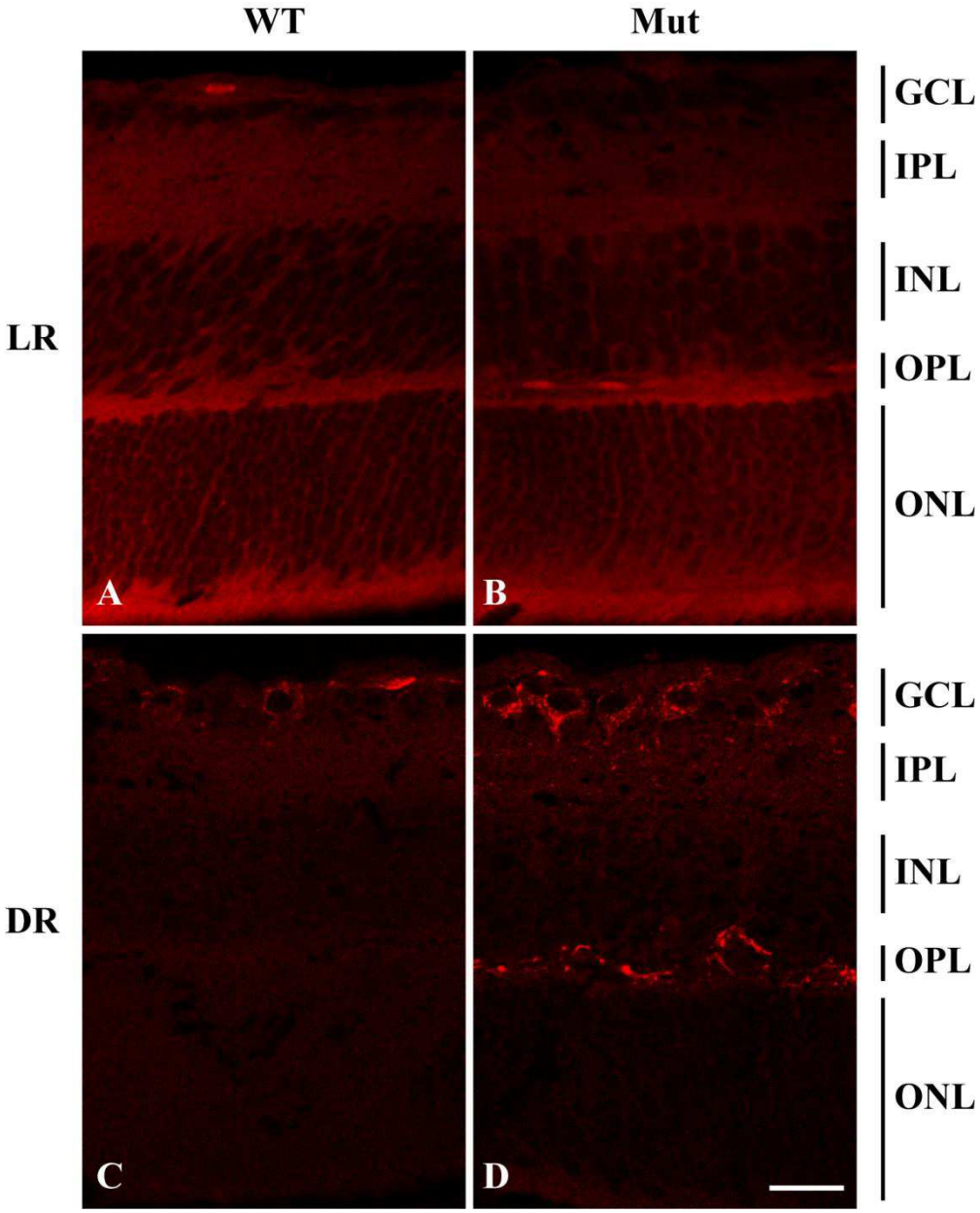
WT
Mut
LR
DR
GCL
IPL
INL
OPL
ONL
A
B
C
D

Figure 3.15: Differential neurofilament accumulation in P16 retina. Confocal images of P16 retinas are displayed for **(A)** wildtype (WT), **(B)** *Scn8a*^{dmu} mutant (Mut), **(C)** dark-reared wildtype, and **(D)** dark-reared *Scn8a*^{dmu} mutant animals. Light-reared (LR) WT animals at this timepoint display weak neurofilament (NF-L) staining in only the ganglion cells layer (GCL), while LR Mut display strong staining in the GCL and a mild accumulation of NF-L staining at the outer plexiform layer (OPL). Dark-reared (DR) animals display both strong NF-L staining in the GCL, with intense punctate accumulation along the inner plexiform layer (IPL). In addition to this, DR Mut also have increased NF-L staining along the OPL that is far greater in intensity than that observed in LR Mut. Meanwhile, the outer nuclear layer (ONL) of all genotypes and rearing conditions remain unremarkable for NF-L staining. Images are magnified 400x to better illustrate the punctate NF-L staining observed in IPL. N = 3 for each genotype examined. Scale bar = 25µm.

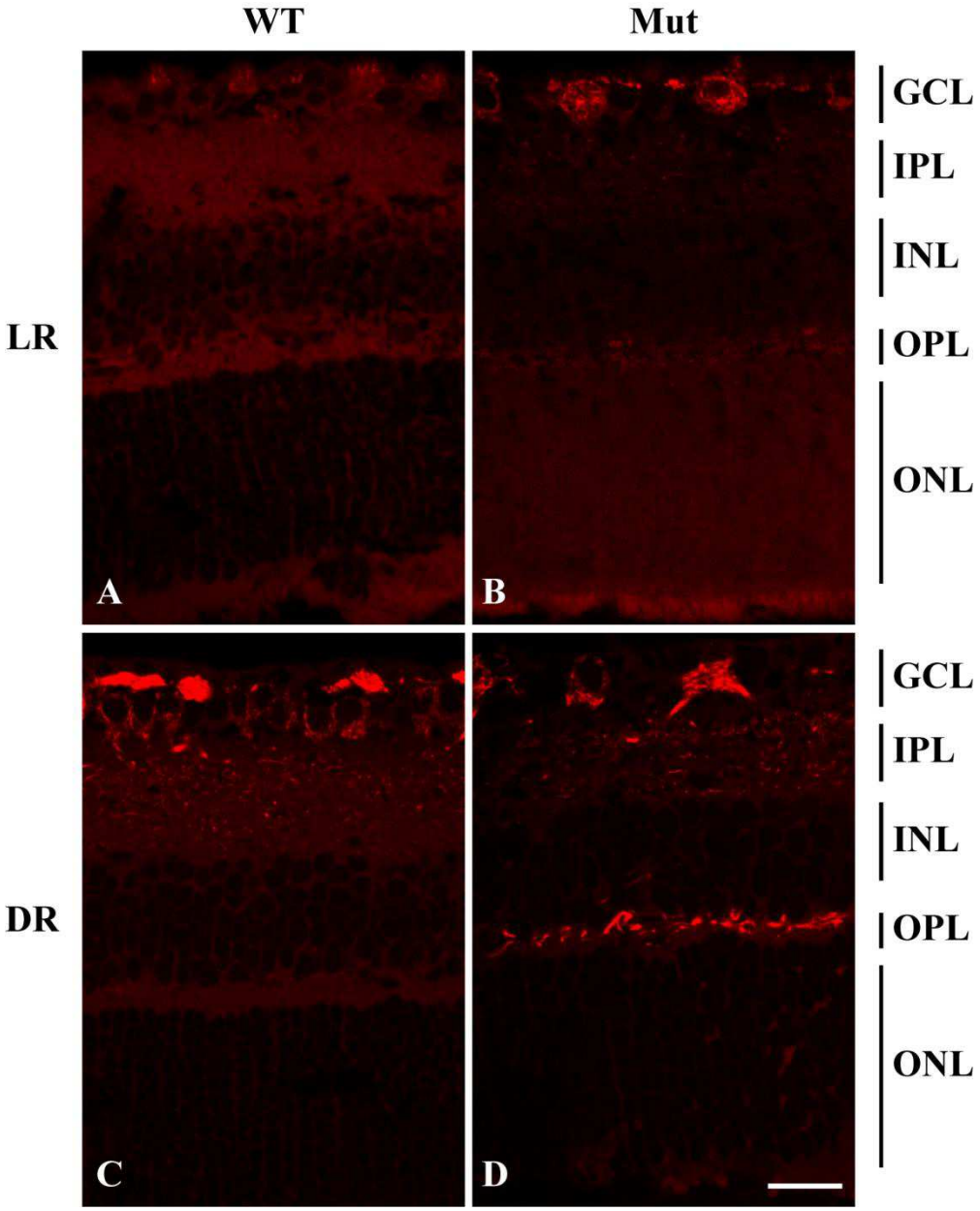
WT
Mut
LR
DR
GCL
IPL
INL
OPL
ONL
A
B
C
D

Figure 3.16: Differential neurofilament accumulation in P21 retina. Confocal images of P21 retinas are displayed for **(A)** wildtype (WT), **(B)** *Scn8a*^{dmu} mutant (Mut), **(C)** dark-reared wildtype, and **(D)** dark-reared *Scn8a*^{dmu} mutant animals. Light-reared (LR) WT animals at this timepoint display barely detectable neurofilament (NF-L) staining in only the ganglion cells layer (GCL), while LR Mut display mild staining in the GCL and a noticeable accumulation of NF-L staining at the outer plexiform layer (OPL). Dark-reared (DR) animals display both strong NF-L staining in the GCL, with intense punctate accumulation along the inner plexiform layer (IPL). In addition to this, DR Mut also have increased NF-L staining along the OPL that is far greater in intensity than that observed in LR Mut. Meanwhile, the outer nuclear layer (ONL) of all genotypes and rearing conditions remain unremarkable for NF-L staining. Images are magnified 400x to better illustrate the punctate NF-L staining observed in IPL. N = 3 for each genotype examined. Scale bar = 25µm.

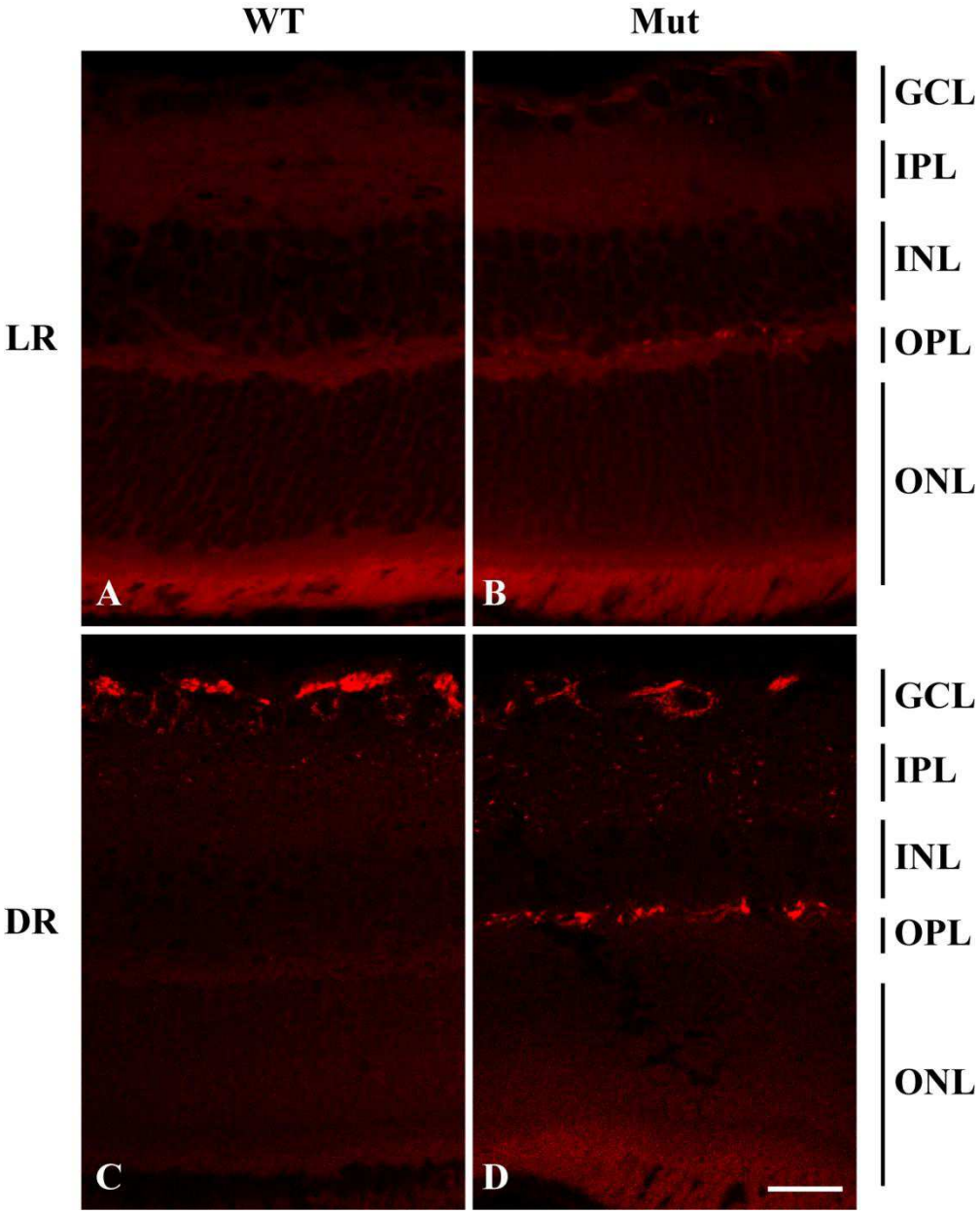
WT
Mut
LR
DR
GCL
IPL
INL
OPL
ONL
A
B
C
D

accumulation of NF-L in ganglion cells at an earlier timepoint than LR WT counterparts starting at P12 (Figure 3.14C). By P16, the intensity of the NF-L accumulation in ganglion cells throughout the GCL was brighter than that observed in LR WT animals. Noticeable speckling of punctate NF-L accumulations were now present and observable throughout the IPL at this timepoint (Figure 3.15C), but similar to LR WT, the NF-L in the OPL remained diffused. NF-L accumulation in the GCL that filled the entire cytoplasm of ganglion cells at P16 began to diffuse by P21 in the adult WT retina (Figure 3.16C). The speckling pattern was also weaker than it was at P16 in the P21 retina. DR WT animals retained diffused NF-L staining in the OPL throughout postnatal development (Figures 3.13-3.16) (Table 3.2).

DR Mut presented the most dramatic staining of NF-L accumulations in all three timepoints examined from P12 to P21 (Figure 3.13). DR Mut had striking NF-L accumulations in ganglion cells throughout the GCL, similar to DR WT animals, as well as the punctate speckling of NF-L foci throughout the IPL (Figures 3.13, 3.14D, 3.15D, and 3.16D). In addition, there was a strong presence of NF-L accumulations in the OPL, as early as P12 (Figure 3.14D), which was then carried well into the adult mature Mut retina by P21 (Figures 3.13, 3.14D, 3.15D, and 3.16D). This NF-L accumulation in the OPL was more intense than LR Mut counterparts (Figures 3.13-3.16) (Table 3.2).

3.2.2 Neurofilament branching in Scn8a$^{dmu/dmu}$ *cerebella*

An examination using confocal microscopy revealed greater detail in the organization of the neurofilament network within each lobe of the cerebellum. Cerebella from both P16 LR WT and LR Mut animals were compared to illustrate the distinctive patterns that emerged through the use of confocal microscopy (Figure 3.17). LR WT cerebella displayed clear NF-L accumulations, highlighting the Purkinje cells found in the cerebella. The fiber projections from Purkinje cells could be seen extending into the white matter to form fiber bundles following the midline of each cerebellar lobe (Figure 3.17A). There was directionality in the organization of neurofilaments and the distribution of these filaments resulted in a branch-like phenotype that eventually led down to form the main stalk of the fiber bundles (Figure 3.17B). LR Mut cerebella was compared with LR WT animals, and although morphologically, the Mut cerebella was similar to WT, the NF-L staining pattern was markedly different. LR Mut animals

Figure 3.17: Neurofilament branching is disorganized in mutants. Cerebella of light-reared (LR) P16 animals were stained for neurofilament light-chain (NF-L). NF-L staining was detected within Purkinje cells of the cerebellum as well as NF-L-rich projections that extend through the internal granule layer to form a central fiber bundle in the cerebellum white matter. **(A, B)** Wildtype (WT) animals display intricate branching, while **(C, D)** mutant (Mut) animals have a much less developed branching network that is reduced to NF-L-rich punctate granules. NF-L stained fibers in Mut animals display a lack of directionality, with many fibers ending in NF-L-rich punctate accumulations. Figures **(B)** and **(D)** are magnified further to clearly illustrate the observed fiber disorganization in LR WT vs. LR Mut animals. N = 3 for each genotype examined. Scale bar for **(A)** and **(C)** = 50µm. Scale bar for **(B)** and **(D)** = 25µm.

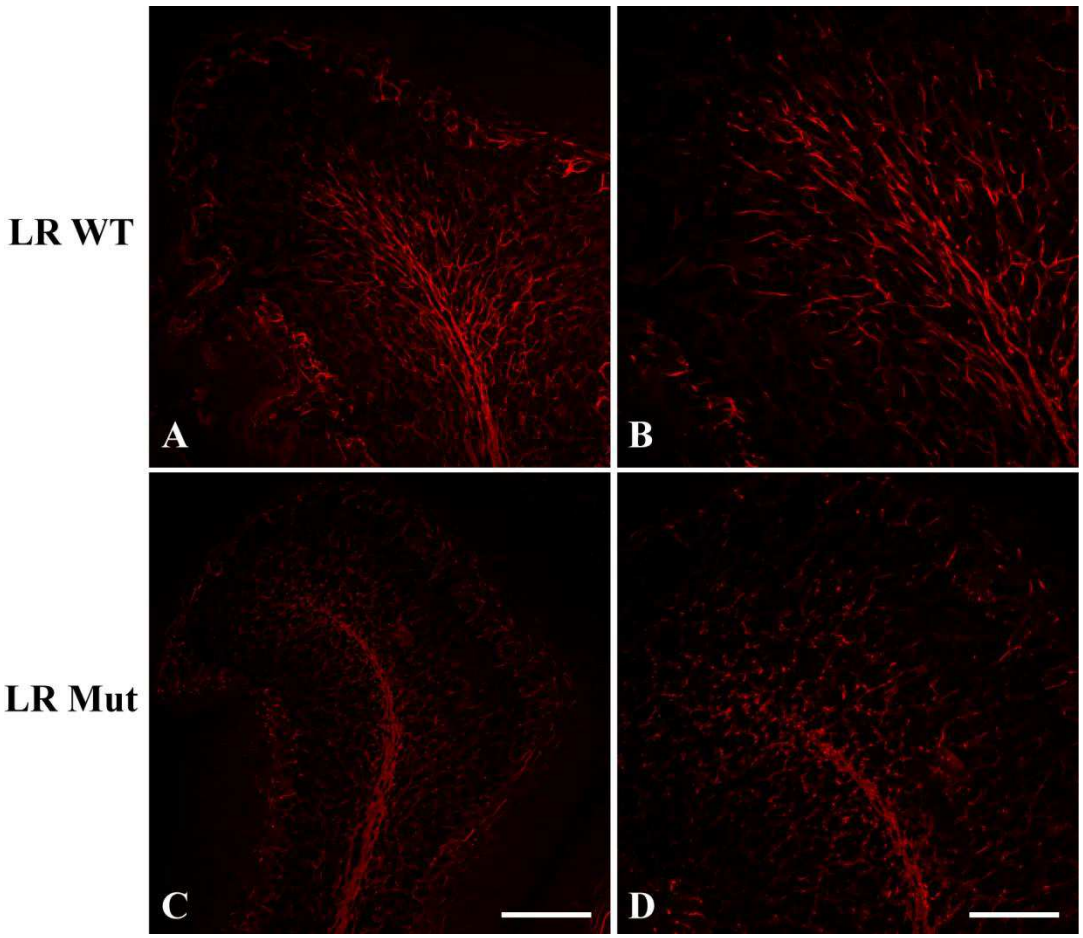
LR WT
LR Mut
A
B
C
D

displayed a punctate and apparently disorganized NF-L pattern (Figure 3.17C) in comparison to the continuous branching pattern observed in LR WT animals (Figure 3.17D). Although the standard features of fibrous extensions coming together to form the central fiber bundle was present, the disruption in LR Mut was indicated by the more diffused appearance of the central fiber bundle and the broken and disorganized appearance of the smaller branches leading up to the fiber bundle.

3.2.3 Scn8a$^{dmu/dmu}$ *visual cortex displays punctate App accumulations*

An App derivative (amyloid beta peptide, Aβ) plays a large role in Alzheimer's disease (Zhou *et al*., 2016). Experiments so far have revealed novel findings in the organization of neurofilament networks in both the retina and the cerebellum. Since what appeared to be accumulations have been observed in neurofilament networks already, an important question came to light as to what other proteins might be doing in the presence of a disrupted neurofilament network? To address this question, P16 WT and Mut brains were stained for the presence of App (Figure 3.18). Although P16 WT and Mut retinas were also stained for the presence of App, no clear staining patterns were observed in both retinal and cerebellar tissue (not shown). While WT animals in both LR (Figure 3.18B) and DR conditions (Figure 3.18D) displayed a general diffuse App pattern throughout the mouse brain, Mut animals revealed another surprising finding. Mut animals from both LR (Figure 3.18C) and DR conditions (Figure 3.18E) displayed punctate App accumulations located specifically in the deeper layers of the visual cortex. This punctate accumulation pattern was most prominent in LR Mut animals (in layers 2/3 and 4, Figure 3.18C). DR Mut had a more muted distribution of these App accumulations (Figure 3.18E) which seemed also to be more restricted to the deeper layers (layers 4 and 5) of the visual cortex. H&E staining revealed that cells of the visual cortex layers were all apparently not apoptotic at P16, as cellular and pyknotic nuclear debris were absent in this morphological stain.

3.3 The discovery of the spontaneous $Na_v1.6$ rescue (*snr*) mice: a potential new substrain within the *Scn8a*^{dmu} mouse line

While *Scn8a*$^{dmu/dmu}$ mice are born normal, they quickly deteriorate due to muscle weakness and paralysis, eventually dying at approximately three weeks of age. However,

Figure 3.18: Mutants animals display App accumulations in the visual cortex. The cortex of light-reared (LR) P16 wildtype (WT) and mutant (Mut) animals were stained for the presence of amyloid precursor protein (App). **(A)** H & E stained normal section is displayed as a morphological reference for immunohistochemistry (IHC) photos with the outer most layer of the cortex to the left of the photo and the hippocampus located in the lower right corner. **(B)** Negative control was prepared with the primary antibody omitted during the staining procedure. **(C, D)** LR WT and LR Mut are displayed respectively. **(E, F)** DR WT and DR Mut are displayed respectively. There is an absence of App staining in both **(C)** LR WT and **(E)** DR WT visual cortices. App accumulations were detected most strongly among cells in the LR Mut animals spanning the inner layers of the visual cortex. Mild App accumulations were also observed in DR Mut visual cortex to a lesser degree compared to LR Mut counterparts. Dashed lines in **(A)** (red) and solid lines in **(D, F)** (white) demarcate the six layers of the visual cortex, labeled with Roman numerals I-VI. N = 3 for each genotype examined. Scale bar = 200µm.

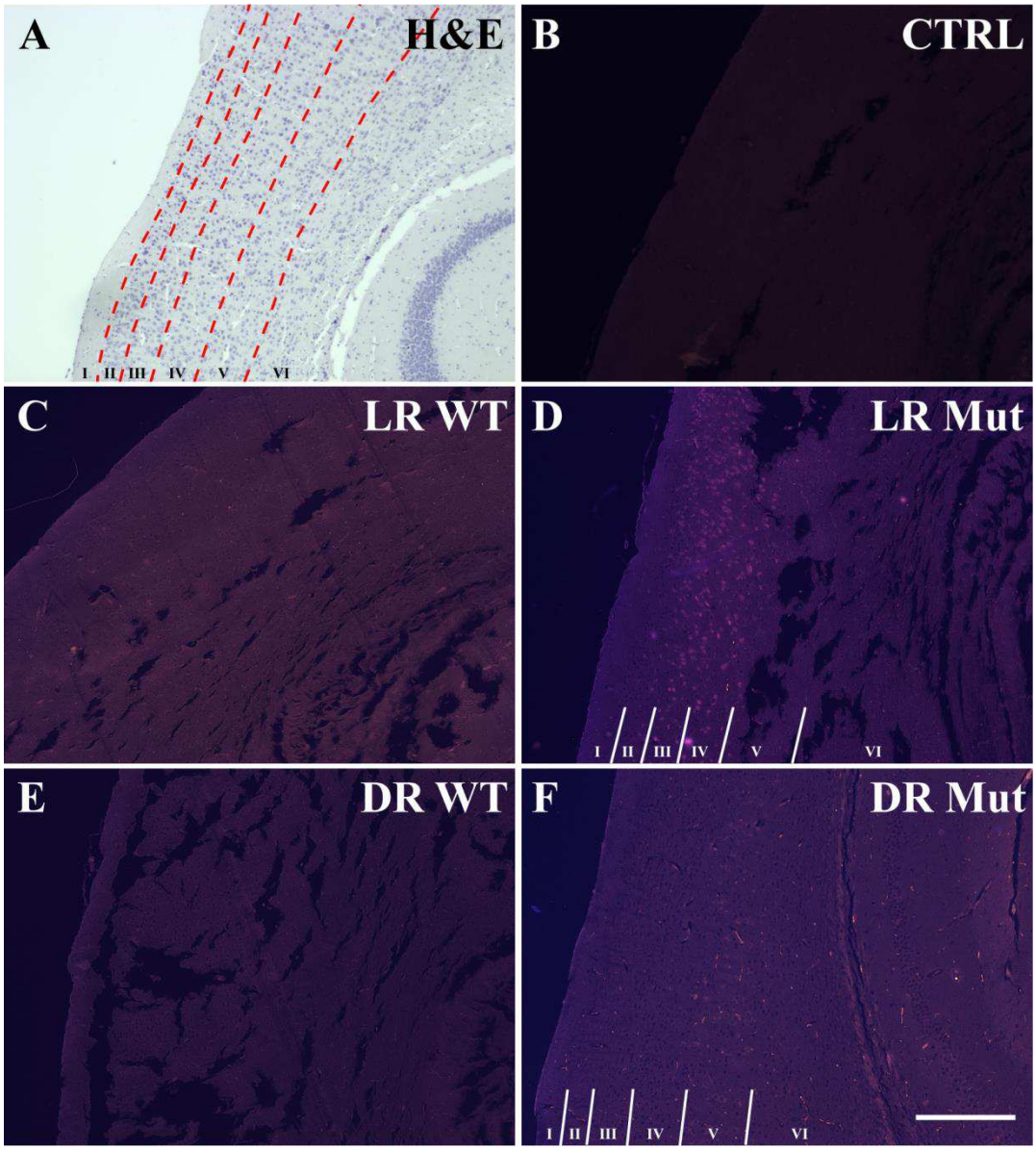
A
H&E
I II III IV V VI
B
CTRL
C
LR WT
D
LR Mut
I II III IV V VI
E
DR WT
F
DR Mut
I II III IV V VI

in late August 2008, what appeared to be a spontaneous mutation within the *Scn8a*^{dmu} mouse strain was discovered. These mice did not display the characteristic *Scn8a*$^{dmu/dmu}$ motor phenotype but harboured the *dmu* allele were identified in our colony. This potential substrain has been tentatively termed *snr* (**s**pontaneous **N**a$_v$1.6 **r**escue) (Figure 3.19A). In total, there were four *snr* mice identified: two females (from litter 'A') and one male and one female (from litter 'B'). In litter 'A', there were a total of 17 pups: four WT (*Scn8a*$^{+/+}$, ~24% transmission); eight heterozygotes (*Scn8a*$^{dmu/+}$, ~47% transmission); three Mut (*Scn8a*$^{dmu/dmu}$, ~18% transmission); and two *snr* (~12% transmission). In litter 'B', there were a total of 11 pups: three WT (*Scn8a*$^{+/+}$, ~27% transmission); five heterozygotes (*Scn8a*$^{dmu/+}$, ~45% transmission); one Mut (*Scn8a*$^{dmu/dmu}$, ~9% transmission); and two *snr* (~18% transmission). Both litters 'A' and 'B' were produced from the same *Scn8a*$^{dmu/+}$ harem mating cage. This mating cage produced over 12 litters, with only litters 'A' and 'B' generating *snr* mice. Based on these two litters, the transmission of the *snr* trait did not appear to follow a Mendelian ratio (~25%).

The genotype of all *Scn8a*^{dmu} mice was first determined using our standard genotyping strategy with *Scn8a*^{dmu} primers (Appendix 2.10). Since the only distinguishing trait between homozygous *Scn8a*$^{dmu/dmu}$ and *snr* mutant mice is the presence or absence of a characteristic motor phenotype, homozygous *snr* mutant mice were identified based on both genotype and phenotype (i.e. positive identification of homozygous *dmu* alleles combined with a lack of hindlimb paralysis past P16 and prolonged lifespan of ~1.5 years). A preliminary ERG tracing was performed on only one female *snr* at the P16 timepoint (ERG experiment performed by B.J. Smith, unpublished data). As shown in (Figure 3.19C), while the ERG components are clearly shown in the P16 WT (*Scn8a*$^{+/+}$) control littermate, these components are strongly reduced and delayed in both the P16Mut (*Scn8a*$^{dmu/dmu}$) and P16 *snr* mice.

An immunohistochemical assay was performed on *snr* sciatic nerves to examine for the presence of Na$_v$1.6 at the nodes of Ranvier (Figure 3.19B). Using an anti-Na$_v$1.6 antibody specifically made against an epitope encoded by a portion of the *Scn8a* mRNA located 5' of the *dmu* mutation, the presence of Na$_v$1.6 was detected in *snr* sciatic tissues, but not in *Scn8a*$^{dmu/dmu}$ sciatic tissues. (Immunohistochemical assay performed by Dr. S.R. Levinson, unpublished data). Interestingly, *snr* mice have abnormal ERG tracings that are similar to the ones typically observed in *Scn8a*$^{dmu/dmu}$ mice (Figure 3.19C).

Figure 3.19: The discovery of the *snr* mouse substrain. (**A**) A *snr* mouse (left) and a *dmu* mouse (*Scn8a*$^{dmu/dmu}$) (right), both at the age of P16. The *dmu* mouse clearly shows the lethal degenerating muscle phenotype, while the *snr* mouse does not. (**B**) Nodes of Ranvier in sciatic nerves from C57BL/6 control mice (I, IV), *snr* mice (II, V), and *Scn8a*$^{dmu/dmu}$ mice (III, VI), are presented. Both C57BL/6 and *snr* panels (I) and (II) act as negative controls where antibodies were blocked with antigen peptides. Panel (III) act as a *Scn8a*$^{dmu/dmu}$ wildtype positive control, where the tissue was stained with an anti-pan-Na_v antibody, that stains for all Na_v channels. Panels (IV, V, and VI) have been stained with an anti-$Na_v1.6$ antibody to detect the presence of $Na_v1.6$ channels within each of the genotypes listed. Scale bar = 33µm. (**C**) A comparison of representative scotopic bright flash electroretinogram (ERG) responses between a P16 *Scn8a*^{dmu} wildtype littermate (WT, left), *snr* (center), and a P16 *Scn8a*$^{dmu\ -/-}$ (*dmu*, right). The ERGs were elicited by flashes of white light in increasing intensities, ranging from -3.0 (top) to 1.4 (bottom) log cds/m^2. Normal ERG components are clearly shown in the P16 WT (the a-wave, the initial negative deflection ( ), the b-wave, the positive deflection ( ) following the a-wave, and the oscillatory potentials, the low-amplitude wavelets ( ) on the ascending limb of the b-wave). However, these ERG components are strongly reduced and delayed in both the *snr* and *dmu* (*Scn8a*$^{dmu/dmu}$). Immunohistochemistry experiments in **(B)** were performed by Dr. S.R. Levinson, University of Colorado, USA. ERG experiments in **(C)** were performed by B.J. Smith, Côté Laboratory, Dalhousie Univeristy, Canada (unpublished data).

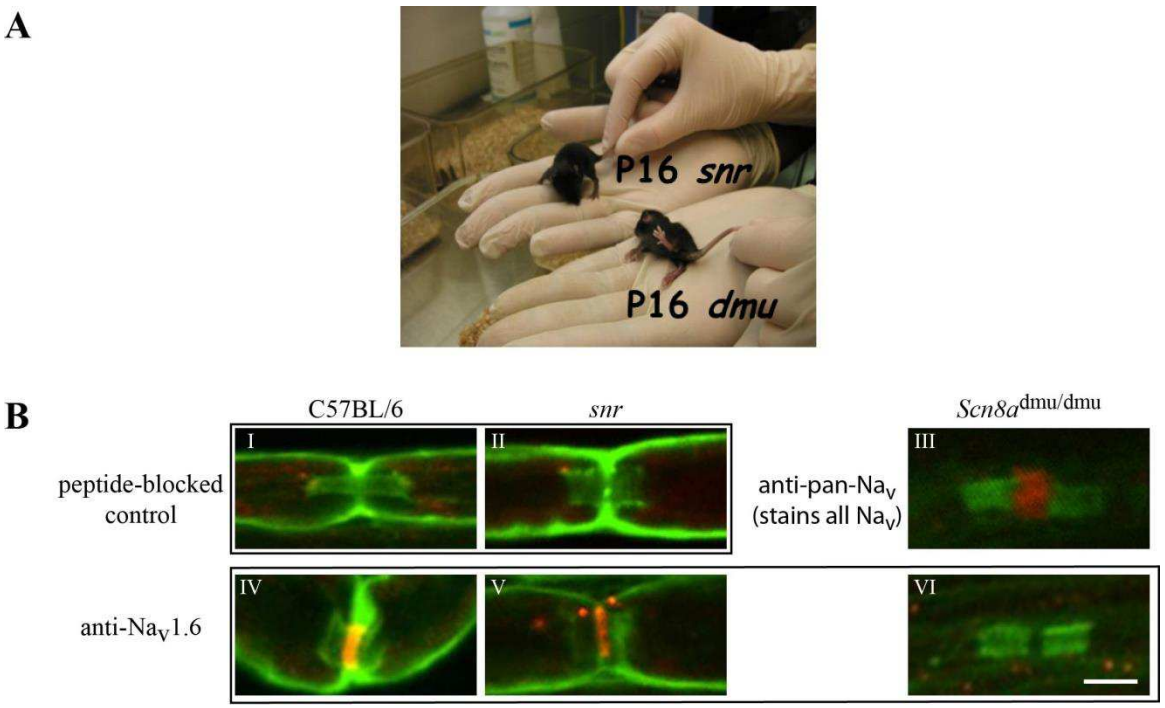
A
P16 snr
P16 dmu
B
C57BL/6
snr
Scn8a dmu/dmu
peptide-blocked control
anti-pan-Na V (stains all Na V)
anti-Na V 1.6
I
II
III
IV
V
VI
C
P16 WT
P16 snr
200υV
75ms
P16 Scn8a dmu/dmu

Wildtype (*Scn8a*$^{+/+}$) and *snr* mice were weighed every other day, from P9-P65, and both were found to steadily increase in weight. Since the *Scn8a*$^{dmu/dmu}$ mice do not survive past P21, they were also weighed every other day, from P9-P18 (humane endpoint for *Scn8a*$^{dmu/dmu}$ mice) (Figure 3.20). Observations from weighing the *snr* mice every other day exhibited an upward trend, similar to that observed for WT mice.

To assess the *snr* mice, I performed studies in behavioural monitoring, sensorimotor coordination, overall motor function, and sensorimotor integration, focusing on hindlimb function. For the *behavioural monitoring study*, there were no noticeable differences between WT and *snr* mice, with the exception of walking behaviour (Figure 3.21). In this case, *snr* mice displayed more time walking when compared to WT mice (unpaired Student's *t*-test, $p = 0.007$), suggesting they spent more time exploring their new surroundings through touch rather than relying on sight.

In the *sensorimotor integration and hindlimb function study using the balance beam*, the *Scn8a*$^{dmu/dmu}$ mice all failed this motor coordination test as they were unable to proactively use their motor skills to maintain balance as soon as the test trial started. In contrast, results from this motor coordination and balance study strongly suggested that *snr* mice retained motor control skills that were similar or equivalent to WT mice (Figure 3.22).

In the *sensorimotor coordination and overall motor function study using the Rotarod*, the performance of *Scn8a*$^{dmu/dmu}$ mice on the Rotarod was significantly different ($p<0.0001$) from both WT and *snr* mice, mainly from their hindlimb paralysis which prevented the mice from properly gripping the grooved cylinder and maintaining balance. The *Scn8a*$^{dmu/dmu}$ mice all failed this motor coordination and function test as they were unable to proactively use their motor skills to maintain balance as soon as the test trial started. Again, results from this motor coordination and function study strongly suggested that *snr* mice retained motor control skills that were similar or equivalent to WT mice (Figure 3.23).

Unfortunately, repeated attempts to maintain the potential *snr* substrain mouse line have failed. Interestingly, repeated matings between several combinations of a reproductive-aged heterozygous (*Scn8a*$^{dmu/+}$) male (the original male breeder from the harem mating cage) and the two female *snr* mice (from litter 'A') should have produced offspring. The fertilization rate of C57BL/6 WT females where a vaginal mucus plug has

Figure 3.20: The average weight values for wildtype (n = 4), *snr* (n = 4), and *Scn8a*$^{dmu/dmu}$ (n = 4) mice. **(A)** The wildtype and *snr* mice were weighed every other day (Explorer Ohaus Corp. with weighing basket), from P9-P65, and were found to steadily increase in weight. Since *Scn8a*$^{dmu/dmu}$ mice do not survive past P21, they were also weighed every other day, from P9-P18 (humane endpoint for *Scn8a*$^{dmu/dmu}$ mice). **(B)** Wildtype (n = 4), *snr* (n = 4), and *Scn8a*$^{dmu/dmu}$ (n = 4) were all compared, using a 1-way ANOVA with Tukey's post-hoc test with significance indicated as * = $p \leq 0.05$, ** = $p \leq 0.01$, and *** = $p \leq 0.001$. Error bars represent standard error of the mean (±SEM). Statistics were performed in GraphPad Prism 5.

A

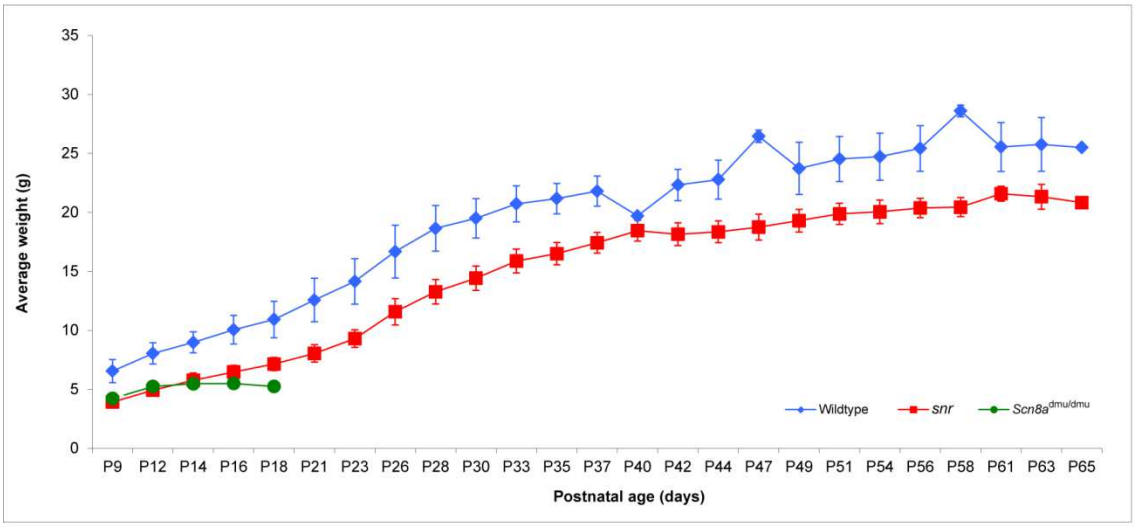
Average weight (g)
35
30
25
20
15
10
5
0
P9 P12 P14 P16 P18 P21 P23 P26 P28 P30 P33 P35 P37 P40 P42 P44 P47 P49 P51 P54 P56 P58 P61 P63 P65
Postnatal age (days)
Wildtype
snr
Scn8a dmu/dmu

B

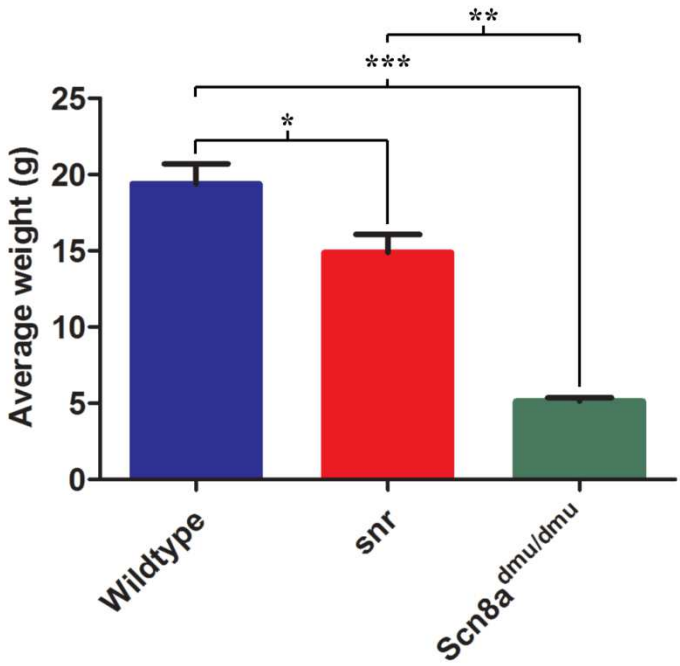
**
***
*
Average weight (g)
25
20
15
10
5
0
Wildtype
snr
Scn8a dmu/dmu

Figure 3.21: Behavioural monitoring assay. (**A**) After acclimating in a new cage for 1 hr, each mouse was monitored for 30 minutes/day for 5 days. Monitoring measurements were recorded in the same room at the same time, every day, by the same researcher that did not know the genotype of the experimental mice. Well-defined behaviours were recorded every 15 seconds for each mouse. (**B**) Behavioural monitoring measurements. Wildtype mice (n = 4) were compared to *snr* mice (n = 4) using a set of well-defined behaviours. An unpaired Student's *t*-test was used to show significance, where * = $p \leq 0.05$, ** = $p \leq 0.01$, and *** = $p \leq 0.001$. Statistical significance was observed for the walking behaviour in *snr* mice ($p = 0.007$). Error bars represent standard error of the mean (±SEM). Statistics were performed in MS Excel.

A

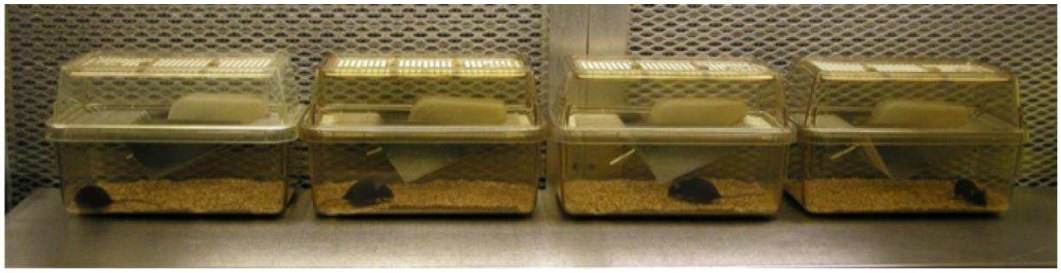

B

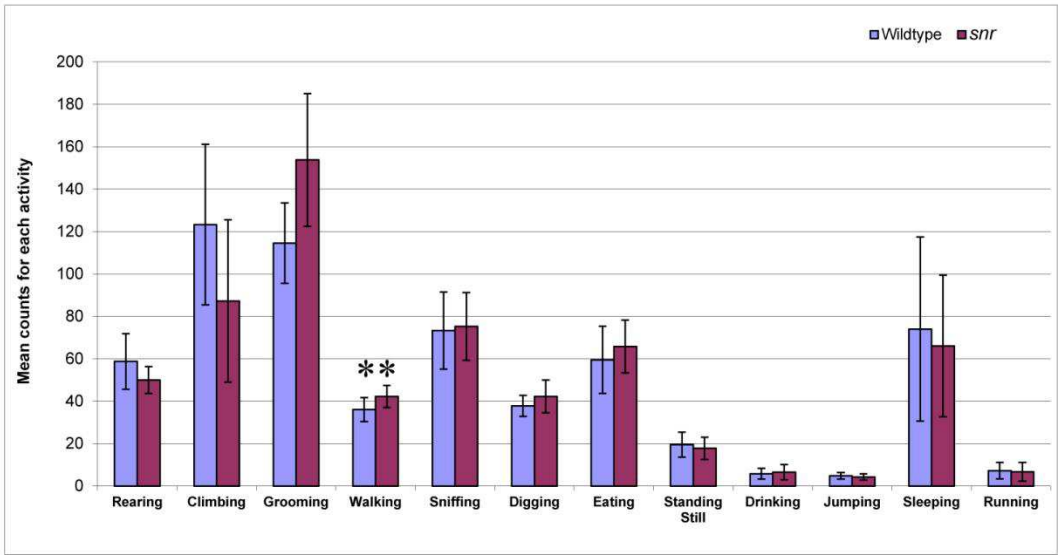
Wildtype
snr
Mean counts for each activity
200
180
160
140
120
100
80
60
40
20
0
**
Rearing
Climbing
Grooming
Walking
Sniffing
Digging
Eating
Standing Still
Drinking
Jumping
Sleeping
Running

Figure 3.22: Sensorimotor integration and hindlimb function measurements assay using the Balance Beam. (**A**) Mice were given a 2 hr learning period. After the learning period, mice were subjected to 2 trials/day for 5 days, with each trial lasting a total of 2 minutes. The balance beam apparatus is 100 cm in length. The total distance traveled (in cm) and footslips were all video recorded using a Canon 2R800 NTSC MiniDV digital video camcorder. (**B**) Sensorimotor integration measurements using the balance beam. Wildtype (n = 4), *snr* (n = 4), and *Scn8a*$^{dmu/dmu}$ (n = 4) were all compared, using a 1-way ANOVA with Tukey's post-hoc test with significance indicated as * = $p \leq 0.05$, ** = $p \leq 0.01$, and *** = $p \leq 0.001$. Lack of statistical significance is mainly due to high variance (some animals did not want to walk across the beam and stopped during the test). Error bars represent $\pm$ standard error of the mean (SEM). Since *Scn8a*$^{dmu/dmu}$ mice do not survive past P21, the 4 *Scn8a*$^{dmu/dmu}$ mice were tested at P18/P19, while the other mice were >2 months old during this assay. (**C**) Hindlimb function measurements using the balance beam. Wildtype (n = 4), *snr* (n = 4), and *Scn8a*$^{dmu/dmu}$ (n = 4) were all compared, using a 1-way ANOVA with Tukey's post-hoc test with significance indicated as * = $p \leq 0.05$, ** = $p \leq 0.01$, and *** = $p \leq 0.001$. Lack of statistical significance is mainly due to high variance (some animals did not want to walk across the beam and fell off during the test). Error bars represent standard error of the mean ($\pm$SEM). Since *Scn8a*$^{dmu/dmu}$ mice do not survive past P21, the 4 *Scn8a*$^{dmu/dmu}$ mice were tested at P18/P19, while the other mice were >2 months old during this assay. Statistics were performed in MS Excel.

A

B

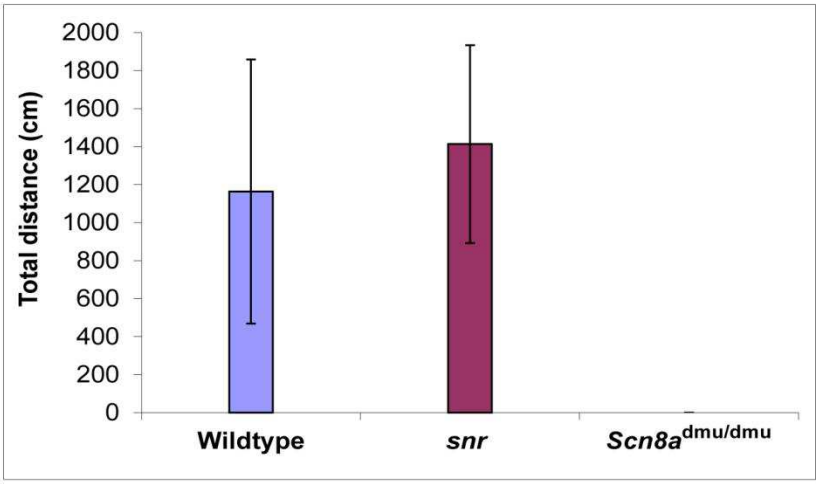
Total distance (cm)
2000
1800
1600
1400
1200
1000
800
600
400
200
0
Wildtype
snr
Scn8a dmu/dmu

C

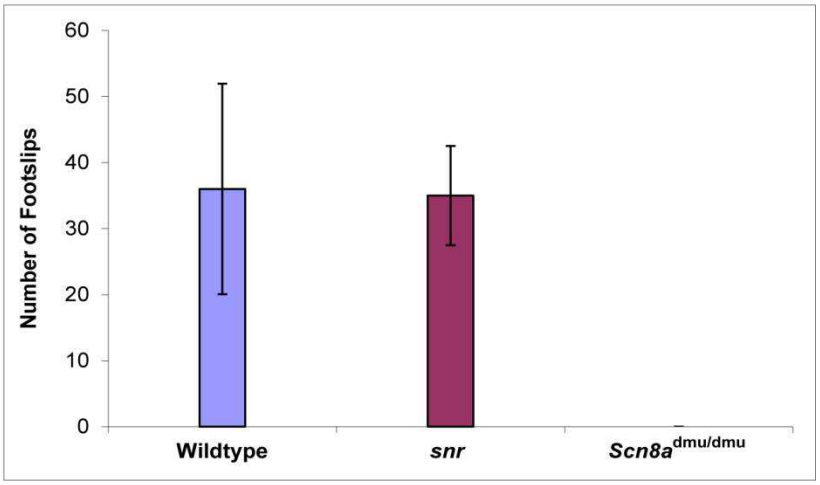
Number of Footslips
60
50
40
30
20
10
0
Wildtype
snr
Scn8a dmu/dmu

Figure 3.23: Sensorimotor coordination and overall motor function measurements assay using the Rotarod. (**A**) Mice were given a 2 hr learning period by performing 3 trials/day. After the learning period, mice were subjected to 6 trials/day for 5 days. The Rotarod apparatus was set to go from 0 to 50 rotations/minute over 6 minutes (360 seconds). The latency to fall (in seconds) was recorded, as there were timers that stopped the moment a mouse fell on a pressure-sensitive surface. (**B**) Wildtype (n = 4), *snr* (n = 4), and *Scn8a*$^{dmu/dmu}$ (n = 4) were all compared, using a 2-way ANOVA with Bonferroni post-hoc test with significance indicated as * = $p \leq 0.05$, ** = $p \leq 0.01$, and *** = $p \leq 0.001$. Error bars represent standard error of the mean (±SEM). The performance of *Scn8a*$^{dmu/dmu}$ mice on the Rotarod is significantly different ($p < 0.0001$) from both wildtype and *snr* mice. Since *Scn8a*$^{dmu/dmu}$ mice do not survive past P21, the 4 *Scn8a*$^{dmu/dmu}$ mice were tested at P18/P19, while the other mice were >2 months old during this assay. Statistics were performed in GraphPad Prism 5.

A

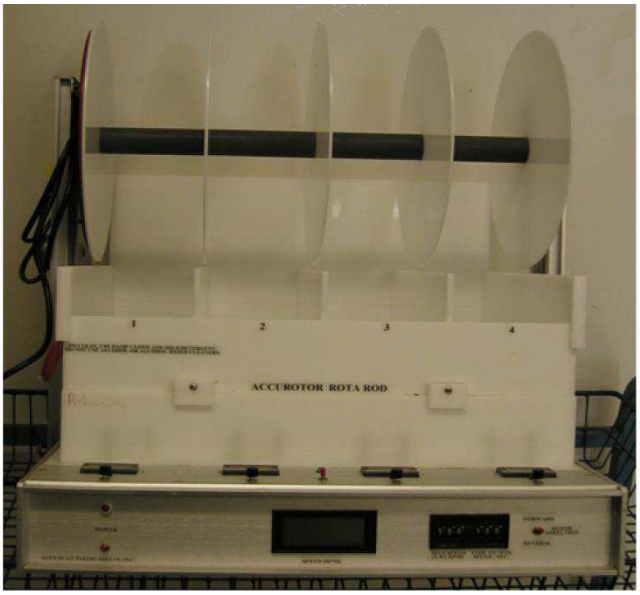
ACCUROTOR ROTA ROD

B

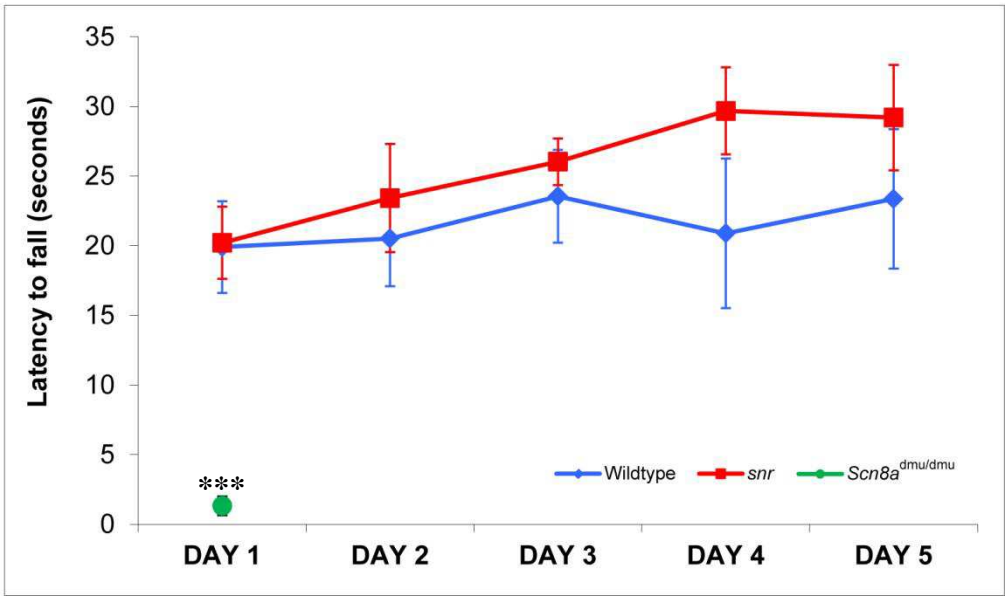
Latency to fall (seconds)
35
30
25
20
15
10
5
0
***
Wildtype
snr
Scn8a dmu/dmu
DAY 1
DAY 2
DAY 3
DAY 4
DAY 5

been identified ranges from 39% with plugs found on the third day of the estrous cycle, and 69% for those with mucus plugs found on the fourth day. (JAX notes: How to time mouse pregnancy, 2006). In my attempts to breed the *snr* mice, I observed and recorded a total of 56 vaginal mucus plugs. Of these mated females, none were identified as pregnant by visual inspection nor produced any viable offspring. DNA samples from all *snr* mice as well as siblings and parents have been preserved to allow the eventual characterization of the *snr* allele.

CHAPTER 4: DISCUSSION

4.1 Findings from qRT-PCR experiments

The *Scn8a*$^{dmu/dmu}$ mutant displays hindlimb paralysis and reduced retinal function as major phenotypes in mice deficient in functional $Na_v1.6$ sodium channels. I chose 11 genes, each having a role related to the normal function of sodium channels to obtain insight into the factors that lead to these phenotypes. The first group includes *NF-L*, *Jip1*, *App*, *Ank3*, and *Scn1b* are all genes involved in the recruitment, presentation, and function of $Na_v1.6$. The second group of genes include *Bdnf*, *TrkB*, and *Pum2*. *Scn8a* was also analyzed with this group. These genes are involved in the regulation of *Scn8a* transcription. Finally, the third group of genes, *Gfap* and *Cntf*, are involved in the normal function of Müller glia cells which are functional pillars of the retina tasked with maintenance of homeostasis, light transmission and neurotrophic as well as substrate support of other cell types that make up the retina.

4.1.1 Vesicular transport could be partially dysregulated in Scn8a$^{dmu/dmu}$ *mutants*

Retinal ganglion cells (RGC), the cells that project axons to the brain, express the highest levels of $Na_v1.6$ in the retina. Vesicular transport is an important process by which functional $Na_v1.6$ assembled in the endoplasmic reticulum (ER) is transported from the soma of the neuron to the nodes of Ranvier, where $Na_v1.6$ performs its sole function as a fast-gating sodium channel that is necessary for the propagation of electrical signals along the axon of a firing neuron. As such an important process, I have chosen to study five key genes involved in the recruitment, transport, and function of $Na_v1.6$. The five genes that I have chosen to study are *NF-L*, *Jip1*, *App*, *Ank3*, and *Scn1b* which all interact to help bring functional $Na_v1.6$ from the ER to the nodes of Ranvier.

Neurofilaments are a major part of the substantial cytoskeletal network that also includes microtubules, actin microfilaments, and a host of secondary support molecules, interweaving to create the cellular cytoskeletal network within neuronal cells, including those of the retina. This network serves as a scaffold for growth, support, and the transport of molecules both to and from the soma of each cell type. qRT-PCR revealed that *NF-L* expression was steady across the timepoints chosen for this study and that there were no statistically significant fluctuations before (P10-P12), during (P12-P14), or after eye-opening (P16-P30) in postnatal retinal development. There is a trend for decreased

NF-L expression at P16, where expression of only about a 2.75-fold decrease (equivalent to a 63.70% downregulation) of light-reared wildtype (LR WT) expression, but it was statistically insignificant, possibly due to a large standard error of the mean (SEM) in WT animal samples (Figure 3.2).

App was chosen because Liu *et al.* (2015) demonstrated that App co-localized and interacts with $Na_v1.6$ in mouse cortical neurons. This App-$Na_v1.6$ interaction appeared to enhance $Na_v1.6$ cell surface expression (Liu *et al.*, 2015). App is also a single spanning transmembrane protein that has been found as a component in synaptic vesicles (Groemer *et al.*, 2011). App may then serve as an anchor and linker molecule used for vesicular transport of materials to and from the cell soma by acting as a point of contact that is embedded in cargo vesicles. Therefore, I looked at the expression level of *App* transcripts throughout postnatal development of the retina, spanning the period of eye-opening and into adulthood. The levels of *App* expression remained relatively unchanged across the timepoints studied and was statistically unaffected by neither the presence nor absence of functional $Na_v1.6$ (Figure 3.4). There is, however, a trend towards decreased *App* expression despite no statistical significance, starting as early as P10 right through to P21. Without statistical significance between WT ($Scn8a^{+/+}$) and mutant (Mut, $Scn8a^{dmu/dmu}$) *App* expression, my data suggest that *App* is not engaged specifically in $Na_v1.6$ transport. *App* most likely serves a broader function as a linker molecule embedded in vesicles that is then used to help specific vesicles transverse the cytoskeletal network as part of the vesicular transport network. This supports the role of *App* as an adaptor/anchor molecule in vesicle transport.

Lending support to this *App* adaptor/anchor model is the next gene chosen for this study, *Jip1*. *App* is transported from the cell body by the molecular motor kinesin-1; however this interaction is facilitated by the linker molecule Jip1 (Matsuda *et al.*, 2003). Jip1 therefore, serves as a molecule linking App to the kinesin molecular motor, transporting cargo in an anterograde direction away from the cell soma. Fu and Holzbaur (2013) demonstrated that phosphorylation of S421 of Jip1 serves as a molecular switch that directs the transport direction; either anterograde or retrograde transport of App in neurons. Chiba *et al.* (2014) identified a subdomain in Jip1 that is responsible for fast-velocity enhanced App anterograde transport observed in neurons. Taken together, this information supports App function as a vesicular adaptor and anchor involved in cargo transport. My data indicate that, despite a lack of statistical significance, there is a trend

towards diminished *Jip1* expression at P12 and P16, during the period of eye-opening (Figure 3.3). Looking at the fold change graph for Jip1 (Figure 3.3B), at P12, LR Mut had a 2.21-fold decrease (equivalent to a 54.85% downregulation) in *Jip1* expression, dark-reared (DR) WT had a 4.51-fold decrease (equivalent to a 77.82% downregulation), and DR Mut had a 4.71-fold decrease (equivalent to a 78.78% downregulation) in *Jip1* expression. At P16, LR Mut had a 2.33-fold decrease (equivalent to a 56.92% downregulation), DR WT had a 4.71-fold decrease (equivalent to a 73.04% downregulation) and DR Mut had a 4.28-fold decrease (equivalent to a 76.61% downregulation) of expression of *Jip1* relative to LR WT animals. By P21, *Jip1* expression levels increased. This result shows that *Jip1* expression was diminished at the critical timepoint when eye-opening occurred from P12 to P16. As a result of decreased expression, there is a possibility that transport of App-linked cargo transport is affected in a diminished capacity. Finally, an observation can be made concerning reactivity to light stimulation which is most apparent. Figure 3.3 showed a trend towards diminished *Jip1* expression in DR animals, especially between the critical timepoints P12 to P16, suggesting that expression of *Jip1* may be responsive to light stimulation.

Ank3 is important in the clustering and localization of sodium channels. Van Wart *et al*. (2007) demonstrated that Ank3 is responsible for the localization and accumulation of $Na_v1.6$ at the distal end of the axon initial segment (AIS). Ank3 is also an important regulator of $Na_v1.6$ gating properties at the nodes of Ranvier (Shirahata *et al*., 2006). Ank3 is involved then in both the transport and normal function of $Na_v1.6$; therefore, it was included in my study to characterize the effect that a null mutation in *Scn8a* may have on this protein. An analysis of *Ank3* expression between P10 to P30 revealed that there is a trend in expression differences between WT and Mut at both P16 and P21. This is a stage when the retina is supposed to become functionally mature; during these five days is when it is most important for $Na_v1.6$ to travel to the nodes of Ranvier in RGC, facilitating in the propagation of electrical impulses to the brain after eye-opening. My results showed a trend towards reduced *Ank3* expression during this critical maturing period in postnatal retinal development. Specifically, there was decreased expression of *Ank3* in both the normalized and fold change graphs (Figure 3.5A and B). *Ank3* expression was significantly decreased at P21 in Figure 3.5A, compared to WT expression. This is illustrated further in Figure 3.5B where LR Mut expression was decreased down to a 2.98-fold decrease (equivalent to 66.46% downregulation) compared

to LR WT expression at P16, then raised to a 1.38-fold decrease (equivalent to a 27.54% downregulation) compared to LR WT expression at P21. Looking at Figure 3.5B, it is evident that at a time when the retina is supposed to mature into its final adult confirmation, there were significant differences in *Ank3* expression levels at P16 and P21. This decreased expression in *Ank3* suggests that there may be a delay or perhaps even an inability of the retina to mature properly in the absence of $Na_v1.6$ as a result of a failure to properly cluster and localize sodium channels present in the retina.

Lastly, I chose to look at *Scn1b* in this study because it is a multifunctional protein that is involved in current modulation, channel cell surface expression, and cytoskeletal recruitment (Fein *et al.*, 2007). Of importance, *Scn1b*-null mice exhibit slowed action potential conduction and decreased numbers of nodes of Ranvier (Fein *et al.*, 2007). Co-expression of *Scn1b* with voltage-gated sodium channel (VGSC) α-subunits has been demonstrated to increase the level of sodium channels 2-to 4-fold (Isom *et al.*, 1995). Finally, sodium channel α-subunits and Scn1b β-subunits interact to recruit the cytoskeleton protein ankyrin G (product of *Ank3* gene) (Malhotra *et al.*, 2000). Given its roles in both the recruitment and localization of sodium channels, I chose to study this gene further with qRT-PCR. Analysis of qRT-PCR results for *Scn1b* expression showed that there was a change in expression levels between Mut animals with respect to WT animals at P16 (Figure 3.6). Normalized expression of *Scn1b* peaked at P16, coinciding with the need for sodium channels to reach their appropriate destinations during the final phase of retinal maturity (Figure 3.6A). Looking at the fold change differences at P16 (Figure 3.6B), it is evident that in the absence of functional $Na_v1.6$, there was a decreased expression of *Scn1b*. This decrease during such a critical moment in final retinal maturity is likely to be detrimental, possibly leaving the retina with an inability to properly cluster and transport sodium channels into their proper microdomains to facilitate normal action potential propagation.

Taken together, the five genes I propose are those that support the formation of the cytoskeletal network (*NF-L*), act as an anchor molecule in cargo vesicles as well as tether $Na_v1.6$ channels (*App*), function as an adaptor protein linking cargo vesicles to molecular transport machinery (*Jip1*), provide cellular anchoring to the cytoskeletal network and aid in the proper clustering of $Na_v1.6$ (*Ank3*), and lastly, a multipurpose protein that aids in linking cytoskeletal proteins to sodium channels to aid in their proper sorting and clustering (*Scn1b*).

All of these genes and their products are important to the proper function of $Na_v1.6$ as well as other sodium channels necessary for the retina to mature and function normally in the postnatal mouse eye. Therefore, a disruption or deviation away from the normal levels of expression could be detrimental towards the finalization of the functional retinal network. As my data suggest, there appears to be a negligible change in the expression patterns of both *NF-L* and *App*; therefore the levels of protein expression is likely to be steady and unchanging across developmental timepoints as well. Interestingly, my immunohistochemical results from NF-L staining in the retina appears to indicate that there may be disorganization of the neurofilamentous network, as illustrated with NF-L accumulations, rather than an increase in NF-L protein production. However, the expression patterns of *Jip1*, *Ank3*, and *Scn1b* have significant changes spanning important postnatal developmental timepoints P12 to P21 that includes eye-opening and finalization of sodium channel localization within retinal neurons. There is a strong trend in all three of these genes where *Scn8a*$^{dmu/dmu}$ mutants consistently express a decreased level of each respective gene under scrutiny. Given the important and multi-faceted involvement of each of these three proteins, it can be detrimental to the maturing retina if even one of these genes were dysregulated. In the *Scn8a*$^{dmu/dmu}$ mutants, all three genes are concurrently dysregulated. My data illustrate that all three of these proteins undergo downregulation in expression levels as a result of being on a *Scn8a* functionally-null background. Therefore, my data suggest that the vesicular trafficking mechanism necessary for the clustering, transport, and cell surface presentation of sodium channels may be partially dysregulated by the downregulation of *Jip1*, *Ank3*, and *Scn1b* between P12 to P21, leading to a dysfunctional transport network causing reduced retinal function in *Scn8a*$^{dmu/dmu}$ mice.

4.1.2 Postnatal regulation of Scn8a *transcription*

As part of any study on mutant animals, it is natural to want to understand the regulation of the gene of interest. That is why I have chosen to look at four specific genes that are linked to the regulation of *Scn8a* transcription. These genes include the neurotrophin *Bdnf*, its high affinity receptor *TrkB*, *Pum2*, the direct transcription repressor of *Scn8a*, and the main sodium channel of interest in my work, *Scn8a*.

Bdnf is a part of the neurotrophin family and is a major neurological signaling molecule which possesses neuroprotective effects (Afarid *et al*., 2016). Bdnf initiates

activation of various intracellular signaling cascades such as the MAPK/ERK, PLCγ and PI3K pathways that are essential for cell differentiation, survival, and synaptic function (Numakawa *et al*., 2011). As a signaling molecule that is capable of controlling several key developmental intracellular cascades, I have chosen to include *Bdnf* in my study. An analysis of *Bdnf* expression pattern in postnatal time periods spanning the period of eye-opening and retinal nervous network finalization into adulthood were presented (Figure 3.8). Looking at the normalized expression pattern of *Bdnf*, it is clear that *Bdnf* is responsive to light stimulation as LR animals had consistently higher *Bdnf* expression than those reared in DR conditions (Figure 3.8A). Expectedly, given the wide spread implications that *Bdnf* has on gene transcription, it had the highest expression level at P12, at a point in time when the retina is preparing itself for the period of eye-opening. An observation of note here is that at P21, Mut animals (LR and DR) significantly expressed a lower amount of *Bdnf* than their WT counterparts. A look at the fold change graph where expression has been calculated relative to LR WT animals at each timepoint, there were notable expression level changes at P16 and P21, a key time for the finalization of axonal connections into the mature adult retinal form (Figure 3.8B). Mutant animals demonstrated a strong trend toward decreased *Bdnf* expression from P16 to P21. At P16, LR Mut had a 1.82-fold decrease (equivalent to a 45.03% downregulation), DR WT had a 3.22-fold decrease (equivalent to a 68.99% downregulation), and DR Mut had a 4.15-fold decrease (75.88% downregulation) compared to LR WT *Bdnf* expression (Figure 3.8B). At P21, LR Mut had a 1.97-fold decrease (equivalent to a 49.27% downregulation), DR WT had a 3.17-fold decrease (equivalent to a 68.41% downregulation), and DR Mut had a 2.33-fold decrease (equivalent to a 57.11% downregulation) compared to LR WT *Bdnf* expression (Figure 3.8B). Therefore, my data suggest that this decreased period of *Bdnf* expression is limited to only the critical period during eye-opening to the finalization of retinal maturity between P12 to P21. This disruption in *Bdnf* expression may have detrimental effects on numerous pathways given the wide spread effects that *Bdnf* is capable of interacting with.

A study on *Bdnf* is not complete without studying its high affinity receptor *TrkB*. TrkB is the cognate receptor to Bdnf, the binding of which activates intracellular cascades involved in neuronal survival, neurogenesis, and synaptic plasticity (Iuvone *et al*., 2014). Following qRT-PCR analysis, normalized expression and fold change relative to LR WT animals were presented (Figure 3.9). Statistical analysis indicated that the level of *TrkB*

expression was relatively steady across all timepoints in my study, with the exception of P21. Similar to *Bdnf*, at P21, WT *TrkB* expression was significantly different from that of Mut animals, again highlighting the importance of this time period during the finalization phase of retinal axon connectivity establishment into the mature adult form. This difference in expression was further established in P21 where LR Mut *TrkB* expression had dropped to a 3.27-fold decrease (equivalent to a 69.46% downregulation) in expression compared to LR WT animals (Figure 3.9B). This trend of diminished *TrkB* expression was again observed at P16-P21. The relative unchanging levels of *TrkB* expression would perhaps suggest that *TrkB* expression is regulated independent of *Bdnf* stimulus. Therefore, the quantity and presence of Bdnf may solely be responsible for the strength and activation of all intracellular cascade pathways that the Bdnf:TrkB ligand-receptor complex is responsible for.

One of the genes indirectly controlled by the Bdnf:TrkB signaling complex is *Pum2* (Fiore *et al*., 2009). The Bdnf:TrkB signaling complex controls Pum2 activity through the activation of mitogen-activated protein kinase 5 (Erk5), which in turn activates myocyte enhancing factor 2 (Mef2) that then activates the transcription of the micro-RNA cluster miR379-410 (Fiore *et al*., 2009; Khudayberdiev *et al*., 2009). Micro-RNA-134, part of the miR379-410 cluster, acts as an inhibitor to *Pum2* translation (Khudayberdiev *et al*., 2009). Pum2 itself is a translational repressor of *Scn8a* (Driscoll *et al*., 2013). Thus, Bdnf appears to be indirectly responsible for controlling the transcription of *Scn8a* in WT animals. As a direct translational repressor of *Scn8a*, I included *Pum2* in my qRT-PCR study in order to understand how *Scn8a* transcription is regulated by the levels of its repressor. An analysis of qRT-PCR data for *Pum2* expression during the postnatal retina developmental period is presented in Figure 3.10A and Figure 3.10B for normalized expression and calculated fold change relative to LR WT animals respectively. *Scn8a*$^{dmu/dmu}$ mutant animals had expression patterns that were similar to that of WT animals. *Pum2* expression has proved to be the exception among the 11 genes chosen for my study in that the *Scn8a* functionally-null background did not have a diminishing effect on expression levels over the period between P12 – P21. Looking at both the graphs for normalized expression and relative expression, it appeared that *Pum2* expression was significantly different from those observed for DR animals across these three timepoints. It is uncertain what the biological significance of this finding may be. However, this finding certainly is different from the behaviour of the

other ten genes chosen for this study and may be an interesting avenue to pursue in future studies. My data suggest that in both WT and in Mut animals the levels of *Pum2* were nearly identical. Therefore, the functionally-null truncated version of $Na_v1.6$ from *Scn8a*$^{dmu/dmu}$ mutant animals may have been transcribed at the same levels as that of WT animals, at least from what can be inferred by the *Pum2* expression pattern observed here.

Finally, I looked at the expression level of *Scn8a* directly to study the regulation of expression by visual experience throughout the postnatal developmental period. Figure 3.7A and Figure 3.7B depicts the normalized expression profile and fold change relative to LR WT animals respectively. There is a trend of decreased *Scn8a* expression in Mut animals early on at P10 and P12 compared to WT animals, mirroring a trend observed at P10 for *Pum2*. It was surprising that DR animals showed a trend toward rising *Scn8a* expression. Interestingly, it is worth noting that DR animals exhibited a trend at P12 and P16 towards higher *Scn8a* expression than that observed for those raised in LR conditions (Figure 3.7A, B). This could suggest that the retina of DR animals are trying to compensate for a lack of action potential conductance by ramping up the production of $Na_v1.6$ to levels nearly doubled that of LR WT counterparts during this critical eye-opening period.

Taken together, I have chosen four genes that are critical in the regulation of multiple functions contributing toward cell survival, synaptic function, and *Scn8a* transcription. My data demonstrated that the levels of *TrkB* were unchanging and its expression may be independently regulated outside of Bdnf stimulation. As such, I surmise that the signaling cascades which are responsive to the Bdnf:TrkB signaling complex may depend on the amount and intensity of Bdnf at any point in time to activate intracellular signaling cascades. One of these signaling cascades leads to the transcription regulation of *Pum2*, a direct *Scn8a* transcriptional repressor. Therefore, Bdnf may be indirectly responsible for the regulation of *Scn8a* transcription through controlling the action of Pum2. For the chosen genes it is interesting to note that the lack of functional $Na_v1.6$ diminishes gene expression on a large scale, across the period that includes eye-opening and axonal connection finalization as exemplified here by the *Bdnf*, *TrkB*, and *Pum2* expression profiles. It is uncertain exactly what or why such a global change in gene downregulation is happening. It would have been interesting to include the expression profiles of *Scn1a* and *Scn2a* as well, as their gene products are also highly expressed sodium channels in the retina. Unfortunately, due to the extreme similarity of

RNA sequences between these two genes, designing primers specific to each one that would not cross react to some degree with the other proved to be insurmountable given the time and resource constraints of the current experimental design. Therefore, as part of some future work, I recommend the inclusion of these genes to further elucidate and characterize gene regulation changes on a *Scn8a*^{dmu} background compared to WT animals.

4.1.3 Müller glia cell support through postnatal development

Müller glia cells provide the substrate in which other retinal cells embed and align themselves radially into functional layers to facilitate the conversion of photon capture into action potential transduction (Reichenbach and Bringmann, 2013). As such, Müller cell homeostasis is of utmost importance to the retina and its normal functions. I chose to study two key genes that play significant roles in Müller glia cells. The first is *Gfap* which is the main intermediate filament protein in glia cells (Middeldorp and Hol, 2011). The second is *Cntf*, another important neurotrophic factor with neuroprotective properties.

Gfap is an important component of the cytoskeleton in glia cells and consists of numerous distinct isoforms that enhances the complexity of the astrocyte cytoskeletal network toward specific subtype functionality (Middeldorp and Hol, 2013). Being part of the intermediate filament cytoskeleton network in astrocytes, Gfap also performs a role in the dynamic trafficking of vesicles (Potokar *et al*., 2010). Having important multifaceted roles within the main glia cell type in the retina, Gfap serves as an important indicator for the function and overall state of Müller glia cells, where an increased expression may reveal the presence of gliosis. An analysis of *Gfap* expression by qRT-PCR is presented in Figure 3.11A, and Figure 3.11B; representing the normalized *Gfap* expression profile and a fold change graph calculated to reflect expression relative to LR WT animals respectively. Normalized expression of *Gfap* across postnatal developmental timepoints remained generally steady in WT animals, with a small peak at P12, possibly as a result of the retina entering a period critical to eye-opening. There is a general trend in Mut animals towards reduced *Gfap* expression between P12 to P21. At P12, LR Mut *Gfap* expression was reduced to a 12.85-fold decrease (equivalent to a 92.21% downregulation) of LR WT levels. This trend of reduced expression was carried right through eye-opening into timepoints spanning the finalization process toward retina axonal maturity at P21. My data suggest that the expression of *Gfap* was diminished during this critical time

period in the absence of functional $Na_v1.6$. This continues the trend as seen previously in other genes where there is diminished expression on a *Scn8a*^{dmu} mutant background.

The last gene I chose as part of my study is *Cntf*, another important neurotrophic factor with neuroprotective properties. Cntf, together with Bdnf, are known to exert prosurvival signals to retinal cells under diseased conditions, such as glaucoma (Harada *et al*., 2002). Müller glia cells are the major Cntf-responsive cells in the retina (Wen *et al*., 2012). Cntf is able to induce *Gfap* expression through the action of the JAK/STAT pathway (Wang *et al*., 2002). For these reasons, I chose to examine *Cntf* gene expression as the last gene in my study. Figure 3.12A and Figure 3.12B represents a plot of the normalized *Cntf* expression profile and a plot of the fold change differences when calculated relative to LR WT animals. Across all timepoints, the expression of *Cntf* was reduced in DR animals (WT and Mut) compared to LR animals (WT and Mut). Therefore, this suggests that *Cntf* expression is light responsive. This difference was apparent during the time of eye-opening, between P12 to P16 (Figure 3.12A). At P16, LR Mut had a 4.33-fold decrease (equivalent to a 76.93% downregulation) in *Cntf* expression relative to LR WT animals. This suggests that the expression of Cntf may be downregulated in the absence of functional $Na_v1.6$.

Looking at the difference in expression levels relative to LR WT animals, DR animals in general had significantly reduced *Cntf* expression across all timepoints in my study. This trend continued into P21 although it was no longer statistically significant at this timepoint.

Müller glia cell function is of importance to the general state of the retina, both as structural support as well as providing important chemical support to promote homeostasis of other retinal cell types. As my data demonstrated, there was diminished gene expression for both *Gfap* and *Cntf* in *Scn8a*$^{dmu/dmu}$ mutants at the most critical time, spanning eye-opening and finalization of retina functional maturity. My data suggest that Mut animals with functionally-null $Na_v1.6$ have Müller glia cells that are most likely unable to properly provide the proper prosurvival signals with diminished *Cntf* expression. Also, with decreased *Gfap* expression, Müller glia cells in mutant animals are most likely unable to provide the proper structural support to other retinal cell types and cytoskeletal network, which is important for vesicular trafficking/recycling (Potokar *et al*., 2010; Middeldorp and Hol, 2013).

4.2 Findings from immunohistochemistry experiments

Alzheimer's disease, Parkinson's disease, Huntington's disease, Amyotrophic lateral sclerosis (ALS) and Charcot-Marie-Tooth disease are only a few among the plethora of neurological disorders that affect millions world-wide. These diseases share something in common: abnormal protein aggregates found in the diseased brain (Irvine *et al*., 2008; Arrasate and Finkbeiner, 2012; Wakabayashi *et al*., 2013; Adebola *et al*., 2015). Protein aggregates are a common feature of neurodegenerative diseases (Gadad *et al*., 2011). Aggregates of insoluble proteins can be found inside neurons that are at risk, in glia cells, and even in extracellular space as a result of secreted proteins, or proteins released from cells that have undergone apoptosis or necrosis as a result of disease (Arawaka *et al*., 2010; Gadad *et al*., 2011).

Neurofilament light-chain aggregation is a classic hallmark of unhealthy neurons and an early sign of disease onset for numerous neurodegenerative diseases such as ALS, Alzheimer's, Parkinson's, Huntington's and Charcot-Marie-Tooth diseases (Irvine *et al*., 2008; Wakabayashi *et al*., 2013; Adebola *et al*., 2015; Muresan and Ladescu Muresan, 2016). This study sought to identify the differences between neurofilament light-chain (NF-L) distributions between WT and Mut animals that were raised in LR and DR conditions.

4.2.1 Absence of $Na_v1.6$ leads to developmental NF-L dysregulation in the postnatal retina

Using P16 as a hallmark postnatal age in the midst of retinal maturation between eye-opening at P12 and final retinal connectivity maturation at P21, marked differences between NF-L distributions were observed (Figures 3.14-3.16). Neurofilament accumulations can be seen at the outer plexiform layer (OPL) in LR Mut. This accumulation was only present in Mut and became more intense in DR Mut. Another finding of note was the presence of increased NF-L staining in the ganglion cell layer (GCL) layer in DR animals. NF-L staining was much brighter compared to that of LR WT animals which was barely visible. Finally, there were punctate NF-L accumulations observed in the inner plexiform layer (IPL) in DR animals. Taken together, this suggests that NF-L distribution may be dysregulated in the absence of a functional $Na_v1.6$, and that

the absence of light stimulus further encourages this dysregulation, leading to NF-L staining that is more intense than LR counterparts.

Next, to put these observations into a developmental context, a panel of NF-L stained retinas from P7 to P21 was compiled to characterize NF-L behaviour across postnatal development (Figure 3.13). The major finding from Figure 3.13 is that neurofilament accumulation was only observed very early on in postnatal development at P7 in LR WT animals in the OPL, while neurofilament staining was diffused at all other timepoints. In the absence of functional $Na_v1.6$ however, there appeared to be a temporal delay in the appearance of NF-L accumulation in the OPL, as evident by panels at P10 and P12. NF-L accumulation was especially noticeable in the GCL of P16 LR Mut animals, a distinctive feature not observed in LR WT counterparts. This accumulation suggests another point of dysregulation as a prelude to final retinal synapse maturation completion by P21. The removal of light further enhances NF-L dysregulation as evidenced by DR animals. The GCL was highlighted with intense NF-L staining in both DR WT and DR Mut animals, similar to that observed for the P16 LR Mut, demonstrating that the absence of light may lead to further delay due to increased NF-L accumulation. The IPL in DR Mut was characterized with intense NF-L staining that spans the time of eye-opening and retinal synapse maturation. Compared to the LR Mut counterparts, the removal of light stimulus led to a delay of normal maturation and increased NF-L accumulation. Taken together, Figure 3.13 illustrates that in the absence of functional $Na_v1.6$, there may be a developmental delay in the neurofilament system, leading to aberrant NF-L accumulations in the OPL at later timepoints shifted from WT P7 presentation. Figure 3.13 also illustrates the importance of light as a stimulus in the proper maturation of the retinal neurofilament network, as the removal of light in DR animals led to noticeable delays in the proper development of the neurofilament network evidenced by the aberrant NF-L accumulations in both the GCL and IPL in DR animals.

Although the root cause of this NF-L accumulation is unknown, the accumulation in the OPL, punctate speckling of NF-L in the IPL and in the soma of RGC in the GCL suggest some possible scenarios. Both the OPL and IPL consist of a dense network of synapses where many retinal cell types make contact with each other. In DR animals, NF-L accumulation was observed to be the most intense in the GCL, located in what appeared to be RGC soma. Consequently, if the NF-L accumulations are in the RGC, this could explain the reduced level of $Na_v1.6$ observed in Mut animals (Côté *et al.*, 2005), as

RGC express the highest levels of $Na_v1.6$ in the retina. As my data suggest that normal NF-L distribution is dependent on normal $Na_v1.6$ function, either through sodium currents produced or via a direct interaction, this could explain why Mut animals (both LR and DR) have more NF-L accumulations compared to their WT counterparts. Some possible future experiments could be to examine the distribution of other NF, a comparison of the distribution of unphosphorylated vs. phosphorylated NF, and perhaps examine what these apparent NF-L accumulations look like under the electron microscope for more accurate morphological identification.

The cause of the *Scn8a*$^{dmu/dmu}$ electroretinogram (ERG) phenotype (reduced a- and b-waves at P16 with amplitudes and implicit times that are similar to traces found in WT P12 mice, Côté *et al.*, 2005) is currently unknown; however, the abnormal accumulation of NF-L protein in the OPL suggests some possible scenarios. The OPL is the site where photoreceptor synapses make contact with bipolar and horizontal cell dendrites. Consequently, if the accumulations are in the photoreceptors, this could affect the function of these cells which could explain the reduction in the a-wave (which originates directly from the photoreceptors) and the b-wave reduction could stem from this effect on the a-wave. Alternatively, an accumulation in bipolar cell dendrites could result in disrupted signal transmission and could explain the reduction in the b-wave. The a-wave reduction in this context would be more difficult to explain but the disruption of an unidentified retrograde signal to the photoreceptors could potentially explain this effect.

4.2.2 Absence of $Na_v1.6$ disrupts the organization of cerebellar central fiber bundles

In addition to documented visual impairment, *Scn8a*$^{dmu/dmu}$ mutant mice also exhibit another distinctive phenotype: the development of hindlimb paralysis by ~P12. All mice harbouring the *Scn8a*^{dmu} homozygous mutation display hindlimb paralysis. As such a prevalent phenotype, it was natural to look at the cerebellum of *Scn8a*$^{dmu/dmu}$ mice, as the cerebellum is the main part of the brain responsible for receiving information from the sensory systems and other parts of the brain and then regulates motor movements in response (Kohrman *et al.*, 1996b).

Inspection of NF-L stained cerebella of LR WT and LR Mut animals revealed distinctive branching patterns for the central fiber bundle in each cerebellar lobe (Figure 3.17). P16 LR WT animals at low magnification (Figure 3.17A) showed a vast network of NF-L stained branches emanating from Purkinje cells, extending into the center of each

cerebellar lobe to form the central fiber bundle. At high magnification (Figure 3.17B), the branches were observed as they extend unidirectionally toward the center of each lobe and come together to form the central fiber bundle. Each branch was clearly seen as long, slender, well orientated tracks. Contrary to the WT distribution pattern, P16 LR Mut animals had a more diffused appearance for this branching pattern at low magnification (Figure 3.17C). The central fiber bundle was still present, however, while the distinctive branches that lead up to its formation appeared to be more disorganized. Under high magnification, (Figure 3.17D), it was clear that this branching pattern was disrupted in the absence of functional $Na_v1.6$. Branches in Mut had become saturated with punctate accumulations of NF-L-rich nodules. The distinctive unidirectionality of each branch observed in WT was diminished in Mut animals, leaving only weak strands that are at a higher degree of disorganization than WT animals. Taken together, this strongly suggests that the absence of functional $Na_v1.6$ disrupts the organization and distribution of the neurofilament network, leading to a diminished and disorganized fiber bundle system in the cerebella of Mut animals.

4.2.3 Punctate App accumulations in the visual cortex of mutants

Since mutant retinal development was affected by the absence of functional $Na_v1.6$, the visual cortex region of the brain was investigated. Using H&E staining, cells in the different visual cortex layers displayed a normal morphology (Figure 3.18A). The typical signs of necrosis and apoptosis such as punctate cellular appearance, scattered punctate nuclear bodies resulting from pykonosis were absent across all layers of the visual cortex (Figure 3.18A). However, when immunohistochemistically probed with anti-App antibody, a distinct pattern of App accumulations was observed (Figure 3.18). Both LR and DR WT animals (Figure 3.18C, E) had a diffused distribution of App throughout the different layers of the visual cortex. LR and DR Mut animals however, displayed clear App accumulations within the deeper layers of the visual cortex (Figure 3.18D, F). This lends further evidence to support that the lack of functional $Na_v1.6$ may be disruptive to intracellular organization, and possibly point to a general disruption of the intracellular transport network.

Finally, with additional information obtained from immunohistochemistry experiments in this study, there is strong evidence to suggest that the neurofilamentous network is disrupted in *Scn8a*$^{dmu/dmu}$ mutant animals. As a result of neurofilamentous

network disruption, both microfilament and microtubule networks that are built upon the neurofilament network may also experience disruption. Figure 4.1 illustrates this disruption in the transport network potentially experienced by *Scn8a*$^{dmu/dmu}$ mutant animals in light of this disrupted neurofilament network. This figure illustrates aberrant accumulations of NF-L that leaves the neurofilamentous network in disarray. As a result of a perturbed neurofilament network, microtubules, which are the backbone of the intracellular transport network, is misaligned and disorderly, leaving vesicular cargo unable to properly transverse the axon and deliver their goods to their proper locations.

4.3 Findings from experiments with *snr* mice

Data gathered from the experiments using the *snr* mice suggest there may be a rescue of the *Scn8a*^{dmu} motor phenotype. Initial results suggest that *snr* mice may be a potentially new substrain that spontaneously arose from within the *Scn8a*^{dmu} mouse strain. In this potential new substrain, the vision impairment appears to be separate from the degenerating muscle phenotype, possibly alluding to multiple loci contributing to the *Scn8a*^{dmu} condition. This suggests that an independent gene or another novel mutation in *Scn8a* affects the severity of the motor phenotype.

The first two confirmed *snr* females were mated back with their father, in hopes of separating and maintaining this potential new mouse substrain. While mating was observed to occur with 56 mucus plugs found, no viable offspring resulted from both of these females. A male and female from a different litter were placed together as a mating pair, and similarly, no viable offspring were generated despite successful mating observed. Unfortunately, these four animals of this potentially new *snr* substrain are no longer available.

In an effort to characterize the *snr* substrain, sequencing the *Scn8a* gene in its entirety may prove to be useful when comparing *Scn8a*$^{dmu/dmu}$ and *snr*. Perhaps another spontaneous insertion/deletion occurred, shifting the reading frame, resulting in gene transcription leading to a distinct, yet functional $Na_v1.6$ protein. As the cost of whole genome sequencing decreases, it may be possible to compare the entire sequenced genomes of *Scn8a*^{dmu} and *snr* (from which DNA has been reserved), potentially demonstrating a possible second, novel mutation that delineates the visual impairment phenotype from the neuropathy phenotype.

Figure 4.1: Proposed mechanism for the formation of neurofilament accumulations that cause disruptions in the intracellular transport network. Specifically depicted in this figure is the formation of neurofilament accumulations. As the neurofilamentous network becomes disorganized, this in turn may cause disruptions in the other cytoskeletal systems (the microtubule and actin microfilament networks). Overall disorganization to the cytoskeleton may cause the formation of more aggregates, eventually becoming enough to significantly inhibit the function of the entire intracellular trafficking network. Figure drawn by L.W.G.Chu, 2016.

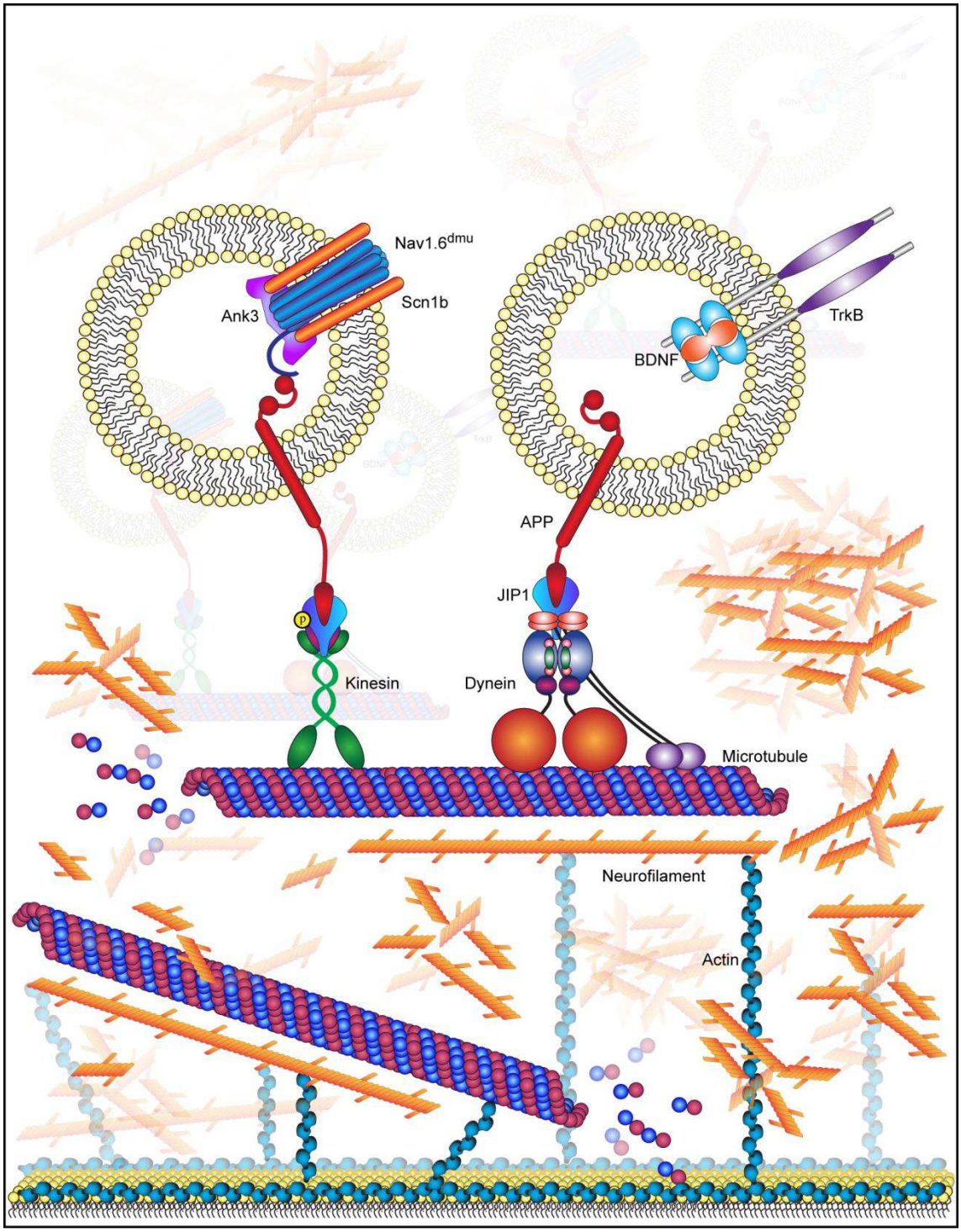
Nav1.6dmu
Scn1b
Ank3
TrkB
BDNF
APP
JIP1
P
Kinesin
Dynein
Microtubule
Neurofilament
Actin

Another possibility to explain the appearance of the *snr* substrain may be due to the 'reshuffling' of the sodium channel transmembrane units. Although observed in chloride channels, it may be possible that the sodium channel transmembrane units of *snr* are formed in a unique way that results in a 'rescue' phenotype (Dr. V. Chappe, Dalhousie University, Canada, personal communication). Further genetic characterization of both *Scn8a*^{dmu} and *snr* mice may perhaps one day reveal the mode of inheritance of this new modifier allele.

4.4 Synthesis of overall findings and possible ramifications

The findings in this study thus far have been described separately. Results from qRT-PCR experiments focused on mRNA levels describing the behaviour of 11 genes over the postnatal period encompassing eye-opening and beyond. Results from immunohistochemistry experiments are heavily based on NF-L immunohistochemistry data. Finally, in this final chapter of my thesis, I will integrate findings from both qRT-PCR and immunohistochemistry experiments together to form an overall view of what *Scn8a*$^{dmu/dmu}$ mutant animals most likely experience due to the lack of functional $Na_v1.6$ and discuss possible ramifications below.

4.4.1 Scn8a$^{dmu/dmu}$ *mutant animals experience substantial downregulation in gene expression*

Results from qRT-PCR data suggest that Mut animals, both LR and DR, experience substantial downregulation in gene expression. I have chosen to study three different groups of interacting genes where each group is responsible for a different function within the cell. An examination of the 11 genes that were characterized in this study revealed that during the period between the postnatal age P12 to P21, there is a general downregulation of gene expression in mutants. Nine out of 11 genes, equivalent to 82% of genes characterized by qRT-PCR, exhibited this trend of reduced gene expression during this period of eye-opening. This trend toward reduced gene expression in mutants may be of biological importance and could be responsible for the overall phenotypes manifested by Mut animals.

I surmise that the reason for such a noticeable and substantial downregulation of gene expression in Mut animals is a result of disruptions to the neurofilamentous network. Numerous processes within the cell, including proper signal transduction which controls

gene expression, are dependent on the cell's ability to properly relay information upon a structured network (Janmey, 1998). Neurons depend on the integral neurofilamentous network for physical structural support as it allows cells to properly separate and compartmentalize organelles and cellular functions (Kim and Coulombe, 2007; Yuan *et al.*, 2009). Neurofilaments, along with integrator molecules, can be thought of as the backbone upon which microtubule and actin filament networks are built upon (Fuchs and Cleveland, 1998; Yang *et al.*, 1999). Therefore, I reason that if the neurofilament network is perturbed, this disruption would further translate to the other cytoskeletal networks. In this situation, signaling cascades are disrupted, leaving neurons unable to integrate external information and react accordingly to external stimuli.

Using qRT-PCR data, the relative expression of *NF-L* appears to be relatively steady and unchanging throughout postnatal retinal development (Figure 3.2). As I have demonstrated with immunohistochemistry data, the neurofilament network appears to be disrupted in mutant retina and cerebellum (Figures 3.13, and 3.17), my data support this sequence of events as a possible cause that results in the observed substantial but not ubiquitous downregulation of gene expression experienced by *Scn8a*$^{dmu/dmu}$ mutant animals. I surmise that it is unlikely that a general downregulation of gene expression may be the cause of the observed NF-L abnormality; if this were to occur, the *NF-L* mRNA expression would therefore be changing throughout postnatal development. Under the examination of several developmental timepoints, rearing conditions and various genotype groups, the relative expression of NF-L from my qRT-PCR results did not show any significant changes. This may indicate that the *Scn8a*$^{dmu/dmu}$ mutant mice are displaying early signs of neurological disease, similar to those observed in Alzheimer's disease, Parkinson's disease and Charcot-Marie-Tooth disease, where protein aggregates are hallmark indicators.

4.4.2 Neurofilament network disruption in mutants may be due to altered NF-L phosphorylation

Intermediate filaments, of which neurofilaments are a subclass, undergo post transcriptional modification that modulates their behaviour and function (Snider and Omary, 2014). Neurofilaments are extremely dynamic structures with numerous phosphorylation sites that can be acted upon by different protein kinases, including protein kinase A (PKA) and protein kinase C (PKC) (Julien and Mushynski, 1998). At

different states of phosphorylation, neurofilaments can be prompted to either assemble into useful filaments that later serve as a scaffold upon which other cytoskeletal networks can build upon, or disassemble, allowing the cell to remodel itself as in the case of axonal growth and repair (Pant *et al*., 2000; Yates, *et al*., 2009; Dale and Garcia, 2012). Specifically, the NF-L head group is responsible for this ability to either assemble or disassemble. Phosphorylated NF-L head groups are prevented from assembly into filaments (Pant *et al*., 2000). While unphosphorylated, NF-L head groups promote assembly into filaments by recruitment of both NF-M and NF-H (Pant *et al*., 2000). Therefore, regulation of NF-L phosphorylation is of utmost importance to overall neuronal structural integrity and may affect processes such as axonal transport that is necessary for the proper function of neurons. The lack of functional $Na_v1.6$ may be the root cause of substantial downregulation of gene expression experienced by *Scn8a*$^{dmu/dmu}$ mutant animals. I surmise that this substantial gene downregulation may be a contributing factor to the dysregulation of NF-L phosphorylation in Mut animals and suggest that the dysregulation of NF-L phosphorylation be investigated in future work to examine the neurofilamentous network in Mut animals when compared to WT counterparts.

Another supporting line of evidence that phosphorylation states may be responsible for disruptions in the neurofilament network of Mut animals comes from the exposure to light stimuli. I suggest that, at least in part, the presence and absence of light stimuli is responsible for some of the results obtained in the immunohistochemistry data observed between LR and DR animals. It is well documented that the action of Bdnf is responsive to light stimuli (Liang *et al*., 2000; Karpova *et al*., 2010; Chang *et al*., 2014). The Bdnf/TrkB complex triggers the activation of PLCγ signal transduction cascade (McCarty and Feinstein, 1999; Koponen *et al*., 2004; Cheng and Yeh, 2005) (Figure 4.2). One of the molecules that responds to the PLCγ signaling cascade is PKC that is responsible for phosphorylating NF-L head groups (Julien and Mushynski, 1998) (Figure 4.2). Therefore, light stimuli may be one of the regulators of NF-L head group phosphorylation through the action of PKC (Figure 4.2). Light stimuli have also been demonstrated to regulate the activity of dopamine receptors (Dubocovich *et al*., 1985; He *et al*., 2013) (Figure 4.2). Activation of dopamine receptors can induce Bdnf expression (Williams and Undieh, 2009), and Bdnf regulates the expression of dopamine receptors (Do *et al*., 2007), resulting in a cycle that promotes activation of downstream

Figure 4.2: An illustration depicting the signaling cascades that lead to neurofilament light-chain (NF-L) phosphorylation. On the left, Bdnf binds to its receptor TrkB, forming a complex that activates the PLCγ signaling cascade. One molecule that is responsive to the PLCγ signaling cascade is PKC. Active PKC is a protein kinase that is able to phosphorylate the head group of NF-L which prevents assembly into neurofilaments. On the right is the signaling molecule dopamine that is bound to the dopamine receptor complex. The binding of dopamine to its receptor complex then activates adenylyl cyclase which in turn activates cAMP. One of the responsive molecules down this signaling cascade is PKA. Active PKA is a protein kinase that is able to phosphorylate the head group of NF-L which prevents assembly into neurofilaments. Through the action of these pathways, the phosphorylation states of neurofilament monomers can be modulated, allowing the cell to assemble or disassemble neurofilaments as necessary in response to external stimuli. Figure drawn by L.W.G.Chu, 2016.

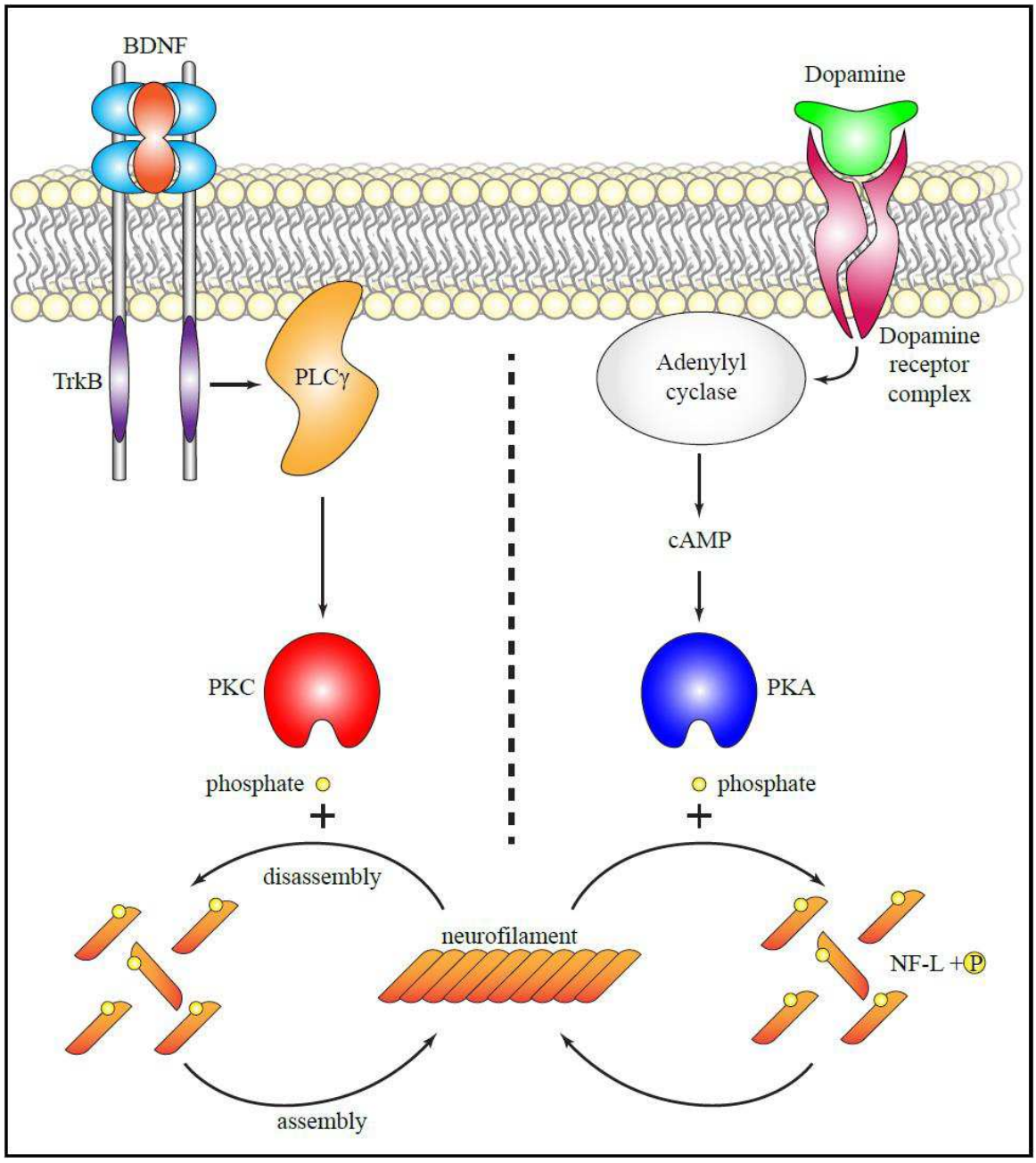
BDNF
Dopamine
TrkB
PLCγ
Adenylyl cyclase
Dopamine receptor complex
cAMP
PKC
PKA
phosphate
phosphate
disassembly
neurofilament
NF-L +P
assembly

mechanisms. Dopamine receptor activation in turn activates adenylyl cyclase which then goes on to activate PKA (Calabresi *et al*., 2014) (Figure 4.2). PKA is another known protein kinase responsible for phosphorylating NF-L head groups, specifically at the Ser55 position (Julien and Mushynski, 1998) (Figure 4.2). Therefore, light stimuli may also regulate NF-L head group phosphorylation through the action of the dopamine receptor and subsequent signaling pathway (Figure 4.2). Taken together, both dopamine receptors and Bdnf demonstrate responsiveness to light stimuli, therefore, phosphorylation states of NF-L may be modulated in the presence and absence of light in accordance with cellular needs. Results from DR animals would support the hypothesis that light stimulation and thus, phosphorylation states of NF-L are altered in mutant animals. DR animals display greater NF-L related accumulations and abnormalities compared to LR counterparts in the retina (Figures 3.13-3.16). Consequently, this NF-L accumulation pattern which was present in LR Mut was further exacerbated by the removal of light as evident in DR mutant comparisons.

4.5 Conclusion

An overall examination of the data gathered in this study has been reviewed together. My data suggest that *Scn8a*$^{dmu/dmu}$ mutant animals exhibit many of their phenotypical characteristics as a result of substantial downregulation of gene expression in the absence of functional $Na_v1.6$. This gene downregulation may in part be caused by a disruption in the neurofilament network within mutant animals, leaving neurons unable to properly interpret and respond to external signaling cues. Therefore, in the presence of a disrupted structural support network, gene expression is substantially downregulated in mutant animals. A further examination into the neurofilament network leads me to conclude that the dysregulation in phosphorylation states of NF-L may be responsible for the overall disruption to the neurofilament network. This disruption to the neurofilament network not only caused substantial downregulation in gene expression, it also resulted in temporal dysregulation of gene expression and NF-L protein expression within *Scn8a*$^{dmu/dmu}$ mutant animals, causing disarray to the natural maturation time table necessary for neuron pruning and maturation. However, in the presence of neurofilament disruption, this transport network is also interrupted, leaving cargo undelivered.

References

Ackerman, M.J., Siu, B.L., Sturner, W.Q., Tester, D.J., Valdivia, C.R., Makielski, J.C., Towbin, J.A. 2001. Postmortem molecular analysis of *SCN5A* defects in sudden infant death syndrome. *JAMA*. **286:** 2264-2269.

Adebola, A.A., Di Castri, T., He, C.Z., Salvatierra, L.A., Zhao, J., Brown, K., Lin, C.S., Worman, H.J., Liem, R.K. 2015. Neurofilament light polypeptide gene N98S mutation in mice leads to neurofilament network abnormalities and a Charcot-Marie-Tooth Type 2E phenotype. *Hum Mol Genet*. **24:** 2163-2174.

Afarid, M., Torabi-Nami, M., Zare, B. 2016. Neuroprotective and restorative effects of the brain-derived neurotrophic factor in retinal diseases. *J Neurol Sci*. **363:** 43-50.

Akai, J., Makita, N., Sakurada, H., Shirai, N., Ueda, K., Kitabatake, A., Nakazawa, K., Kimura, A., Hiraoka, M. 2000. A novel *SCN5A* mutation associated with idiopathic ventricular fibrillation without typical ECG findings of Brugada syndrome. *FEBS Lett*. **479:** 29-34.

Akerman, C.J., Smyth, D., Thompson, I.D. 2002. Visual experience before eye-opening and the development of the retinogeniculate pathway. *Neuron*. **36:** 869-879.

Akimov, N.P., Rentería, R.C. 2014. Dark rearing alters the normal development of spatiotemporal response properties but not of contrast detection threshold in mouse retinal ganglion cells. *Dev Neurobiol*. **74:** 692-706.

Akin, E.J., Solé, L., Dib-Hajj, S.D., Waxman, S.G., Tamkun, M.M. 2015. Preferential targeting of $Na_v1.6$ voltage-gated Na^+ channels to the axon initial segment during development. *PLoS One*. **10:**e0124397.

Al-Chalabi, A., Miller, C.C. 2003. Neurofilaments and neurological disease. *Bioessays*. **25:** 346-355.

Andavan, G.S., Lemmens-Gruber, R. 2011. Voltage-gated sodium channels: mutations, channelopathies and targets. *Curr Med Chem*. **18:** 377-397.

Arawaka, S., Machiya, Y., Kato, T. 2010. Heat shock proteins as suppressors of accumulation of toxic prefibrillar intermediates and misfolded proteins in neurodegenerative diseases. *Curr Pharm Biotechnol*. **11:** 158-166.

Arrasate, M., Finkbeiner, S. 2012. Protein aggregates in Huntington's disease. *Exp Neurol*. **238:** 1-11.

Astafurov, K., Dong, C.Q., Panagis, L., Kamthan, G., Ren, L., Rozenboym, A., Perera, T.D., Coplan, J.D., Danias, J. 2014. Complement expression in the retina is not influenced by short-term pressure elevation. *Mol Vis*. **20:** 140-152.

Audenaert, D., Claes, L., Ceulemans, B., Lofgren, A., Van Broeckhoven C., De Jonghe, P. 2003. A deletion in *SCN1B* is associated with febrile seizures and early-onset absence epilepsy. *Neurology*. **61:** 854-856.

Baines, R.A. 2003. Postsynaptic protein kinase A reduces neuronal excitability in response to increased synaptic excitation in the Drosophila CNS. *J Neurosci*. **23:** 8664-8672.

Barry, J., Gu, Y., Jukkola, P., O'Neill, B., Gu, H., Mohler, P.J., Rajamani, K.T., Gu, C. 2014. Ankyrin-G directly binds to kinesin-1 to transport voltage-gated Na^+ channels into axons. *Dev Cell*. **28:** 117-131.

Beck, K.A., Nelson, W.J. 1996. The spectrin-based membrane skeleton as a membrane protein-sorting machine. *Am J Physiol*. **270(5 Pt 1):** C1263-1270.

Bendahhou, S., Cummins, T.R., Griggs, R.C., Fu, Y.H., Ptacek, L.J. 2001. Sodium channel inactivation defects are associated with acetazolamide-exacerbated hypokalemic periodic paralysis. *Ann Neurol*. **50:** 417-420.

Bennett, P.B., Yazawa, K., Makita, N., George, A.L.Jr. 1995. Molecular mechanism for an inherited cardiac arrhythmia. *Nature*. **376:** 683-685.

Bennett, V., Baines, A.J. 2001. Spectrin and ankyrin-based pathways: metazoan inventions for integrating cells into tissues. *Physiol Rev*. **81:** 1353-1392.

Benson, D.W., Wang, D.W., Dyment, M., Knilans, T.K., Fish, F.A., Strieper, M.J., Rhodes, T.H., George, A.L.Jr. 2003. Congenital sick sinus syndrome caused by recessive mutations in the cardiac sodium channel gene (*SCN5A*). *J Clin Invest*. **112:** 1019-1028.

Berkovic, S.F., Heron, S.E., Giordano, L., Marini, C., Guerrini, R., Kaplan, R.E., Gambardella, A., Steinlein, O.K., Grinton, B.E., Dean, J.T., Bordo, L., Hodgson, B.L., Yamamoto, T., Mulley, J.C., Zara, F., Scheffer, I.E. 2004. Benign familial neonatal-infantile seizures: characterization of a new sodium channelopathy. *Ann Neurol*. **55:** 550-557.

Bezzina, C., Veldkamp, M.W., van Den Berg, M.P., Postma, A.V., Rook, M.B., Viersma, J.W., van Langen, I.M., Tan-Sindhunata, G., Bink-Boelkens, M.T., van Der Hout, A.H., Mannens, M.M., Wilde, A.A. 1999. A single Na^+ channel mutation causing both long QT and Brugada syndromes. *Circ Res*. **85:** 1206-1213.

Blackshaw, S., Harpavat, S., Trimarchi, J., Cai, L., Huang, H., Kuo, W.P., Weber, G., Lee, K., Fraioli, R.E., Cho, S.H., Yung, R., Asch, E., Ohno-Machado, L., Wong, W.H., Cepko, C.L. 2004. Genomic analysis of mouse retinal development. *PLoS Biol*. **2:**e247.

Blanchard, M.G., Willemsen, M.H., Walker, J.B., Dib-Hajj, S.D., Waxman, S.G., Jongmans, M.C., Kleefstra, T., van de Warrenburg, B.P., Praamstra, P., Nicolai, J., Yntema, H.G., Bindels, R.J., Meisler, M.H., Kamsteeg, E.J. 2015. *De novo* gain-of-function and loss-of-function mutations of *SCN8A* in patients with intellectual disabilities and epilepsy. *J Med Genet*. **52:** 330-337.

Bloom, G.S., Vallee, R.B. 1983. Association of microtubule-associated protein 2 (MAP 2) with microtubules and intermediate filaments in cultured brain cells. *J Cell Biol*. **96:** 1523-1531.

Boiko, T., Rasband, M.N., Levinson, S.R., Caldwell, J.H., Mandel, G., Trimmer, J.S., Matthews, G. 2001. Compact myelin dictates the differential targeting of two sodium channel isoforms in the same axon. *Neuron*. **30:** 91-104.

Boiko, T., Van Wart, A., Caldwell, J.H., Levinson, S.R., Trimmer, J.S., Matthews, G. 2003. Functional specialization of the axon initial segment by isoform-specific sodium channel targeting. *J Neurosci*. **23:** 2306-2313.

Bourges, J.L., Bloquel, C., Thomas, A., Froussart, F., Bochot, A., Azan, F., Gurny, R., BenEzra, D., Behar-Cohen, F. 2006. Intraocular implants for extended drug delivery: therapeutic applications. *Adv Drug Deliv*. **58:** 1182-1202.

Brackenbury, W.J., Isom, L.L. 2011. Na channel β subunits: overachievers of the ion channel family. *Front Pharmacol*. **2:** 53.

Brenner, M. 2014. Role of GFAP in CNS injuries. *Neurosci Lett*. **565:** 7-13.

Bringmann, A., Pannicke, T., Biedermann, B., Francke, M., Iandiev, I., Grosche, J., Wiedemann, P., Albrecht, J., Peichenbach, A. 2009b. Role of retinal glial cells in neurotransmitter uptake and metabolism. *Neurochem. Int*. **54:** 143-160.

Buchner, D.A., Seburn, K.L., Frankel, W.N., Meisler, M.H. 2004. Three ENU-induced neurological mutations in the pore loop of sodium channel *Scn8a* ($Na_v1.6$) and a genetically linked retinal mutation, *rd13*. *Mamm Genome*. **15:** 344-351.

Bulinski, J.C., McGraw, T.E., Gruber, D., Nguyen, H.L., Sheetz, M.P. 1997. Overexpression of MAP4 inhibits organelle motility and trafficking *in vivo*. *J Cell Sci*. **110:** 3055-3064.

Bulman, D.E., Scoggan, K.A., van Oene, M.D., Nicolle, M.W., Hahn, A.F., Tollar, L.L., Ebers, G.C. 1999. A novel sodium channel mutation in a family with hypokalemic periodic paralysis. *Neurology*. **53:** 1932-1936.

Burgess, D.L., Kohrman, D.C., Galt, J., Plummer, N.W., Jones, J.M., Spear, B., Meisler, M.H. (1995). Mutation of a new sodium channel gene, *Scn8a*, in the mouse mutant 'motor endplate disease'. *Nat Genet*. **10:** 461-465.

Calabresi, P., Picconi, B., Tozzi, A., Ghiglieri, V., Di Filippo, M. 2014. Direct and indirect pathways of basal ganglia: a critical reappraisal. *Nat Neurosci*. **17:** 1022-1030.

Caldwell, J.H. 2000. Clustering of sodium channels at the neuromuscular junction. *Microsc Res Tech*. **49:** 84-89.

Caldwell, J.H., Schaller, K.L., Lasher, R.S., Peles, E., Levinson, S.R. 2000. Sodium channel $Na_v1.6$ is localized at nodes of Ranvier, dendrites, and synapses. *Proc Natl Acad Sci USA*. **97:** 5616-5620.

Cannon, S.C., Strittmatter, S.M. 1993. Functional expression of sodium channel mutations identified in families with periodic paralysis. *Neuron*. **10:** 317-326.

Cannon, S.C. 1996. Ion-channel defects and aberrant excitability in myotonia and periodic paralysis. *Trends Neurosci*. **19:** 3-10.

Cannon, S.C. 1997. From mutation to myotonia in sodium channel disorders. *Neuromuscul Disord*. **7:** 241-249.

Cao, W., Wen, R., Li, F., LaVail, M.M., Steinberg, R.H. 1997. Mechanical injury increases bFGF and CNTF mRNA expression in the mouse retina. *Exp Eye Res*. **65:** 241-248.

Casula, M.A., Facer, P., Powell, A.J., Kinghorn, I.J., Plumpton, C., Tate, S.N., Bountra, C., Birch, R., Anand, P. 2004. Expression of the sodium channel beta3 subunit in injured human sensory neurons. *Neuroreport*. **15:** 1629-1632.

Catterall, W.A. 2000. From ionic currents to molecular mechanisms: the structure and function of voltage-gated sodium channels. *Neuron*. **26:** 13-25.

Catterall, W.A., Goldin, A.L., Waxman, S.G. 2005. International Union of Pharmacology. XLVII. Nomenclature and structure-function relationships of voltage-gated sodium channels. *Pharmacol. Rev*. **57:** 397-409.

Cepko, C.L., Austin, C.P., Yang, X., Alexiades, M., Ezzeddine, D. 1996. Cell fate determination in the vertebrate retina. *Proc. Natl. Acad. Sci. USA*. **93:** 589-595.

Chahine, M., George, A.L.Jr., Zhou, M., Ji, S., Sun, W., Barchi, R.L., Horn, R. 1994. Sodium channel mutations in paramyotonia congenita uncouple inactivation from activation. *Neuron*. **12:** 281-294.

Chambers, J.C., Zhao, J., Terracciano, C.M., Bezzina, C.R., Zhang, W., Kaba, R., Navaratnarajah, M., Lotikar, A., Sehmi, J.S., Kooner, M.K., Deng, G., Siedlecka, U., Parasramka, S., El-Hamamsy, I., Wass, M.N., Dekker, L.R., de Jong, J.S., Sternberg, M.J., McKenna, W., Severs, N.J., de Silva, R., Wilde, A.A., Anand, P., Yacoub, M., Scott, J., Elliott, P., Wood, J.N., Kooner, J.S. 2010. Genetic variation in *SCN10A* influences cardiac conduction. *Nat Genet*. **42:** 149-152.

Chang, L., Goldman, R.D. 2004. Intermediate filaments mediate cytoskeletal crosstalk. *Nat Rev Mol Cell Biol*. **5:** 601-613.

Chang, K.Y., Woo, D., Jung, H., Lee, S., Kim, S., Won, J., Kyung, T., Park, H., Kim, N., Yang, H.W., Park, J.Y., Hwang, E.M., Kim, D., Heo, W.D. 2014. Light-inducible receptor tyrosine kinases that regulate neurotrophin signalling. *Nat Commun*. **5:** 4057.

Chen, Q., Kirsch, G.E., Zhang, D., Brugada, R., Brugada, J., Brugada, P., Potenza, D., Moya, A., Borggrefe, M., Breithardt, G., Ortiz-Lopez, R., Wang, Z., Antzelevitch, C., O'Brien, R.E., Schulze-Bahr, E., Keating, M.T., Towbin, J.A., Wang, Q. 1998. Genetic basis and molecular mechanism for idiopathic ventricular fibrillation. *Nature*. **392:** 293-296.

Chen, K., Sprunger, L.K., Meisler, M.H., Waller, H.J., Godfrey, D.A. 1999. Reduced spontaneous activity in the dorsal cochlear nucleus of *Scn8a* mutant mice. *Brain Res*. **847:** 85-89.

Chen, C., Westenbroek, R.E., Xu, X., Edwards, C.A., Sorenson, D.R., Chen, Y., McEwen, D.P., O'Malley, H.A., Bharucha, V., Meadows, L.S., Knudsen, G.A., Vilaythong, A., Noebels, J.L., Saunders, T.L., Scheuer, T., Shrager, P., Catterall, W.A., Isom, L.L. 2004. Mice lacking sodium channel beta1 subunits display defects in neuronal excitability, sodium channel expression, and nodal architecture. *J Neurosci*. **24:** 4030-4042.

Cheng, Q., Yeh, H.H. 2005. PLCγ signaling underlies BDNF potentiation of Purkinje cell responses to GABA. *J Neurosci Res*. **79:** 616-627.

Chiba, K., Araseki, M., Nozawa, K., Furukori, K., Araki, Y., Matsushima, T., Nakaya, T., Hata, S., Saito, Y., Uchida, S., Okada, Y., Nairn, A.C., Davis, R.J., Yamamoto, T., Kinjo, M., Taru, H., Suzuki, T. 2014.

Côté, P.D., De Repentigny, Y., Coupland, S.G., Schwab, Y., Roux, M.J., Levinson, S.R., Kothary, R. 2005. Physiological maturation of photoreceptors depends on the voltage-gated sodium channel $Na_v1.6$ (*Scn8a*). *J. Neurosci*. **25:** 5046-5050.

Coward, K., Jowett, A., Plumpton, C., Powell, A., Birch, R., Tate, S., Bountra, C., Anand, P. 2001. Sodium channel β1 and β2 subunits parallel *SNS*/*PN3* α-subunit changes in injured human sensory neurons. *Neuroreport*. **12:** 483-488.

Cummins, T.R., Dib-Hajj, S.D., Waxman, S.G. 2004. Electrophysiological properties of mutant $Na_v1.7$ sodium channels in a painful inherited neuropathy. *J Neurosci*. **24:** 8232-8236.

Cusdin, F.S., Clare, J.J., Jackson, A.P. 2008. Trafficking and cellular distribution of voltage-gated sodium channels. *Traffic*. **9:** 17-26.

Dale, J.M., Garcia, M.L. 2012. Neurofilament phosphorylation during development and disease: which came first, the phosphorylation or the accumulation? *J Amino Acids*. **2012:** 382107.

Davis, T.H., Chen, C., Isom, L.L. 2004. Sodium channel β1 subunits promote neurite outgrowth in cerebellar granule neurons. *J Biol Chem.* **279:** 51424-51432.

De Jonghe, P., Mersivanova, I., Nelis, E., Del Favero, J., Martin, J.J., Van Broeckhoven, C., Evgrafov, O., Timmerman, V. 2001. Further evidence that neurofilament light chain gene mutations can cause Charcot-Marie-Tooth disease type 2E. *Ann Neurol.* **49:** 245-249.

de Kovel, C.G., Meisler, M.H., Brilstra, E.H., van Berkestijn, F.M., van 't Slot, R., van Lieshout, S., Nijman, I.J., O'Brien, J.E., Hammer, M.F., Estacion, M., Waxman, S.G., Dib-Hajj, S.D., Koeleman, B.P. 2014. Characterization of a *de novo SCN8A* mutation in a patient with epileptic encephalopathy. *Epilepsy Res*. **108:** 1511-1518.

De Repentigny, Y., Côté, P.D., Pool, M., Bernier, G., Girard, S., Vidal, S.M., Kothary, R. 2001. Pathological and genetic analysis of the degenerating muscle (*dmu*) mouse: a new allele of *Scn8a*. *Hum Mol Genet*. **10:** 1819-1827.

Desai, N.S., Rutherford, L.C., Turrigiano, G.G. 1999. Plasticity in the intrinsic excitability of cortical pyramidal neurons. *Nat Neurosci.* **2:** 515-520.

Dib-Hajj, S.D., Tyrrell, L., Black, J.A., Waxman, S.G. 1998. NaN, a novel voltage-gated Na channel, is expressed preferentially in peripheral sensory neurons and down-regulated after axotomy. *Proc Natl Acad Sci. USA*. **95:** 8963-8968.

Dib-Hajj, S.D., Rush, A.M., Cummins, T.R., Hisama, F.M., Novella, S., Tyrrell, L., Marshall, L., Waxman, S.G. 2005. Gin-of-function mutation in $Na_v1.7$ in familial erythromelalgia induces bursting of sensory neurons. *Brain.* **128:** 1847-1854.

Dichgans, M., Freilinger, T., Eckstein, G., Babini, E., Lorenz-Depiereux, B., Biskup, S., Ferrari, M.D., Herzog, J., van den Maagdenberg, A.M., Pusch, M., Strom, T.M. 2005. Mutation in the neuronal voltage-gated sodium channel *SCN1A* in familial hemiplegic migraine. *Lancet.* **366:** 371-377.

Do, T., Kerr, B., Kuzhikandathil, E.V. 2007. Brain-derived neurotrophic factor regulates the expression of D1 dopamine receptors. *J Neurochem.* **100:** 416-428.

Domingo, A.M., Kaku, T., Tester, D.J., Torres, P.I., Itty, A., Ye, B., Valdivia, C.R., Makielski, J.C., Quintero, S.C., Luna, T.T., Ackerman, M.J. 2006. Sodium channel β4 subunit mutation causes congenital long QT syndrome. *Heart Rhythm.* **3:** S34.

Dowling, J.E. 2012. *The retina: an approachable part of the brain*. Belknap Press of Harvard University Press. 2nd edition.

Driscoll, H.E., Muraro, N.I., He, M., Baines, R.A. 2013. Pumilio-2 regulates translation of $Na_v1.6$ to mediate homeostasis of membrane excitability. *J Neurosci.* **33:** 9644-9654.

Dubocovich, M.L., Lucas, R.C., Takahashi, J.S. 1985. Light-dependent regulation of dopamine receptors in mammalian retina. *Brain Res*. **335:** 321-325.

Duchen, L.W., Searle, A.G., Strich, S.J. 1967. An hereditary motor end-plate disease in the mouse. *J Physiol*. **189:** 4-6.

Duchen, L.W. 1970. Hereditary motor end-plate disease in the mouse: light and electron microscopic studies. *J Neurol Neurosurg Psychiatry*. **33:** 238-250.

Dutta, R., McDonough, J., Chang, A., Swamy, L., Siu, A., Kidd, G.J., Rudick, R., Mirnics, K., Trapp, B.D. 2007. Activation of the ciliary neurotrophic factor (CNTF) signalling pathway in cortical neurons of multiple sclerosis patients. *Brain*. **130(Pt 10):** 2566-2576.

Dyer, M.A., Cepko, C.L. 2001. Regulating proliferation during retinal development. *Nat Rev Neurosci*. **2:** 333-342.

Ebneth, A., Godemann, R., Stamer, K., Illenberger, S., Trinczek, B., Mandelkow, E. 1998. Overexpression of tau protein inhibits kinesin-dependent trafficking of vesicles, mitochondria, and endoplasmic reticulum: implications for Alzheimer's disease. *J Cell Biol*. **143:** 777-794.

Ehlers, M.D. 2003. Activity level controls postsynaptic composition and signaling via the ubiquitin-proteasome system. *Nat Neurosci*. **6:** 231-242.

Erickson, P.A., Feinstein, S.C., Lewin, G.P., Fisher, S.K. 1992. Glial fibrillary acidic protein and its mRNA: ultrastructural detection and determination of changes after CNS injury. *J Struct Biol*. **108:** 148-161.

Erickson, J.N., Spana, E.P. 2006. Mapping Drosophila genomic aberration breakpoints with comparative genome hybridization on microarrays. *Methods Enzymol*. **410:** 377-386.

Escayg, A., MacDonald, B.T., Meisler, M.H., Baulac, S., Huberfeld, G., An-Gourfinkel, I., Brice, A., LeGuern, E., Moulard, B., Chaigne, D., Buresi, C., Malafoss, A. 2000. Mutations of *SCN1A*, encoding a neuronal sodium channel, in two families with GEFS+2. *Nat Genet*. **24:** 343-345.

Fein, A.J., Meadows, L.S., Chen, C., Slat, E.A., Ison, L.L. 2007. Cloning and expression of a zebrafish SCN1B ortholog and identification of a species-specific slice variant. *BMC Genomics*. **8:** 226.

Felix, R. 2000. Channelopathies: ion channel defects linked to heritable clinical disorders. *J Med Genet*. **37:** 729-740.

Fiore, R., Khudayberdiev, S., Christensen, M., Siegel, G., Flavell, S.W., Kim, T.K., Greenberg, M.E., Schratt, G. 2009. Mef2-mediated transcription of the miR379-410 cluster regulates activity-dependent dendritogenesis by fine-tuning Pumilio2 protein levels. *EMBO J*. **28:** 697-710.

Fjell, J., Dib-Hajj, S., Fried, K., Black, J.A., Waxman, S.G. 1997. Differential expression of sodium channel genes in retinal ganglion cells. *Brain Res Mol Brain Res*. **50:** 197-204.

Flannery, J.G. 1999. Transgenic animal models for the study of inherited retinal dystrophies. *ILAR J*. **40:** 51-58.

Fletcher, E.L., Jobling, A.I. Vessey, K.A., Luu, C., Guymer, R.H., Baird, P.N. 2011. Animal models of retinal disease. *Prog Mol Biol Transl Sci*. **100:** 211-286.

Fontaine, B., Khurana, T.S., Hoffman, E.P., Bruns, G.A., Haines, J.L., Trofatter, J.A., Hanson, M.P., Rich, J., McFarlane, H., Yasek, D.M., Romano, D., Gusella, J.F., Brown, R.H. Jr. 1990. Hyperkalemic periodic paralysis and the adult muscle sodium channel α-subunit gene. *Science*. **250:** 1000-1002.

Franze, K., Grosche, J., Skatchkov, S.N., Schinkinger, S., Foja, C., Schild, D., Uckermann, O., Travis, K., Reichenbach, A., Guck, J. 2007. Müller cells are living optical fibers in the vertebrate retina. *Proc Natl Acad Sci USA*. **104:** 8287-8292.

Fu, Q.L., Li, X., Yip, H.K., Shao, Z., Wu, W., Mi, S., So, K.F. 2009. Combined effect of brain-derived neurotrophic factor and LINGO-1 fusion protein on long-term survival of retinal ganglion cells in chronic glaucoma. *Neuroscience*. **162:** 375-382.

Fu, M.M., Holzbaur, E.L. 2013. JIP1 regulates the directionality of APP axonal transport by coordinating kinesin and dynein motors. *J Cell Biol*. **202:** 495-508.

Fuchs, E., Cleveland, D.W. 1998. A structural scaffolding of intermediate filaments in health and disease. *Science*. **279:** 514-519.

Fujiwara, T., Sugawara, T., Mazaki-Miyazaki, E., Takahashi, Y., Fukushima, K., Watanabe, M., Hara, K., Morikawa, T., Yagi, K., Yamakawa, K., Inoue, Y. 2003. Mutations of sodium channel α subunit type 1 (*SCN1A*) in intractable childhood epilepsies with frequent generalized tonic-clonic seizures. *Brain*. **126(Pt 3):** 531-546.

Fukuma, G., Oguni, H., Shirasaka, Y., Watanabe, K., Miyajima, T., Yasumoto, S., Ohfu, M., Inoue, T., Watanachai, A., Kira, R., Matsuo, M., Muranaka, H., Sofue, F., Zhang, B., Kaneko, S., Mitsudome, A., Hirose, S. 2004. Mutations of neuronal voltage-gated Na^+ channel α1 subunit gene *SCN1A* in core severe myoclonic epilepsy in infancy (SMEI) and in borderline SMEI (SMEB). *Epilepsia*. **45:** 140-148.

Gadad, B.S., Britton, G.B., Rao, K.S. 2011. Targeting oligomers in neurodegenerative disorders: lessons from α-synuclein, tau, and amyloid-β peptide. *J Alzheimers Dis*. **24 Suppl 2:** 223-232.

Gardiner, J., Overall, R., Marc, J. 2013. The nervous system cytoskeleton under oxidative stress. *Diseases*. **1:** 36-50.

Gastaldi, M., Bartolomei, F., Massacrier, A., Planells, R., Robaglia-Schlupp, A., Cau, P. 1997. Increase in mRNAs encoding neonatal II and III sodium channel α-isoforms during kainate-induced seizures in adult rat hippocampus. *Brain Res Mol Brain Res*. **44:** 179-190.

George, A.L.Jr., Knittle, T.J., Tamkun, M.M. 1992. Molecular cloning of an atypical voltage-gated sodium channel expressed in human heart and uterus: evidence for a distinct gene family. *Proc Natl Acad Sci USA*. **89:** 4893-4897.

George, A.L.Jr. 2005. Inherited disorders of voltage-gated sodium channels. *J Clin Invest*. **115:** 1990-1999.

Goldin, A.L., Barchi, R.L., Caldwell, J.H., Hofmann, F., Howe, J.R., Hunter, J.C., Kallen, R.G., Mandel, G., Meisler, M.H., Netter, Y.B., Noda, M., Tamkun, M.M., Waxman, S.G., Wood, J.N., Catterall, W.A. 2000. Nomenclature of voltage-gated sodium channels. *Neuron*. **28:** 365-368.

Gomes, F.C., Paulin, D., Moura Neto, V. 1999. Glial fibrillary acidic protein (GFAP): modulation by growth factors and its implication in astrocyte differentiation. *Braz J Med Biol Res*. **32:** 619-631.

Gorter, J.A., Zurolo, E., Lyer, A., Fluiter, K., van Vliet E.A., Baayen, J.C., Aronica, E. 2010. Induction of sodium channel Na_x (*SCN7A*) expression in rat and human hippocampus in temporal lobe epilepsy. *Epilepsia*. **51:** 1791-1800.

Groemer, T.W., Thiel, C.S., Holt, M., Riedel, D., Hua, Y, Hüve, J., Wilhelm, B.G., Klingauf, J. 2011. Amyloid Precursor Protein is Trafficked and Secreted via Synaptic Vesicles. *PLoS One*. **6:**e18754.

Groenewegen, W.A., Firouzi, M., Bezzina, C.R., Vliex, S., van Langen, I.M., Sandkuijl, L., Smits, J.P., Hulsbeek, M., Rook, M.B., Jongsma, H.J., Wilde, A.A. 2003. A cardiac sodium channel mutation cosegregates with a rare connexin40 genotype in familial atrial standstill. *Circ Res*. **92:** 14-22.

Gupta, V., You, Y., Li, J., Gupta, V., Golzan, M., Klistorner, A., van den Buuse, M., Graham, S. 2014. BDNF impairment is associated with age-related changes in the inner retina and exacerbates experimental glaucoma. *Biochim Biophys Acta*. **1842:** 1567-1578.

Gyoeva, F.K., Gelfand, V.I. 1991. Coalignment of vimentin intermediate filaments with microtubules depends on kinesin. *Nature*. **353:** 445-448.

Hains, B.C., Klein, J.P., Saab, C.Y., Craner, M.J., Black, J.A., Waxman, S.G. 2003. Upregulation of sodium channel $Na_v1.3$ and functional involvement in neuronal hyperexcitability associated with central neuropathic pain after spinal cord injury. *J Neurosci*. **23:** 8881-8892.

Hamann, M., Meisler, M.H., Richter, A. 2003. Motor disturbances in mice with deficiency of the sodium channel gene *Scn8a* show features of human dystonia. *Exp Neurol*. **184:** 830-838.

Harada, T., Harada, C., Kohsaka, S., Wada, E., Yoshida, K., Ohno, S., Mamada, H., Tanaka, K., Parada, L.F., Wada, K. 2002. Microglia-Müller glia cell interactions control neurotrophic factor production during light-induced retina degeneration. *J Neurosci*. **22:** 9228-9236.

He, Q., Wang, P., Tian, N. 2011. Light-evoked synaptic activity of retinal ganglion and amacrine cells is regulated in developing mouse retina. *Eur J Neurosci*. **33:** 36-48.

Heidemann, S.R. 1996. Cytoplasmic mechanisms of axonal and dendritic growth in neurons. *Int Rev Cytol*. **165:** 235-296.

Helfand, B.T., Mikami, A., Vallee, R.B., Goldman, R.D. 2002. A requirement for cytoplasmic dynein and dynactin in intermediate filament network assembly and organization. *J Cell Biol*. **157:** 795-806.

Helfand, B.T., Loomis, P., Yoon, M., Goldman, R.D. 2003. Rapid transport of neural intermediate filament protein. *J Cell Sci*. **116:** 2345-2359.

Heron, S.E., Crossland, K.M., Andermann, E., Phillips, H.A., Hall, A.J., Bleasel, A., Shevell, M., Mercho, S., Seni, M.H., Guiot, M.C., Mulley, J.C., Berkovic, S.F., Scheffer, I.E. 2002. Sodium-channel defects in benign familial neonatal-infantile seizures. *Lancet*. **360:** 851-852.

Herrmann, H., Bär, H., Kreplak, L., Strelkov, S.V., Aebi, U. 2007. Intermediate filaments: from cell architecture to nanomechanics. *Nat Rev Mol Cell Biol*. **8:** 562-573.

Hirokawa, N., Takemura, R. 2004. Molecular motors in neuronal development, intracellular transport and diseases. *Curr Opin Neurobiol*. **14:** 564-573.

Hirokawa, N., Niwa, S., Tanaka, Y. 2010. Molecular motors in neurons: transport mechanisms and roles in brain function, development, and disease. *Neuron*. **68:** 610-638.

Hitt, A.L., Luna, E.J. 1994. Membrane interactions with the actin cytoskeleton. *Curr Opin Cell Biol*. **6:** 120-130.

Hiyama, T.Y., Watanabe, E., Ono, K. Inenaga, K., Tamkun, M.M., Yoshida, S., Noda, M. 2002. Na_x channel involved in CNS sodium-level sensing. *Nat Neurosci*. **5:** 511-512.

Hol, E.M., Pekny, M. 2015. Glial fibrillary acidic protein (GFAP) and the astrocyte intermediate filament system in diseases of the central nervous system. *Curr Opin Cell Biol*. **32:** 121-130.

How to time mouse pregnancy. (2006). Retrived from http:\\www.jax.org\news-and-insights\2006\april\how-to-time-mouse-pregnancy#

Hrytsenko, O., Wright, J.R. Jr., Morrison, C.M., Pohajdak, B. 2007. Insulin expression in the brain and pituitary cells of tilapia (*Oreochromis niloticus*). *Brain Res*. **1135:** 31-40.

Huang, E.J., Reichardt, L.F. 2003. Trk receptors: roles in neuronal signal transduction. *Annu Rev Biochem*. **72:** 609-642.

Irvine, G.B., El-Agnaf, O.M., Shankar, G.M., Walsh, D.M. 2008. Protein aggregation in the brain: the molecular basis for Alzheimer's and Parkinson's diseases. *Mol Med*. **14:** 451-464.

Isom, L.L., De Jongh, K.S., Patton, D.E., Reber, B.F.X., Offord, J., Charbonneau, H., Walsh, K., Goldin, A.L., Catterall, W.A. 1992. Primary structure and functional expression of the β1 subunit of the rat brain sodium channel. *Science*. **256:** 839-842.

Isom, L.L., Scheuer, T., Brownstein, A.B., Ragsdale, D.S., Murphy, B.J., Catterall, W.A. 1995. Functional co-expression of the beta 1 and type IIA alpha subunits of sodium channels in a mammalian cell line. *J Biol Chem*. **270:** 3306-3312.

Iuvone, P.M., Boatright, J.H., Tosini, G., Ye, K. 2014. N-acetylserotonin: circadian activation of the BDNF receptor and neuroprotection in the retina and brain. *Adv Exp Med Biol*. **801:** 765-771.

Janmey, P.A. 1998. The cytoskeleton and cell signaling: component localization and mechanical coupling. *Physiol. Rev*. **78:** 763-781.

Jenkins, S.M., Bennett, V. 2001. Ankyrin-G coordinates assembly of the spectrin-based membrane skeleton, voltage-gated sodium channels, and L1 CAMs at Purkinje neuron initial segments. *J Cell Biol*. **155:** 739-746.

Jones, J.M., Dionne, L., Dell'Orco, J., Parent, R., Krueger, J.N., Cheng, X., Dib-Hajj, S.D., Bunton-Stasyshyn, R.K., Sharkey, L.M., Dowling, J.J., Murphy, G.G., Shakkottai, V.G., Shrager, P., Meisler, M.H. 2016. Single amino acid deletion in transmembrane segment D4S6 of sodium channel *Scn8a* ($Na_v1.6$) in a mouse mutant with a chronic movement disorder. *Neurobiol. Dis*. **89:** 36-45.

Julien, J.P., Mushynski, W.E. 1998. Neurofilaments in health and disease. *Prog Nucleic Acid Res Mol Biol*. **61:** 1-23.

Julien, J.P. 1999. Neurofilaments function in health and disease. *Curr Opin Neurobiol*. **9:** 554-560.

Jurkat-Rott, K., Mitrović, N., Hang, C., Kouzmenkine, A., Iaizzo, P., Herzog, J., Lerche, H., Nicole, S., Vale-Santos, J., Chauveau, D., Fontaine, B., Lehmann-Horn, F. 2000. Voltage-sensor sodium channel mutations cause hypokalemic periodic paralysis type 2 enhanced inactivation and reduced current. *Proc Natl Acad Sci USA*. **97:** 9549-9554.

Kalil, R.E., Dubin, M.W., Scott, G., Stark, L.A. 1986. Elimination of action potentials blocks the structural development of retinogeniculate synapses. *Nature*. **323:** 156-158.

Kamiya, K., Kaneda, M., Sugawara, T., Mazaki, E., Okamura, N., Montal, M., Makita, N., Tanaka, M., Fukushima, K., Fujiwara, T., Inoue, Y., Yamakawa, K. 2004. A nonsense mutation of the sodium channel gene *SCN2A* in a patient with intractable epilepsy and mental decline. *J Neurosci*. **24:** 2690-2698.

Kanai, K., Hirose, S., Oguni, H., Fukuma, G., Shirasaka, Y., Miyajima, T., Wada, K., Iwasa, H., Yasumoto, S., Matsuo, M., Ito, M., Mitsudome, A., Kaneko, S. 2004. Effect of localization of missense mutations in *SCN1A* on epilepsy phenotype severity. *Neurology*. **63:** 329-334.

Karpova, N.N., Rantamäki, T., Di Lieto, A., Lindemann, L., Hoener, M.C., Castrén, E. 2010. Darkness reduces BDNF expression in the visual cortex and induces repressive chromatin remodeling at the BDNF gene in both hippocampus and visual cortex. *Cell Mol Neurobiol*. **30:** 1117-1123.

Kearney, J.A., Buchner, D.A., De Haan, G., Adamska, M., Levin, S.I., Furay, A.R., Albin, R.L., Jones, J.M., Montal, M., Stevens, M.J., Springer, L.K., Meisler, M.H. 2002. Molecular and pathological effects of a modifier gene on deficiency of the sodium channel *Scn8a* ($Na_v1.6$). *Hum Mol Genet*. **11:** 2765-2775.

Khaliq, Z.M., Gouwens, N.W., Raman, I.M. 2003. The contribution of resurgent sodium current to high-frequency firing in Purkinje neurons: an experimental and modeling study. *J Neurosci*. **23:** 4899-4912.

Khudayberdiev, S., Fiore, R., Schratt, G. 2009. MicroRNA as modulators of neuronal responses. *Commun Integr Biol*. **2:** 411-413.

Kim, S., Coulombe, P.A. 2007. Intermediate filament scaffolds fulfill mechanical, organizational, and signaling functions in the cytoplasm. *Genes Dev*. **21:** 1581-1597.

Kohrman, D.C., Plummer, N.W., Schuster, T., Jones, J.M., Jang, W., Burgess, D.L., Galt, J., Spear, B.T., Meisler, M.H. 1995. Insertional mutation of the *motor endplate disease* (*med*) locus on mouse chromosome 15. *Genomics*. **26:** 171-177.

Kohrman, D.C., Harris, J.B., Meisler, M.H. 1996. Mutation detection in the *med* and *med*^{J} alleles of the sodium channel *Scn8a*. Unusual splicing due to a minor class AT-AC intron. *J Biol Chem*. **271:** 17576-17581.

Kohrman, D.C., Smith, M.R., Goldin, A.L., Harris, J., Meisler, M.H. 1996b. A missense mutation in the sodium channel *SCN8A* is responsible for cerebellar ataxia in the mouse mutant *jolting*. *J Neurosci*. **16:** 5993-5999.

Koopmann, T.T., Bezzina, C.R., Wilde, A.A. 2006. Voltage-gated sodium channels: action players with many faces. *Ann Med*. **38:** 472-482.

Koponen, E., Võikar, V., Riekki, R., Saarelainen, T., Rauramaa, T., Rauvala, H., Taira, T., Castrén, E. 2004. Transgenic mice overexpressing the full-length neurotrophin receptor TrkB exhibit increased activation of the TrkB-PLCγ pathway, reduced anxiety, and facilitated learning. *Mol Cell Neurosci.* **26:** 166-181.

Kordeli, E., Lambert, S., Bennett, V. 1995. $Ankyrin_G$. A new ankyrin gene with neural-specific isoforms localized at the axonal initial segment and node of Ranvier. *J Biol Chem.* **270:** 2352-2359.

Krzemien, D.M., Schaller, K.L., Levinson, S.R., Caldwell, J.H. 2000. Immunolocalization of sodium channel isoform NaCh6 in the nervous system. *J Comp Neurol.* **420:** 70-83.

Kuzmenkin, A., Muncan, V., Jurkat-Rott, K., Hang, C., Lerche, H., Lehmann-Horn, F., Mitrović, N. 2002. Enhanced inactivation and pH sensitivity of Na^+ channel mutations causing hypokalaemic periodic paralysis type II. *Brain.* **125(Pt 4):** 835-843.

Lai, J., Gold, M.S., Kim, C.S., Bian, D., Ossipoy, M.H., Hunter, J.C., Porreca, F. 2002. Inhibition of neuropathic pain by deceased expression of the tetrodotoxin-resistant sodium channel, $Na_v1.8$. *Pain.* **95:** 143-152.

Lampert, A., O'Reilly, A.O., Reeh, P., Leffler, A. 2010. Sodium channelopathies and pain. *Pflugers Arch.* **460:** 249-263.

Larionov, A., Krause, A., Miller, W. 2005. A standard cure based method for relative real time PCR data processing. *BMC Bioinformatics*. **6:** 62.

Larson, J., Carvil, G.L., Gardella, E., Kluger, G., Schmiedel, G., Barisic, N., Depienne, C., Brilstra, E., Mang, Y., Nielsen, J.E., Kirkpatrick, M., Goudie, D., Goldman, R., Jähn, J.A., Jepsen, B., Gill, D., Döcker, M., Biskup, S., McMahon, J.M., Koeleman, B., Harris, M., Braun, K., de Kovel, C.G., Marini, C., Specchio, N., Djémié, T., Weckhuysen, S., Tommerup, N., Troncoso, M., Troncoso, L., Bevot, A., Wolff, M., Hjalgrim, H., Guerrini, R., Scheffer, I.E., Mefford, H.C., Møller, R.S., EuroEPINOMICS RES Consortium CRP. 2015. The phenotypic spectrum of *SCN8A* encephalopathy. *Neurology.* **84:** 480-489.

LaVail, M.M., Unoki, K., Yasumura, D., Matthes, M.T., Yancopoulos, G.D., Steinberg, R.H. 1992. Multiple growth factors, cytokines, and neurotrophins rescue photoreceptors from the damaging effects of constant light. *Proc. Natl. Acad. Sci. USA*. **89:** 11249-11253.

LaVail, M.M., Yasumura, D., Matthes, M.T., Lau-Villacorta, C., Unoki, K., Sung, C.H., Steinberg, R.H. 1998. Protection of mouse photoreceptors by survival factors in retinal degenerations. *Invest Ophthalmol Vis*. **39:** 592-602.

Lee, M.K., Cleveland, D.W. 1996. Neuronal intermediate filaments. *Annu Rev Neurosci.* **19:** 187-217.

Lerche, H., Heine, R., Pika, U., George, A.L.Jr., Mitrović, N., Browatzki, M., Weiss, T., Rivet-Bastide, M., Franke, C., Lomonaco, M., Ricker, K., Lehmann-Horn, F. 1993. Human sodium channel myotonia: slowed channel inactivation due to substitutions for a glycine within the III-IV linker. *J Physiol.* **470:** 13-22.

Lewis, G.P., Fisher, S.K. 2003. Up-regulation of glial fibrillary acidic protein in response to retinal injury: its potential role in glial remodeling and a comparison to vimentin expression. *Int Rev Cytol.* **230:** 263-290.

Li, Y., Tao, W., Luo, L., Huang, D., Kauper, K., Stabila, P., LaVail, M.M., Laties, A.M., Wen, R. 2010. CNTF induces regeneration of cone outer segments in a rat model of retinal degeneration. *PLoS One.* **5:**e9495.

Liang, F.Q., Allen, G., Earnest, D. 2000. Role of brain-derived neurotrophic factor in the circadian regulation of the suprachiasmatic pacemaker by light. *J Neurosci.* **20:** 2978-2987.

Liu, W., Saint, D.A. 2002. Validation of a quantitative method for real time PCR kinetics. *Biochem Biophys Res Commun.* **294:** 347-353.

Liu, C., Tan, F.C.K., Xiao, Z.C., Dawe, G.S. 2015. Amyloid Precursor Protein enhances $Na_v1.6$ sodium channel cell surface expression. *J Biol Chem.* **290:** 12048-12057.

Livesey, F.J., Cepko, C.L. 2001. Vertebrate neural cell-fate determination: lessons from the retina. *Nat. Rev. Neurosci.* **2:** 109-118.

London, A., Benhar, I., Schwartz, M. 2013. The retina as a window to the brain-from eye research to CNS disorders. *Nat Rev Neurol.* **9:** 44-53.

Lopez-Santiago, L.F., Pertin, M., Morisod, X., Chen, C., Hong, S., Wiley, J., Decosterd, I., Isom, L.L. 2006. Sodium channel beta2 subunits regulate tetrodotoxin-sensitive sodium channels in small dorsal root ganglion neurons and modulate the response to pain. *J Neurosci.* **26:** 7984-7994.

Casula, M.A., Facer, P., Powell, A.J., Kinghorn, I.J., Plumpton, C., Tate, S.N., Bountra, C., Birch, R., Anand, P. 2004. Expression of the sodium channel beta3 subunit in injured human sensory neurons. *Neuroreport.* **15:** 1629-1632.

Lorincz, A., Nusser, Z. 2008. Cell-type-dependent molecular composition of the axon initial segment. *J Neurosci.* **28:** 14329-14340.

Lorincz, A., Nusser, Z. 2010. Molecular identity of dendritic voltage-gated sodium channels. *Science.* **328:** 906-909.

Lossin, C. 2009. A catalog of *SCN1A* variants. *Brain Dev.* **31:** 114-130.

Lundkvist, A., Reichenbach, A., Betsholtz, C., Carmeliet, P., Wolburg, H., Pekny, M. 2004. Under stress, the absence of intermediate filaments from Müller cells in the retina has structural and functional consequences. *J Cell Sci.* **117(Pt 16):** 3481-3488.

Mackenzie, F.E., Parker, A., Parkinson, N.J., Oliver, P.L., Brooker, D., Underhill, P., Lukashkina, V.A., Lukashkin, A.N., Holmes, C., Brown, S.D. 2009. Analysis of the mouse mutant *Cloth-ears* shows a role for the voltage-gated sodium channel *Scn8a* in peripheral neural hearing loss. *Genes Brain Behav*. **8:** 699-713.

Malhotra, J.D., Kazen-Gillespie, K., Hortsch, M., Isom, L.L. 2000. Sodium channel β subunits mediate homophilic cell adhesion and recruit ankyrin to points of cell-cell contact. *J Biol Chem*. **275:** 11383-11388.

Malhotra, J.D., Koopmann, M.C., Kazen-Gillespie, K.A., Fettman, N., Hortsch, M., Isom, L.L. 2002. Structural requirements for interaction of sodium channel β1 subunits with ankyrin. *J Biol Chem*. **277:** 26681-26688.

Malhotra, J.D., Thyagarajan, V., Chen, C., Isom, L.L. 2004. Tyrosine-phosphorylated and nonphosphorylated sodium channel beta1 subunits are differentially localized in cardiac myocytes. *J Biol Chem*. **279:** 40748-40754.

Mantegazza, M., Gambardella, A., Rusconi, R., Schiavon, E., Annesi, F., Cassulini, R.R., Labate, A., Carrideo, S., Chifari, R., Canevini, M.P., Canger, R., Franceschetti, S., Annesi, G., Wanke, E., Quattrone, A. 2005. Identification of an $Na_v1.1$ sodium channel (*SCN1A*) loss-of-function mutation associated with familial simple febrile seizures. *Proc Natl Acad Sci. USA*. **102:** 18177-18182.

Marder, E., Goaillard, J.M. 2006. Variability, compensation and homeostasis in neuron and network function. *Nat Rev Neurosci*. **7:** 563-574.

Matsuda, S., Matsuda, Y., D'Adamio, L. 2003. Amyloid beta protein precursor (AbetaPP), but not AbetaPP-like protein 2, is bridged to the kinesin light chain by the scaffold protein JNK-interacting protein 1. *J Biol Chem*. **278:** 38601-38606.

Maurice, N., Tkatch, T., Meisler, M., Sprunger, L.K., Surmeier, D.J. 2001. D1/D5 dopamine receptor activation differentially modulates rapidly inactivating and persistent sodium currents in prefrontal cortex pyramidal neurons. *J Neurosci*. **21:** 2268-2277.

McCarty, J.H., Feinstein, S.C. 1999. The TrkB receptor tyrosine kinase regulates cellular proliferation via signal transduction pathways involving SHC, PLCγ, and CBL. *J Recept Signal Transduct Res*. **19:** 953-974.

McEwen, D.P., Meadows, L.S., Chen, C., Thyagarajan, V., Isom, L.L. 2004. Sodium channel β1 subunit-mediated modulation of $Na_v1.2$ currents and cell surface density is dependent on interactions with contactin and ankyrin. *J Biol Chem*. **279:** 16044-16049.

McNair, W.P., Ku, L., Taylor, M.R., Fain, P.R., Dao, D., Wolfel, E., Mestroni, L., Familial Cardiomyopathy Registry Research Group. 2004. *SCN5A* mutation associated with dilated cardiomyopathy, conduction disorder, and arrhythmia. *Circulation*. **110:** 2163-2167.

Meadows, L.S., Malhotra, J., Loukas, A., Thyagarajan, V., Kazen-Gillespie, K.A., Koopman, M.C., Kriegler, S., Isom, L.L., Ragsdale, D.S. 2002. Functional and biochemical analysis of a sodium channel beta1 subunit mutation responsible for generalized epilepsy with febrile seizures plus type 1. *J Neurosci.* **22:** 10699-10709.

Mee, C.J., Pym, E.C., Moffat, K.G., Baines, R.A. 2004. Regulation of neuronal excitability through pumilio-dependent control of a sodium channel gene. *J Neurosci.* **24:** 8695-8703.

Meisler, M.H., Kearney, J., Escayg, A., MacDonald, B.T., Sprunger, L.K. 2001. Sodium channels and neurological disease: insights from *Scn8a* mutations in the mouse. *Neuroscientist*. **7:** 136-145.

Meisler, M.H., Plummer, N.W., Burgess, D.L., Buchner, D.A., Sprunger, L.K. 2004. Allelic mutations of the sodium channel *SCN8A* reveal multiple cellular and physiological functions. *Genetica*. **122:** 37-45.

Meisler, M.H., Kearney, J.A. 2005. Sodium channel mutations in epilepsy and other neurological disorders. *J Clin Invest*. **115:** 2010-2017.

Meregalli, P.G., Wilde, A.A., Tan, H.L. 2005. Pathophysiological mechanisms of Brugada syndrome: depolarization disorder, repolarization disorder, or more? *Cardiovasc Res*. **67:** 367-378.

Mersiyanova, I.V., Perepelov, A.V., Polyakov, A.V., Sitnikov, V.F., Dadali, E.L., Oparin, R.B., Petrin, A.N., Evgrafov, O.V. 2000. A new variant of Charcot-Marie-Tooth disease type 2 is probably the result of a mutation in the neurofilament-light gene. *Am J Hum Genet*. **67:** 37-46.

Middeldorp, J., Hol, E.M. 2011. GFAP in health and disease. *Prog Neurobiol*. **93:** 421-443.

Minichiello, L. 2009. TrkB signalling pathways in LTP and learning. *Nat Rev Neurosci.* **10:** 850-860.

Mitchell, D.J., Blasier, K.R., Jeffery, E.D., Ross, M.W., Pullikuth, A.K., Suo, D., Park, J., Smiley, W.R., Lo, K.W., Shabanowitz, J., Deppmann, C.D., Trinidad, J.C., Hunt, D.F., Catling, A.D., Pfister, K.K. 2012. Trk activation of the ERK1/2 kinase pathway stimulates intermediate chain phosphorylation and recruits cytoplasmic dynein to signaling endosomes for retrograde axonal transport. *J Neurosci.* **32:** 15495-15510.

Mitrović, N., George, A.L.Jr., Lerche, H., Wagner, S., Fahlke, C., Lehmann-Horn, F. 1995. Different effects on gating of three myotonia-causing mutations in the inactivation gate of the human muscle sodium channel. *J Physiol.* **487(Pt 1):** 107-114.

Mojumder, D.K., Frishman, L.J., Otteson, D.C., Sherry, D.M. 2007. Voltage-gated-sodium channel alpha-subunits $Na_v1.1$, $Na_v1.2$, and $Na_v1.6$ in the distal mammalian retina. *Mol Vis*. **13:** 2163-2182.

Muraro, N.I., Weston, A.J., Gerber, A.P., Luschnig, S., Moffat, K.G., Baines, R.A. 2008. Pumilio binds para mRNA and requires Nanos and Brat to regulate sodium current in Drosophila motoneurons. *J Neurosci*. **28:** 2099-2109.

Muresan, V., Ladescu Muresan, Z. 2016. Shared molecular mechanisms in Alzheimer's disease and Amyotrophic lateral sclerosis: Neurofilament-dependent transport of sAPP, FUS, TDP-43 and SOD1, with endoplasmic reticulum-like tubules. *Neurodegener Dis*. **16:** 55-61.

Nabbout, R., Gennaro, E., Dalla Bernardina, B., Dulac, O., Madia, F., Bertini, E., Capovilla, G., Chiron, C., Cristofori, G., Elia, M., Fontana, E., Gaggero, R., Granata, T., Guerrini, R., Loi, M., La Selva, L., Lispi, M.L., Matricardi, A., Romeo, A., Tzolas, V., Valseriati, D., Veggiotti, P., Vigevaano, F., Vallée, L., Dagna Bricarelli, F., Bianchi, A., Zara, F. 2003. Spectrum of *SCN1A* mutations in severe myoclonic epilepsy of infancy. *Neurology*. **60:** 1961-1967.

Namadurai, S., Yereddi, N.R., Cusdin, F.S., Huang, C.L., Chirgadze, D.Y., Jackson, A.P. 2015. A new look at sodium channel β subunits. *Open Biol*. **5:** 140192.

Nassar, M.A., Levato, A., Stirling, L.C., Wood, J.N. 2005. Neuropathic pain develops normally in mice lacking both $Na_v1.7$ and $Na_v1.8$. *Mol Pain*. **1:** 24.

Nixon, R.A., Sihag, R.K. 1991. Neurofilament phosphorylation: a new look at regulation and function. *Trends Neurosci*. **14:** 501-506.

Noda, M. 2006. The subfornical organ, a specialized sodium channel, and the sensing of sodium levels in the brain. *Neuroscientist*. **12:** 80-91.

Noda, M., Hiyama, T.Y. 2015. The Na_x channel: what it is and what it does. *Neuroscientist*. **21:** 399-412.

Noujaim, S.F., Kaur, K., Milstein, M., Jones, J.M., Furspan, P., Jiang, D., Auerbach, D.S., Herron, T., Meisler, M.H., Jalife, J. 2012. A null mutation of the neuronal sodium channel $Na_v1.6$ disrupts action potential propagation and excitation contraction coupling in the mouse heart. *FASEB J*. **26:** 63-72.

Numakawa, T., Suzuki, S., Kumamaru, E., Adachi, N., Richards, M., Kunugi, H. 2010a. BDNF function and intracellular signaling in neurons. *Histol Histopathol*. **25:** 237-258.

Numakawa, T., Richards, M., Adachi, N., Kishi, S., Kunugi, H., Hashido, K. 2011. MicroRNA function and neurotrophin BDNF. *Neurochem Int*. **59:** 551-558.

O'Brien, J.E., Sharkey, L.M., Vallianatos, C.N., Han, C., Blossom, J.C., Yu, T., Waxman, S.G., Dib-Hajj, S.D., Meisler, M.H. 2012. Interaction of voltage-gated sodium channel $Na_v1.6$ (SCN8A) with microtubule-associated protein Map1b. *J Biol Chem*. **287:** 18459-18466.

O'Malley, H.A., Shreiner, A.B., Chen, G.H., Huffnagle, G.B., Isom, L.L. 2009. Loss of Na^+ channel beta2 subunits is neuroprotective in a mouse model of multiple sclerosis. *Mol Cell Neurosci*. **40:** 143-155.

O'Malley, H.A., Isom, L.L. 2015. Sodium channel β subunits: emerging targets in channelopathies. *Annu Rev Physiol*. **77:** 481-504.

Orrico, A., Galli, L., Grosso, S., Buoni, S., Pianigiani, R., Balestri, P., Sorrentino, V. 2009. Mutational analysis of the *SCN1A*, *SCN1B* and *GABRG2* genes in 150 Italian patients with idiopathic childhood epilepsies. *Clin Genet*. **75:** 579-581.

Oyama, F., Miyazaki, H., Sakamoto, N., Becquet, C., Machida, Y., Kaneko, K., Uchikawa, C., Suzuki, T., Kurosawa, M., Ikeda, T., Tamaoka, A., Sakurai, T., Nukina, N. 2006. Sodium channel beta4 subunit: down-regulation and possible involvement in neuritic degeneration in Huntington's disease transgenic mice. *J Neurochem*. **98:** 518-529.

Pant, H.C., Veeranna, Grant, P. 2000. Regulation of axonal neurofilament phosphorylation. *Curr Top Cell Regul*. **36:** 133-150.

Papale, L.A., Beyer, B., Jones, J.M., Sharkey, L.M., Tufik, S., Epstein, M., Letts, V.A., Meisler, M.H., Frankel, W.N., Escayg, A. 2009. Heterozygous mutations of the voltage-gated sodium channel *SCN8A* are associated with spike-wave discharges and absence epilepsy in mice. *Hum Mol Genet*. **18:** 1633-1641.

Patino, G.A., Claes, L.R., Lopez-Santiago, L.F., Slat, E.A., Dondeti, R.S., Chen, C., O'Malley, H.A., Gray, C.B., Miyazaki, H., Nukina, N., Oyama, F., De Jonghe, P., Isom, L.L. 2009. A functional null mutation of *SCN1B* in a patient with Dravet syndrome. *J Neurosci*. **29:** 10764-10778.

Perrot, R., Berges, R., Bocquet, A., Eyer, J. 2008. Review of the multiple aspects of neurofilament functions, and their possible contribution to neurodegeneration. *Mol Neurobiol*. **38:** 27-65.

Pertin, M., Ji, R.R., Berta, T., Powell, A.J., Karchewski, L., Tate, S.N., Isom, L.L., Woolf, C.J., Gilliard, N., Spahn, D.R., Decosterd, I. 2005. Upregulation of the voltage-gated sodium channel beta2 subunit in neuropathic pain models: characterization of expression in injured and non-injured primary sensory neurons. *J Neurosci*. **25:** 10970-10980.

Pertin, M., Allchorne, A.J., Beggah, A.T., Woolf, C.J., Decosterd, I. 2007. Delayed sympathetic dependence in the spared nerve injury (SNI) model of neuropathic pain. *Mol Pain*. **3:** 21.

Plummer, N.W., Meisler, M.H. 1999. Evolution and diversity of mammalian sodium channel genes. *Genomics*. **57:** 323-331.

Potokar, M., Stenovec, M., Gabrijel, M., Li, L., Kreft, M., Grilc, S., Pekny, M., Zorec, R. 2010. Intermediate filaments attenuate stimulation-dependent mobility of endosomes/lysosomes in astrocytes. *Glia*. **58:** 1208-1219.

Prahlad, V., Yoon, M., Moir, R.D., Vale, R.D., Goldman, R.D. 1998. Rapid movements of vimentin on microtubule tracks: kinesin-dependent assembly of intermediate filament networks. *J Cell Biol*. **143:** 159-170.

Priest, B.T., Murphy, B.A., Lindia, J.A., Diaz, C., Abbadie, C., Ritter, A.M., Liberator, P., Iyer, L.M., Kash, S.F., Kohler, M.G., Kaczorowski, G.J., MacIntyre, D.E., Martin, W.J. 2005. Contribution of the tetrodotoxin-resistant voltage-gated sodium channel $Na_v1.9$ to sensory transmission and nociceptive behavior. *Proc Natl Acad Sci USA*. **102:** 9382-9387.

Priller, C., Bauer, T., Mitteregger, G., Krebs, B., Kretzschmar, H.A., Herms, J. 2006. Synapse formation and function is modulated by the amyloid precursor protein. *J Neurosci*. **26:** 7212-7221.

Probst, V., Allouis, M., Sacher, F., Pattier, S., Babuty, D., Mabo, P., Mansourati, J., Victor, J, Nguyen, J.M., Schott, J.J., Boisseau, P., Escande, D., Le Marec, H. 2006. Progressive cardiac conduction defect is the prevailing phenotype in carriers of a Brugada syndrome *SCN5A* mutation. *J Cardiovasc Electrophysiol*. **17:** 270-275.

Ptacek, L.J., Tawil, R., Griggs, R.C., Storvick, D., Leppert, M. 1992. Linkage of atypical myotonia congentia to a sodium channel locus. *Neurology*. **42:** 431-433.

Qu, Y., Curtis, R., Lawson, D., Gilbride, K., Ge, P., DiStefano, P.S., Silos-Santiago, I., Catterall, W.A., Scheuer, T. 2001. Differential modulation of sodium channel gating and persistent sodium currents by the β1, β2, and β3 subunits. *Mol Cell Neurosci*. **18:** 570-580.

Rabert, D.K., Koch, B.D., Ilnicka, M., Obernolte, R.A., Naylor, S.L., Herman, R.C., Eglen, R.M., Hunter, J.C., Sangameswaran, L. 1998. A tetrodotoxin-resistant voltage-gated sodium channel from human dorsal root ganglia, *hPN3*/*SCN10A*. *Pain*. **78:** 107-114.

Raman, I.M., Sprunger, L.K., Meisler, M.H., Bean, B.P. 1997. Altered subthreshold sodium currents and disrupted firing patterns in Purkinje neurons of *Scn8a* mutant mice. *Neuron*. **19:** 881-891.

Rao, M.V., Engle, L.J., Mohan, P.S., Yuan, A., Qiu, D., Cataldo, A., Hassinger, L., Jacobsen, S., Lee, V.M., Andreadis, A., Julien, J.P., Bridgman, P.C., Nixon, R.A. 2002. Myosin Va binding to neurofilaments is essential for correct myosin Va distribution and transport and neurofilament density. *J Cell Biol*. **159:** 279-290.

Reichenbach, A., Bringmann, A. 2013. New functions of Müller cells. *Glia*. **61:** 651-678.

Roesch, K., Stadler, M.B., Cepko, C.L. 2012. Gene expression changes within Müller glial cells in retinitis pigmentosa. *Mol Vis*. **18:** 1197-1214.

Ruiz-Ederra, J., García, M., Hicks, D., Vecino, E. 2004. Comparative study of the three neurofilament subunits within pig and human retinal ganglion cells. *Mol Vis*. **10:** 83-92.

Russo, S.J., Mazei-Robison, M.S., Ables, J.L., Nestler, E.J. 2009. Neurotrophic factors and structural plasticity in addiction. *Neuropharmacology*. **56(Suppl.1):** 73-82.

Savio-Galimberti, E., Gollob, M.H., Darbar, D. 2012. Voltage-gated sodium channels: biophysics, pharmacology, and related channelopathies. *Front Pharmacol*. **3:** 124.

Schaller, K., Krzemien, D., Yarowsky, P., Krueger, B., Caldwell, J. 1995. A novel, abundant sodium channel expressed in neurons and glia. *J Neurosci*. **15(5 Pt 1):** 3231-3242.

Schaller, K.L., Caldwell, J.H. 2000. Developmental and regional expression of sodium channel isoform NaCh6 in the rat central nervous system. *J Comp Neurol*. **420:** 84-97.

Scheffer, I.E., Harkin, L.A., Grinton, B.E., Dibbens, L.M., Turner, S.J., Zielinski, M.A., Xu, R., Jackson, G., Adams, J., Connellan, M., Petrou, S., Wellard, R.M., Briellmann, R.S., Wallace, R.H., Mulley, J.C., Berkovic, S.F. 2007. Temporal lobe epilepsy and GEFS+ phenotypes associated with *SCN1B* mutations. *Brain*. **130:** 100-109.

Schott, J.J., Alshinawi, C., Kyndt, F., Probst, V., Hoorntje, T.M., Hulsbeek, M., Wilde, A.A., Escande, D., Mannens, M.M., Le Marec, H. 1999. Cardiac conduction defects associate with mutations in *SCN5A*. *Nat Genet*. **23:** 20-21.

Sharkey, L.M., Cheng, X., Drews, V., Buchner, D.A., Jones, J.M., Justice, M.J., Waxman, S.G., Dib-Hajj, S.D., Meisler, M.H. 2009. The *ataxia3* mutation in the N-terminal cytoplasmic domain of sodium channel $Na_v1.6$ disrupts intracellular trafficking. *J Neurosci*. **29:** 2733-2741.

Shieh, P.B., Ghosh, A. 1999. Molecular mechanisms underlying activity-dependent regulation of BDNF expression. *J Neurobiol*. **41:** 127-134.

Shirahata, E., Iwasaki, H., Takagi, M., Lin, C., Bennett, V., Okamura, Y., Hayasaka, K. 2006. Ankyrin-G regulates inactivation gating of the neuronal sodium channel, Nav1.6. *J Neurophysiol*. **96:** 1347-1357.
Sisodia, S.S., Price, D.L. 1995. Role of beta-amyloid protein in Alzheimer's disease. *FASEB J*. **9:** 366-370.

Sjoberg, M., Vennström, B., Forrest, D. 1992. Thyroid hormone receptors in chick retinal development: differential expression of mRNAs for α and N-terminal variant β receptors. *Development*. **114:** 39-47.

Smith, M.R., Goldin, A.L. 1999. A mutation that causes ataxia shifts the voltage-dependence of the *Scn8a* sodium channel. *Neuroreport*. **10:** 3027-3031.

Smith, B.J., Côté, P.D. 2012. Reduced retinal function in the absence of $Na_v1.6$. *PLoS One*. **7:**e31476.

Snider, N.T., Omary, M.B. 2014. Post-translational modifications of intermediate filament proteins: mechanisms and functions. *Nat Rev Mol Cell Biol*. **15:** 163-177.

Spampanato, J., Escayg, A., Meisler, M.H., Goldin, A.L. 2001. Functional effects of two voltage-gated sodium channel mutations that cause generalized epilepsy with febrile seizures plus type 2. *J Neurosci*. **21:** 7481-7490.

Stamer, K., Vogel, R., Thies, E., Mandelkow, E., Mandelkow, E.M. 2002. Tau blocks traffic of organelles, neurofilaments, and APP vesicles in neurons and enhances oxidative stress. *J Cell Biol*. **156:** 1051-1063.

Steinert, P.M., Chou, Y.H., Prahlad, V., Parry, D.A., Marekov, L.N., Wu, K.C., Jang, S.I., Goldman, R.D. 1999. A high molecular weight intermediate filament-associated protein in BHK-21 cells is nestin, a type VI intermediate filament protein. Limited co-assembly *in vitro* to form heteropolymers with type III vimentin and type IV alpha-internexin. *J Biol Chem*. **2:** 9881-9890.

Sugawara, T., Tsurubuchi, Y., Agarwala, K.L., Ito, M., Fukuma, G., Mazaki-Miyazaki, E., Nagafuji, H., Noda, M., Imoto, K., Wada, K., Mitsudome, A., Kaneko, S., Montal, M., Nagata, K., Hirose, S., Yamakawa, K. 2001b. A missense mutation of the Na^+ channel α_{II} subunit gene $Na_v1.2$ in a patient with febrile and afebrile seizures causes channel dysfunction. *Proc Natl Acad Sci. USA*. **98:** 6384-6389.

Svitkina, T.M., Verkhovsky, A.B., Borisy, G.G. 1996. Plectin sidearms mediate interaction of intermediate filaments with microtubules and other components of the cytoskeleton. *J Cell Biol*. **135:** 991-1007.

Tan, H.L., Bezzina, C.R., Smits, J.P., Verkerk, A.O., Wilde, A.A. 2003. Genetic control of sodium channel function. *Cardiovasc Res*. **57:** 961-973.

Tate, S., Benn, S., Hick, C., Trezise, D., John, V., Mannion, R.J., Costigan, M., Plumpton, C., Grose, D., Gladwell, Z., Kendall, G., Dale, K., Bountra, C., Woolf, C.J. 1998. Two sodium channels contribute to the TTX-R sodium current in primary sensory neurons. *Nat Neurosci*. **1:** 653-655.

Tian, N., Copenhagen, D.R. 2001. Visual deprivation alters development of synaptic function in inner retina after eye opening. *Neuron*. **32:** 439-449.

Tian, N., Copenhagen, D.R. 2003. Visual stimulation is required for refinement of ON and OFF pathways in postnatal retina. *Neuron*. **39:** 85-96.

Tint, I.S., Hollenbeck, P.J., Verkhovsky, A.B., Surgucheva, I.G., Bershadsky, A.D. 1991. Evidence that intermediate filament reorganization is induced by ATP-dependent contraction of the actomyosin cortex in permeabilized fibroblasts. *J Cell Sci*. **98:** 375-384.

Trinczek, B., Ebneth, A., Mandelkow, E.M., Mandelkow, E. 1999. Tau regulates the attachment/detachment but not the speed of motors in microtubule-dependent transport of single vesicles and organelles. *J Cell Sci.* **112:** 2355-2367.

Trudeau, M.M., Dalton, J.C., Day, J.W., Ranum, L.P., Meisler, M.H. 2006. Heterozygosity for a protein truncation mutation of sodium channel *SCN8A* in a patient with cerebellar atrophy, ataxia and mental retardation. *J Med Genet.* **43:** 527-530.

Tsacopoulos, M., Magistretti, P.J. 1996. Metabolic coupling between glia and neurons. *J. Neurosci.* **16:** 877-885.

Turner, D.L., Cepko, C.L. 1987. A common progenitor for neurons and glia persists in rat retina late in development. *Nature*. **328:** 131-136.

Turner, P.R., O'Connor, K., Tate. W.P., Abraham, W.C. 2003. Roles of amyloid precursor protein and its fragments in regulating neural activity, plasticity and memory. *Prog Neurobiol*. **70:** 1-32.

Turrigiano, G., Abbott, L.F., Marder, E. 1994. Activity-dependent changes in the intrinsic properties of cultured neurons. *Science*. **264:** 974-977.

Turrigiano, G.G., Nelson, S.B. 1998. Thinking globally, acting locally: AMPA receptor turnover and synaptic strength. *Neuron*. **21:** 933-935.

Turrigiano, G.G. 1999. Homeostatic plasticity in neuronal networks: the more things change, the more they stay the same. *Trends Neurosci*. **22:** 221-227.

Turrigiano, G.G., Nelson, S.B. 2004. Homeostatic plasticity in the developing nervous system. *Nat Rev Neurosci*. **5:** 97-107.

Tzoumaka, E., Tischler, A.C., Sangameswaran, L., Eglen, R.M., Hunter, J.C., Novakovic, S.D. 2000. Differential distribution of the tetrodotoxin-sensitive rPN4/NaCh6/*Scn8a* sodium channel in the nervous system. *J Neurosci Res*. **60:** 37-44.

Vacher, H., Trimmer, J.S. 2012. Trafficking mechanisms underlying neuronal voltage-gated ion channel localization at the axon initial segment. *Epilepsia*. **53(Suppl 9):** 21-31.

Vaher, U., Nõukas, M., Nikopensius, T., Kals, M., Annilo, T., Nelis, M., Ounap, K., Reimand, T., Talvik, I., Ilves, P., Piirsoo, A., Seppet, E., Metspalu, A., Talvik, T. 2014. *De novo SCN8A* mutation identified by whole-exome sequencing in a boy with neonatal epileptic encephalopathy, multiple congenital anomalies, and movement disorders. *J Child Neurol*. **29:** NP202-NP206.

van Gassen, K.L., de Wit, M., van Kempen, M., van der Hel, W.S., van Rijen, P.C., Jackson, A.P., Lindhout, D., de Graan, P.N. 2009. Hippocampal Nabeta3 expression in patients with temporal lobe epilepsy. *Epilepsia*. **50:** 957-962.

van Oterendorp, C., Sgouris, S., Schallner, N., Biermann, J., Lagrèze. W.A. 2014. Retrograde neurotrophic signaling in rat retinal ganglion cells is transmitted via the ERK5 but not the ERK1/2 pathway. *Invest Ophthalmol Vis Sci*. **55:** 658-665.

Van Wart, A., Matthews, G. 2006. Impaired firing and cell-specific compensation in neurons lacking $Na_v1.6$ sodium channels. *J Neurosci*. **26:** 7172-7180.

Van Wart, A., Trimmer, J.S., Matthews, G. 2007. Polarized distribution of ion channels within microdomains of the axon initial segment. *J Comp Neurol*. **500:** 339-352.

Veeramah, K.R., O'Brien, J.E., Meisler, M.H., Cheng, X., Dib-Hajj, S.D., Waxman, S.G., Talwar, D., Girirajan, S., Eichler, E.E., Restifo, L.L., Erickson, R.P., Hammer, M.F. 2012. *De novo* pathogenic *SCN8A* mutation identified by whole-genome sequencing of a family quartet affected by infantile epileptic encephalopathy and SUDEP. *Am J Hum Genet*. **90:** 502-510.

Veldkamp, M.W., Wilders, R., Baartscheer, A., Zegers, J.G., Bezzina, C.R., Wilde, A.A. 2003. Contribution of sodium channel mutations to bradycardia and sinus node dysfunction in LQT3 families. *Circ Res*. **92:** 976-983.

Verhey, K.J., Meyer, D., Deehan, R., Blenis, J., Schnapp, B.J., Rapoport, T.A., Margolis, B. 2001. Cargo of kinesin identified as JIP scaffolding proteins and associated signaling molecules. *J Cell Biol*. **152:** 959-970.

Vermehren-Schmaedick, A., Khanjian, R.A., Balkowiec, A. 2015. Cellular mechanisms of activity-dependent BDNF expression in primary sensory neurons. *Neuroscience*. **310:** 665-673.

Wagnon, J.L., Meisler, M.H. 2015. Recurrent and non-recurrent mutations of *SCN8A* in epileptic encephalopathy. *Front Neurol*. **6:** 104.

Wakabayashi, K., Tanji, K., Odagiri, S., Miki, Y., Mori, F., Takahashi, H. 2013. The Lewy body in Parkinson's disease and related neurodegenerative disorders. *Mol Neurobiol*. **47:** 495-508.

Wallace, R.H., Wang, D.W., Singh, R., Scheffer, I.E., George, A.L.Jr., Phillips, H.A., Saar, K., Reis, A., Johnson, E.W., Sutherland, G.R., Berkovic, S.F., Mulley, J.C. 1998. Febrile seizures and generalized epilepsy associated with a mutation in the Na^+-channel beta1 subunit gene *SCN1B*. *Nat Genet*. **19:** 366-370.

Wallace, R.H., Scheffer, I.E., Barnett, S., Richards, M., Dibbens, L., Desai, R.R., Lerman-Sagie, T., Lev, D., Mazarib, A., Brand, N., Ben-Zeev, B., Goikhman, I., Singh, R., Kremmidiotis, G., Gardner, A., Sutherland, G.R., George, A.L. Jr., Mulley, J.C., Berkovic, S.F. 2001. Neuronal sodium-channel α1-subunit mutations in generalized epilepsy with febrile seizures plus. *Am J Hum Genet*. **68:** 859-865.

Wallace, R.H., Scheffer, I.E., Parasivam, G., Barnett, S., Wallace, G.B., Sutherland, G.R., Berkovic, S.F., Mulley, J.C. 2002. Generalized epilepsy with febrile seizures plus: mutation of the sodium channel subunit *SCN1B*. *Neurology*. **58:** 1426-1429.

Wallace, R.H., Hodgson, B.L., Grinton, B.E., Gardiner, R.M., Robinson, R., Rodriguez-Casero, V., Sadleir, L., Morgan, J., Harkin, L.A., Dibbens, L.M., Yamamoto, T., Andermann, E., Mulley, J.C., Berkovic, S.F., Scheffer, I.E. 2003. Sodium channel α1-subunit mutations in severe myoclonic epilepsy of infancy and infantile spasms. *Neurology*. **61:** 765-769.

Wang, Q., Shen, J., Li, Z., Timothy, K., Vincent, G.M., Priori, S.G., Schwartz, P.J., Keating, M.T. 1995. Cardiac sodium channel mutations in patients with long QT syndrome, an inherited cardiac arrhythmia. *Hum Mol Genet*. **4:** 1603-1607.

Wang, Q., Shen, J., Splawski, I., Atkinson, D., Li, Z., Robinson, J.L., Moss, A.J., Towbin, J.A., Keating, M.T. 1995b. *SCN5A* mutations associated with an inherited cardiac arrhythmia, long QT syndrome. *Cell*. **80:** 805-811.

Wang, S.W., Mu, X., Bowers, W.J., Klein, W.H. 2002. Retinal ganglion cell differentiation in cultured mouse retinal explants. *Methods*. **28:** 448-456.

Wang, Y., Smith, S.B., Ogilvie, J.M., McCool, D.J., Sarthy, V. 2002. Ciliary neurotrophic factor induces glial fibrillary acidic protein in retinal Müller cells through the JAK/STAT signal transduction pathway. *Curr Eye Res*. **24:** 305-312.

Wasserman, D., Geijer, T., Rozanov, V., Wasserman, J. 2005. Suicide attempt and basic mechanisms in neural conduction: relationships to the *SCN8A* and *VAMP4* genes. *Am J Med Genet B Neuropsychiatr Genet*. **133B:** 116-119.

Waxman, S.G. 2012. Sodium channels, the electrogenisome and the electrogenistat: lessons and questions from the clinic. *J Physiol*. **590:** 2601-2612.

Weiss, L.A., Escayg, A., Kearney, J.A., Trudeau, M., MacDonald, B.T., Mori, M., Reichert, J., Buxbaum, J.D., Meisler, M.H. 2003. Sodium channels *SCN1A*, *SCN2A* and *SCN3A* in familial autism. *Mol Psychiatry*. **8:** 186-194.

Wen, R., Tao, W., Li, Y., Sieving, P.A. 2012. CNTF and Retina. *Prog Retin Eye Res*. **31:** 136-151.

Whitaker, W.R, Faull, R.L., Dragunow, M., Mee, E.W., Emson, P.C., Clare, J.J. 2001. Changes in the mRNAs encoding voltage-gated sodium channel types II and III in human epileptic hippocampus. *Neuroscience*. **106:** 275-285.

Williams, S.N., Undieh, A.S. 2009. Dopamine D1-like receptor activation induces brain-derived neurotrophic factor protein expression. *Neuroreport*. **20:** 606-610.

Wilson, R.B., Kunchithapautham, K., Rohrer, B. 2007. Paradoxical role of BDNF: BDNF $^{+/-}$ retinas are protected against light damage-mediated stress. *Invest Ophthalmol Vis Sci*. **48:** 2877-2886.

Wu, M.L., Chiao, C.C. 2007. Light deprivation delays morphological differentiation of bipolar cells in the rabbit retina. *Brain Res*. **1170:** 13-19.

Xiao, Z-C., Ragsdale, D.S., Malhotra, J.D., Mattei, L.N., Braun, P.E., Schachner, M., Isom, L.L. 1999. Tenascin-R is a functional modulator of sodium channel β subunits. *J Biol Chem.* **274:** 26511-26517.

Yang, Y., Bauer, C., Strasser, G., Wollman, R., Julien, J.P., Fuchs, E. 1999. Integrators of the cytoskeleton that stabilize microtubules. *Cell.* **98:** 229-238.

Yang, Y., Wang, Y., Li, S., Xu, Z., Li, H., Ma, L., Fan, J., Bu, D., Liu, B., Fan, Z., Wu, G., Jin, J., Ding, B., Zhu, X., Shen, Y. 2004. Mutations in *SCN9A*, encoding a sodium channel alpha subunit, in patients with primary erythermalgia. *J Med Genet.* **41:** 171-174.

Yates, D.M., Manser, C., De Vos, K.J., Shaw, C.E., McLoughlin, D.M., Miller, C.C. 2009. Neurofilament subunit (NFL) head domain phosphorylation regulates axonal transport of neurofilaments. *Eur J Cell Biol.* **88:** 193-202.

Yoshimura, N., Seki, S., Novakovic, S.D., Tzoumaka, E., Erickson, V.L., Erickson, K.A., Chancellor, M.B., de Groat, W.C. 2001. The involvement of the tetrodotoxin-resistant sodium channel $Na_v1.8$ (*PN3*/*SNS*) in a rat model of visceral pain. *J Neurosci.* **21:** 8690-8696.

Yu, F.H., Catterall, W.A. 2003. Overiew of the voltage-gated sodium channel family. *Genome Biol.* **4:** 207.

Yuan, A., Sasaki, T., Rao, M.V., Kumar, A., Kanumuri, V., Dunlop, D.S., Liem, R.K., Nixon, R.A. 2009. Neurofilaments form a highly stable stationary cytoskeleton after reaching a critical level in axons. *J Neurosci.* **29:** 11316-11329.

Yuan, A., Rao, M.V., Nixon, V., Nixon, R.A. 2012. Neurofilaments at a glance. *J Cell Sci.* **125(Pt 14):** 3257-3263.

Zhang, W., Linden, D.J. 2003. The other side of the engram: experience-driven changes in neuronal intrinsic excitability. *Nat Rev Neurosci.* **4:** 885-900.

Zhou, D., Lambert, S., Malen, P.L., Carpenter, S., Boland, L.M., Bennett, V. 1998. AnkyrinG is required for clustering of voltage-gated Na channels at axon initial segments and for normal action potential firing. *J Cell Biol.* **143:** 1295-1304.

Appendix 2.1: Schematic depicting work flow from experimental animal generation to qRT-PCR sample for analysis. **(A)** is a schematic representation of the number of mice generated per genotype in each rearing condition [light-reared (LR), or dark-reared (DR)] (n = 3 animals per genotype as experimental triplicates). There are two different genotypes of animals generated for this study (wildtype (WT), and mutant (Mut). **(B)** illustrates what happens to each experimental animal at the time of their sacrifice. Both eyes from each experimental animal are extracted and the retinas pooled to generate one sample per experimental animal. Retinal samples from different animals with the same genotype are not pooled. Therefore, for every genotype, there are three samples per timepoint per rearing condition. **(C)** Total retinal RNA is isolated and purified with the use of a RNeasy Plus Mini Kit (Qiagen) (Appendix 2.2). **(D)** Purified total RNA is then quantified using a nanodrop spectrophotometer and 100 ng/uL is then converted into cDNA using Superscript III reverse transcriptase reaction (Appendix 2.2). **(E)** qRT-PCR samples are prepared by adding SYBR Green master mix and appropriate primers and then loaded into a 384-well plate for qRT-PCR quantification and data generation (Appendix 2.1). Each prepared sample is loaded in triplicate as technical triplicates into the 384-well plate. Collected data are then analyzed with statistical analyses in GraphPad Prisim 5.0 and tested for significance between treatment groups, between age groups, between genotypes...etc., results are reported in Chapter 3.

APPENDIX 2.1: qRT-PCR experimental flow-chart

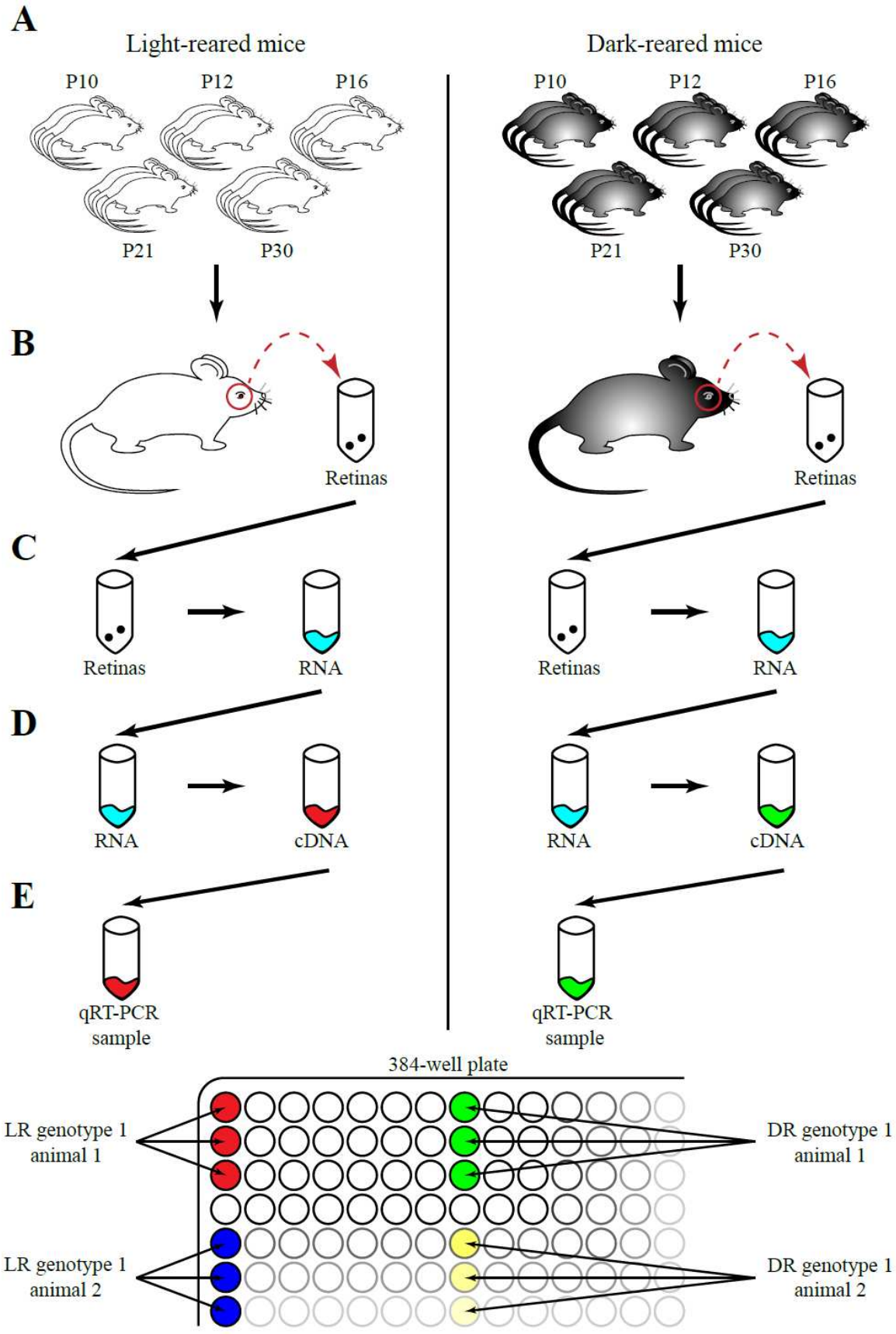

APPENDIX 2.2: Conversion of RNA into cDNA

A. Retinal tissue RNA extraction and quantification for qRT-PCR:

Total RNA was isolated using the RNeasy Plus Mini Kit (Qiagen, Hilden, Germany). Purified RNA was then quantified using a nanodrop spectrophotometer (NanoDrop 2000, Thermo Scientific, USA). Each RNA sample was quantified a minimum of three times before the average concentration was averaged.

B. Quantitative reverse transcriptase polymerase chain reaction (qRT-PCR):

All purified RNA samples were first diluted to a working concentration of 100ng/µL. To each RNA sample, the following were added:

RNA annealing reaction setup:

Reagent	Stock concentration	Volume per reaction (µL)
ddH_2O	-----	10
Oligo$(dT)_{12\text{-}18}$ primer	0.5ng/uL	1
RNA template	100ng/uL	1
dNTP Mix	10mM	1
TOTAL		13µL

1. Heat to 65°C for 5 minutes.
2. Incubate on ice for 1 minute.
3. To each RNA sample, the following were added:

cDNA synthesis reaction setup:

Reagent	Stock concentration	Volume per reaction (µL)
First-strand Buffer	5X	4
DTT	0.1M	1
RNaseOUT	40units/uL	1
Superscript III RT	200units/uL	1
TOTAL		20µL

4. Mix by pipetting up/down gently.
5. Incubate at 50°C for 1 hour.
6. Heat inactivate at 70°C for 15 minutes.
7. The resulting cDNA samples were diluted to a working concentration of 0.1ng/uL and stored at -20°C until use.

C. Determining the amplification efficiency of the qRT-PCR experiments:

In order to determine the amplification efficiency of all the qRT-PCR primers used in this study, one to two qRT-PCR samples were performed for each set of primers along with the same wildtype cDNA for all qPCR experiments (refer to Appendix 2.3 for qRT-PCR details). These qRT-PCR samples were then ran out on a 1% agarose gel and each cDNA band was extracted using the QIAquick Gel Extraction Kit (Qiagen, Hilden, Germany). The purified cDNA was then quantified using a nanodrop spectrophotometer (NanoDrop 2000, Thermo Scientific, USA). The ratio of the absorbance at 260 nm and

280 nm ($A_{260/280}$) of ~2 was used to assess the purity of the RNA. Each cDNA sample was quantified a minimum of three times before the mean concentration was calculated. Using this mean calculation of cNDA amount (in ng) and the predicted PCR product size (in bp), the number of copies of the template was calculated. The formula used was: **number of copies = (ng * number/mole) / (bp * ng/g * g/ mole of bp).**

A series of ten 10-fold serial dilutions of this cDNA template was prepared for each gene in this study. Each serial dilution was used in qRT-PCR experiments, and the threshold cycle values (C_T) were determined. Using a base-10 semi-logarithmic graph, the C_T values vs. the dilution factor were plotted, fitting the data to a straight trend line. From the equation of this trend line, the correlation coefficient (R^2) was confirmed to be 0.99 or greater. The closer the slope of this straight trend line is to -3.32, the closer the amplification efficiency is to 100%. The formula used was: **amplification efficiency = [10(-1/slope)]-1**.

Disposables/Reagents/Equipment used:

Disposables:

- 0.2mL tubes (Axygen 0.2mL PCR tubes with flat caps. Cat# PCR-02-C)
- 0.5mL tubes (Axygen 0.5mL PCR tubes with flat caps. Cat# PCR-05-C)
- 384-well white opaque microplates with film lids (Axygen Scientific from VWR, Cat# 89131-748)
- Ultra clear pressure sensitive sealing film (Axygen Scientific from VWR, Cat# UC-500)
- Filter tips

Reagents used:

- RNeasy Plus Mini Kit (Qiagen, Cat# 74134)
- Oligo$(dT)_{12-18}$ Primers (Invitrogen, Cat# 18418-012)
- 10mM dNTP Mix (Invitrogen, Cat# 18427-088)
- RNaseOUT Ribonuclease Inhibitor (Invitrogen, Cat# 10777-019)
- SuperScript III Reverse Transcriptase (Invitrogen, Cat# 18080-044)
- PerfeCTa SYBR Green FastMix (Quanta BioSciences, Cat# 95072-012)
- QIAquick Gel Extraction Kit (Qiagen, Cat# 28704)

Equipment used:

- Bench top centrifuge (eppendorf centrifuge 5424)
- Vortexer (VWR Vortex-Genie 2)
- adhesive seal plate roller (Light Labs, Dallas, TX, USA)
- Roche Lightcycler II 480 Real-Time PCR system
- nanodrop spectrophotometer (NanoDrop 2000, Thermo Scientific, USA)
- Gilson Pipetman Classics—P2, P20, P200

APPENDIX 2.3: qPCR primer sequences and qRT-PCR programs

A. Validated qPCR primers purchased from RealTimePrimers.com:

Gene	Size (bp)	Forward (5' - 3')	Reverse (5' - 3')
Gapdh	223	CTGGAGAAACCTGCCAAGTA	TGTTGCTGTAGCCGTATTCA
Hprt1	242	GCTGACCTGCTGGATTACAT	TTGGGGCTGTACTGCTTAAC
Scn1b	211	CATCTTCATCACCAACGTCA	CACAAGCCATATGGTCAACA
NF-L	230	GAGCTGAGAAGCACGAAGAG	AAGTAGGAGCTGCTCTGCAA
Gfap	205	AGGGGCAGATTTAGTCCAAC	AGGGAGTGGAGGAGTCATTC
Bdnf	219	GGTGCAGAAAAGCAACAAGT	GCACAAAAAGTTCCCAGAGA
Cntf	202	GATTCCACAGGCACAAAATC	AAGCCATCCCCTAAATCAAC
Ank3	215	GGACCACTTGGTCATACTGC	CGGGAATGAATGTGAGTTTC
Pum2	192	GCTCATCAGTTGGCAGTTCT	GTGAATGTCCTGGAGTTTGG
Jip1	183	GCGACTCTGCCACTGTCTAT	GGCCACTCATGAAGACATTC
TrkB	247	CAGATCTCCGCTCACTTCAT	ACTTGAGCAGGAGCAACATC

qRT-PCR setup using validated primers from RealTimePrimers.com:

Reagent	Stock concentration	Volume per reaction (µL)
ddH_2O	-----	3.8
forward primer	50µM	0.1
reverse primer	50µM	0.1
cDNA template	-----	1
QB SYBR Green FastMix	2X	5
TOTAL		10µL

qRT-PCR cycling program (Roche Lightcycler II 480)

1. Initiation denaturation T=95°C, 15 minutes
2. qPCR cycling protocol (validated primers) X 45 cycles
3. Denaturation T=95°C, 15 seconds
4. Annealing T=58°C, 30 seconds
5. Elongation T=72°C, 30 seconds
6. Melt curve analysis
7. Cooling/store T=10°C, ∞

B. qPCR primers purchased from Integrated DNA Technologies (IDT):

Gene	Size (bp)	Forward (5' - 3')	Reverse (5' - 3')
App	115	TCCGAGAGGTGTGCTCTGAA	CCACATCCGCCGTAAAAGAATG
Scn8a	115	GCAAGCTCAAGAAACCACCC	CCGTAGATGAAAGGCAAACTCT

qRT-PCR setup using IDT primers:

Reagent	Stock concentration	Volume per reaction (µL)
ddH_2O	-----	3.6
forward primer	100µM	0.2
reverse primer	100µM	0.2
cDNA template	-----	1
QB SYBR Green FastMix	2X	5
TOTAL		10µL

qRT-PCR cycling program (Roche Lightcycler II 480)

1. Initiation denaturation T=95°C, 15 minutes
2. qPCR cycling protocol (IDT primers) X 45 cycles
3. Denaturation T=95°C, 15 seconds
4. Annealing T=61°C, 45 seconds
5. Elongation T=72°C, 45 seconds
6. Melt curve analysis
7. Cooling/store T=10°C, ∞

Disposables/Reagents/Equipment used:

Disposables:

- 0.5mL tubes (Axygen 0.5mL PCR tubes with flat caps. Cat# PCR-05-C)
- 1.5mL tubes (Axygen 1.5mL Microtubes, Homo-polymer, boil-proof. Cat# MCT-150-C)
- 384-well white opaque microplates with film lids (Axygen Scientific from VWR, Cat# 89131-748)
- Ultra clear pressure sensitive sealing film (Axygen Scientific from VWR, Cat# UC-500)
- Filter tips

Reagents used:

- PerfeCTa SYBR Green FastMix (Quanta BioSciences, Cat# 95072-012)

Equipment used:

- Bench top centrifuge (eppendorf centrifuge 5424)
- Vortexer (VWR Vortex-Genie 2)
- adhesive seal plate roller (Light Labs, Dallas, TX, USA)
- Roche Lightcycler II 480 Real-Time PCR system
- Gilson Pipetman Classics—P2, P20, P200

APPENDIX 2.4: Isolation and embedding of retinal tissues for frozen sections

A. Isolation of retinal tissues for immunohistochemistry experiments:

All animals were first genotyped before tissue collection. Animals were anesthetized with isoflurane and then euthanized by cervical dislocation. After decapitation, the eyes were removed and immediately submerged into 4% paraformaldehyde (PFA) solution.

B. Fixation and embedding of retinal tissues for immunohistochemistry experiments:

Retinal tissues were fixed for a minimum of 24 hours at 4°C, until the tissues sank to the bottom of the tube. After fixation, the lens was carefully removed from each eye and the retinal tissues were cryoprotected with a 30% sucrose/phosphate buffer solution for 24 hours at 4°C, until the tissues sank to the bottom of the tube. The tissues were then transferred to a 30% sucrose/O.C.T. solution for 24 hours at 4°C, until the tissues sank. Two retinal tissue samples from each mouse was then separately placed into a disposable plastic cryomold, submerged and embedded with a fresh solution of 30% sucrose/O.C.T. compound, and flash frozen with liquid nitrogen-chilled isopentane, and stored at -80°C until further use.

C. Cryostat sectioning of retinal tissues for immunohistochemistry experiments:

Each retinal tissue sample was quickly removed from the -80°C freezer and allowed to equilibrate to -30°C in the cryostat before sectioning. All retinal tissues were cut at a thickness of 10µm. For each tissue sample, the entire eyeball was cut; all serial sections were collected on poly-L-lysine coated slides or charged slides. Each slide contained a total of four sections: two sections from a wildtype animal, and two sections from an age-matched mutant animal of the same developmental timepoint. All slides were allowed to air dry for several hours, and then stored in -20°C until further use.

D. Solutions used:

0.2M NaH_2PO_4:

NaH_2PO_4	MW=119.98g/mol	24.0g/L

0.2M Na_2HPO_4:

$Na_2HPO_4 \cdot 7H_2O$	MW=268.07g/mol	53.6g/L

Phosphate (PB) buffer (0.1M solution, pH 7.4):

4.75mL 0.2M NaH_2PO_4
20.25mL 0.2M $Na_2HPO_4 \cdot 7H_2O$
Make final volume up to 50mL by adding ddH_2O

4% paraformaldehyde (PFA) in 0.1M PB (pH 7.4):

2g	paraformaldehyde powder
25mL	ddH_2O
4.75mL	0.2M NaH_2PO_4
20.25mL	0.2M $Na_2HPO_4 \cdot 7H_2O$

Mix paraformaldehyde powder and ddH_2O together in clean glassware.
Stir and heat this solution briefly, no higher than 55°C.
Add a few drops of 10N NaOH, until paraformaldehyde powder dissolves completely.
Then add PB solutions to paraformaldehyde solution.
Filter this final solution before use.
This solution must be made fresh weekly.

60% sucrose solution (2X stock solution in 50mL):

30g sucrose
Make final volume up to 50mL by adding ddH_2O

30% sucrose/PB solution:

25mL	60% sucrose solution
4.75mL	0.2M NaH_2PO_4
20.25mL	0.2M $Na_2HPO_4 \cdot 7H_2O$

Store at 4°C.

30% sucrose/O.C.T. solution:

25mL	60% sucrose solution
25mL	O.C.T. compound

E. Disposables/Chemicals and Reagents/Equipment used:

Disposables:

- 1.5mL tubes (Axygen 1.5mL Microtubes, Homo-polymer, boil-proof. Cat# MCT-150-C)
- 50mL polypropylene conical tubes (BD Biosciences, Cat#352070)
- Vinyl specimen cryomolds (15mm X 15mm X 5mm, Tissue-Tek, Cat#4566)
- Microscope slides (Fisherbrand double frosted, 25mm X 75mm X 1.0mm, Fisher Scientific, Cat# 12-552-5)
- Superfrost/Plus microscope slides (Fisherbrand, 25mm X 75mm X 1.0mm, Fisher Scientific, Cat# 12-550-15)

Chemicals and Reagents:

- Paraformaldehyde powder (reagent grade, crystalline) (Sigma-aldrich, Cat# P6148)
- sucrose (Fisher Scientific, BP220-1, Cat# 57-50-1)
- sodium phosphate (MW=119.98g/mol) (monobasic, anhydrous, NaH_2PO_4, Fisher Scientific, BP329-500, Cat# 7558-80-7)
- sodium phosphate (MW=268.07g/mol) (dibasic heptahydrate, $Na_2HPO_4 \cdot 7H_2O$, Fisher Scientific, BP331-500, Cat# 7782-85-6)
- O.C.T. compound (optimal cutting temperature) (Sakura Finetek USA, Cat#4583)
- Isopentane (2-Methylbutane) (Fisher Scientific, Cat# 78-78-4)
- Poly-L-lysine solution (0.1% w/v, in water) (Sigma-aldrich, Cat# P8920-100mL)
- NaOH (sodium hydroxide) (MW=40g/mol) (10N, 4L) (Fisher Scientific, SS255-4, Cat# 7732-18-5)
- Liquid nitrogen

Equipment used:

- -80^{o}C freezer (Sanyo VIP Series)
- -20^{o}C freezer (Wood's brand)
- 4^{o}C fridge (Sanyo Labcool)
- Leica CM 1900 cryostat
- Zeiss dissecting stereomicroscope
- Scale (Acculab VI-350)
- Stirrer (Thermolyne nuova II stirrer)
- Vortexer (VWR Vortex-Genie 2)
- Gilson Pipetman Classics—P2, P20, P200
- Forceps (Dumont, #4, Fine Science Tools, Cat# 11241-30)
- Optic scissors (Vannas-Tübingen Spring scissors, Fine Science Tools, Cat# 15005-08)
- Beakers
- Erlenmeyer flasks

APPENDIX 2.5: Isolation and paraffin embedding of brain tissues

A. Isolation of brain tissues for immunohistochemistry experiments:

All animals were first genotyped before tissue collection. Animals were first deeply anesthetized with isoflurane, and then fixed by transcardial perfusion using a 4% paraformaldehyde (PFA) solution. After decapitation, the brains were carefully removed from the skull, cut in half in a sagittal plane with a razor, and immediately immersed into a 10% neutral buffered formalin (NBF) solution; brain tissues were fixed for five days.

B. Fixation and paraffin embedding of brain tissues for immunohistochemistry experiments:

After five days of fixation, all brain tissues were dehydrated through a series of graded ethanol solutions, and finally infiltrated with paraffin wax in tissue embedding cassettes. All paraffin embedded brain tissues were stored at room temperature until further use.

Processing brain tissues (from 10% NBF fixation→ paraffin embedding):

Each solution change of the protocol lasts for a duration of **2 hours**. Steps #1-5 (all water and ethanol steps) are performed at room temperature. Steps #6-10 (all CitriSolv and paraffin wax steps) are performed at ~55°C – 60°C in Stabil-Therm Gravity Ovens (Blue M Electric Company, Model# OV-8A).

1. ddH_2O 2 X changes
2. 20% ethanol 1 X change
3. 50% ethanol 1 X change
4. 70% ethanol 1 X change
5. 100% ethanol 3 X changes
6. CitriSolv (100%) 2 X changes
7. 50:50 (paraffin:CitriSolv) 3 X changes
8. Paraffin wax (100%) 4 X changes
9. Place/orient tissues in metal mold→wait for ~2 hours (degassing)
10. Embed→top up tissue molds with paraffin wax, entirely submerging tissues

C. Sectioning of paraffin embedded brain tissues for immunohistochemistry experiments:

All brain tissue sections were cut at a thickness of 5µm. For each tissue sample, all serial sections were first floated in a 40°C waterbath, and then collected on poly-L-lysine coated slides or charged slides. Each slide contained a total of four sections: two sections from a wildtype animal, and two sections from an age-matched mutant animal of the same developmental timepoint. All slides were placed in a 40°C Dry Type Bacteriological Incubator (Blue M Electric Company) for 24 hours, and then stored at room temperature until further use.

D. Solutions used:

0.2M NaH_2PO_4:

NaH_2PO_4 MW=119.98g/mol 24.0g/L

0.2M Na_2HPO_4:

$Na_2HPO_4 \cdot 7H_2O$ MW=268.07g/mol 53.6g/L

Phosphate (PB) buffer (0.1M solution, pH 7.4):

4.75mL 0.2M NaH_2PO_4
20.25mL 0.2M $Na_2HPO_4 \cdot 7H_2O$
Make final volume up to 50mL by adding ddH_2O

4% paraformaldehyde (PFA) in 0.1M PB (pH 7.4):

2g paraformaldehyde powder
25mL ddH_2O
4.75mL 0.2M NaH_2PO_4
20.25mL 0.2M $Na_2HPO_4 \cdot 7H_2O$
Mix paraformaldehyde powder and ddH_2O together in clean glassware.
Stir and heat this solution briefly, no higher than 55^{o}C.
Add a few drops of 10N NaOH, until paraformaldehyde powder dissolves completely.
Then add PB solutions to paraformaldehyde solution.
Filter this final solution before use.
This solution must be made fresh weekly.

E. Disposables/Chemicals and Reagents/Equipment used:

Disposables:

- 20mL syringes (Luer-Lok Tip) (BD Biosciences, Cat# 309661)
- 25 gauge X 1 ½ inch needles (PrecisionGlide, regular bevel) (BD Biosciences, Cat# 305127)
- 20mL scintillation vials (borosilicate glass with white polyethylene caps) (Fisher Scientific, Cat# 03-337-14)
- Single edge industrial razor blades (surgical carbon steel, No.9) (VWR, Cat# 55411-050)
- Tissue processing/embedding cassettes (M490-Histosette I, Simport, Cat#490-2)
- Embedding rings (M460, Simport, Cat# M460)
- Microscope slides (Fisherbrand double frosted, 25mm X 75mm X 1.0mm, Fisher Scientific, Cat# 12-552-5)
- Superfrost/Plus microscope slides (Fisherbrand, 25mm X 75mm X 1.0mm, Fisher Scientific, Cat# 12-550-15)

Chemicals and Reagents:

- Paraformaldehyde powder (reagent grade, crystalline) (Sigma-aldrich, Cat# P6148)
- sodium phosphate (MW=119.98g/mol) (monobasic, anhydrous, NaH_2PO_4, Fisher Scientific, BP329-500, Cat# 7558-80-7)
- sodium phosphate (MW=268.07g/mol) (dibasic heptahydrate, $Na_2HPO_4 \cdot 7H_2O$, Fisher Scientific, BP331-500, Cat# 7782-85-6)
- Poly-L-lysine solution (0.1% w/v, in water) (Sigma-aldrich, Cat# P8920-100mL)
- 10% neutral buffered formalin (NBF) (Fisher Scientific, Cat# 67-56-1)
- CitriSolv clearing agent (Fisher Scientific, Cat# 22-143-975)
- Paraffin wax compound (TissePrep, Fisher Scientific, Cat # T565)
- Ethanol (100%)

Equipment used:

- Leica Leitz 1512 manual rotary microtome
- Scale (Acculab VI-350)
- Heater/Stirrer (Thermolyne nuova II stirrer)
- Metal container capable of holding hot water (for makeshift waterbath)
- Vortexer (VWR Vortex-Genie 2)
- Forceps (Dumont, #4, Fine Science Tools, Cat# 11241-30)
- Dissection scissors
- Dissection tray with 4 tacks
- Stainless steel base molds (M474, 15mm X 15mm X 5mm, Simport, Cat# M474-2)
- Stabil-Therm Gravity Oven, Blue M Electric Company, Model# OV-8A
- Dry Type Bacteriological Incubator, Blue M Electric Company
- Beakers
- Erlenmeyer flasks

APPENDIX 2.6: Immunohistochemical analysis using frozen retinal tissues

A. Immunohistochemistry protocol using murine retinal tissues (all steps performed at room temperature unless otherwise stated):

1.	Permeabilize with PBS/0.1% Triton-X 100 solution	3 X 5 minutes
2.	**antigen retrieval*** by using a 1% SDS/PBS solution	1 X 5 minutes
3.	wash with phosphate buffered saline (PBS)	3 X 5 minutes
4.	apply Blocking buffer to tissues	1 X 1 hour
5.	apply primary antibody (refer to Table 2.4)	1 X overnight at 4^{o}C
6.	wash with PBS	3 X 5 minutes
7.	apply secondary antibody (refer to Table 2.4)	1 X 1 hour
8.	wash with PBS	3 X 5 minutes
9.	apply nuclear stain (refer to Table 2.4)	1 X 10 minutes
10.	wash with PBS	3 X 5 minutes
11.	mount coverslips with aqueous mounting medium	
12.	seal coverslips with nail polish	

* Although antigen retrieval is generally not necessary for frozen tissues, I did include this step in my experiments to facilitate staining intensity. Antigen retrieval details listed in Table 2.4 refer to the use of antibody instructions as given by the particular companies.

B. Solutions used:

Phosphate buffered saline (PBS) (10X stock solution, pH 7.4):

137mM NaCl	MW=58.44g/mol
2.7mM KCl	MW=74.56g/mol
10mM $Na_2HPO_4 \cdot 7H_2O$	MW=268.07g/mol
2mM KH_2PO_4	MW=136.09g/mol

PBS/0.1% Triton-X 100 solution:

49.95mL	1 X PBS solution
50µL	Triton-X 100 stock

Mix well until completely dissolved. Store at room temperature.

10% SDS stock solution:

10g	SDS (sodium dodecyl sulphate)
100mL	ddH_2O

Mix well until completely dissolved. Store at room temperature.

1% SDS/PBS solution:

1mL	10% SDS stock solution
90mL	1 X PBS solution

Blocking buffer:

5mL	Normal goat serum
95mL	1 X PBS solution

Aqueous mounting medium:

0.25g	DABCO
5mL	Glycerol
5mL	1 X PBS solution

Keep in 4^{o}C and away from light (use foil to cover solution).

C. Disposables/Chemicals and Reagents/Equipment used:

Disposables:

- Microscope slide coverslips (22X22, #0) (VWR, Cat# 080912-9)
- Microscope slide coverslips (24X50, #0) (VWR, Cat# 101110-9)

Chemicals and Reagents:

- sodium chloride (NaCl) MW=58.44g/mol) (Sigma-aldrich, Cat# S3014-1KG)
- potassium chloride (KCl) (MW=74.56g/mol) (Sigma-aldrich, Cat# P9541-500g)
- sodium phosphate (MW=268.07g/mol) (dibasic heptahydrate, $Na_2HPO_4 \cdot 7H_2O$, Fisher Scientific, BP331-500, Cat# 7782-85-6)
- potassium phosphate (KH_2PO_4) (MW=136.09g/mol) (monobasic, Sigma-aldrich, Cat# P9791-500g)
- Glycerol (Fisher Scientific, BP229-1, Cat# 58-81-5)
- SDS (sodium dodecyl sulphate) (Fisher Scientific, Cat# 151-21-3)
- Triton-X 100 (Fisher Scientific, BP151-500, Cat# 9002-93-1)
- DABCO (1,4-Diazabicyclo[2.2.2]octane (Sigma-aldrich, Cat# D2522)
- Normal goat serum (ThermoFisher Scientific, Cat# 31873)
- Vectastain ABC Kit (Rabbit IgG) (Vector Labs, Cat# PK-4001)

Equipment used:

- Plastic box with lid (to serve as a humidity chamber)

APPENDIX 2.7: Immunohistochemical analysis using paraffin embedded brain tissues

A. Deparaffinize slides using a series of graded ethanol solutions (all steps performed at room temperature):

1.	CitriSolv	3 X 5 minutes
2.	100% ethanol	3 X 2 minutes
3.	90% ethanol	2 X 2 minutes
4.	70% ethanol	2 X 2 minutes
5.	50% ethanol	2 X 2 minutes
6.	20% ethanol	2 X 2 minutes
7.	ddH_2O	2 X 2 minutes

B. Immunohistochemistry protocol using murine brain tissues (all steps performed at room temperature unless otherwise stated):

1.	wash with phosphate buffered saline (PBS)	3 X 5 minutes
2.	antigen retrieval by using a 1N HCl solution	1 X 20 minutes
3.	wash with PBS	3 X 5 minutes
4.	apply Blocking buffer to tissues	1 X 1 hour
5.	apply primary antibody (refer to Table 2.4)	1 X overnight at 4^oC
6.	wash with PBS	3 X 5 minutes
7.	apply secondary antibody (refer to Table 2.4)	1 X 1 hour
8.	wash with PBS	3 X 5 minutes
9.	apply nuclear stain (refer to Table 2.4)	1 X 10 minutes
10.	wash with PBS	3 X 5 minutes
11.	mount coverslips with aqueous mounting medium	
12.	seal coverslips with nail polish	

C. Solutions used:

Phosphate buffered saline (PBS) (10X stock solution, pH 7.4):

137mM NaCl	MW=58.44g/mol
2.7mM KCl	MW=74.56g/mol
10mM $Na_2HPO_4 \cdot 7H_2O$	MW=268.07g/mol
2mM KH_2PO_4	MW=136.09g/mol

Blocking buffer:

5mL	Normal goat serum
95mL	1 X PBS solution

Aqueous mounting medium:

0.25g	DABCO
5mL	Glycerol
5mL	1 X PBS solution

Keep in 4^oC and away from light (use foil to cover solution).

D. Disposables/Chemicals and Reagents/Equipment used:

Disposables:

- Microscope slide coverslips (22X22, #0) (VWR, Cat# 080912-9)
- Microscope slide coverslips (24X50, #0) (VWR, Cat# 101110-9)

Chemicals and Reagents:

- CitriSolv clearing agent (Fisher Scientific, Cat# 22-143-975)
- sodium chloride (NaCl) MW=58.44g/mol) (Sigma-aldrich, Cat# S3014-1KG)
- potassium chloride (KCl) (MW=74.56g/mol) (Sigma-aldrich, Cat# P9541-500g)
- sodium phosphate (MW=268.07g/mol) (dibasic heptahydrate, $Na_2HPO_4 \cdot 7H_2O$, Fisher Scientific, BP331-500, Cat# 7782-85-6)
- potassium phosphate (KH_2PO_4) (MW=136.09g/mol) (monobasic, Sigma-aldrich, Cat# P9791-500g)
- Glycerol (Fisher Scientific, BP229-1, Cat# 58-81-5)
- 10N HCl (Fisher Scientific, 2.5L, A144212, UN 1789, Cat# 7647-01-0)
- Ethanol (100%)
- DABCO (1,4-Diazabicyclo[2.2.2]octane (Sigma-aldrich, Cat# D2522)
- Normal goat serum (ThermoFisher Scientific, Cat# 31873)

Equipment used:

- Glass staining dishes
- Metal staining racks
- Plastic box with lid (to serve as a humidity chamber)

APPENDIX 2.8: Hematoxylin & Eosin staining (Regressive method) for paraffin embedded brain tissues

A. Deparaffinize slides using a series of graded ethanol solutions (all steps performed at room temperature):

1.	CitriSolv	3 X 5 minutes
2.	100% ethanol	3 X 2 minutes
3.	90% ethanol	2 X 2 minutes
4.	70% ethanol	2 X 2 minutes
5.	50% ethanol	2 X 2 minutes
6.	20% ethanol	2 X 2 minutes
7.	Running tap water	rinse off ethanol, ~1 minute

B. Hematoxylin & Eosin staining protocol using murine brain tissues (all steps performed at room temperature):

1.	Harris Hematoxylin	1 X 5 minutes
2.	Running tap water	quickly rinse off excess stain, ~30 seconds
3.	Scott's tap H_2O	1 X 2 minutes
4.	Running tap water	quickly rinse off excess, ~30 seconds
5.	0.5% acid alcohol solution	1 X 10 seconds
6.	Running tap water	quickly rinse off excess, ~30 seconds
7.	Scott's tap H_2O	1 X 2 minutes
8.	Running tap water	quickly rinse off excess, ~30 seconds
9.	Eosin Y	1 X 20 dips

C. Dehydrate slides using a series of graded ethanol solutions (all steps performed at room temperature):

1.	70% ethanol	20 dips
2.	90% ethanol	3 X 20 dips
3.	100% ethanol	2 X 20 dips
4.	CitriSolv	3 X 20 dips
5.	Mount slides with xylene-based mounting medium (Cytoseal XYL)	
6.	Allow slides to air dry in fumehood overnight	

D. Solutions used:

Scott's tap water (Bluing agent):

30g $MgSO_4$
2g NaHCO3 (sodium bicarbonate)
3L tap water
Mix well and store at room temperature.

0.5% acid alcohol solution:

0.5mL HCl, 10N concentrate
95.5mL 70% ethanol
Mix well and store at room temperature

E. Disposables/Chemicals and Reagents/Equipment used:

Disposables:

- Microscope slide coverslips (22X22, #0) (VWR, Cat# 080912-9)
- Microscope slide coverslips (24X50, #0) (VWR, Cat# 101110-9)

Chemicals and Reagents:

- CitriSolv clearing agent (Fisher Scientific, Cat# 22-143-975)
- 10N HCl (Fisher Scientific, 2.5L, A144212, UN 1789, Cat# 7647-01-0)
- Ethanol (100%)
- Magnesium sulphate (Fisher Scientific, Cat#10034-99-8)
- Sodium bicarbonate (Fisher Scientific, Cat# 144-55-8)
- Harris modified Hematoxylin solution (Sigma-aldrich, Cat# HHS128-4L)
- Eosin Y solution, alcoholic (sigma-aldrich, Cat# HT1101128-4L)
- Cytoseal XYL mounting medium (Thermo Scientific, Richard-Allen Scientific, Cat# 8312-4)

Equipment used:

- Glass staining dishes
- Metal staining racks

APPENDIX 2.9: DNA extraction and isolation from mouse tissues for PCR

A. Tissue collection/digestion:

1. Collect animal tissue from ear notch or ~2mm of tail tip for genomic DNA extraction in a labeled 1.5mL centrifuge tube.
2. Make up active tissue digestion buffer (recipe below) by adding the appropriate amount of Proteinase K to the tissue prep solution. Make up enough active tissue digestion buffer for all animal tissues collected.
3. Aliquot 30-50uL of the active tail digestion buffer to each tissue sample, enough to submerge the entire tissue.
4. Incubate samples at 55^{o}C for 3 hours-overnight (depending on size of tissue).
5. Remove from 55^{o}C waterbath and centrifuge for 5 minutes at room temperature on maximum speed on bench top centrifuge to pellet anything that has not been digested by Proteinase K (i.e. fur, bone, etc.). Carefully remove supernatant and place in a new labeled 1.5mL centrifuge tube. Discard pellet.
6. This 'dirty prep' can be stored at -20^{o}C until ready for DNA isolation.

B. Genomic DNA isolation:

7. Thaw out frozen dirty preps (if necessary). Add equal volume of phenol (30-50uL) to each sample. Vortex for ~30 seconds to mix well.
8. Centrifuge for 5 minutes at room temperature on maximum speed.
9. Carefully transfer supernatant to a new labeled 1.5mL centrifuge tube. Discard pellet.
10. Add equal volume of chloroform (30-50uL) to each sample. Vortex for ~30 seconds to mix well.
11. Centrifuge for 5 minutes at room temperature on maximum speed.
12. Carefully transfer supernatant to a new labeled 1.5mL centrifuge tube. Discard pellet.
13. Add 1/10 volume of 3M sodium acetate to each sample.
14. Add 2X volume of ice cold 100% ethanol to each sample. Gently invert 3-4 times to mix contents (DO NOT VORTEX).
15. Precipitate DNA at -20^{o}C overnight (if in a hurry, at -80^{o}C for ~1 hour).
16. Centrifuge for 20 minutes at room temperature on maximum speed.
17. Remove and discard supernatant CAREFULLY (DNA pellet may be loose).
18. Add 1mL of ice cold 70% ethanol to each sample (DO NOT VORTEX!).
19. Centrifuge for 10 minutes at room temperature on maximum speed.
20. Remove and discard supernatant CAREFULLY.
21. Air dry DNA pellets at room temperature for ~10-15 minutes.
22. Rehydrate DNA pellet in either:
    - 1X TE buffer (30-50uL)
    - 10mM Tris-HCl pH7.5 (30-50uL)
    - ddH_2O (30-50uL)
23. This 'clean prep' can be stored at -20^{o}C until ready for PCR experiments.

C. Gel electrophoresis:

1. Assemble agarose gel casting apparatus to fit suitably sized gel for experiment.
2. Weigh out agarose powder and mix in gel running buffer in a clean Erlenmeyer flask (1X TAE buffer, 1X TBE buffer, or 1X SB buffer). A 100mL agarose gel typically fits well into the Bio-Rad Wide Mini-Sub GT Cell apparatus.
3. Microwave agarose-buffer solution in 30 second increments until the agarose powder is completely dissolved.
4. Cool this agarose solution under cold running tap water until the solution becomes slightly viscous in consistency.
5. Add EtBr to 0.5µg/mL final concentration. Mix well by swirling the flask until the agarose gel solution is uniform in color (should be colorless, but with a hint of red from the EtBr).
6. Pour agarose gel solution into gel casting apparatus and allow to set.
7. Prepare enough running buffer to fill the Bio-Rad Wide Mini-Sub GT Cell apparatus (~650mL). Must use the same buffer (1X TAE buffer, 1X TBE buffer, or 1X SB buffer) that was used to make agarose gel.
8. Submerge set agarose gel into running buffer in the Bio-Rad Wide Mini-Sub GT Cell apparatus.
9. Load PCR samples along with 100bp DNA ladder and run for ~30 minutes at 90V using the Bio-Rad PowerPac Basic Power Supply.

D. Reagents used:

Sodium borate (SB) buffer (20X stock solution in 1L, pH 8.0):
45g Boric acid
8g NaOH
Make final volume up to 1L by adding ddH_2O

Tissue prep solution:
5mM Tris-HCl, pH 8.0
10mM EDTA
10mM NaCl
0.3% SDS

Tissue digestion buffer:
Tissue prep solution
Proteinase K

- Make up enough 'active' tissue digestion buffer to submerge all collected tissues, by adding Proteinase K into tissue prep solution for a final concentration of 0.08mg/mL

Tris-acetate-EDTA (TAE) buffer (50X stock solution in 1L):
242g Tris base
57.1mL Glacial acetic acid
100mL 0.5M EDTA, pH 8.0
Make final volume up to 1L by adding ddH_2O

Tris-borate-EDTA (TBE) buffer (5X stock solution in 1L):
54g Tris base
27.5g Boric acid
20mL 0.5M EDTA, pH 8.0
Make final volume up to 1L by adding ddH_2O

Tris-EDTA (TE) buffer (10X stock solution):
100mM Tris-HCl, pH7.4
10mM EDTA, pH 8.0

Tris-HCl (1M solution in 1L):
121g Tris base in 800mL ddH_2O
Adjust pH with HCl
Make final volume up to 1L by adding ddH_2O

E. Disposables/Chemicals and Reagents/Equipment used:

Disposables:

- 1.5mL tubes (Axygen 1.5mL Microtubes, Homo-polymer, boil-proof. Cat# MCT-150-C)

Chemicals and Reagents:

- 100bp DNA Ladder (500µg/mL) (New England BioLabs, Cat# N3231S)
- Agarose (electrophoresis grade) (Bioshop, Cat# AGA002.100)
- Boric acid (MW=61.83g/mol) (electrophoresis grade) (Fisher Scientific, Cat# BP168-1)
- Chloroform (MW=119.38g/mol) (molecular biology grade, peroxide free) (Fisher Scientific, Cat# BP1145-1)
- EDTA (Ethylenediaminetetraacetic acid, free acid, electrophoresis grade) (MW=292.25g/mol) (Fisher Scientific, Cat# BP118-500)
- EtBr (Ethidium Bromide solution, 10mg/mL) (Bio-Rad, Cat# 161-0433)
- Ethanol (100% and 70%)
- Glacial acetic acid (MW=60.05g/mol) (Fisher Scientific, Cat# A38212)
- Phenol (125:24:1) (phenol/chloroform 5:1 with Isoamy Alcohol, pH 4.3 $\pm$0.2, biotech grade) (Fisher Scientific, Cat# BP1754-400)
- Proteinase K (20mg/mL) (New England BioLabs, Cat# P8102S)
- NaOAc (sodium acetate, anhydrous, enzyme grade) (MW=82.03g/mol) (Fisher Scientific, Cat# BP333-500)
- NaCl (sodium chloride) (MW=58.44g/mol) (Fisher Scientific, Cat# BP358-10)
- SDS (sodium (lauryl) dodecyl sulfate) (MW=288.42g/mol) (Thermo Scientific, Cat# 28365)
- NaOH (sodium hydroxide) (MW=40g/mol) (pellets, caustic soda) (Fisher Scientific, Cat# S320-500)
- Tris base (Tris (Hydroxymethyl) Aminomethane) (MW=121.14g/mol) (Bioshop, Cat# TRS001.10)

Equipment used:

- -80°C freezer (Sanyo VIP Series)
- -20°C freezer (Wood's brand)
- 4°C fridge (Sanyo Labcool)
- 55°C waterbath (Thermolyne Dri-Bath)
- Bench top centrifuge (eppendorf centrifuge 5424)
- Gel apparatus (Bio-Rad Wide Mini-Sub GT Cell apparatus)
- Gel apparatus power supply (Bio-Rad PowerPac Basic Power Supply)
- Scale (Acculab VI-350)
- Stirrer (Thermolyne nuova II stirrer)
- Vortexer (VWR Vortex-Genie 2)

APPENDIX 2.10: Genotyping assay for *Scn8a*^{dmu} mice

The *degenerating muscle* (*dmu*) mutation consists of a single nucleotide deletion in exon 10A of the *Scn8a* coding sequence (position 1538 of GenBank accession number NM_011323) (Côté et al., 2005). This mutation results in the ablation of a *Bsl*I recognition sequence (Côté et al., 2005). Amplifying a segment of the *Scn8a* coding sequence that contains the mutation and cutting the products with the *Bsl*I restriction enzyme, we obtain the following (Figure 2.1):

Wildtype: 174bp, 41bp*
Heterozygote: 215bp, 174bp, 41bp*
dmu homozygote: 215bp
(*this PCR product is difficult to detect)

1. Collect animal tissue for genomic DNA extraction using proteinase K and isolate with phenol chloroform extraction (refer to Appendix 2.10).
2. Amplify a segment of the *Scn8a* coding sequence that contains the mutation using the following primers to set up PCR samples:
   (*dmu* forward) 5'-CGG-GCA-CCG-TCT-CAG-AAG-AT-3'
   (*dmu* reverse) 5'-TCC-TTC-TCA-TGC-CAT-CTT-CC-3'

***dmu* PCR sample setup:**

Reagent	Stock concentration	Volume per reaction (µL)
ddH_2O	-----	6
dmu forward primer	10µM	1
dmu reverse primer	10µM	1
DNA template	-----	2
Taq 2X Master Mix	2X	10
TOTAL		20µL

3. Run PCR samples using the **'*dmu*' program** (PCR program below).
4. Digest PCR products using the *Bsl*I restriction enzyme at 37°C for a minimum of 5 minutes in 1.5mL tubes.

***dmu* PCR product digestion reaction setup:**

Reagent	Stock concentration	Volume per reaction (µL)
ddH_2O	-----	8.5
FastDigest Buffer	10X	1
*Bsl*I	-----	0.5
PCR product	-----	5
TOTAL		15µL

5. Run digested PCR product on a 1% agarose gel along with 100bp DNA ladder (refer to Appendix 2.10).

'*dmu*' PCR program (G-Storm GS1 Thermal Cycler)

1. Heated lid/hot start — T=94°C, 3 minutes
2. DMU X 35 cycles
3. Denaturation — T=94°C, 1 minute
4. Annealing — T=59°C, 1 minute
5. Elongation — T=72°C, 2 minutes
6. Elongation (final) — T=72°C, 10 minutes
7. Hold/store — T=4°C, ∞

Disposables/Reagents/Equipment used:

Disposables:

- 0.2mL tubes (Axygen 0.2mL PCR tubes with flat caps. Cat# PCR-02-C)
- 1.5mL tubes (Axygen 1.5mL Microtubes, Homo-polymer, boil-proof. Cat# MCT-150-C)

Reagents used:

- *BslI* restriction enzyme (FastDigest BseLI) (Thermo Fisher Scientific Fermentas, Cat# FD1204)
- *Taq* 2X Master Mix (New England BioLabs, Cat# M0270S)

Equipment used:

- 37°C waterbath (PolyScience Temperature Controller)
- Bench top centrifuge (eppendorf centrifuge 5424)
- Thermocycler (G-Storm GS1 Thermal Cycler)
- Vortexer (VWR Vortex-Genie 2)